GEOLOGY, DISTRIBUTION AND GEOCHEMISTRY OF IMPACT MELT AT THE MISTASTIN LAKE IMPACT CRATER, LABRADOR

CASSANDRA LORRAINE MARION

Geology, distribution and geochemistry of impact melt at the Mistastin Lake impact crater, Labrador.

By
Cassandra Lorraine Marion, B.Sc. (Hons.)

A thesis submitted to the School of Graduate Studies in partial fulfillment of the requirements for the degree of

Master of Science

Department of Earth Sciences
Memorial University of Newfoundland
St. John's Newfoundland

July 2009

Abstract

The Mistastin Lake crater in Labrador, Canada (55°53'N; 63°18'W) contains a 3 km wide central uplift within a 19 x 12 km wide lake and has a rim diameter of 28 km. The projectile impacted Mesoproterozoic crystalline target rocks approximately 36 Ma ago.

This study consists of detailed field observations; geology, geochemistry, and geochronology of impact melt and target rocks of the Mistastin impact crater. To determine (1) the significance of the relationship between preserved melt thickness and vesicularity in the melt rocks; 2) the scale and origin of compositional heterogeneities in impact melts produced in craters of moderate size and the relationship between entrained mineral clasts and impact melt composition; and 3) the origin of zircon clasts in the impact melts.

Melt rocks that are distributed around two thirds of the lake in patchy outcrops vary in thickness from <1m to 80 m. Previous estimates suggested that a coherent melt sheet up to 200m thick formed in the crater and that the much smaller preserved unit thicknesses are the result of glacial erosion. New field observations and laboratory measurements identify a relationship between distribution, thickness and vesicularity of melt rock units. The thickest melt-rock occurrence, at Discovery Hill, is massive, crystalline, non-vesicular and 80 m thick. In contrast, 1-2 m thick melt-rock occurrences elsewhere in the crater are glassy and vesicular. Measured vesicularities vary from 0.1 to 31 % and follow an empirical relationship ($\varphi = 30 \pm 2\ h^{-0.8 \pm 0.1}$) whereby vesicularity φ increases with decreasing melt rock thickness h. Plagioclase microlite crystallization temperatures of thin melt rock outcrops are very high (>1300 °C), indicating rapid cooling rates. Lower crystallization temperatures (~1245 °C) for the Discovery Hill melt are consistent with slower cooling rates. The data suggest that the pre-erosional melt sheet at Mistastin was not uniform and, consequently, previous estimates for the level of erosion and the volume of the melt produced have been overestimated.

Target rocks which contributed to the impact melt consist principally of anorthosite, mangerite and granodiorite. Chemical compositions of bulk samples of thirty-three melt rocks and fourteen target rocks were measured by XRF and SN-ICPMS. Matrix compositions of nine samples of impact melt rocks were determined by EPMA and LA-ICPMS. Zircon grains from four samples of target rock and zircon clasts from three samples of impact melt rock were measured for multi-element composition, U-Pb age and Hf-isotopic composition by LA-(MC)-ICPMS.

The data reveal compositional heterogeneities in the impact melts on the scales of both bulk samples and matrices. Bulk samples can be divided into compositions with high and low concentrations of high-field strength elements (HFSE; Ti, Zr, Nb) and Fe, Ba, Ce and Y. High HFSE-type melt rocks formed when impact melt entrained large quantities of clasts from mangerite, which is rich in HFSE. Matrix compositions of bulk samples do not show the HFSE distinction but are affected by the introduction of low-temperature melts from the clasts to form dispersed, micron-scale silica-rich heterogeneities. Both clast entrainment and melting are more extensive for the thicker flow units which had a higher heat capacity for melting and cooled more slowly than thinner flows.

The best estimate of the sources of the initial impact melt is ~73% anorthosite, ~7% mangerite and ~20% granodiorite, based on least-squares modeling of major element compositions of the matrices of thinner flows. Zircon derived from anorthosite can be distinguished from zircon from mangerite and granodiorite on the basis of higher Nb/Ta and Eu/Eu* ratios and more negative initial ε Hf values. Zircon clasts greater than 40 microns in size in the impact melt rocks are dominantly or exclusively derived from mangerite and granodiorite. Hence zircon may be a poor provenance indicator for target rock contributors to impact melts.

Acknowledgements

Many people contributed to the production and completion of this thesis. Firstly I would to thank my supervisor, Paul Sylvester for his continued advice and academic support. Thank you for presenting me with this project and providing me with the tools to complete it. Paul worked extensively throughout this thesis, especially during the final stages where I really needed his expertise and guidance.

Thanks to Alison Leitch, a member of my thesis committee who actively became involved in the geophysical aspects of Chapter 2 in this thesis. Her expertise in this area was very beneficial and aided significantly to my learning experience. And Derek Wilton, for his initiative to discover all the wonders of Mistastin Lake and for his continued interest in this project.

Many technical staff at Memorial University contributed to this thesis. I would particularly like to thank Mike Tubrett, Michael Shaffer, Marc Beauchamp and Rebecca Lam from the MAFIIC geochemistry labs and Pam King, Lakmali Hewa and Wanda Aylward in the Earth Sciences department. Their assistance in many aspects of sample preparation, sample analysis and data reduction is greatly appreciated as well as the many discussions we shared. Thank you to Douglas Hall at the microanalysis lab at the University of NB. And Samantha Primmer for a productive and entertaining summer of vesicularity measurements.

This study was made possible by the generous financial contributions of NSERC, the Canadian Space Agency's Canadian Analogue Research Program (CARN), Memorial University of Newfoundland and the Indian and Northern Affairs Canada Northern Scientific Training Program.

I would also like to thank the Innu Nation for graciously allowing me to conduct research at Mistastin Lake and to Tony Jenkinson for providing me with a wealth of knowledge about the field area. To Wayne Jenkins for his patience with satellite phones and for organizing helicopter rides at a moment's notice.

Many of my fellow graduate students must be thanked for their assistance and participation in academic discussions which helped to complete this project. To Kate Souders, who helped with just about anything from geochemistry to a place to stay since the day we arrived in Newfoundland. Andreas Atle, for being a mathematical mastermind and having a good Swedish sense of humour and to many others including: Karina Zavala, Peter Valley and Dave Lowe.

I would like to thank my whole family for their love and support, encouragement and confidence in me. Mom, you are the best fan a gal could have. Above all, I must thank my partner in life and field assistant, Marc Beauchamp. He is the best person I have ever known. He gave me endless support, patience and love and this experience would not have been the same without him. In addition, his geological expertise and

strong back were invaluable. His effort never wavered in the field or at home, he always gave me 100% even when the black flies were at their worst. Thank you.

Table of Contents

List of Figures

List of Tables

Chapter 1

Introduction and Overview

1.1 INTRODUCTION

The search for impact craters on Earth has increased exponentially in the last 30 years as the interest in cratering studies has grown with our understanding of cratering processes. One of the most elusive processes is shock induced melt production and distribution. The Mistastin Lake crater, Labrador, may provide some important insights into this process. The crater was first identified as an impact crater by Taylor and Dence (1969). The melt rocks at Mistastin have since been studied in some detail by Currie (1971), Grieve (1975) and Marchand and Crockett (1977).

The present study focuses on the geology of impactites, in particular; the geochemistry, petrology and distribution of preserved impact melt rocks at Mistastin Lake. This study aspires 1) to evaluate the significance of the relationship between preserved melt thickness and vesicularity in the melt rocks at Mistastin; 2) to reevaluate the scale of heterogeneities in the impact melt rocks and the relationship between entrained mineral clasts and impact melt composition; and 3) to determine if the origin of zircon clasts in the impact melts can be used to estimate target rock contributions to impact melts.

This chapter is the background and framework for this thesis. First a basic description of the importance and formation of impact craters is explained, followed by a discussion on shock melting, production and distribution. A brief description of planetary

differences in impact melting is presented followed by the role of clasts in impact melts and impact melt composition. The regional geology and a brief history of the Mistastin area are introduced, followed by the thesis objectives and a brief summary of the main chapters.

1.2 IMPACT CRATERS

1.2.1 Importance of impact craters

With the exception of Earth, Venus and Jupiter's satellite Io, impact craters are the most common surface feature observed on all solid planetary bodies in our solar system. Unfortunately, Earth's cratering record is incomplete as there are many factors working against the preservation of impact craters and related deposits. Earth is subjected to continuous erosion by wind, water and ice and a variety of geological processes, most important of which is plate tectonics. As Earth's crust is continuously recycled, so too is the cratering record. What's more, the population of craters on Earth is partial to larger and younger craters (French, 1998). The Moon's cratering record, not afflicted by Earth's destructive forces is in much better shape where the sole destructive force are impacts themselves.. The Moon, Mars and even Venus have been used to determine impact rates, bombardment history and cratering processes where impact structures are well preserved. The bombardment history is an important tool for the understanding and prediction of future cratering rates. Voyages to the Moon, such as in the Apollo and Luna missions, have provided information for over a billion years of planetary evolution. However, no matter how much we learn from the Moon and other planets, only Earth is accessible at present to groundtruth and compare and confirm computational and experimental results

of cratering processes (Grieve, 1987). In addition, meteorite fragments recovered from small craters can help identify the origin of the impactor. On Earth, meteorite impacts have been identified as the likely cause of mass extinctions (Raup, 1991). The dinosaurs for example, are thought to have been wiped out by the Chicxulub impact into the Gulf of Mexico ~65 Ma ago and the effects it had on the atmosphere. Mistastin Lake may be related to a late Eocene extinction accompanied by the Popigai and Chesapeake Bay events, but this hypothesis is in need of more precise age constraints. Impacts may also facilitate massive tsunami deposits, and incinerating wildfires (Marvin, 1990).

1.2.2 Crater Formation

Cratering mechanics (e.g. Holsapple and Schmidt, 1987; Melosh, 1989; O'Keefe and Ahrens, 1993) are a series of stages through which an impact crater is created. Firstly, a projectile, possibly an asteroid or comet traveling at $\geq$15 km/s impacts a planetary body. During the (1) contact and compression stage, the projectile intrudes the target at about the same depth as the diameter of the projectile. The kinetic energy transferred to the target by the hypervelocity impact compresses and accelerates the target material downwards and outwards. The increase in internal energy in the target rocks upon impact results in large shock pressures and temperatures that can deform, melt and vaporize the projectile and/or target material. These modifications to target materials are regarded as shock metamorphic effects; of which shock induced melting and melt products will be discussed in detail in this study. A powerful shock wave is created during stage (1) which propagates into the target, expands and then weakens to elastic waves during the (2) excavation stage. A rarefaction wave excavates the target material (fractured and

brecciated target rocks and impact melt) to form an approximately hemispherical transient cavity. This is followed by (3) a modification stage where normal geological processes, such as gravity, take over to form the final crater. At this point, the outer portions of the cavity and surrounding area collapse inward and downward. The size of the crater can be up to 20-30 times the size of the projectile itself (French, 1998).

The size and type of crater depend upon the energy released. Impact craters are divided into three classes: simple, complex and multi-ring basins. Simple craters are formed from small impacts and form a bowl-like hemispherical shape (e.g. Barringer crater, Arizona). Complex craters are shallower craters, typically larger than simple craters and are identified by a characteristic central structural uplift in the form of a peak or peak-ring rim (e.g. Mistastin Lake, NL and West Clearwater, QC, respectively). In addition to a central uplift, the final form of a complex crater has faulted rim terraces and annular trough. Multi-ring basins are the result of very large impacts and consist of large craters with multiple rings. All three types of craters are observed on the Moon but multi-ring basins on Earth are rare and those suspected of being multi-ring basins are still debated as they are among the oldest and least preserved craters (Vredefort, Sudbury and Chicxulub). Details about the formation of central uplifts can be found in Dence (1968), Grieve et al. (1981), Melosh (1989) and Grieve and Cintala (1992; 1994).

1.2.3 Shock Melting

The initial post-shock temperatures can reach over 2000°C in the target rocks close to the impact point (O'Keefe and Ahrens, 1975; Melosh, 1989; in French, 1998). When the immense pressures of the shock waves disperse, the extremely high

temperatures incur immediate and complete melting of a large volume of rock. Though many minerals and materials have different melting points, these temperatures are significantly higher. Complete melting of target rocks occurs at shock pressures of over 60 GPa and partial melts occur between 40-50 GPa (Stoffler and Grieve, 2007). Once produced, the impact melt joins the general movement and flow, downward and outward while engulfing less strongly shocked and accelerated target materials in the outer parts of the growing crater (Melosh, 1989). This process is quite complex and is still not well understood.

1.2.4 Impact melt production and scaling

Impact melt production and volume in addition to other cratering concepts have largely been explored through combined computational and model studies from observational data of small craters, e.g. the 3.8 km diameter Brent crater in Ontario (Grieve and Cintala, 1981; 1992). Recent numerical modeling (Pierazzo et al. 1997), field observation studies (Grieve and Cintala 1992) and experimental studies (Kiel et al., 1997) have provided some understanding of melt production in crystalline targets. Factors that may control the production of melt include: the kinetic energy released upon impact, the target density (lithology), the impactor's mass, density (lithology) and velocity, the angle of the impact, gravity, etc. Scaling of crater phenomena consists of dimensional analysis of both target and impactor variables to derive numerical relationships which can be applied to craters of varying size. Noted studies of impact melt production and scaling include O'Keefe and Ahrens (1977), Dence et al. (1977), Croft (1982; 1985), Grieve and Cintala (1981), Holsapple and Schmidt (1987), Schmidt

and Holsapple (1982), Schmidt and Housen (1987) and more recently and commonly accepted is by Grieve and Cintala (1992). Results of this study are supported by numerical modeling by Pierazzo et al. (1997). It is clear that there is a threshold velocity under which no melt will be formed such as in very small simple craters. Unfortunately, it is as yet impossible to properly address shock melting through experimentation because the threshold velocities (≥15 km/s) required for significant melting or vaporization cannot be attained in a laboratory (Holsapple and Schmidt, 1987; Melosh, 1989).

Many important relationships however have been identified through observation. Simplified they outline a single relationship: "impact melt volume relative to crater size increases with increasing size of the event" (Grieve and Cintala, 1992). This indicates that as the crater diameter increases, the volume of melt and vaporized material may approach the volume of the crater itself (Melosh, 1989). Schmidt and Housen (1987) derived the following relationship for the transient cavity diameter (D_{tc}), defined as

$$D_{tc} = 1.16\left(\frac{\rho_p}{\rho_t}\right)^{1/2} D_p^{\,0.78} V_i^{\,0.44} g^{-0.22} \qquad (1),$$

Where ρ_p and ρ_t are the density of the projectile and target, respectively, D_p is the diameter of the projectile, V_i is the impact velocity and g is the surface gravity. Therefore any transient cavity diameter can be estimated for any given D_p and V_i (units in cgs).

Assuming a parabolic transient cavity in cross-section, Grieve and Cintala (1992) consider a spherical projectile impacting onto a planar target and the resulting shock stress and impact heating. Using equation (1) to define transient cavity diameters, they suggest that for an impact into a crystalline target, the volume of melt, V_m (km^3),

produced increases exponentially with the transient crater diameter, D_{tc} (km), in this general form:

$$V_m=cD_{tc}^{d} \quad (2),$$

where c and d are constants derived from theoretical and experimental cratering studies for different impactor lithologies. Approximate values for a chondrite (dense basalt) impactor at a velocity of 15 km/s are c=0.000621 and d=3.85. Constants are listed in Table 3 in Grieve and Cintala (1992) for iron, chondrite and water-ice projectiles at varying impact velocities. For complex craters, modification scaling by Croft (1985) is considered to determine the transient cavity diameter.

The method outlined above is not useful for determining the amount of melt produced in dominantly sedimentary targets such as for the Ries and Logoisk craters. Impact melt volumes in these craters are significantly lower than those of crystalline targets, due to the massive expansion of volatiles from the shock-heated sediments (Kieffer and Simonds, 1980; Grieve and Cintala, 1992). However some studies disagree, Osinski et al. (2008) and Wünneman et al. (2008) explain that the apparent lack of impact melt rocks is due to the difficulties in recognizing impact melts from sedimentary rocks.

Grieve and Cintala (1992) compared the numerical models derived from equations (1) and (2) to observed melt volumes, which are calculated assuming vertical cylinder volumes, the radial extent and thickness of preserved impact melt rocks. Measured melt volumes are different than calculated values by a factor of 2 - 7. These uncertainties make this model good enough for rough predictions but more study is needed on the constraints of the variables in these equations, on the origin of the uncertainties and better field data to improve the precision of impact melt modeling.

Melt rock preservation varies from crater to crater, as most craters on Earth are eroded or buried. In the case of buried craters, it would be difficult to determine the radial extent of the melt even if the thickness is known, as drilling is very costly and geophysical data is not as reliable as field observations. In the case of erosion, it is likely that both the radial extent and original thickness of the melt rocks have been modified. Erosion, particularly by large ice sheets, is unsteady and non-uniform, which makes it difficult to estimate how much has been removed and in what proportions. In addition, impact melt in ejecta and breccias may not be included in the measurement of the total observed melt volume as these are the first deposits subjected to erosion.

1.2.5 Impact melt products and distribution

The resulting melt products and distribution of impact melt depend largely on the volume of melt produced, the target lithology and the crater type. For example, impacts into crystalline targets form more melt than those of sedimentary targets. Small impacts tend to produce less melt but eject much more melt than larger craters. Variations in crater type, and therefore crater structure result in variations of melt distribution. As a result, impact melt rock can occur 1) as isolated glassy bombs; 2) as glassy or recrystallized masses in mixed breccias; 3) as thick sheets of igneous rock; and 4) as minor dikes and irregular intrusions into the basement of the crater (Dence, 1971). Any and all of these occurrences may be observed at a single crater. In small craters only the first and second type of melt may be found whereas in medium to large craters, some of the melt is ejected outside the rim and the remainder coats and intrudes the cavity floor.

Glassy melt bombs typically form part of the ejecta found inside and outside the crater rim. In larger craters, these bombs may be more than 25 cm in diameter, contain clasts of target material and are commonly vesicular. The glassy or recrystallized melt particles are part of suevite: unconsolidated breccias that can be deposited through ground surge at the base of a larger melt body or as fall-in and fall-out breccias. These are observed at the Ries crater, the origin of the term suevite, where the melt particles show evidence of aerodynamic quenching. In small craters, the majority of melt occurs as glassy bombs or particles and the ejection of any melt occurs prior to crater wall slumping and deposition of fallback breccias.

In medium to large craters, impact melt remains within the crater and spreads out along the crater floor prior to wall collapse, breccia fallback, and uplift formation. Where sufficient amounts of melt are produced, the melt occurs as a subhorizontal melt sheet. In small to medium-sized craters, or larger craters with sedimentary targets, melt occurs as fragments and as lenses of melt bodies within breccias. Table 1.1 lists examples of the extent of preserved melt sheets and the estimated volume of melt rocks within terrestrial craters. For the specific conditions and uncertainties of each crater, refer to Grieve and Cintala (1992). The thick sheets are commonly distributed in an annulus around one or more central uplifts within the crater. The radial extent of the melt increases with increasing size of craters with similar target lithologies; thick igneous sheets spread increasingly further towards the rim of the crater, and in some cases even overlap the rim. The outer limits of the melt sheets may thin and spread out into tongues.

In many cases, field constraints make it very difficult to outline the dimensions of preserved melt sheets. The Vredefort crater, South Africa, is reportedly the largest impact

crater recorded on Earth, but only impact melt dikes in basement rocks escaped erosion. The Sudbury impact crater has been intensely deformed tectonically and eroded at the margins, making it very difficult to define the exact radial extent of the melt sheet. In addition, the melt sheet has been differentiated and its origin and thickness has long been debated. It is also thought that some impact-induced internal magmatism contributed to the Sudbury Igneous complex. West Clearwater, Mistastin, Lappajärvi and many other craters are presently filled by large lake(s) and lake sediment where the principal locations to look for the thickest unit of melt is submerged. At these locations there are a very limited number of melt rock exposures.

Finally, impact melt occurs as dikes in basement rocks and breccias. The dikes are commonly fracture-fill deposits from the later stages of crater formation. They have been observed in all areas of complex craters, particularly within central uplift regions. Note that pseudotachylite veins are not considered a shock-induced melt rock as it is formed through the frictional melting of mobilized basement rocks rather than shock metamorphism. The primary sources for the discussion in this section are Dence (1971), Dressler and Reimold (2001) and Grieve and Cintala (1992).

1.2.6 Planetary differences in crater scaling and melting

In the context of impact cratering, the principal characteristics that distinguish terrestrial planets are gravity, the velocity of the impacting projectile and atmospheric pressure in the case of very small impacts. The Moon has an abundant source of pristine craters to which terrestrial structures may be compared but the conditions under which craters form on both bodies are different enough that direct comparisons cannot easily be

made. Gravity on the Moon is one sixth of that on Earth and Venus. An impactor on the Moon would form a larger crater than the same impactor on Earth (Schmidt and Housen, 1987; Cintala and Grieve, 1994). This also affects the type of impact structure, for example, the transition from a simple crater to a complex crater on Earth occurs between a crater diameter of 2-4 km (sedimentary – crystalline targets), whereas on the Moon it occurs at ~20 km diameter (French, 1998). For equally-sized projectiles and velocities, crater diameter on the Moon is ~50% larger than the same impact on Earth, and transient cavity volumes on the Moon are more than a factor of 3 larger than on Earth (Cintala and Grieve, 1994).

Although crater size is largely dependant on gravity, its effect is insignificant on the amount of impact melting when compared to the velocity and mass of the impactor. Between the Moon and larger terrestrial bodies, a tiny difference in impact velocity (e.g. 1-5 km/s) is enough to produce a much larger volume of melt and vapour on Earth or Venus for a projectile of identical size. In fact, the volume of melt on Earth and Venus relative to the transient cavity size can be over a factor of 5 and 6, respectively more than for craters on the Moon (Cintala and Grieve, 1994).

1.2.7 The role of clasts in melt rocks

Most melt rocks contain target rock fragments or clasts which were entrained into the melt during the excavation stage or deposited thereafter by fallback breccias. For this reason, the basal and upper contacts of melt sheets are clast-rich and generally grade to clast-poor melt in the centre. Very small (μm to mm-scale) clasts are found in every type of melt occurrence whereas larger clasts up to several meters in diameter occur solely in

thick melt sheets. Phinney and Simonds (1977) suggest that extensive and extremely rapid mixing of target materials results from turbulent flow of the melt sheet. In large craters, clasts can be carried over distances of tens of kilometers, which explains why clasts within the melt rocks located several kilometers from the impact point may be intensely shocked. As the volume of melt increases, so does capacity to incorporate more clasts (Onorato et al., 1978). Some of the clasts, even the most refractory ones may suffer complete melting, partial melting and digestion or simply be frozen in the melt. Clasts play an important role in the cooling and crystallization of the melt. An increase in clast abundance decreases the mean temperature of the melt, and larger volumes of melt are capable of resorbing more clasts. Many small clasts are much more effective cooling agents than several large clasts, but much smaller clasts melt more quickly than the larger ones (Onorato et al. 1978). Once an equilibrium temperature is reached, the clasts are no longer an encumbrance on the cooling process. As crystallization is affected by cooling rates, textures in the melt matrix become glassy and occasionally show preferred orientation in proximity to larger cm- to m-scale clasts. Melted and partially melted clasts contribute to the overall composition of the melt matrix.

1.2.8 Melt composition

Impact melt rocks are similar to volcanic igneous rocks in that they may exhibit a variety of igneous textures; however there are many features by which they can be differentiated. Impact melts are most often formed from a mixture of different target lithologies which result in peculiar melt chemistries. In addition, fractionation only occurs in the thickest melt sheets due to rapid crystallization. Melting takes place in

Earth's near-surface, just below the point of impact which typically produces crustal melts with a crustal signature (Dressler and Reimold, 2001). Melts also have a distinctive clast distribution and content, shock-metamorphosed inclusions and evidence of extremely high temperatures (French, 1998). Also, impact melts can be enriched in elements from the projectile as it melted and/or vaporized in conjunction with target rocks. Projectile contamination is commonly in the form of siderophile elements (Ni, Co, Cr) and platinum group elements (PGEs) such as osmium and iridium. These geochemical signatures are often used to identify the origin of individual impactors and are more easily identified in impact melts of crustal rocks which are poor in siderophile elements. However, this becomes increasingly difficult when there are numerous target lithologies or the target is mantle-derived. Comet impacts rarely leave any geochemical signatures as more than 50 % of the projectile consists of volatiles which easily escape into the atmosphere (Dressler and Reimold, 2001).

1.3 REGIONAL GEOLOGY

Labrador has a long and interesting geologic history. In this study, the target area of the Mistastin impact is of some importance as these rocks were permanently altered by the impact. The projectile impacted the north-east corner of the Mesoproterozoic Mistastin batholith (Emslie et al., 1980) an approximately 5,000 km^2 and 80-km wide magmatic body, which is part of the larger Nain Plutonic Suite (NPS) of Labrador. The NPS extends for more than 20,000 km^2 and is composed of a range of lithologies: principally anorthosite, leuconorite, quartz monzonite and granite with secondary gabbro, troctolite, ferrodiorite and mangerite (e.g. Ryan and James, 2004). Mistastin Lake is

located within a large granodiorite body that includes belts of anorthosite and mangerite which are elongated from NW to SE across the lake, and minor outcrops of meta-quartz gabbro. The granodiorite and mangerite contain xenoliths of gneiss and other granitic sources. The rim of the crater extends more than 9 km from the lakeshore. To the north, the most prominent target lithology is a series of reworked Archean gneisses and granitic intrusions.

1.4 BRIEF HISTORY OF THE MISTASTIN AREA

Mistastin is known to the native peoples of Labrador as Kamestastin. Mistastin has long been the home of many native peoples from the Clovis culture over 11,000 years ago, to the Inuit and Innu. Kamestastin translates to 'the place where the winds never stop'. In fact, the Innu claim that if you point at Discovery Hill, it will bring bad weather. Mistastin is rich with archeological wonders ranging from chert spearheads and tools to teepee rings. Presently, the Innu own the rights to the land around the Mistastin area. There are no permanent residents today but many Innu benefit from the great caribou hunting grounds and very large lake trout in the summer and fall. The lowlands are lined with black spruce and alders and everywhere else is covered in shrubs, tundra grass, till and berries, particularly wild blueberries, partridgeberries and the occasional bakeapple plants. There are so many blueberries; it is difficult not to step on them. Apart from the winds, Mistastin is a beautiful and thoroughly enjoyable location.

1.5 THE MISTASTIN IMPACT

Mistastin was impacted by a projectile approximately 1.4 kilometers in diameter (according to the equations suggested by French (1998)). The composition and origin of the projectile has not yet been identified as there is very little projectile contamination in the Mistastin impactites (Morgan et al. 1975; Palme et al. 1978).

Assuming a spherical impactor traveling at a velocity of 20 km/s and a vertical impact, the impactor hit with an energy of 1.0×10^{21} J. Note that a vertical impact is highly unlikely, and the most probable impact angle of a comet or asteroid is 45° (Artemieva and Ivanov, 2001). This was enough energy to form a complex structure with a final crater of 28 km in diameter Grieve (1975). Using the numerical relationships derived by Grieve and Pesonen (1992), Grieve and Pilkington (1996) and Therriault et al. (1997) for a complex crater with a crystalline target, the depth of the apparent Mistastin crater would be approximately 628 m with a structural uplift 9.3 km wide and rise 2.6 km above the crater floor. At present, the erosional remnant of the Mistastin crater has an unknown depth; the central uplift rises about 70 m above the lake level (400m above SL) and has an exposed width of approximately 3.5 x 4 km.

1.6 THESIS OBJECTIVES

This thesis presents detailed field observations of impactites, a geochemical and textural analysis of impact melt rocks as well as geochemical and geochronological data on the target rocks of the Mistastin Lake impact crater in Labrador, Canada. The overall goals of this study are to describe and characterize the Mistastin impactites, particularly the melt rocks in order to 1) explain the significance of the preserved melt thicknesses

and associated textures; 2) to determine the source and scale of heterogeneities in the impact melt rocks and their relationship with target inclusions; and 3) to determine the origin of zircon inclusions in the melt rocks.

1.7 STRUCTURE OF THE THESIS

1.7.1 Introduction

This thesis is divided into four chapters: Chapter 1 is an introductory chapter intended to excite and provide the reader with sufficient background on impact cratering and impact melt studies in addition to detailing the scope and goals of the research. Chapters 2 and 3 are extended versions of papers submitted to be published that focus on specific features of this study. Some foreseeable repetition throughout the thesis was inevitable as chapters 2 and 3 were designed to be stand-alone manuscripts. Chapter 4 is a summary and conclusion to the study designed to unite all the material presented together. The following is a brief summary of the objectives of chapter 2 and 3.

1.7.2 Chapter Two – "Geology and impact melt thickness of Mistastin Lake crater, Labrador." (C.L. Marion, P.J. Sylvester and A.M. Leitch)

This paper addresses the geology of impactites and the distribution of preserved impact melt rock thicknesses at the Mistastin Lake impact crater, Labrador. The paper provides a detailed account of the stratigraphic relationships and petrological analysis of the impactites, specifically, an analysis of vesicularities and plagioclase crystallization temperatures in impact melt rocks. The data are used to present a petrological explanation for the variation of impact melt texture and preserved melt thicknesses.

1.7.3 Chapter Three – "Composition and heterogeneity of impact melt at Mistastin lake crater, Labrador." (C.L. Marion and P.J. Sylvester)

This paper addresses the geochemistry of impact melt rocks and the complex relationships between them and their target rocks at the Mistastin Lake crater, Labrador. This is accomplished by characterizing the major and trace element composition of the impact melt rocks and target rocks distributed around the lake. In addition, geochemistry, Hf isotope chemistry and geochronology of target zircons and zircons present in the impact melt rocks are determined to confirm melt rock chemistry. The relationship between melt rocks and their target rocks is of importance in understanding the processes involved in impact melting and current melt rock distribution.

1.8 CO-AUTHOR CONTRIBUTIONS

Chapters 2 and 3 have each been submitted for publication to the international journal of Meteoritics and Planetary Science and Planetary and Space Science, respectively. These submissions include two co-authors. My supervisor, Dr. Paul Sylvester, conceived and managed the project and provided considerable instructional and supervisory input toward the thesis. Dr Alison Leitch assisted solely with respect to Chapter 2, particularly with the geophysical aspects of the study such as the explanations for the formation and preservation of vesicles and the Archimedes' method. I estimate the co-author contributions to Chapters 2 and 3 to be no more than 20%.

Table 1.1. Comparison of melt sheet thickness and radial extent in some terrestrial craters.

Crater	Target lithology*	Diameter (km)	Preserved max. melt sheet thickness (m)	Radial extent (km)	Melt volume post-erosion (km^3)	Estimate of melt volume pre-erosion (km^3)	Sources
Vredefort	Mixed	300	0	-	-	-	Gibson and Reimold, 1999; 2000
Sudbury	Crystalline	250	2500?	27 x 60	>8000	5000 - 24000	Lakomy 1989; Grieve et al, 1991; Grieve and Cintala, 1992; Zieg and Marsh, 2005.
Manicouagan	Mixed	100	230 (up to 1500)	55 - 60	600	1200	Floran et al. 1976; Simonds et al. 1978; Grieve and Cintala, 1992; Spray and Thompson 2008.
Popigai	Mixed	100	>1000	>48**	>1750	-	Masaitis, 1994; Grieve and Cintala, 1992; Masaitis et al. 2005.
Morokweng	Crystalline	70	>170	30	?	?	Dressler and Reimold, 2001
West Clearwater	Mixed	32	130	13	40	80	Grieve and Cintala, 1992
Mistastin	Crystalline	28	80	6.5	10	20	Grieve, 1975; Grieve and Cintala, 1992
Boltysh	Crystalline	24	220	12	11	11	Gurov et al. 1986; Grieve and Cintala, 1992; Gurov et al., 2006.
Lappajärvi	Crystalline	23	144	8?	8	-	Grieve and Cintala, 1992
Kaluga	Crystalline	15	90 (melt breccia)	13	8	8	Grieve and Cintala, 1992
Brent	Crystalline	3.8	34	0.2	0.021	-	Grieve and Cintala, 1981; 1992

* Mixed refers to a dominantly crystalline target with sedimentary cover.
**Estimated from Masaitis et al. 2005, figure 1: they describe differential erosion from 50 to 300 m of removal.

Chapter 2

Geology and impact melt thickness of Mistastin Lake crater, Labrador

2.1 ABSTRACT

The ~36 Ma Mistastin Lake crater in Labrador, Canada contains melt rocks that are distributed around two thirds of the lake in patchy outcrops varying in thickness from <1m to 80 m. Previous estimates suggested that a coherent melt sheet up to 200m thick formed in the crater and that the much smaller preserved unit thicknesses are the result of glacial erosion. Through new field observations and laboratory measurements, this work identifies a relationship between distribution, thickness and vesicularity of melt rock units. The thickest melt-rock occurrence, at Discovery Hill, is massive, crystalline, non-vesicular and 80 m thick. In contrast, 1-2 m thick melt-rock occurrences elsewhere in the crater are glassy and vesicular. Measured vesicularities vary from 0.1 to 31 % and follow an empirical relationship ($\varphi = 30 \pm 2\ h^{-0.8 \pm 0.1}$) whereby vesicularity φ increases with decreasing melt rock thickness h. Plagioclase microlite crystallization temperatures of thin melt rock outcrops are very high (>1300 °C), indicating rapid cooling rates. Lower crystallization temperatures (~1245 °C) for the Discovery Hill melt are consistent with slower cooling rates. The data suggest that the pre-erosional melt sheet at Mistastin was not uniform and consequently, previous estimates for the level of erosion and the volume of the melt produced have been overestimated.

2.2 INTRODUCTION

Meteorite impacts add tremendous amounts of kinetic energy to target rocks, sometimes resulting in the formation of significant volumes of impact melts. Impact melt production varies in part as a function of crater size. In small structures (<15 km), impact melt rock occurs as melt particles within ejecta deposits and/or crater-fill polymict breccias, e.g. at Couture, Québec, Canada (Grieve, 2006). Not only is there less impact melt formed in smaller craters, but a larger proportion is ejected as well, so melt glasses are less likely to be preserved (Grieve and Cintala, 1992). Conversely, in very large craters (~100 to 300 km) in crystalline target rocks, impact melt commonly forms large coherent bodies and/or continuous sheets, which can extend over many kilometres along the crater floor and be tens to hundreds of metres thick, e.g. up to 6 km at Sudbury (Canada) (Deutsch et al. 1995), Manicouagan (Canada) (Floran et al., 1978), and Popigai (Russia)(Masaitis, 1994). How melt forms and is dispersed in intermediate-sized craters (~20 to 75 km) is less clear. Melt rocks preserved in intermediate-sized craters range from glassy particles in lithic breccias to collections of larger, more coherent melt rock bodies. Multiple units of discontinuous crater-fill impact melt rock are commonly interpreted to represent erosional remnants of a once coherent melt sheet though it is difficult to verify such models.

Mistastin Lake, Labrador, Canada is an intermediate-size crater (28 km diametre) that preserves discontinuous outcrops of impact melt rock ranging in thickness from 80 m to less than 1 m (Fig. 2.1). Phinney and Simonds (1977) and Grieve and Cintala (1992) assumed that these variations were the result of differential glacial erosion of a single coherent melt sheet at least 200 m thick and, consequently, estimated a 20 km^3 pre-

erosional impact melt volume. In this paper, the significance of preserved thicknesses of melt rocks at Mistastin is reevaluated, focusing on their vesicularity and crystallization temperature, which suggest that the original thickness of the impact melt was quite variable. I also report the discovery and significance of suevite (polymict breccia containing impact melt clasts) that was emplaced as a hot lithic flow within the crater rather than as an airborne deposit ballistically ejected from the crater as has been reported at the Ries impact structure (see Osinski, 2004, for a review).

One of the reasons that it is important to understand how impact melt is formed and dispersed in terrestrial craters is to apply the results to the Moon where geological relationships between specific craters and their impact melt rocks are very poorly constrained. Radiometric age dates of lunar impact melt glasses provide the most complete chronology of the cratering history of the inner solar system but are limited by uncertainties about the numbers and sizes of craters that produced glasses of particular ages and compositions (e.g., Hartmann et al., 2007). In this regard, Mistastin is an invaluable lunar analogue as its size is comparable to many of the larger impact melt-forming craters on the Moon (150-200 km in diametre, when scaled for gravity differences) and its target rocks included anorthosites as the dominant lithology (Grieve 1975), as is the case for impacts in the lunar highlands. The physical behavior of anorthositic impact melt flows at Mistastin may have relevance to understanding the distribution of their counterparts on the Moon.

2.3 PREVIOUS STUDIES AT MISTASTIN

The Mistastin Lake crater (locally known as Kamestastin) was originally identified as an impact structure by Taylor and Dence (1969). Grieve (1975), Grieve and Cintala (1992), Marchand and Crocket (1977) and Mak et al. (1976) identified a large number of shock metamorphic features in the Mistastin impactites. The crater is located in northern Labrador, Canada (55°53'N; 63°18'W) on stable cratonic rocks of Mesoproterozic age (ca. 1.4 Ga). These rocks are components of the 5,000 km^2, 80 km wide , Mesoproterozoic Mistastin batholith (Emslie et al., 1980), which is part of the Nain Plutonic Suite (NPS) of Labrador. The NPS extends for more than 20,000 km^2 and is composed of a range of lithologies: Principally leuconorite, anorthosite, quartz monzonite and granite with secondary gabbro, troctolite, ferrodiorite and mangerite (e.g., Ryan and James, 2004). The target rocks from which the impact melt was produced are thought to consist principally of anorthosite (~62%) and lesser mangerite (~38%) based on geochemical modeling (Grieve, 1975; Marchand and Crocket, 1977). The major rock type in the region, the 'augen granodiorite' of Currie (1971), apparently contributed only trivial amounts (<1%) of rock to the impact melt (Grieve, 1975; Marchand and Crocket, 1977). This may indicate that the granodiorite was only a minor lithological component in the area.

Mistastin crater is thought to be ~28 km in diametre based on the location of a ring of outlying hills that may represent the collapsed crater rim (Grieve, 1975). An oval-shaped lake occupies the inner ~16 km diametre portion of the crater. Two islands, ~3-km wide Horseshoe Island and tiny Bullseye Island, are located in the centre of the lake. These represent a central uplift and thus classify the Mistastin structure as a complex crater.

The topography directly surrounding the lake is slightly elevated in plateaus extending up to 5 km away from the edge of the water. These plateaus transition into steeply dipping ramps elevated up to 350 metres above the lake level. The ramps are interpreted as the terraced rim of the crater. Depth measurements taken during this study gave lake depths of 27 to greater than 47 m, the limit of our apparatus. Otherwise, the present depth and topography of the crater floor is unknown. Grieve (1975) estimated a transient cavity diametre of 12 km and depth of 4 km for Mistastin based on comparisons with the 22 km wide (rim diametre) Gosses Bluff, Australia. The transient cavity is the maximum size achieved in the excavation stage of crater formation, before rim collapse begins in the modification stage (Grieve at al., 1977; Melosh, 1989). The lake basin itself (at present, 19 x 12 km in its maximum dimensions) could represent the extent of the collapsed transient cavity. Today the basin appears enlarged and elongated by glaciers that moved across the area from the southwest to northeast (Klassen and Thompson, 1990).

The impact age of Mistastin is late Eocene, 36 ± 4 Ma, based on $^{40}Ar/^{39}Ar$ stepheating dating of six impact melt rocks (Mak et al., 1976). The crater is well preserved because it has not been significantly affected by metamorphism and deformation since the impact. Impact-induced, low-temperature hydrothermal alteration has been proposed to explain the deposition of clay minerals in voids in some impact melt rocks (Newsom and Hagerty, 2003) but otherwise, erosion and sediment deposition have produced the only significant morphological changes to the crater since the Eocene. Many of the impactites, including the impact melt rocks have been exposed and incised by glacial and fluvial erosion but, as noted above, the original topography of the crater rim appears to be well-

preserved so that the crater is not deeply eroded (Fig. 2.2). The degree of erosion will be discussed further in the paper.

The melt rocks at Mistastin are distributed over the western two thirds of the edge of the lake and vary in thickness from exposure to exposure (Fig.2.1). They are unevenly distributed on top of the target rocks and not preferentially associated with any particular target lithology. Anorthosite and mangerite are exposed in belts cutting across the lake within the more extensive areas of granodiorite. All of the melt rocks are aphanitic to glassy and many contain vesicles. Much of the melt rock is clast-rich and the clast content increases with increasing proximity to the underlying brecciated basement. Grieve (1975) gave a detailed description of the petrology of the melt rocks; a shorter summary was presented by Grieve (2006). Geochemical studies by Grieve (1975) and Marchand and Crocket (1977) indicated that the impact melt rock has a rather homogeneous anorthositic composition (e.g., $SiO_2 = 57.8 \pm 1.9$ wt%). Grieve (1975) concluded that differential shock effects and particle velocities in addition to the highly turbulent state of the melt resulted in the efficient homogenization, though he also indicated that mixing may not have been entirely effective throughout all parts of the melt, resulting in local, small-scale heterogeneities.

2.4 IMPACTITE STRATIGRAPHY AND FIELD RELATIONS

All the major exposures of impactites are re-examined at Mistastin as part of this study (Fig. 2.3). The stratigraphy at Mistastin is best exposed along the banks of creeks. Coté Creek has the most complete measurable sequence, but exposures at both Steep Creek and 'South Creek' are useful aids to understanding the deposition of impactites. In

general the impactite units dip inward toward the lake at between 10° and 25°. The complete preserved stratigraphy, from bottom to top (A to E), is as follows: A) shocked and/or fractured target rocks, B) monomict breccia, C) polymict lithic breccia, D) suevite and E) melt rocks. Not all the units are present in each outcrop and there are widespread variations in unit thickness. There is no evidence of preserved ejecta deposits overlying the melt rocks.

2.4.1 (A) Shocked and fractured target rocks

The target rocks are an autochthonous unit that consist of anorthosite, mangerite and granodiorite (Fig. 2.4), as mapped by Currie (1971). The mangerite and anorthosite exposures occur as curvilinear elongate or irregular strips that extend northwest to south east across the lake. In addition, on the central uplift a small outcrop of meta-quartz gabbro is identified that was not described previously.

The shocked target rocks are much more susceptible to chemical and physical weathering than their unshocked counterparts. The anorthosite is somewhat variable in appearance in different outcrops but is easily identified. Strongly shocked anorthosite is white, but otherwise it is a light shade of pink to purple. The characteristically colorful lustre of labradorite is absent in many cases or has been modified to a deep turquoise green. The anorthosite consists principally of coarse grained labradorite to andesine, ~1% Fe-Ti oxides and varying amounts (2 to 10%) of pyroxene. Pyroxene is identified in most anorthosite samples as mm-scale crystals, but one particular outcrop on Horseshoe Island displays very large pyroxene crystals up to 12 cm long. There are μm-scale biotite inclusions in the plagioclase feldspar.

Mangerite is a pyroxene-rich quartz –bearing monzonite. In fresh unshocked samples of mangerite, the quartz is a deep shade of green. In very weathered samples along the lakeshore, the mangerite is yellow-brown. It is very difficult to distinguish between the granodiorite and mangerite in outcrop or hand sample as they have a similar mineralogy and both commonly display striking potassium feldspar (typically microcline) augen (ovoids) or rapakivi textures, which crumble when weathered. The mangerite is chemically distinguishable from the granodiorite on the basis of higher iron contents (8 – 10 wt. % total Fe_2O_3 compared to about 2 to 5 wt. % in the granitic rocks). In the mangerite, a large amount (50%) of the pyroxene has been altered to hornblende.

Other rock types include the dominant coarse-grained hornblende-biotite granodiorite and small areas of granite, gneiss and granulite material (Currie, 1971). The granodiorite consists of 20-25 vol% potassium feldspar, 30 vol% plagioclase, 20 vol% quartz, 5-15 vol% hornblende, 5% biotite with abundant accessory minerals apatite and zircon. Apatite crystals may reach 0.5 mm long. Hornblende was partly replaced by biotite. Some of the original biotite shows μm-scale kink banding which may be due to shock metamorphism or an inherited metamorphic imprint. Currie (1971) first described gneissic material as south-easterly trending nebulous areas within the granodiorite and combined them with the granodiorite unit on his map of the region. The granitic gneiss to biotite-gneiss is similar in composition to the granodiorite and is identified in hand sample and thin section by its gneissosity. A single outcrop of the weathered gneiss is located on the eastern bank of Steep Creek. The gneiss is also found as large oval-shaped inclusions ~10-60 cm wide within the mangerite, most commonly on the western shores of Horseshoe Island and the south shore of the lake. A large coarse-grained granite sill uo

to 2 m thick, the formation of which was unrelated to the impact event, is located just across from the gneiss on the eastern bank of Steep Creek. The sill is exposed for approximately 10 m and then disappears under the vegetation.

A single, several metre wide outcrop of (meta-) quartz gabbro surrounded by shocked anorthosite is located in the centre of Horseshoe Island. It is medium-grained and moderately shocked as indicated by planar deformation features in the plagioclase. These textures were recognized in the mangerite by Currie (1971). However, the quartz gabbro is easily chemically distinguished from all other target rocks by its low SiO_2 of 44.9 wt% and high total Fe_2O_3 of 19.7 wt% (Marion and Sylvester, submitted). This rock consists of 40-50% pyroxene (~10% of which was altered to hornblende), 35-40% plagioclase, 10% Fe-Ti oxides, ~5% quartz, 5% garnet and 1% chlorite. The presence of garnet indicates that this may be an amphibolite to granulite grade metamorphic rock, however no other metamorphic features are observed.

Shock metamorphism is an essential part of the cratering process and has aided in the discovery of many impact craters. Shock metamorphic effects observed in the target rocks at Mistastin include planar deformation features in feldspars, quartz and zircon as well as shattercones, toasted brown quartz (Whitehead et al., 2002) and maskelynite-bearing anorthosite (Lambert and Grieve, 1984) (Fig. 2.5). Shock pressures in the cental uplift have been recorded to >35 GPa (Grieve and Cintala, 1992).

The shocked and fractured target rocks contain intrusions in the form of dikes and sills originating from overlying melt and breccia units (Fig. 2.6). They are commonly fractured on a microscopic to macroscopic scale (Fig. 2.7A). They grade into overlying monomict breccia as the fractures become more abundant and concentrated.

At Mistastin, reflective intensities of shocked microcline and diaplectic glass of shocked quartz indicate pressures of 26-35 GPa (Langenhorst and Deutsch, 1994; Lambert, 1981); those of shocked labradorite forming maskelynite are consistent with pressures of 33-35 GPa (Lambert and Grieve, 1984). Wholesale melting of anorthosite is thought to require shock pressures in excess of 60 GPa, with post-shock temperatures reaching >1100°C immediately after pressure release (Stöffler and Grieve, 2007b; Lambert and Grieve, 1994).

2.4.2 (B) Monomict Breccia

Monomict breccia is an autochthonous to parautochthonous unit, in this case defined as monolithologic sequences of anorthosite, mangerite or granodiorite breccia. Anorthosite breccia and mangerite breccia are the most common monomict breccias observed at Mistastin. These units have an apparent maximum thickness of 10 m but more commonly are 2-4 m thick. It can be a difficult task to distinguish between shocked rocks and autochthonous monomict breccia on the macroscopic scale as some breccias are partially consolidated. Currie (1971) explained that these units are identifiable by glassy mineral grains, distorted grain structures, the presence of red veinlets and intense microscopic to macroscopic cleavage and powdering of the rocks. Pseudotachylite veins have been observed in this unit, particularly on the south shore of the lake. The mangerite is difficult to distinguish as a monomict breccia relative to a shocked mangerite in the field because the augen feldspar crystals turn to a yellow-orange and appear to float in the weathered black matrix where evidence of shock features or cleavage is lost. It is difficult to determine whether the rock is crumbling simply due to weathering or because

of brecciation or a combination of the two. Brecciated anorthosite is very easy to distinguish from shocked anorthosite as it weathers to material resembling talcum powder. The basal contact of the breccia is transitional into the shocked target rocks.

2.4.3 (C) Polymict lithic breccia

This is an allochthonous clastic impact breccia. In most cases it is dominated by one of the target rock compositions though some parts of the unit consist of significant proportions of two or more rock types. Along the north side of the lake, Steep Creek and Coté Creek expose much of the impactite stratigraphy. At Coté Creek, every unit of the impactite stratigraphy is exposed, including the basal contact of the melt rocks with the underlying polymict breccias. The best exposures are located along the creek bed. The white powdery banks of monomict anorthosite breccia at the mouth of the creek stand out against the browns and greens of the vegetation. About 0.4 km north of the mouth of the creek, on the west bank, there is an 11 m high ridge of polymict breccia which incorporates anorthosite fragments, foreign clasts and locally cm-wide sinuous impact melt breccia intrusions. This breccia consists of mm-scale fragments to metre-sized blocks of target rocks and monomict breccia with a lithic breccia matrix (Figs. 2.7B and 2.7C, the latter is a specific type of polymict breccia discussed in the following section). The dikes and sills intruding this unit are cm-wide pale green sinuous veins amongst the anorthosite rich breccias at Coté Creek. Several large continuous blocks in the breccia are shocked target rocks as they consist primarily of an isotropic feldspar-rich matrix interpreted as maskelynite (i.e., shock-induced plagioclase glass; Fig. 2.8A). Maskelynite and lechatelierite are diaplectic glasses which are formed in solid state process; they are

also observed in the monomict breccias and target rocks. This type of glass may not involve melting (French, 1998). Conversely, some studies have shown that this glass can be formed by melting and quenching under high pressure (Chen and El Goresy, 2000). Many of the more high temperature minerals inherited from target rocks (e.g., zircons) are preserved intact. The existence of planar deformation features in the clast minerals is evidence that they are inherited from the shocked basement rocks. The basal contact of this unit is transitional to irregular, and over ~1 metre in thickness.

2.4.4 (D) Suevite

Suevite is a polymict lithic breccia containing cogenetic melt clasts and lithic and mineral clasts in all stages of shock metamorphism in a clastic matrix (Fig. 2.7C). The melt rock clasts commonly consist of flow-banded glass and are sinuous and elongate. The thickness of this unit is difficult to estimate because the basal and upper contacts are transitional or not visible but range between 10 cm to 2 m. The most common suevite consists of a fine-grained light grey matrix with abundant plagioclase clasts and inclusions of melt fragments. Several larger feldspar clasts are mantled by melt. The melt clasts contain microclasts and are mostly glassy with an elongate and sinuous appearance but no particular orientation. The most prominent outcrop of suevite is at Steep Creek where it intrudes into monomict breccia. This intrusion is approximately 2 m thick at its maximum and dips (~30°) in the direction of the centre of the impact structure. The complete horizontal extent is unknown but is a minimum of 8 m. The upper and lower margins of the monomict breccia intrusion are oxidized to a higher degree than the interior, which supports emplacement of the intrusion at high temperature.

This suevite was intruded several metres into the basement rocks as a passive fracture fill and is strong evidence that this unit was deposited as the result of a hot lithic flow moving laterally (perhaps horizontally) and driven into the breccias during impact. Suevite has been observed at several other craters such as Ries, Rochechouart and Bosumtwi, where this deposit is generally interpreted to have been ejected and emplaced as an airborne deposit during the early excavation phase of the impact event (Osinski, 2004; von Engelhardt, 1997; Lambert, 2008; Boamah and Koeberl, 2006). At the Ries crater in particular, different modes of transport are suggested for suevite as it occurs both as crater-fill (or fallback suevite) and outside the crater rim (or fallout suevite) and these show differing volumes of shocked target clasts and melt clasts (Bringemeier,1994; von Engelhardt, 1997). However, the contacts of those suevites are not commonly bound by the target rocks or overlain with thick units of impact melt. The suevite at Mistastin demonstrates that those sorts of rocks need not be airborne deposits.

2.4.5 (E) Melt Rocks

The melt rocks at Mistastin are distributed around the perimetre of the western two thirds of the lake extending radially approximately 6.5 km from Horseshoe Island, near the centre of the lake. The extent of the melt below the lake is unknown though crater formation models (e.g. Stöffler and Grieve, 2007b) depict the thickest melt as being immediately around the central uplift overlying the other crater fill deposits with the exception of fallback breccias. This suggests that melt rocks are present beneath water level around Horseshoe Island (representing the central uplift of the crater). Several small exposures of melt rocks are present on the island. The melt rocks are very similar in

texture to volcanic rocks; they have a glassy to fine-grained matrix and in places contain clasts and vesicles. The clast content categorization (Stöffler and Grieve, 2007a) divides all melt rocks into three main types: clast-rich, clast-poor and clast-free, and by this classification, all three types are present at Mistastin. Grieve (1975) divided Mistastin melt rocks in his Table 3 into three chemical classes based on silica and potassium content (low: SiO_2 of 53.4-55.5 wt% and K_2O of 1.1-1.5 wt%, intermediate: with an average SiO_2 of 58.4 wt% and K_2O of 2.3 wt% and high: with an average SiO_2 61.6 wt% and K_2O of 3.6 wt% as well as into three separate textural subunits (glassy to very fine grained melt with numerous inclusions; fine-grained microporphyritic melt with numerous inclusions; and fine-medium-grained poikilitic melt with relatively few recognizable inclusions).

Mistastin melt rocks are generally found in a gradational upward sequence with glassy clast-rich melt rocks proximal to the basal contact increasing to crystalline melt rocks with fewer clasts with increasing distance from the underlying target rocks and breccias. Few areas in the melt are completely clast free, even the thickest units contain minor μm-scale clasts. Matrix grain size varies with thickness of the melt unit and clast content; coarser grains are associated with thicker, clast-poor melt units whereas finer grains are associated with the thin melt units and clast-rich areas. Matrix microlites of plagioclase, pyroxene and Fe-Ti oxides are best observed in the clast-poor to clast-free melt rocks of the thickest parts of melt units where they had time to grow (Fig. 2.8B-C) up to 1 mm in length in the case of the dendritic pyroxenes and up to 1 mm in length for plagioclase microlites and up to 1 mm for plagioclase phenocrysts. Clast-rich melt rocks (Fig. 2.8D) have fewer to no microlites (<50%) depending on the size and abundance of clasts in each

sample. Melt rocks from thinner units have a more glassy matrix with few microlites (Fig. 2.8E). Microlites observed in the these melt units are no larger than 150 μm.

2.5 Distribution and description of the melt rocks

Six principal melt rock locations were examined around Mistastin Lake; in counter-clockwise order beginning in the north east, they are: Steep Creek, the North Shore, Coté Creek, Discovery Hill, the South Ridge and the South Shore (Fig. 2.1). A seventh location, West Point, was visited in the field but unfortunately was not sampled during this study. The North Shore, South Shore, West Point and South Ridge locations are field terms used in this study.

A particularly distinctive butte on the west side of the lake, known as Discovery Hill, represents the thickest preserved outcrop of the melt unit, roughly 80 metres thick. The Hill itself is just over 100 m high (Fig.2.9). The basal contact of the melt unit is not exposed. The eastern side of the butte slopes to the East toward the lake at 30-45°, and resembles a steep ramp rising out of the lake when observed from the centre of the lake. There are no melt rocks exposed on the lower two-thirds of the ramp. Two tiers of columnar joints are exposed on the south side of the butte (Fig. 2.9A-B); the west and north side show distinctly smaller jointing and vertical parallel cleavage. Horizontal cleavages cut across many of the joints of the lower tier and the vertical cleavage on the north side. It is evident that there has been intense erosion of Discovery Hill.

The Discovery Hill melt unit consists of a dark blue massive rock, with 70-90% matrix minerals and glass and 10-30% clasts (Fig. 2.8B). The matrix is dominantly crystalline and consists primarily of plagioclase microlites up to 1 mm in length, lesser

dendritic clinopyroxene (augite to pigeonite) up to 2.5 mm long and Fe-Ti-oxides less than 1 mm in diametre. Sub-ophitic texture forms where pyroxene crystals are partially surrounding plagioclase laths. According to Grieve (1975), the chemical composition of the melt matrix at Discovery Hill is relatively homogeneous, with minor variations due to local target rock contributions.

Clasts consist of various assortments of minerals derived from target rocks, most commonly plagioclase and quartz. Additional clasts consist of hypersthene, Fe-Ti oxides, apatite, and zircon. There are both unshocked and shocked grains; the majority are weakly shocked to unshocked. The few vesicles in Discovery Hill melt rock are at the μm- to mm-scale and are spherical. They are easily confused with voids created by erosional excavation of μm-mm-size clasts, which are much more abundant (~5 times) than the vesicles. In places the voids form amygdules filled with clay minerals. The amygdules may have been formed by hydrothermal alteration in the late stages of cooling or are simply altered clasts. The largest observed void was 1 mm wide.

Enormous metre-sized (~6 x 8 m) mangerite clasts are found protruding from the melt on the north side of the butte and atop the hill (Fig. 2.9C). Discovery Hill's vertical joints curve around these mangerite boulders and plagioclase microlites in the melt matrix immediately adjacent to the boulders have a preferred orientation. There is evidence of zonation and gradation of finer grains in the melt matrix over several metres. This zonation appears to be affected by the number and size of clasts in each sample, with zoning better defined when there are more clasts.

The melt rock exposed at Coté Creek blankets the irregular landscape of the underlying breccias. The southernmost melt rock outcrop occurs 0.5 km upstream of the

outwash into the lake. In the creek beds, the melt rock irregularly intrudes the underlying breccias. One large vertical intrusion, a downward injection into the breccias from the overlying melt layer is emplaced at the contact between lobes of the anorthosite and mangerite target rocks. The downward termination of this intrusion is hidden, however a similar intrusion located 0.2 km downstream (toward the lake) is completely exposed (Fig. 2.10A) and this exposure clearly shows that the melt from along the base of the melt sheet was injected into the breccias below. Melt rock at Coté Creek has a maximum thickness of 18 m and all of it contains abundant mm- to cm-scale vesicles at this location beginning only 1 m above the basal contact (Fig. 2.10B). The size and shape of the vesicles vary depending on the thickness and proximity to the basal contact. The melt is not vesicular directly along the contact; it contains a dense clast population (>50%) and is glassy (Fig. 2.11A). A metre up stratigraphy, mm-scale, slightly elongate vesicles are observed. These become more abundant up section (Fig. 2.10B and 2.11B). At the top of this section vesicles are up to centimetre-scale and approximately spherical (Fig. 2.11C).

The melt rock outcrop at Steep Creek consists of a hill on the East side of the creek. The unit is at least 6 m thick; it may be thicker because the base is not exposed. The melt rocks on this hill are relatively massive, non-vesicular, moderately weathered and consist of about 10-15 % of μm-scale clasts.

The North Shore, located about 4-5 km west of Steep Creek, consists of a cluster of outcrops ranging from 2 m to 300 m wide. The thickness of these units are unknown as the outcrops are spread over a kilometre on a vegetated and boulder-rich plateau. Based on their textures (matrix crystallinity and grain size, clast abundance etc), each patch may vary in thickness relative to neighbouring patches. The samples are generally clast-rich

and have a glassy to fine-grained matrix. The clasts are μm to cm in size and although the Coté Creek unit shows larger clasts along the base, the textures of the presumably thinner, clast-rich North Shore melt rocks appear somewhat similar (Figs. 2.10B and 2.11A). All of the voids in these samples are irregularly shaped. This could be due to a forced deformation during escape of gas-filled voids through a clast-rich medium or they may have formed from irregularly shaped dislodged clasts. An estimated 30% of voids may not be vesicles.

The South Ridge, a ridge 4 km SSE of Discovery Hill, consists of weakly vesicular, massive melt rock with a thickness of at least 25 metres. Since the basal contact is not exposed, it is likely the melt rock unit is thicker. A segment of the ridge displays vertical cleavage and what may be columnar joints similar to Discovery Hill.

Along the southern shore of the lake, several dispersed beach outcrops show very large vesicles up to 25 cm in their largest dimension; some rocks are so rich in vesicles that they resemble pumice. These outcrops are 1-2 metres thick, with a glassy matrix (~50 % glass) and elongated vesicles demonstrating flow deformation (Fig. 2.12A-B). Figure 2.12C displays the contact of three units at South shore, (1) a glassy non-vesicular clast-rich unit overlain by (2) a glassy weakly vesicular clast-poor unit which grades over a short distance into (3) a glassy, more vesicular melt rock. Based on the sharp contact between them, it appears as though the clast-poor (2-3) and clast-rich (1) units were two different flows. Many scoriaceous rocks with vesicularities of up to 50% were found in the South shore area.

2.6 VESICLES IN IMPACT MELT ROCKS

The majority of the melt rocks at Mistastin Lake show vesicular textures with the exception of the clast-rich basal melt rocks and the clast-poor massive melt rocks located in the thickest units of melt. Most vesicles are on the order of μm- to mm-scale, although they can be up to several centimetres in diametre. Their shape varies from outcrop to outcrop; some vesicles are spherical and others are elongate and elliptical demonstrating that they were present during flow movement in the melt.

The vesicles formed from volatiles, such as molecules of water, carbon dioxide, sulphur, etc., that existed in a gas state at atmospheric pressures and magmatic temperatures. These gases are rapidly dissolved into the high temperature melts formed under extreme shock pressures produced at the instant of impact. The volatiles then exsolve to form gas bubbles during relaxation of the melt . Several factors control the formation and preservation of vesicles, including initial volatile concent, melt composition, clast and microlite populations, melt layer thickness and temperature. These factors are briefly discussed below. A comprehensive analysis of vesicularity in impact melts has yet to be attempted. Degassing in volcanic systems is studied (e.g. Peck et al., 1977), but the conditions in which vesicles form are admittedly different.

The initial volatile content of the melt is difficult to assess, however in these magmatic target rocks the dominant volatile was almost certainly water. There are a number of possible sources, one being volatile-rich minerals in the target rocks. Minerals such as amphibole and micas have H_2O as fundamental constituents in their crystalline structures, and this water is released upon melting. Loss on ignition (LOI) values for the

three principle target rocks are 2.6 % ± 2.0 in the anorthosite, 3.0 % ± 1.5 in the mangerite and 0.9 % ± 0.4 in the granodiorite (Marion et al., submitted). However, these values may not represent original volatile ratios due to weathering, etc. Additional sources may include groundwater, surface water or glacial ice and volatiles from the impactor. Groundwater within the crystalline target rocks was probably not significant, as the fracture porosity of such rocks is generally low (<0.5%) and restricted to the top ~100m of surface rocks (M. Sukop, pers. comm.). If the impactor was a comet, or the immediate target was covered by a large lake or a glacier and this water was incorporated into the melt, then water contents could have more than a few weight percent.

In equilibrium, volatiles exsolve from a melt when their concentrations are higher than their solubility. The solubility of volatiles increases strongly as pressure increases, due partly to compression of the gas. At Mistastin, the static pressure in the melt is due to the weight of overlying material once the initial shock of the impact is past. Figure 2.13A shows how H_2O saturation increases with increasing depth in the melt, assuming that the melt is at the surface so that the top of the melt layer is at a pressure of 1 bar. To convert pressure to depth, Pascal's Principle for fluid pressure is used:

$$P = \rho g h \qquad (1)$$

where P is pressure, ρ is the density of the melt, g is the acceleration of gravity and h is depth (i.e., the overlying thickness of melt). Pressure increases by about 1 bar for every 4 m of overlying melt. Figure 2.13A shows that at the melt surface the saturated water content is <0.1 wt% and at a depth of 80 m, corresponding to the bottom of the thickest

unit observed at Mistastin crater, the saturated water content is only ~0.45 wt%. This indicates that unless the initial melt were extremely dry, it would have been supersaturated in water at all depths.

To convert initial water supersaturation to an initial maximum vesicularity, the ideal gas law (which works well for water vapour) is used.

$$PV = nRT \qquad (2)$$

where V is volume (of a vesicle), n is the number of moles, R is the Universal Gas constant and T is absolute temperature (in Kelvin). In Figure 2.13B the initial, equilibrium volume vapour fraction is plotted as a function of equivalent depth in the melt layer, assuming a uniform temperature of 1100 °C, for four different, uniform initial water contents. Equivalent depth is the depth that would apply if the overlying melt was not vesiculated – vesiculation increases the layer thickness without increasing pressure. The strong increase in volume vapour fraction as equivalent depth decreases is due partly to decrease in water solubility and partly to decrease in pressure. From Figure 2.13B, if the water content was a uniform 0.4 wt%, then a layer with equivalent depth of <70 m would be vesiculated from top to bottom and more than half of the melt would be a highly vesicular froth.

Figure 2.13 is useful in illustrating that melt layers several tens of metres thick could become highly vesicular, particularly in their upper portions. However, it must be stressed that the actual vesicularity of a melt at a given time or location depends on many

more variables than are considered in Fig. 2.13, and the figure cannot be used to quantitatively predict preserved vesicularity in the melt rocks.

Like crystal nucleation, bubble nucleation depends on cooling rate and on available sites for nucleation. Vesicles in most terrestrial lavas dominantly nucleate heterogeneously (Hurwitz and Navon, 1994), and this is thought to be true in impact melts as well, where vesicles nucleate on crystals that survive impact melting such as Fe and Ti oxides (Cluzel et al., 2006; Gardner, 2007) and (to a lesser extent) zircons and apatites (Hurwitz and Navon, 1994) all of which are present in Mistastin melt rocks. Clasts could also serve as nucleation sites. In impact melts, there may also be some homogeneous nucleation, given the intense decompression-induced volatile oversaturation.

If cooling is sufficiently rapid, a melt can be quenched to a bubble-free glass. At Mistastin, melt inclusions in suevite are bubble free and so are basal units (e.g., the unit in the South Shore outcrop shown in Figure 12C). These basal units are rich in clasts, incorporated from pulverized bedrock into the melt as it radiated outward from the impact site. The incorporation of relatively cool clasts was an important contribution to the rapid cooling of the melt (Onorato et al. 1978). Millimetre-scale clasts could thermally equilibrate with a surrounding equivalent volume of melt in seconds (Phinney and Simonds, 1977). Centimetre-scale clasts, though taking minutes to thermally equilibrate, would cool a mm-scale rind of melt in seconds. For comparison, the timescale τ for cooling a melt layer of width h by thermal conduction is (Carslaw and Jaeger, 1959)

$$\tau \sim h^2/4\kappa \qquad (3)$$

where κ is the thermal diffusivity (~10^{-6} m^2/s for most geological materials). For dikes or melt sheets of thicknesses 10 cm, 2 m and 80 m, the respective timescales are 40 minutes, 10 days and 50 years.

Once nucleation has occurred, bubble growth in magmas involves diffusion of water into the bubble and expansion of the bubble due to overpressure against viscous forces. Complexities arise because the diffusion rate and viscosity both depend on water concentration (Blower et al., 2001; Lensky et al., 2004). In highly viscous magmas, the bubble growth rate can be limited by viscosity (Gardner et al., 1996; 2000). The viscosity of magmas is highly temperature dependent, increasing by orders of magnitude every few hundred degrees (e.g., Murase and McBirney, 1973; Best and Christiansen, 2001), so rapid cooling, leading to rapid increase in viscosity, can inhibit bubble growth. Volcanic glasses often contain tiny, trapped bubbles.

Bubbles rise due to their buoyancy. For an individual bubble of radius r in an isoviscous fluid of viscosity μ and density ρ the Stokes rise velocity v is:

$$v = 2/9\, r^2 g\rho/\mu \qquad (4)$$

where g is the acceleration of gravity. At the liquidus of the Mistastin melt (~1140 °C - calculated with Magma software) the viscosity would be about 1000 Pa-s. Bubbles 1 mm in diametre would take about one week to rise 1m. For bubbles 1 cm in diametre this time is ~2 hours. At 1850 °C, the temperature of total melting of anorthosite (Hiesinger and Head, 2006), the viscosity and therefore the rise times would be a thousand times less,

whereas at 850 °C, viscosities and rise times would be a thousand times more. If total anorthosite melting occurs at 1550 °C, the viscosity would be hundred times less than at 1180 °C. As bubbles rise through a layer they would expand as pressure decreased (Equation (2)). Conversely, they would tend to contract as temperature decreased until frozen in as the magma solidified.

The initial formation of the Mistastin crater and emplacement of the melt was a rapid, violent event, involving vaporization and melting of the impactor, and melting and brecciation of the impactites, over a timescale of a minute or less (Pierazzo and Melosh, 2000). Over this timescale the dynamics of the melt is certain to have been of major importance in cooling, particularly for thin flows. Phinney and Simonds (1977) argued for a very short period of intensely turbulent mixing in impact melts of Manicouagan and other large terrestrial impacts, in order to explain why clasts there are so evenly distributed, given that the incorporation of the clasts would have cooled the melt rapidly. Turbulence itself always leads to heat transfer rates, which are higher than the conductive rates given by Equation (3) (e.g., Schlichting, 1968), however, unless there is mass transfer across the boundaries – by splashing, escape of superheated gas or incorporation of clasts – heat loss from the melt is still limited by the formation of cool, stagnant boundaries. Radiation, the highly turbulent flow, the thinning of the melt as it spreads out, the incorporation of clasts, and perhaps a burst of nucleation and growth of vapour bubbles, would have contributed to a very rapid loss of superheat in those first few seconds or minutes. Onorato et al. (1978) determined that thermal equilibration of clasts in the Manicouagan melt was reached only after 100 minutes to 3 hours. Vesicularity has been identified as a controlling factor of thermal conductivity as well as the effect of

jointing (Peck et al. 1977), which are parametres not considered in calculations by Onorato et al. (1978) for the cooling history of the Manicouagan melt. Cooling of impact melt at Mistastin Lake may differ from that at the Manicouagan crater as Mistastin's melt is quite vesicular compared to the Manicouagan melt and jointing is present in all melt units over 15 m thick.

Thin parts of the melt sheet would have frozen before bubbles could escape, as seen in the highly vesicular outcrops in the South Shore. Flows that incorporated a lot of clasts would have frozen even before the bubbles could nucleate or grow. Thin flows on the South Shore and the bottom boundaries of flows elsewhere, such as at Coté Creek show this. The central and upper parts of thicker flows would have cooled more slowly, as the clast content was lower and they were overlain by superheated air whereas the surface may also have suffered some quenching from incorporation of cold clasts from fallback breccias. In the first minute or so, as the melt was spreading out over the crater floor, bubbles could have nucleated, grown and risen to the top of the flow. Stagnant, gas-rich foams have a moderate rigidity and low thermal conductivity (Weaire and Hutzler, 1999) and might have formed an insulating cap to the flow; however, in this early dynamic environment gas is likely to have escaped easily. If the melt was superheated (heated beyond the liquidus) by ~250°C, it would have been as fluid as basalt at its liquidus (calculated in Magma with a typical basalt composition). Mangan and Cashman (1996) argued that fragmentation of vesiculated lava is due to the hydrodynamics of the two-phase flow. They also argued that supersaturation of a melt (in their case by rapid ascent) can lead to an intense burst of bubble nucleation within a timescale of seconds.

As above, the qualitative observation that the vesicularity of melt units at Mistastin crater increases as the melt unit thickness decreases can be explained. Basically, it is a competition between bubble nucleation and growth on the one hand and cooling and solidification on the other. This suggests that the variation in preserved melt rock thicknesses may largely reflect primary variations. In order to define this relationship quantitatively the vesicularity and crystallization temperature of samples of Mistastin impact melts rocks were determined, as discussed below.

2.7 FIELD SAMPLING AND ANALYTICAL METHODS

Twenty-two melt rock samples were collected from the major outcrops around Mistastin Lake, listed in the "Distribution and description of the melt rocks" section above, as well as from smaller exposures in between. Where possible, samples were collected at different levels within the same outcrop to be able to compare textures. Eight samples were collected from Coté Creek, 2 samples from the North Shore, 3 samples from the South Ridge, 3 samples from the South Shore and 8 samples from the upper 15 metres and lower 20 metres of Discovery Hill. No samples could be collected from the centre of Discovery Hill as the exposed southern face is very steep.

Bulk rock chemistry was determined for 19 melt rock samples. Samples were crushed by hand and powdered in a Siebtechnik puck mill with a tungsten carbide bowl. Major elements were determined using a Fisons/Applied Research Laboratories XRF (model 8420+ sequential wavelength-dispersive x-ray spectrometre). Fused glass disks were made by combining approximately 1.5 grams of rock powder with 6.0 grams of lithium

metaborate, 1.5 grams of lithium tetraborate flux, and heating at ~850°C for 8.5 minutes and fusing at ~1050°C for 11.5 minutes in a muffle furnace.

Thin sections of all the melt rocks were made in order to identify melt rock textures and to allow analysis of matrix material. Analysis of major element compositions for 2-3 plagioclase microlites and adjacent glass in the melt matrix were completed for five samples (CM044, CM067, CM088, CM039, CM052) by EPMA using a JEOL JXA-733 Superprobe at the University of New Brunswick, NB on 3 μm spots, at 15 kV and 20 nA. Microprobe spots were placed in the centre of plagioclase grains to avoid zonation or incorporation of additional matrix material.

2.8 VESICULARITY MEASUREMENTS

2.8.1 Methods

To quantify the vesicularity of Mistastin impact melt rocks, 23 samples were analysed by two methods: Archimedes' method and an *Image Scan* method.

Archimedes' method involves finding the vesicularity φ from the difference between the bulk density of the sample ρ_{rock} and the density of its non-vesicular matrix ρ_{matrix}.

$$\varphi = \frac{\rho_{matrix} - \rho_{rock}}{\rho_{matrix}} \times 100\% \qquad (5)$$

Density is mass divided by volume: $\rho_{rock} = M_{rock}/V_{rock}$. The sample was weighed to determine M_{rock}. V_{rock} was found by weighing the rock while it was submerged in water. The difference between the weights in air and in water gives the volume.

The major source of error in this method is uncertainty in the density of the matrix, ρ_{matrix}. To find ρ_{matrix}, and its associated uncertainty, the density of samples that had very

low vesicularities were measured, and compared with the density calculated from major element composition using the KWare Magma software (Wohletz, 1999), which uses the formulas derived by Bottinga and Weill (1970). Results are shown in Table 1. Calculated densities are sensitive to the assumed water content of the rock and to the oxidation state of iron, so two end-member situations are considered: a dry rock with the oxidation state often assumed for volcanic rocks (Irvine and Baragar, 1971); and a rock with 0.4% H_2O and an oxidation state considered 'reasonable' for all rock types (Wohletz, 1999). It is seen that the density determined by both methods is in broad agreement, with the measured densities usually falling between the two calculated values. The median value of the measurement is about 2.65 g/cm^3, with a variation of ±1.5%. A vesicularity of 0.3%, representative of these rocks, would indicate a matrix density 0.008 g/ cm^3 higher than the rock density (Equation (5)). The difference between the two calculated densities is about ten times as great, with roughly two thirds due to the different oxidation states. Differences in calculated density from sample to sample are related mainly to the iron, silicon and calcium concentrations. Since there is no obvious correlation between measured and calculated densities, the uncertainty in the matrix densities calculated by KWare Magma from bulk analysis for more vesicular rocks is taken to be about ±2%. This means that vesicularities of <2% are considered, as calculated by the Archimedes Method, to be unreliable.

The *Image Scan* method consists of scanning clean melt rock slabs on a flatbed scanner and converting the images in Photoshop with a bi-level thresholding tool to display a 2-bit black and white image (Fig. 2.14). The vesicles are represented by the

black pixels and the groundmass by white pixels. Manual corrections were made to eliminate fractures, amygdules and saw marks that were incorrectly recorded as vesicles. Voids formed by eroded and dislodged clasts are differentiated from vesicles by the presence of glassy mantles around the voids (presumably formed by melt quenching against the now-missing clasts) or the presence of remnant crystal structures in the lining of the voids. The vesicularity of the slab face is calculated as the fraction of black pixels within the area. Simple geometrical reasoning shows that if the vesicularity is uniform and isotropic, the area fraction of vesicles on a two-dimensional slice is the same as the volume fraction of vesicles in a three dimensional volume, although other properties like size distributions are not as simply related (Cheng and Lemlich, 1983). For most samples, voids formed from dislodged clasts are minor in abundance (< 2 % of each sample volume) compared to voids representing gas-derived vesicles (typically 1-5% and much higher in some samples). To assess the uncertainty in vesicularity, two slabs from each rock sample were cut and scanned. Consistency between the two measurements was highly variable, depending on the degree of heterogeneity in the vesicle distribution. Relative errors are estimated between 5 and 50% of the calculated vesicularity.

2.8.2 Results

Table 2 lists the results of the vesicularity measurements. As determined qualitatively in the field, the quantitative laboratory measurements indicate that the thickest melt rock units at Mistastin, such as Discovery Hill and South Ridge, have the lowest vesicularities (0 to ~3 %). Coté Creek, which forms only moderately thick outcrops, has vesicularities ranging from 0% at the base of the section to ~11% at the top (Fig 2.13A-C) and a

representative vesicularity of 4 % in the centre. The thinnest outcrops at the South Shore show extreme vesicularities from 20-30%. The results for the North Shore outcrop are the most complicated as the thickness of each patch of outcrop is unknown and the majority of patches are very clast rich and weathered, making it difficult to distinguish clast voids from gas-derived vesicles.

As preserved vesicularity is typically a function of cooling rate, it increases with proximity to the cooling surfaces at the top and bottom of the melt bodies. If one considers the thickness of the melt relative to the distance from the top of the exposed melt rock, one can better compare the vesicularity of Mistastin melt rocks. In Figure 2.15, the 22 samples are divided into four categories of depth from the top of the melt rock exposures and their vesicularity is plotted as a function of total thickness of each particular melt rock outcrop. Vesicularities vary from 0.1 to 30 % and the data can be fitted approximately to the empirical relationship

$$\varphi = 30 \pm 2\ h^{-0.8 \pm 0.1} \qquad (6)$$

whereby vesicularity φ increases with decreasing melt rock thickness h. Many of the measurements for Discovery Hill (at 80 m total thickness) plot on top of one another (mean = 0.4% ± 0.2 for 7 samples) as the entire unit is massive, whereas units of intermediate thicknesses have intermediate vesicularities, and the very thin melt rock units along the South Shore have very high vesicularities.

2.9 CRYSTALLIZATION TEMPERATURES

2.9.1 Methods

In order to determine whether preserved melt thicknesses reflect primary thicknesses of the melt flows, as suggested above by the vesicle abundance data, crystallization temperatures were calculated in several widely distributed samples of melt rocks. The expectation is that thicker units (except at their quenched basal contacts) cooled more slowly than thinner units and thus equilibrated at lower temperatures. Clast populations and location of microlites relative to clasts were considered when comparing sample temperatures. Crystallization temperatures were calculated from the compositions of plagioclase microlites determined by stoichiometry of microprobe analysis and adjacent glass matrix in several Mistastin impact melt rock samples using the igneous thermometre of Putirka (2005):

$$\frac{10^4}{T(K)} = 6.12 + 0.257\ln\left(\frac{[An^{pl}]}{[Ca^{liq}(Al^{liq})^2(Si^{liq})^2]}\right) - 3.166[Ca^{liq}] + 0.2166[H_2O^{liq}] - 3.137\left[\frac{Al^{liq}}{Al^{liq}+Si^{liq}}\right] + 1.216[Ab^{pl}]^2 - 2.475\times10^{-2}[P(kbar)] \quad (7)$$

where T(K) = temperature in Kelvin; P(kbar)= pressure in kbar; An^{pl} and Ab^{pl} are the cation fractions of anorthite and albite in plagioclase: Ca^{liq}, Al^{liq}, Si^{liq} refer to the anhydrous cation fractions of Ca, Al, Si in the equilibrium liquid (glass or microcrystalline matrix); and H_2O^{liq} is wt% water in the liquid.

There are three unknown variables in equation (7): temperature, pressure and water content. The equation was solved for temperature, with pressure determined on the basis of the weight of the rock overlying each sample, and a constant value of 0.2 wt% H_2O

was assumed for all samples. The value and uniformity of the water content is a matter of some uncertainty. Measurements of volatile contents in the melt rock samples by loss-on-ignition, 1.4 ± 0.8 wt.% (Marion and Sylvester, submitted) reflect a combination of volatiles in secondary phases and clasts, as well as those dissolved in the primary magmatic minerals and glass of impact melt rocks. 0.2 wt% was assumed in the calculations because the target rocks are relatively dry and, as discussed in the previous section, equilibrium-saturated water contents should be between 0.1 and 0.4 wt% in melt flows of up to 80 m in thickness (Figure 2.13A). To test the sensitivity of the results to water content, some of the temperatures were calculated at 0.4 wt%. The result was an approximately linear decrease in crystallization temperature of ~8 °C for every 0.2 wt% increase in H_2O.

In order to compare crystallization temperatures to liquidus temperatures for these samples, liquidus temperatures for the glass matrix compositions of the samples were calculated using the KWare Magma software.

2.9.2 Results

Table 3 presents representative compositions of plagioclase and coexisting glass matrix and their calculated crystallization and liquidus temperatures for each of the Discovery Hill, Coté Creek, South Shore and North Shore melt rock occurrences. The results are summarized in Figure 2.16.

Calculated crystallization temperatures are measurably distinct at each site and, as predicted, decrease systematically as melt thickness increases. The samples from thin melt outcrops at the South Shore have the highest crystallization temperatures of 1313 ± 9

°C. Intermediate temperatures were calculated for intermediate melt thicknesses, i.e., 1291 ± 9 °C for Coté Creek, and the lowest calculated temperatures of 1245 ± 6 °C applied to Discovery Hill, the thickest impact melt unit. Although the difference between the Discovery Hill and Coté Creek outcrops is just outside standard deviations, the variation between the two extremes, Discovery Hill and South Shore, is significant.

2.10 DISCUSSION

2.10.1 Vesicularity Measurements

The Archimedes' and the *Image Scan* methods have particular advantages and disadvantages. The Archimedes' method gives vesicularity as a whole rock volumetric percent, which, given the heterogeneity of some rocks, is more representative of the bulk sample than the two-dimensional, area percent, *Image Scan* result. On the other hand, the Archimedes' method is inaccurate for vesicularities less than 2% because of uncertainties in the matrix density. It also counts all voids within the rock as gas-derived vesicles, which produces an overestimate in the vesicle abundance, given that fractures and dislodged clasts formed some voids. However, it is this author's belief that the Archimedes' method gives superior results for vesicle-rich samples. This is because fractures and voids formed by clast erosion represent only a very small proportion of the total void space in samples containing abundant gas-derived vesicles. In contrast, the *Image Scan* method is thought to be more accurate for samples with low vesicularity. This is because there are proportionally more fractures and clast-derived voids relative to gas-derived vesicles in such samples and the ability to distinguish them is the limiting

factor on accuracy. For samples with intermediate vesicularities, the two methods give comparable values.

Low vesicularities reflect overall slower cooling rates in the thicker units compared to thinner units. Flow units a few metres thick, like that at Coté Creek, apparently froze before bubbles could escape. The shape and orientation of the vesicles indicates that they were carried in the flow and deformed by flow processes immediately prior to the cessation of motion. At Coté Creek, it is expected that entrainment of clasts and the proximity to the underlying breccias caused rapid cooling and limited vesicle nucleation at the base. Based on grain size variations, the North Shore outcrops most likely represent a thin occurrence of melt rock containing a number of thicker sections, particularly in the eastern part of the outcrops where there are more dramatic variations in clast abundance. This is consistent with the visual estimates from the westernmost North Shore patch, which has a much higher vesicularity than the easternmost patches. Thicker flow units, like Discovery Hill, could have lost a large amount of their oversaturated water content in the dynamic first minute or so. Bubbles remaining in the melt after the dust had settled would have had a chance to rise and escape during much longer cooling timescales, leaving the bulk of the solidified unit vesicle poor. The top of thick melt bodies may have been vesicular if some of the excess water was unable to escape in the first few minutes.

Vesicles in impact melt have been recognized at many other craters of various sizes and target lithologies, but the quantity and physical properties of vesicles have rarely been described in detail. Many melt glasses, such as those in suevite, have been described as vesicular (Dressler and Reimold, 2001), but in this study the focus is on

large impact melt bodies. Vesicular texture has been noted at the base of several melt sheets in complex craters with dominantly crystalline targets. For example, they were observed in the lower 0.3 m of the 23 km wide, 77.3 Ma Lappajärvi impact melt sheet, identified in drill cores (Pipping and Lehtinen, 1992) and the impact melt at the 32 km wide, ~290 Ma West Clearwater crater, has ~3 vol% of amygdules up to 1 mm in diametre within a few cm of its base (Phinney et al. 1978). The Manicouagan impact melt from the ~100 km diametre crater in Québec has rare sporadic vesicles (< 2 cm) confined to the lower 20 m and adjacent large clasts (Floran et al., 1978; Simonds et al. 1978), but overall Manicouagan does not have a vesicular melt sheet (Onorato et al. 1978). Dence (1971) explains that the vesicle-rich top of both the Manicouagan and West Clearwater impact melts must have been removed by erosion. Based on statements by Phinney and Simonds (1977), Grieve and Cintala (1992) suggest a possible 130 m was removed from West Clearwater while directly adjacent and of the same age, melt rocks recovered by drilling at the ~20 km East Clearwater crater are fresh and represent the original stratigraphy of the melt sheet. However, little is known of the lateral extent of East Clearwater's melt. The drill hole penetrated a total of 41 m of melt, but the hole became non-vertical with depth, therefore core thicknesses may not be representative. The top ~5 m consist of a fine-grained clast-rich melt followed by a 5 m thick vesicular zone, which overlies clast-poor melt with increasing grain size with depth until the core bottomed out (Palme et al. 1979). The physical properties of the vesicles are not detailed, but Palme et al. (1979) suggest that the vesicular zone was formed during a long, late stage of cooling where a (possibly sulphur-rich) vapour phase could have risen to the top of the melt. As the very top had already crystallized, the vapour phase condensed below

the top of the melt to form the vesicular zone. In all cases it is important to note that the vesicles observed at the base of impact melts are less than 2 cm in diametre and more commonly < 2 mm in diametre. Whereas at Mistastin, this study noted vesicles up to 25 cm long on the South Shore. These undoubtedly represent an upper vesicular zone similar to that at East Clearwater. Discovery Hill is apparently missing its vesicle-rich top and thus was probably thicker than 80 m.

2.10.2 Crystallization Temperatures

The trend in crystallization temperatures is consistent with crystals first forming in ~equilibrium with a high temperature melt and re-equilibrating to differing degrees as the melt cooled. At higher cooling rates (thinner flows) there was less time for diffusion so the crystals were trapped in higher temperature states. Though the trend is expected, the crystallization temperatures obtained are all higher than expected, all at least 100 °C higher than the melt liquidus temperatures of 1120-1150°C calculated from the KWare Magma software. This can be compared with Putirka's (2005) reported error of 24°C on his thermometre. It must be remembered, however, that unlike normal terrestrial magmas, impact melts can form at temperatures well above 2000°C (Pierazzo and Melosh, 2000). Thus, the liquidus temperatures are not constrained by experimental data for terrestrial magma.

2.11 SIGNIFICANCE OF MELT THICKNESS VARIATIONS AT MISTASTIN

Grieve (1975) concluded that variations in the textures of Mistastin impact melt rocks were a consequence of differences in cooling rates of a melt sheet deposited on the

irregular crater floor, with melt pooled in basement lows and deposited over and around topographic highs. This is particularly evident at Coté Creek where the melt is intruded into fractures and follows the irregular top of the underlying brecciated basement units. The inter-relationships of melt rock vesicularity, crystallization temperature, and outcrop thickness documented in this study are evidence that some near-original melt thicknesses are preserved at Mistastin. There are three significant implications of this result: 1) Mistastin may not have had a single coherent, uniform melt sheet; 2) melt volume at Mistastin needs to be reevaluated and 3) glacial erosion may have been overestimated.

2.11.1 Mistastin melt sheet

A coherent melt sheet of near-uniform thickness may not have formed during this intermediate-sized impact event into crystalline rock. Instead, the melt may have been dispersed as channelized flows that followed topographic variations on the crater floor, becoming thicker where it was confined by valleys and ridges, and thinner where it was able to spread out over flatter plains (Fig. 2.17). Melt sheets, where they exist within craters, do not occur as neat, circular discs or annuli of uniform thickness.

In the 100 km diametre Popigai structure, most of the melt occurs as sheets, lenses and irregular bodies within suevite in an annular depression, however, some melt bodies may represent material originally splashed out during crater excavation (Masaitis, 1994). Extensive drilling at the Popigai Structure has revealed an uneven crater floor (Masaitis et al., 1999). Spray and Thompson (2008) showed that the melt sheet thickness of ~90 km diametre Manicouagan crater, originally thought to be a relatively uniform 400m, is highly variable. Modification of the crater in the form of large displacement fault

systems of 100s to 1000s of m occurred while the melt was still fluid, leading to rapid variations in melt sheet depth of up to 1500m. Similarly, the crater rim and annular trough of the deeply eroded, 40 km wide Araguainha impact structure are defined by a complex pattern of radial and concentric fault zones (Lana et al., 2006), most of which are vertical or steeply dipping.

Discovery Hill may be a good example of the distribution of melt along the uneven crater floor. The very different nature of the columnar joints seen on different sides of the butte suggests differing cooling regimes within a small distance. The butte may once have been a more structured terrace that was faulted during crater collapse. The present morphology of the terrace, now a butte, is the result of erosion. Both the North shore and Discovery Hill melt units are located further toward the rim by at least 1 km and the melt units are several metres higher in elevation than the South Shore melt rocks. Target rocks on the lower East end of Discovery Hill are at a higher elevation than the top of the South Shore melt. No structural analysis of the Mistastin crater has been carried out to date, to confirm or deny the existence of such a fault though the change in rock type from granodiorite to mangerite just to the north east of Discovery Hill may provide a suitable location for a fault, since shearing and faulting are favoured at lithological boundaries (Lana et al., 2006; Dressler and Reimold, 2001).

The thin melt units along the South Shore of the lake probably represent sheet flow over an open plain. Dence (1971) suggested that the vesicular igneous rocks on the east side of the Ries crater were probably outlying tongues of the inferred igneous sheet. The Mistastin melt would have had very low viscosities (1000 Pa-s at a liquidus temperature of 1140°C and orders of magnitude less when it was significantly superheated, as

calculated using KWare Magma) and so it tended to flow freely as a broad thin melt sheet unless constrained by topography. The South Shore units are located at a similar distance from the central uplift of the crater (now Horseshoe Island) as all of the other thicker units cropping out around the lake and thus cannot simply represent the thinner, distal parts of a common melt sheet. According to this model, craters of intermediate size into crystalline rocks like Mistastin exhibit impact melt flow characteristics that are transitional between the thick coherent flow sheets at large crystalline rock craters such as the ~250 km diametre Sudbury crater (Deutsch et al., 1995; Dressler and Reimold, 2001) and the melt spatter at small craters like the ~13 km diametre Couture crater (Grieve, 2006). Topographic control of impact melt distribution has previously been suggested for other craters: for instance, in the Chesapeake Bay impact structure, magnetic field anomalies are interpreted as being due to impact melt pooled in kilometre-sized pockets surrounding the base of the central uplift (Shah et al., 2005), and for the lunar crater Tycho, where the melt distribution is thought to be controlled in part by pre-existing topography (Morris et al., 2000).

2.11.2 Melt sheet volume

There have been several studies directed toward relating the amount of melt produced during an impact to the size of the crater (Dressler and Reimold, 2001). One of the uncertainties is how much of the kinetic energy of the impactor is portioned to melting the impactor and target. To assess this, comparisons have been made with field-based estimates from terrestrial craters of various sizes. Combinations of observations and numerical and thermodynamic models have resulted in scaling relations between melt

production and transient crater size, where melt volumes increase by about 4 orders of magnitude as transient crater diametre increases by a factor of ten (Pierazzo et al., 1997; Cintala and Grieve, 1994). According to these relationships, between 10 and 80 km^3 of melting is predicted at Mistastin (Figure 2, Dressler and Reimold, 2001).

Given that the scaling relations rely on calibration from field observations, it should be stressed that establishing melt volumes from field observations is very difficult; uncertainties may be an order of magnitude. One source of uncertainty is the amount of melt ejected from the crater as glass and suevite. Kieffer and Simonds (1980) found that the amount of melt within craters in crystalline rocks is approximately 2 orders of magnitude greater than within craters in sedimentary rocks. Their thermodynamic calculations indicated that melt production should not vary significantly with the target, and concluded that the melt of rocks rich in volatiles is finely dispersed as glass and suevite by the great expansion of shocked volatiles upon release from high pressure. Thus, small differences in volatiles within the target may lead to significant differences in melt sheet volume.

The observation of primary melt thickness variations at Mistastin is that the total volume of impact melt produced in this crater may be less than the previous estimates of ~ 20 km^3, which were based on assumptions of a single coherent melt sheet that was 200 metres thick prior to erosion (Phinney and Simonds, 1977; Grieve and Cintala, 1992). Similar estimates have been made at other complex craters with crystalline targets: the volume of impact melt at the eroded Lappajärvi (32 km) crater in Finland was first estimated based on a 20 km diametre to be a maximum of 10 km^3 (Bischoff, 1981 *in* Reimold, 1982). Grieve and Cintala (1992) estimated a minimum melt volume of 8 km^3.

Grieve and Cintala (1992) also estimated a pre-erosional melt volume of 80 km^3 for West Clearwater. It is important to note that both the Mistastin and West Clearwater estimates are considered uncertain by a minimum factor of two, and that the Lappajärvi estimates are even more uncertain as they are based primarily on geophysical data (Grieve and Cintala, 1992). It is generally accepted that to improve numerical modeling, better field constraints are needed on the volumes of impact melt that may be unrecognized at craters, due to erosional losses, ejection of material far beyond the rim, and the difficulty of accessing melt rocks in craters covered by sediments and/or water. It should be noted that it is not the goal of this paper to discredit the successes of numerical modeling of impact melt volumes, but to become an additional tool in support of these models to understand the formation of impact melts. At Mistastin, the lake covers most of the crater floor, and the thickness and distribution of impact melt rocks below the water level is unknown. Only a small fraction of the crater rim has been mapped in any detail and no detailed geological mapping has been done outside the rim; thus losses of melt rock by ballistic ejection outside the rim are also unknown. The volume of all of the known subaerial exposures of melt rock and suevite at Mistastin were calculated by assuming square volumes and observed melt rock outcrop dimensions in addition to multiplying the proportion of melt particles, ~10-30%, by the volume of suevite outcrops resulting in a minimum volume of 0.02 km^3 of impact melt produced at Mistastin. More realistic estimates must await better approximations of the quantities of melt rock that formed closer to the central uplift of the crater, and that may have been dispersed outside the crater. Our new results do strongly suggest however that model calculations for total melt

volume at Mistastin cannot rely on assumptions of a coherent melt sheet of uniform thickness.

Guided by observations at Mistastin crater, the presently exposed melt rock occurrences are interpreted as representing the irregular edge of the melt sheet, and suggest that the bulk of the melt sheet, rather than being eroded from present exposure levels, may be buried beneath water and sediment of the lake.

2.11.3 Glacial Erosion

The level of glacial erosion at Mistastin (>100 m) may have been overestimated in some areas and there is clear evidence of differential erosion. Mistastin crater experienced several episodes of glaciations in the Pleistocene, when the North American ice sheets successively expanded and retreated approximately every 100,000 years (Bintanja and van de Wal, 2008). It may also (more controversially) have been glaciated in the late Eocene (Eldrett et al. 2004). The extent of resulting glacial erosion of the crater is unknown.

The amount of erosion caused by continental ice sheets has been debated for decades (White, 1972; Laine, 1980; Andrews, 1982; Sugden, 1976b and references therein) and remains a controversial topic (Hallet et al, 1996; Delmas et al., 2009). Glacial erosion rates determined by a variety of methods (e.g., basin sediment loads, cosmogenic ages) for North America range over five orders of magnitude (10^{-4} to 10 mm/yr), permitting Pleistocene erosion of a few metres to a few kilometres. Erosion rates are influenced by bedrock topography and geology: topographic highs tend to erode more

than depressions and poorly consolidated sediments erode more easily than crystalline basement rocks (Sugden, 1976a).

Discovery Hill melt rock may have been initially surrounded by brittle, shocked target rocks and overlain by breccias, which were susceptible to erosion. The melt rocks are much more robust in comparison and that therefore differential erosion created the melt rock butte. Discovery Hill may have been a target for more intense erosion as it was much more exposed as a topographic high, but the underlying target rocks were protected by the melt rock cap. Based on the lack of vesicles, clast-rich material and any reduction in grain size at the top of Discovery Hill, a minimum estimate of 10-20 metres of melt rock was removed. Therefore original estimates ~100 m of erosion (Grieve and Cintala, 1992; Phinney and Simonds, 1977) in some parts of the crater may be reasonable. However, it may be that most erosion was of breccias and suevite units as it is unlikely that significant consolidated melt would have been removed from the flat-lying, extremely vesicular South Shore outcrops. The South Shore outcrops underwent erosion of no more than 10 metres of solid melt rock. This estimate is conservative and does not include any other deposits such as crater-derived sediment (i.e. fallback breccias), fluvial or glacial deposits.

Topography is often a good measure of how much erosion has taken place. At Mistastin, important crater morphologies are still preserved. Figure 2.2 shows that the rim and central uplift of the crater are still prominent features. It is also still unknown whether fallout material has been preserved outside the crater rim. (Sugden, 1976b) concluded that ice sheet erosion in continental shield areas has been restricted to the modification of pre-existing surface morphologies rather than deep erosion. This

implication is not so bold when considering the preservation of Clearwater East's melt sheet of similar composition, which may have been subjected to far more glaciation as it is much older, ~290 Ma (Reimold et al., 1981).

2.11.4 Lunar implications

Finally, the results of this study are of some relevance to the origin of some of the lunar highland impact melts which, like Mistastin, formed in part by total melting of largely anorthositic target rocks. Impact melt rocks constitute some 30-50% of all hand-sized samples from lunar highland sites sampled by Apollo astronauts, and about 50% of soils sampled at all lunar sites (Heiken et al., 1991, p.102). Their radiometric ages are used to date the cratering history of the Moon and by extension the inner solar system, but the genetic relationships of particular melt rock samples to one another and to the specific craters from which they formed are poorly known, complicating interpretations (e.g., Hartmann et al., 2007). This is due especially to the history of repeated impacting of the lunar surface over billions of years, which has mixed older and younger melt rocks and obscured their original distributions and relationships.

The Mistastin results suggest that, in attempting to piece the lunar puzzle of impact melt formation back together, it should be kept in mind that significant heterogeneities would be expected in melt rocks derived from a common lunar crater. The heterogeneities would include variable abundances of country rock clasts and vesicles in lunar impact melt rocks as a function of stratigraphic position within the flow unit, as well as potentially large differences in unit thicknesses produced by topographic controls on the melt flow. Lunar regolith and many glasses recovered in the Apollo missions are

enriched in volatile elements and the vesicular volcanic rocks from the moon are evidence that vesicles can form in the Moon's high vacuum (Heiken et al., 1991). There are even noteable heterogeneities in the matrix compositions of the melt at Discovery Hill, Coté Creek, South Shore and North Shore (table 3). When scaled for gravity differences between Earth and the Moon, lunar craters that would have produced equivalent amounts of impact melt as at Mistastin would be those of 150-200 km in diametre (French, 1998). There are more than 45 craters of this size on the Moon.

2.12 CONCLUSION

Mistastin Lake, Labrador, is a well-preserved, intermediate-sized (28 km diametre) terrestrial impact crater in crystalline rock, dominantly anorthosites. The relationship of preserved melt thicknesses relative to the crystallization temperatures and vesicularities of anorthositic impact melt rocks at Mistastin, in addition to variations of groundmass textures and clast contents of the melt units are significant. They suggest that it is unlikely that subaerial exposures of impact melt rock formed at Mistastin from a uniform coherent melt sheet, some 200 m thick. Instead impact melt at Mistastin was probably dispersed as both channelized and sheet flows of variable thickness (~80 to 1 m) as a result of transport across irregular topography of the faulted crater floor and terraced rim. Lunar craters that produced comparable volumes of anorthositic impact melt as at Mistastin may exhibit similar heterogeneities in their melt rock products, which should be considered in attempts to determine genetic relationships between lunar impact melt breccias of similar ages. The method of comparing vesicularity and crystallization temperature of impact melt rocks with preserved unit thickness could be applied to other

terrestrial craters where pre-erosional melt rock volumes are unclear.

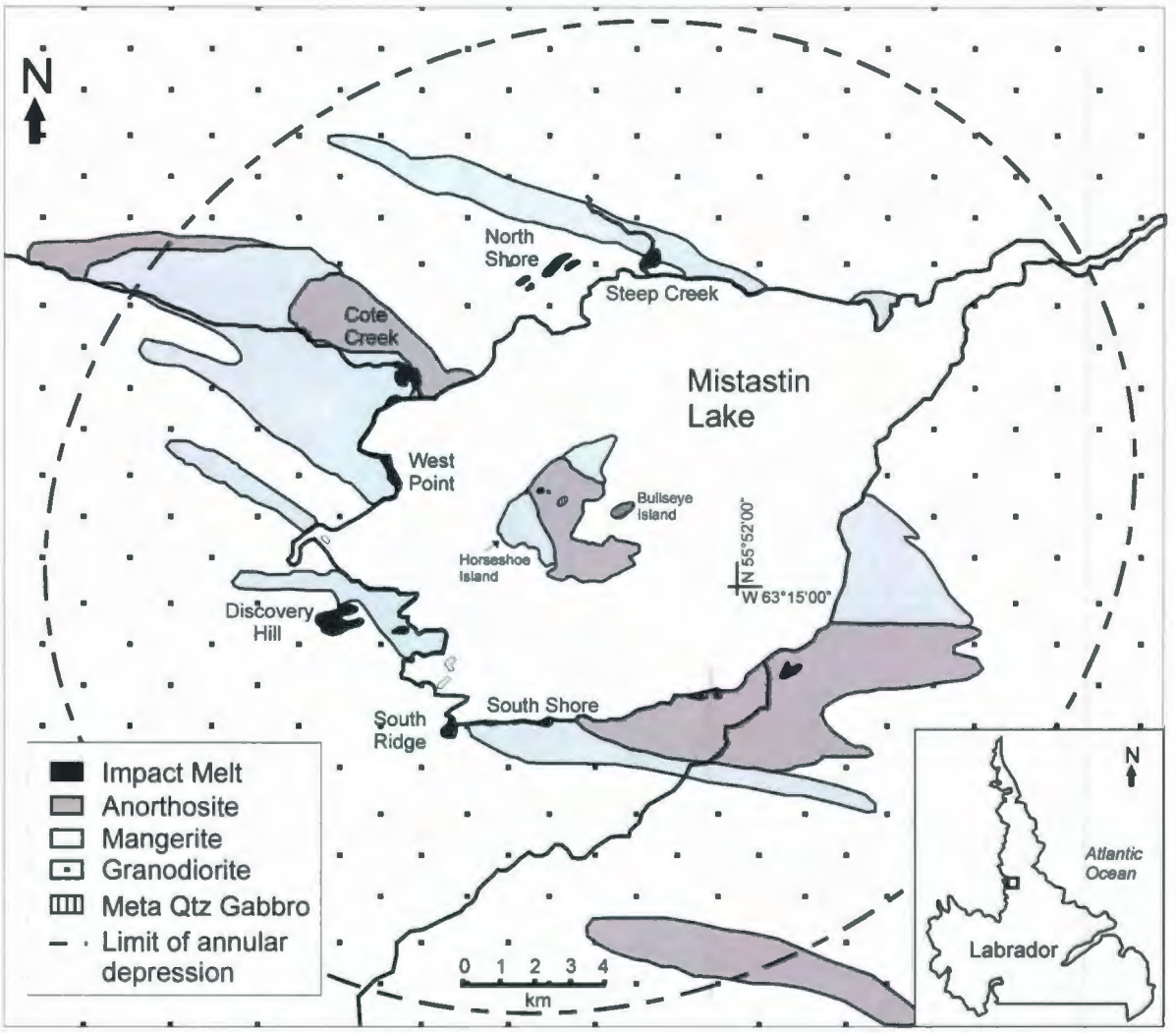

Figure 2.1. Generalized geology map of Mistastin impact structure, modified from Currie (1971) and Grieve (1975) based on new mapping (this study). The location of the map area is identified by the black box on the imbedded map Labrador. Dashed line indicates the approximate position of the inner face of the crater rim inferred by Grieve (1975). Sample codes were used to represent multiple sampling locations. Dh1 represents Cm042, Cm043, Cm044, Cm036 and W05-63; Dh2 represents Cm035, Cm037, Cm039 and W05-61 (from the top centre of Discovery Hill); Cc1 represents Cm015, Cm020, Cm021, Cm023, Cm024, Cm025, Cm028, Cm084, Cm088 and W05-60; Sr1 represents Cm064, Cm065 and Cm066; Ss1 represents Cm071 and W05-65 and Sc1 represents Cm006, Cm007, Cm010 and Cm008.

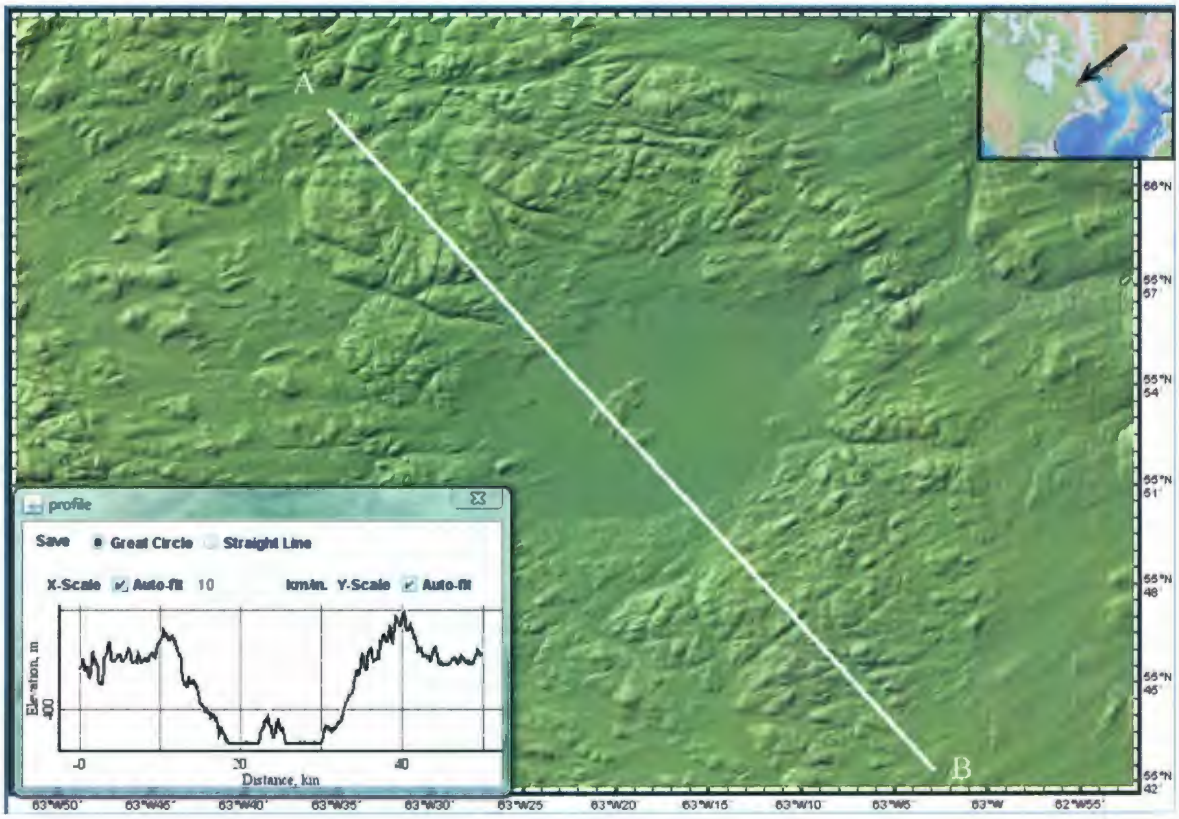

Figure 2.2. Digital Elevation Model (DEM) of the Mistastin Lake area. Inset of topographic profile A-B shows the structure of the rim and central uplift are preserved. Tick marks on the y axis of the topography profile are every 20m. Note the oddity of Discovery Hill on the West side of the Lake. DEM was made courtesy of Geomapapps software, accessed August 27, 2008 at 1:00pm NL time.

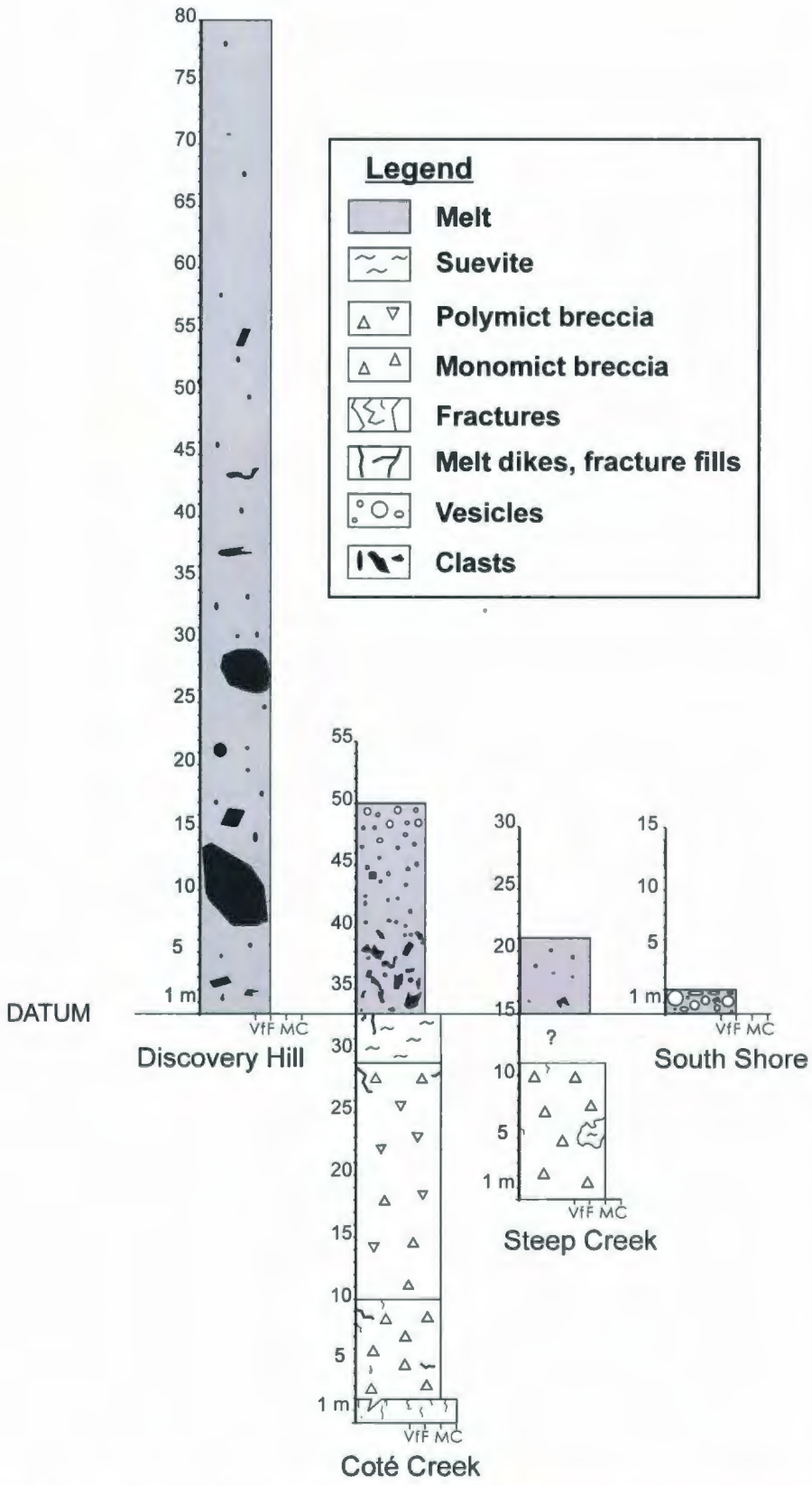

Figure 2.3. Stratigraphy of the Mistastin Lake Impactites: all contacts are transitional; the base of the melt rocks is used as a datum. The large clasts in the Discovery Hill melt are mangerite.

Figure 2.4. Target Rocks A) anorthosite, B) granodiorite and C) mangerite.

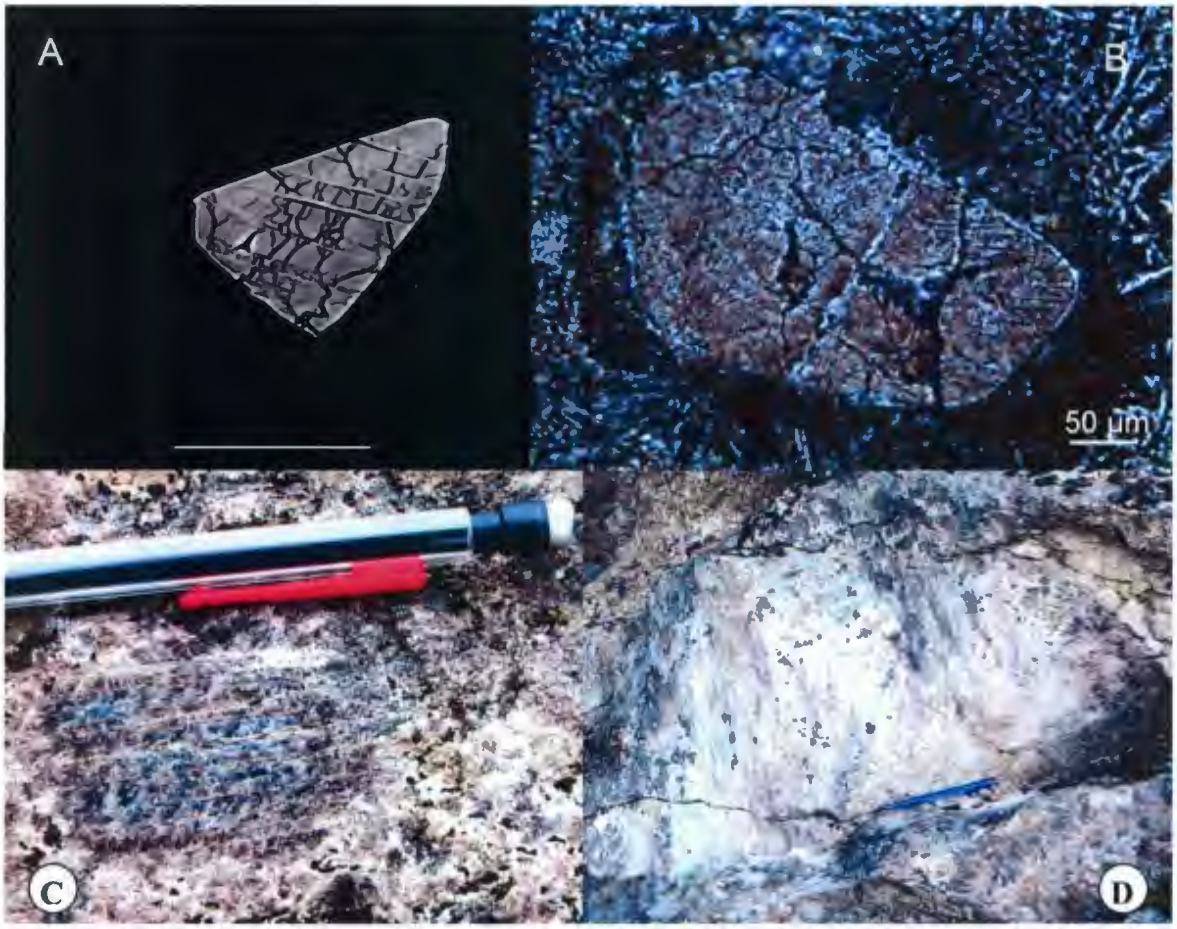

Figure 2.5. Shock metamorphic features: A) BSE image of planar deformation features (PDFs) in fractured zircon from shocked anorthosite, Horseshoe Island (sample CM032); B) PPL photomicrograph of sample CM036 of "toasted" quartz clast with faint PDFs; C) PDFs or shock induced twins in plagioclase, anorthosite from the southern part of Horseshoe Island; and D) shattercones in shocked anorthosite on the southern end of Horseshoe Island, pen for scale.

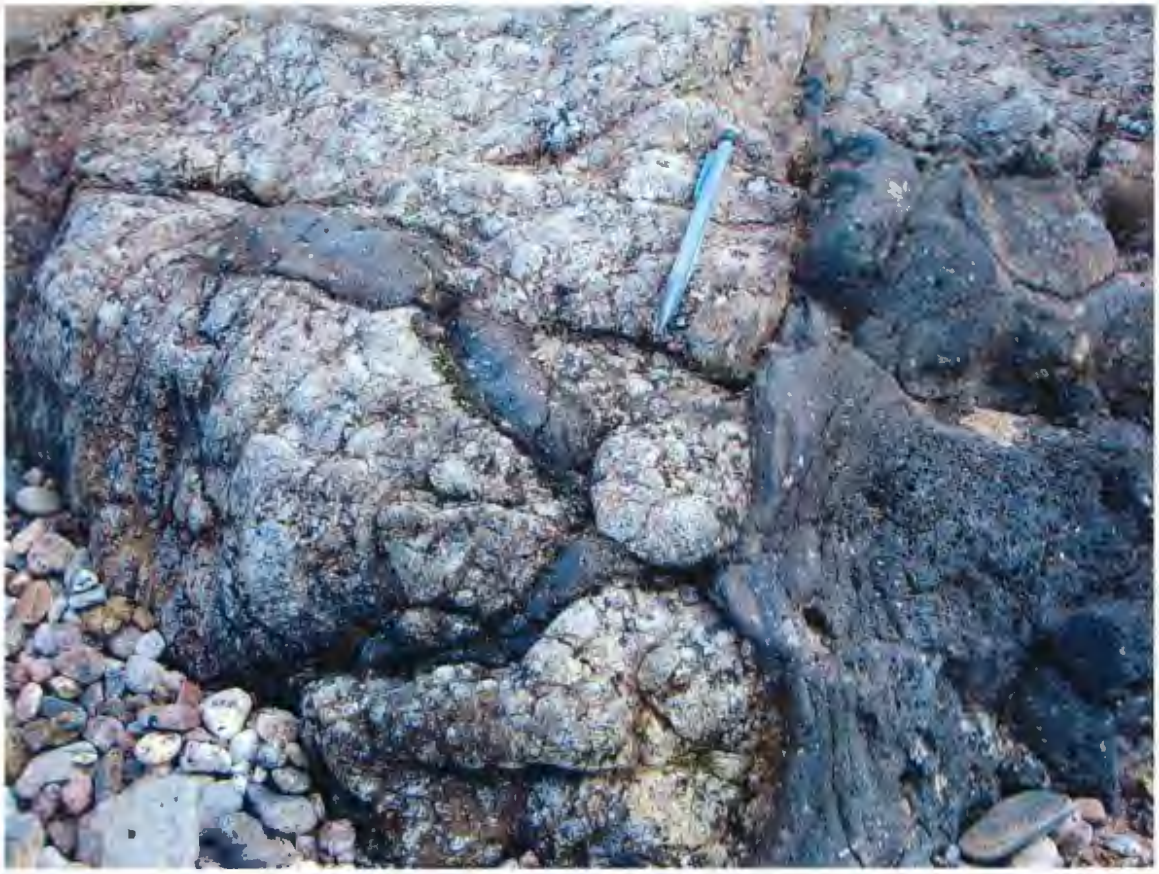

Figure 2.6. Impact melt intrusion in anorthosite, South Shore.

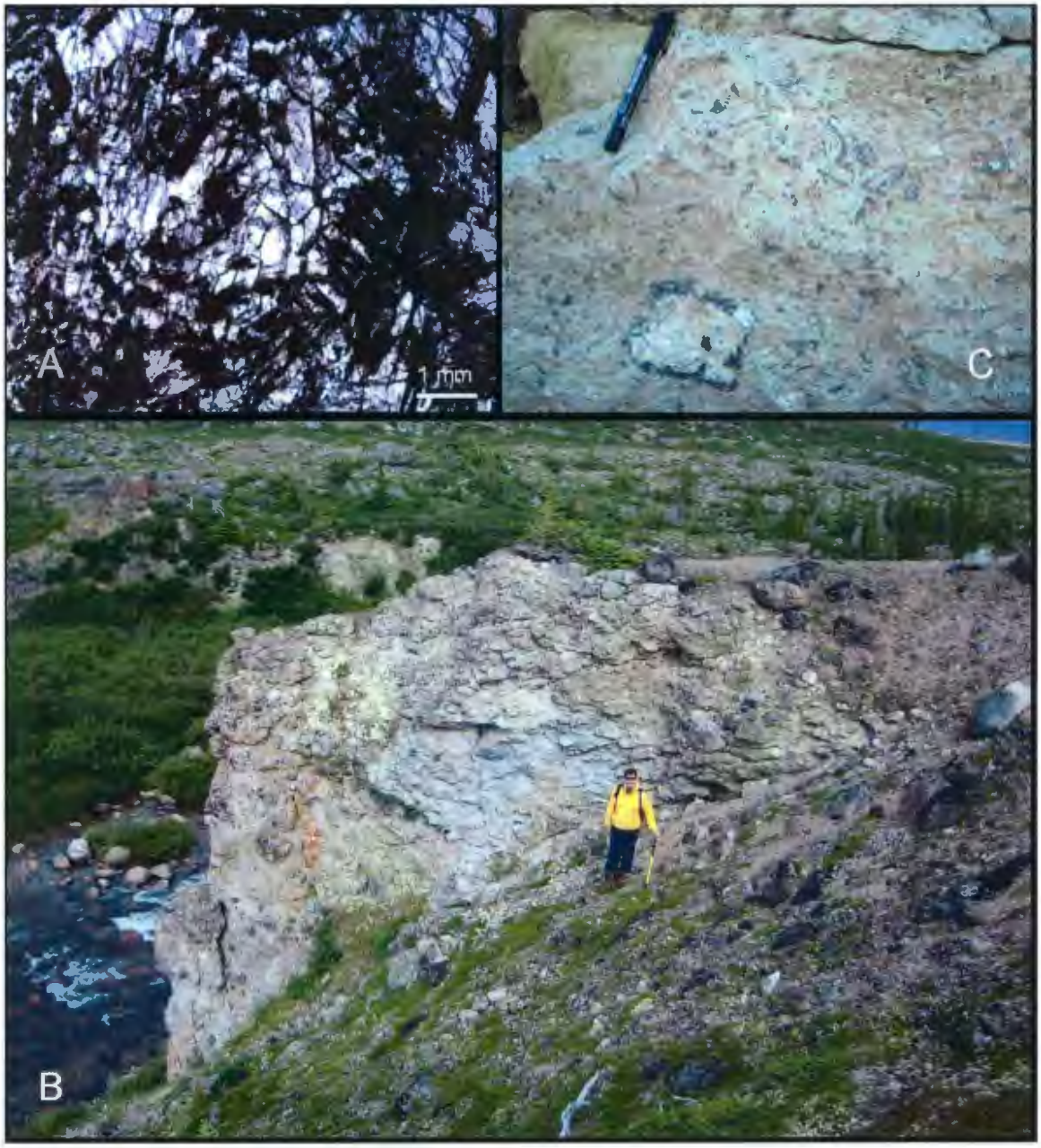

Figure 2.7. Stratigraphic units A, C and D described in the text. A) photomicrograph of brecciated anorthosite (unit A) from Bull's Eye Island, B) polymict breccia ridge (unit C) on the west side of Coté Creek, C) melt-clast rich impact breccia/suevite (unit D). This particular unit forms a large intrusion into target rocks at Steep Creek. Note the melt mantled plagioclase clast.

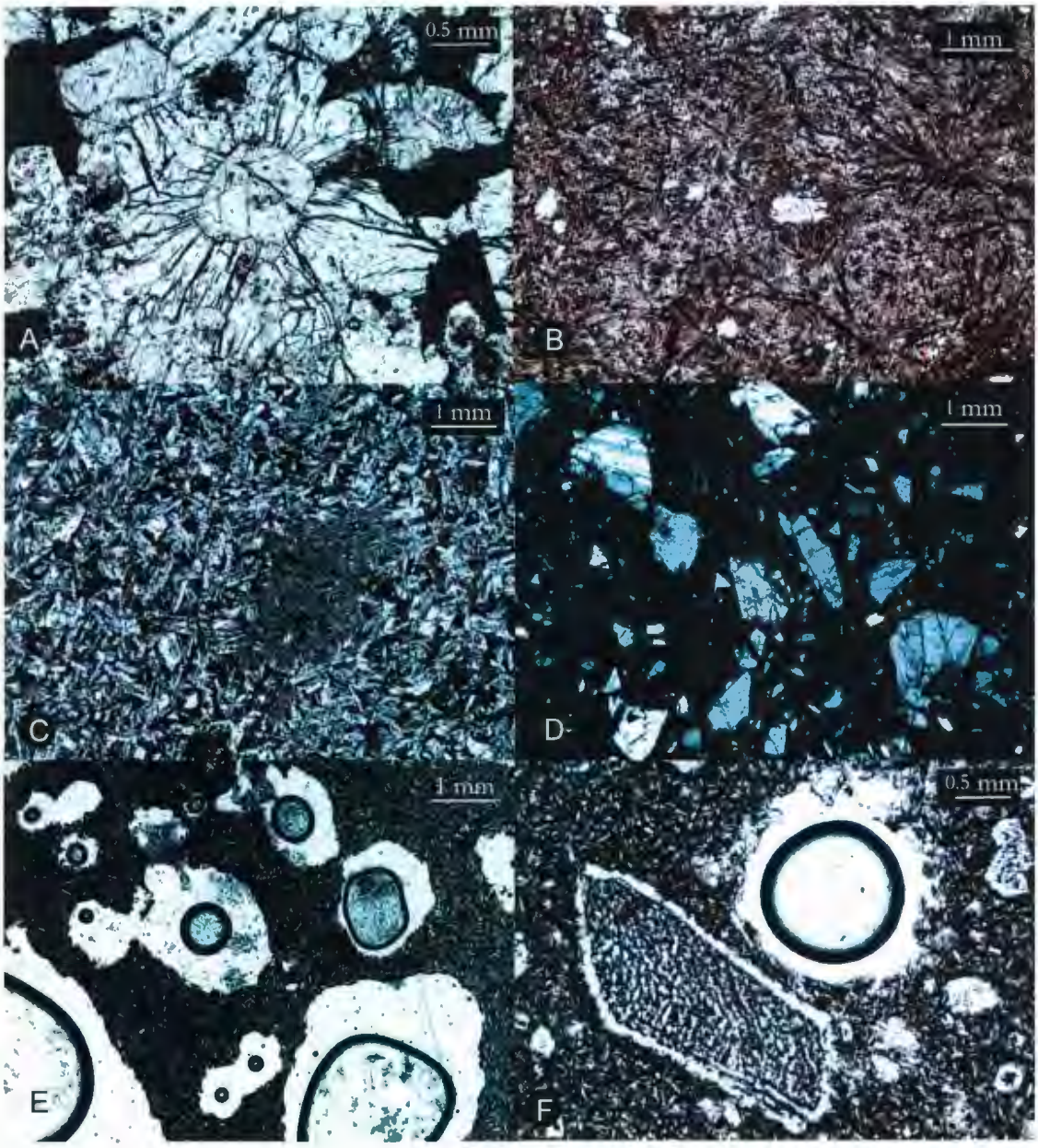

Figure 2.8. Photomicrographs of Mistastin's impactites: A) intensely shocked granodiorite or mangerite from Coté Creek with abundant maskelynite in PPL. This entire section is isotropic under crossed polars; B) impact melt rock from Discovery Hill in PPL (sample CM042): dendritic pyroxene (up to 1 mm) and plagioclase microlites (up to 0.5 mm). The clear to white fragments are quartz and plagioclase clasts; C) North Shore impact melt rock: plagioclase microlites (phenocrystic laths up to 0.75 mm) in PPL. The fine-grained area centre-right is an extremely corroded clast; D) sample CM088, impact melt breccia at the basal contact at Coté Creek in crossed polars; due to rapid cooling clasts are not digested, and the lack of reaction rims suggest that there was insufficient time for bubble nucleation and perhaps partial melting. Microlites are less that 100μm; E) Glassy vesicular impact melt rock in PPL from the south shore (sample CM067, same sample as in figure 10B. Plagioclase microlites are less than 75μm; F) impact melt rock from Coté Creek in PPL (sample CM025) with a mm-size vesicle and mixed glass and crystalline matrix. There is a large plagioclase clast adjacent the vesicle with a rim of melt coating plagioclase and sieve-like texture in the centre. Many of the micro-clasts are partially digested by the melt. Plagioclase microlites are up to 100 μm.

Figure 2.9. Melt rock exposures at Discovery Hill. A) South side view showing maximum height and two-tiered columnar joints; B) columnar joints and transition into parallel joints with a magnification of the massive melt rock shown in the inset; C) north side view with parallel joints and a large mangerite boulder to the right of the person.

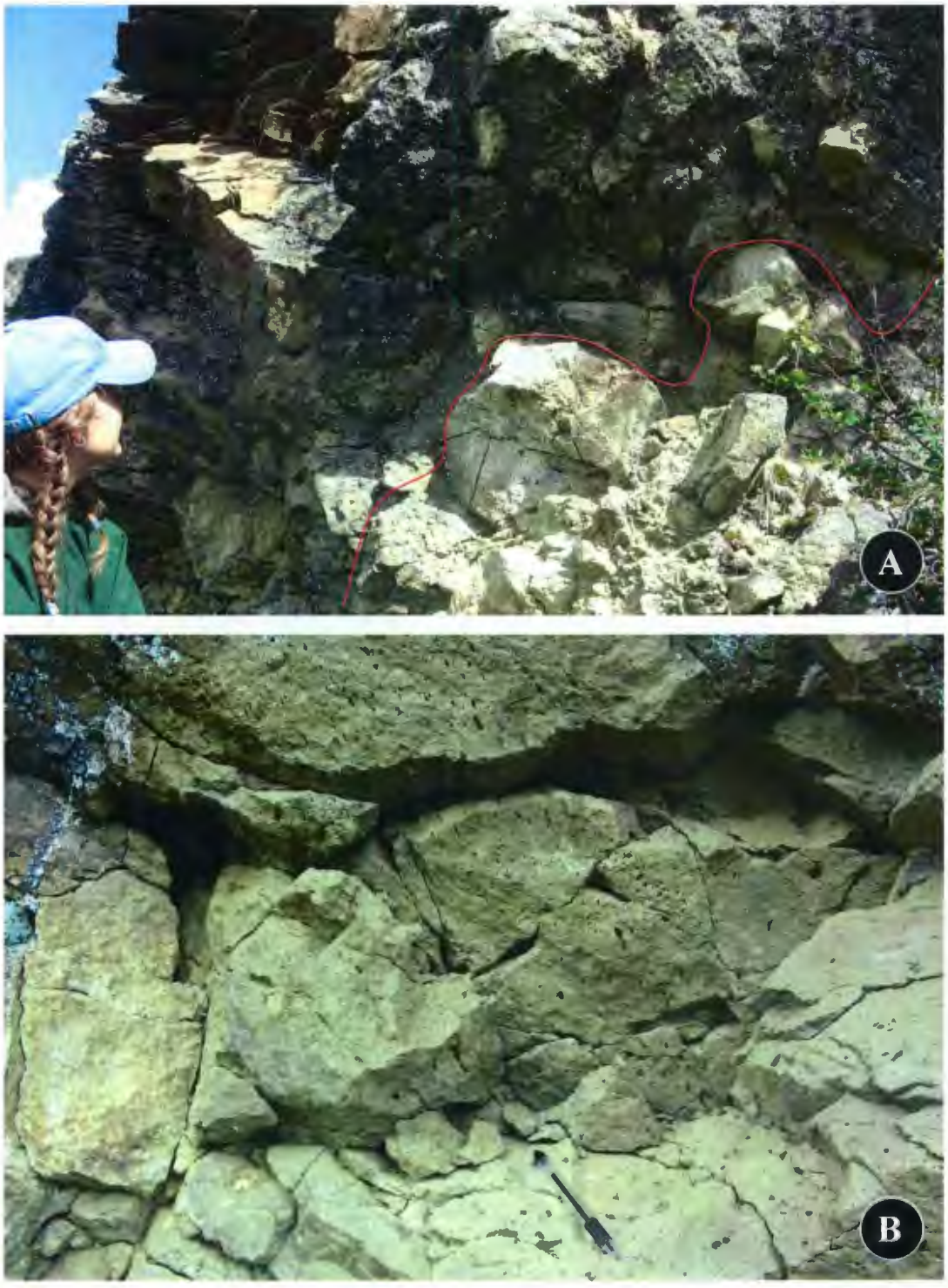

Figure 2.10. Melt rock exposures at Coté Creek: A) Basal contact of the impact melt (top left) with underlying polymict breccias (bottom right), B) weathered impact melt rock located ~ 1m from the basal contact with slightly elongate vesicles.

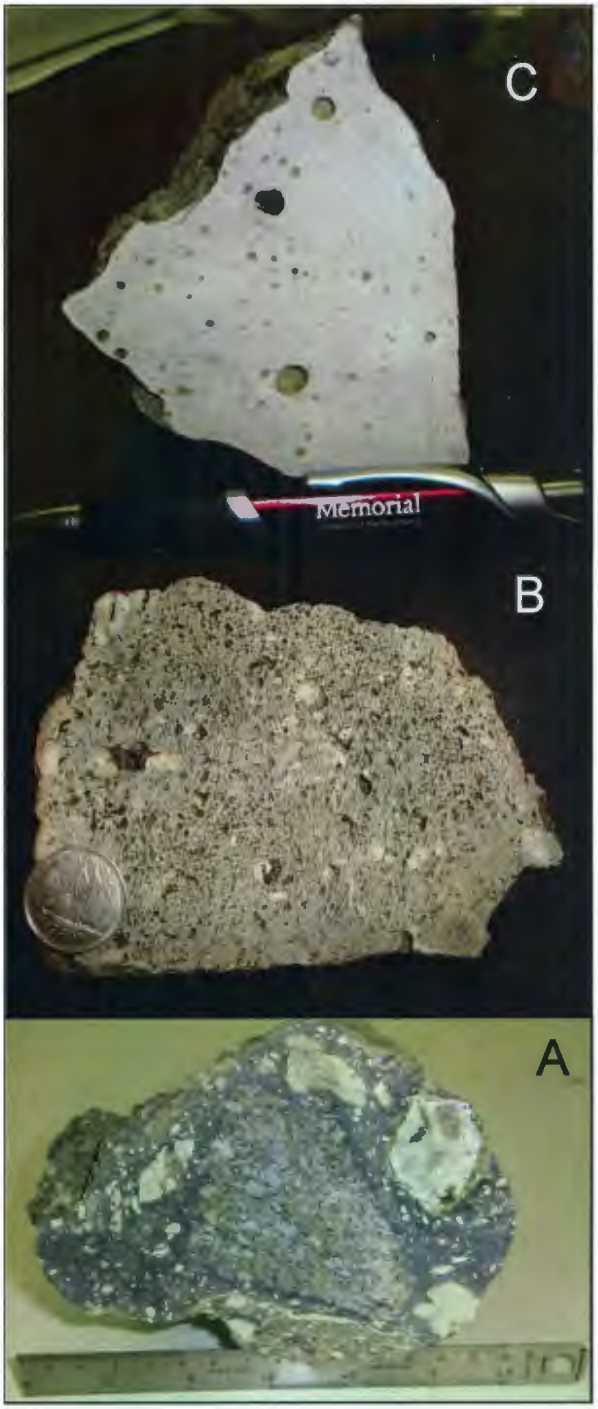

Figure 2.11. Coté Creek samples from bottom (A) to top (C) of the section: A) clast-rich, glassy basal melt rock within 1 m of the basal contact, B) clast-rich, viscous partially glassy, vesicular melt rock (CM021) approximately 4 m from the basal contact; and C) clast-poor, vesicular melt rock with beautiful spherical vesicles (CM025) approximately 12 m from the basal contact.

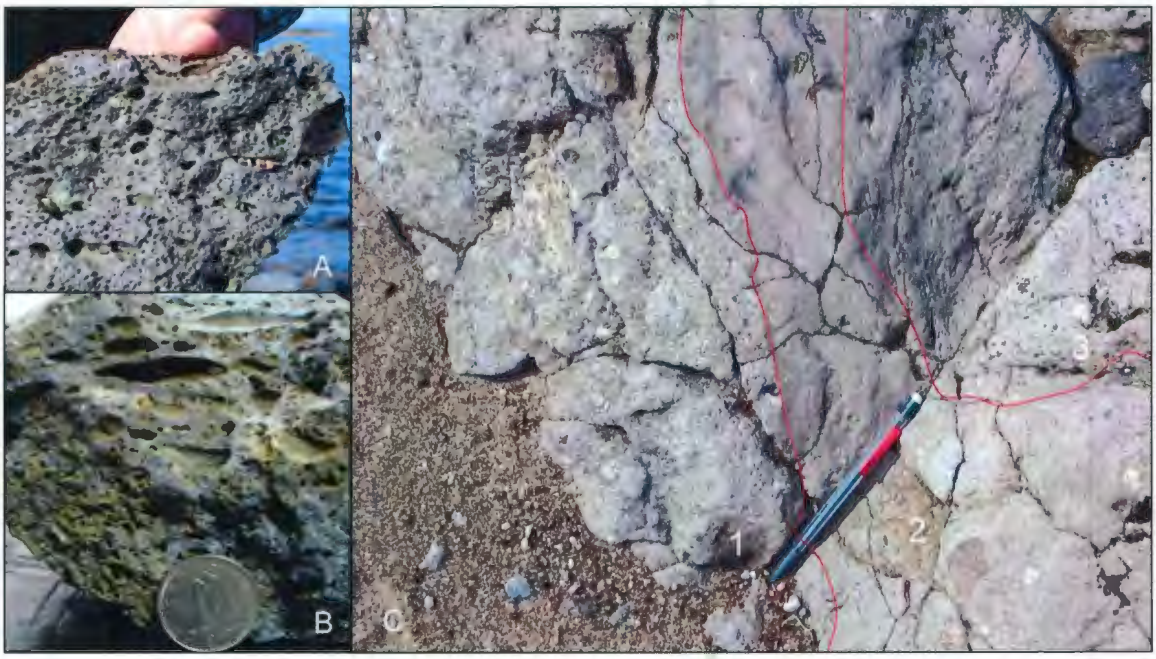

Figure 2.12. Melt rocks from the South shore: A) and B) are samples of very vesicular melt rocks where B is sample CM067, with a mean vesicularity of 22 vol%; C) the basal contact of layered melt rock, 1 is the clast-rich glassy bottom, 2 is an intermediate melt rock and 3 is a vesicular melt rock.

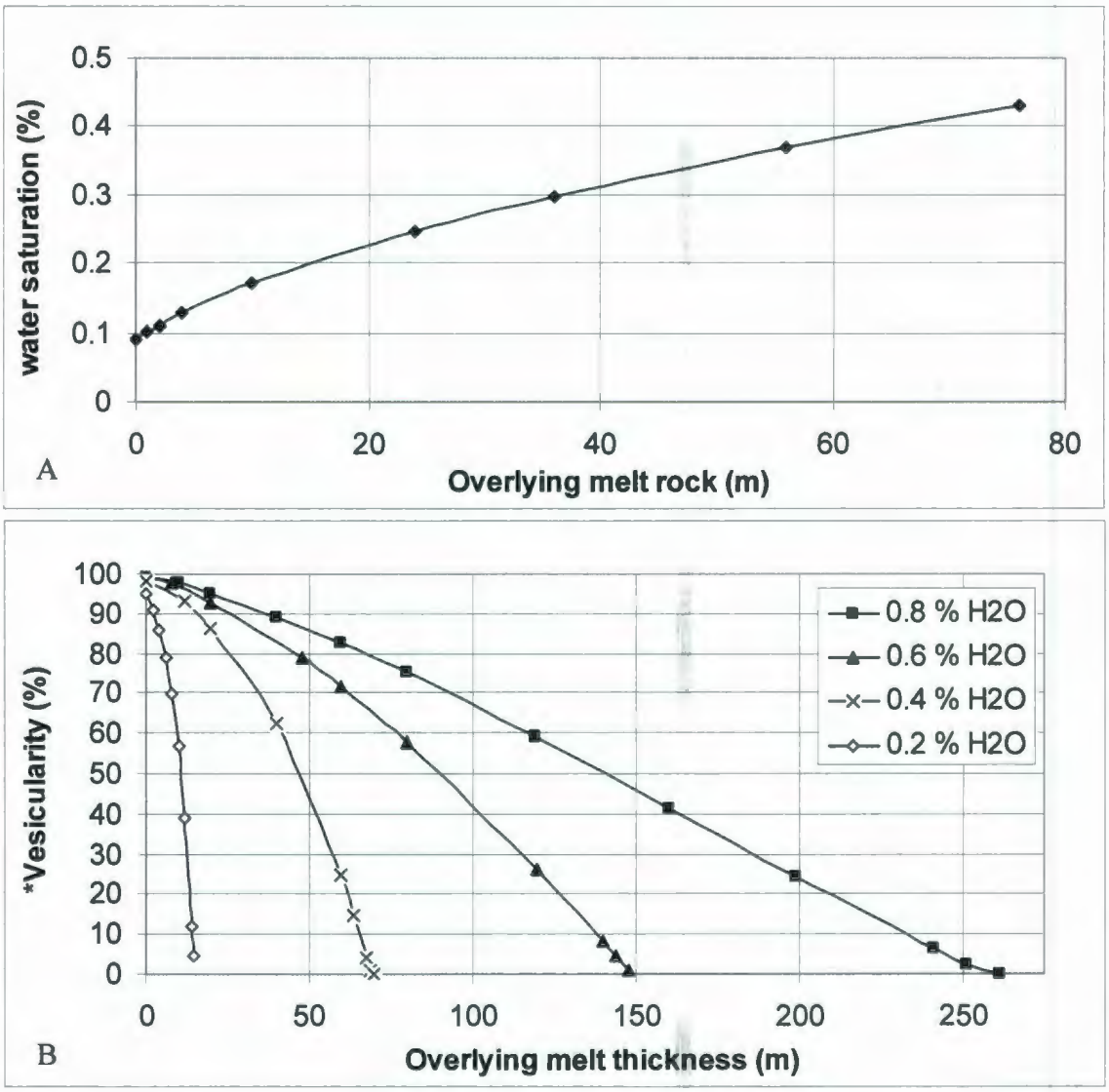

Figure 2.13. A) Model for water saturation as a function of overlying melt thickness. Saturation increases with increasing melt thickness or due to increasing pressure (see text for details); B) Equilibrium vapour fraction as a function of equivalent overlying melt thickness for various wt. % H_2O. *Vesicularity is the volume vapour fraction at a uniform temperature of 1100 °C calculated by KWare Magma (Wohletz, 1999) for typical melt rock sample CM005, assuming thermodynamic equilibrium and no bubble movement. This is based on oversaturation of the magma at each depth and pressure and the specific volume of the vapour phase from equation (2). Equivalent melt thickness is calculated using equation (1).

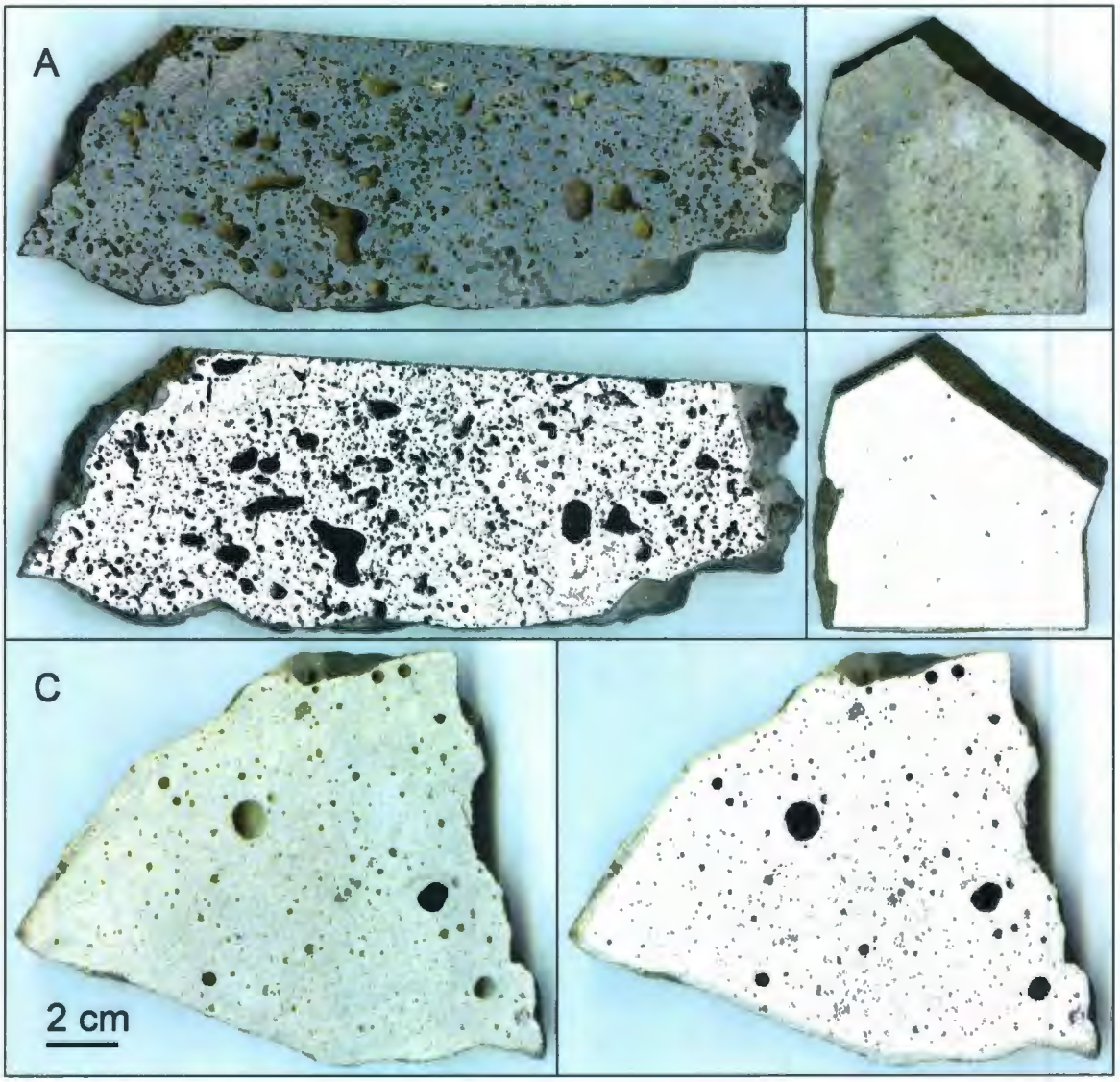

Figure 2.14. Image Scan method applied to vesicular to non-vesicular melt rocks: A) sample CM067 from the South shore. Vesicularity or area percent of black pixels in the selected area is 24 % whereas the Archimedes vesicularity is 20 vol. %; B) sample CM042 from Discovery Hill. Image scan vesicularity is 1%, Archimedes 0 vol.%; and C) sample CM025 from Coté Creek where the Image Scan vesicularity is 5% and the Archimedes vesicularity is 6 vol.%.

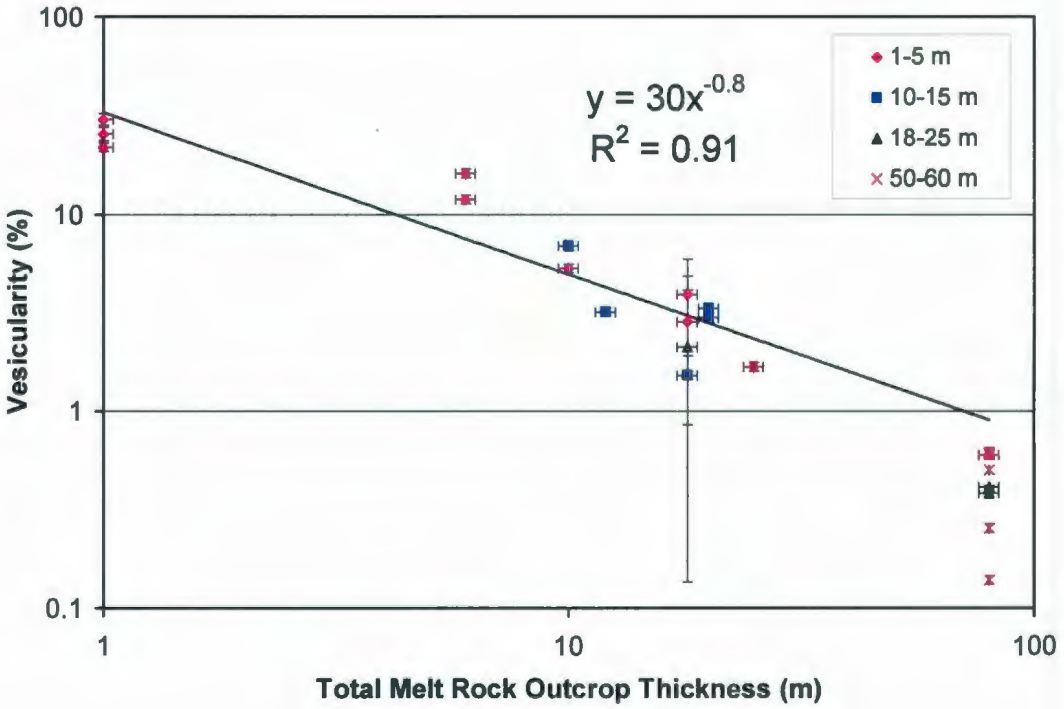

Figure 2.15. Variation in vesicularity of 22 melt rocks sampled at various depths from the surface of melt outcrops as a function of total thickness of melt rock outcrop. Legend displays the sampling depth from top of exposure. Solid line is least-squares fit of the surface outcrop data using a power law relationship. Vertical error bars represent ± 5% for image scan values and mean values and ± 2% for Archimedes values. Horizontal error bars represent 5% error on the position of the sample within outcrop and the outcrop thickness itself as most thicknesses were estimated with a person for scale.

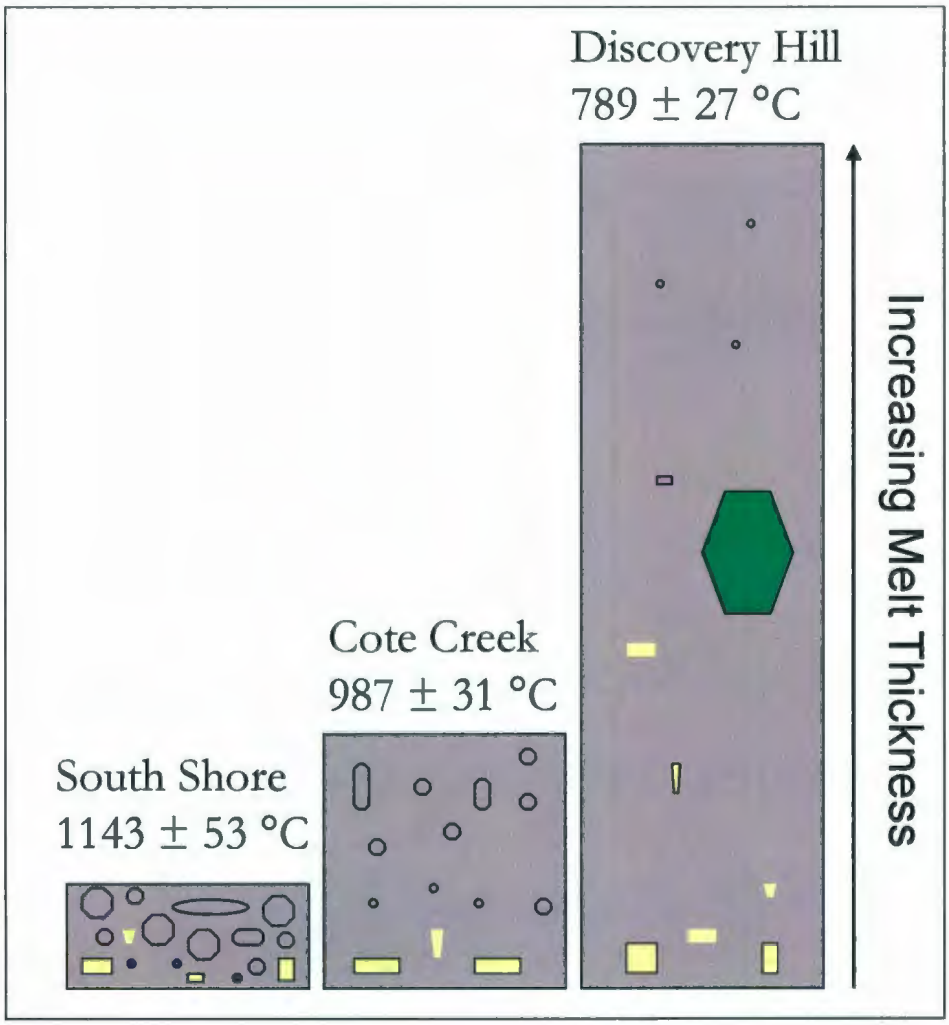

Figure 2.16. Schematic comparison of melt rock thickness, vesicularity and crystallization temperatures for the Discovery Hill, Cote Creek and South Shore locations. This shows that crystallization temperatures at Mistastin increase with a decrease in melt outcrop thickness when examining clast-poor melt rocks. Black circles and ellipses represent vesicles, and the yellow polygons represent clasts; the green polygon represents a mangerite boulder.

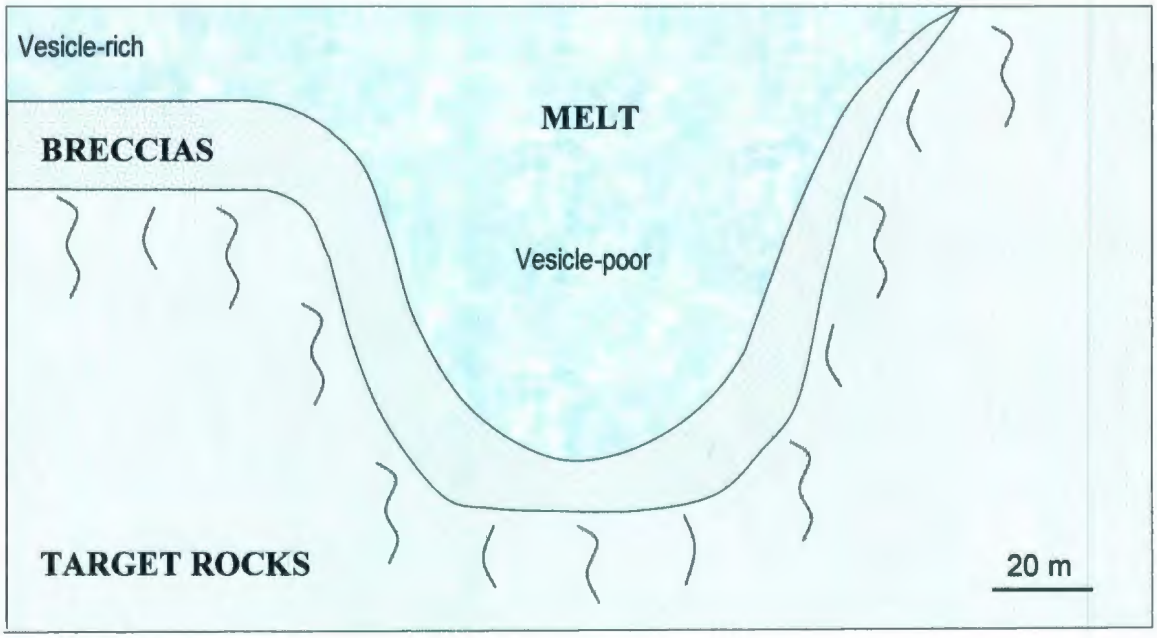

Figure 2.17. Schematic cross section demonstrating the effect of topography on the distribution and thickness of impact melt; the melt may have been distributed just outside the floor of the impact crater by channeling of the flows along topographic lows. Note: it is also possible that melt flows emanating from the central melt zone thinned out and ended up topographically lower than the central melt area.

Table 1. Densities of low vesicularity, clast-poor impact melt rocks from Discovery Hill.

Sample	$\rho_{Arch.}$ (g/cm^3)	ρ_{calc1} Dry, R=0.15	ρ_{calc2} 0.4% H_2O, R=0.47	φ_{scan} (%)
CM037	2.642	2.714	2.627	0.24
CM042	2.656	2.69	2.606	0.62
CM043	2.611	2.72	2.637	0.26
CM044	2.625,2.681	2.655	2.581	0.32

$\rho_{Arch.}$ is the density measured using the Archimedes method; ρ_{calc1} is density calculated using KWare Magma, for different water contents and oxidation states (see text for details). $R=Fe_2O_3/(FeO+Fe_2O_3)$. φ_{scan} is the vesicularity determined by the image scan method. Densities are calculated at T=20°C.
Samples CM042-44 were collected at the base on the south side of the Discovery Hill melt outcrop and sample CM037 was collected from approximately 10 m from the top of the north side of the Discovery Hill outcrop.

Table 2. Results from vesicularity measurements for both methods.

Sample Name	Outcrop	Location (Lat./Lon.)		Arch. Vesicularity (vol. %)	I.S. Vesicularity (area %)	I.S. S.D.	Mean
CM015	Coté Creek	N55° 55' 07.7"	W63° 23' 37.2"	3	3.3	2.3	3.2
CM021	Coté Creek	N55° 55' 09.3"	W63° 23' 39.5"	16	6.5	0.9	11
CM024a	Coté Creek	N55° 55' 14.4"	W63° 23' 51.8"	3	3.2	0.3	3.0
CM024b	Coté Creek	N55° 55' 14.4"	W63° 23' 51.8"	4	3.2	0.3	3.6
CM025	Coté Creek	N55° 55' 07.1"	W63° 23' 29.0"	6	4.8	2.7	5.3
CM028	Coté Creek	N55° 55' 08.8"	W63° 24' 01.2"	2	1.25	0.4	1.5
CM088	Coté Creek	N55° 55' 15.3"	W63° 23' 46.6"	11	2.4	0.9	7
W05-60	Coté Creek	N55° 55' 15.0"	W63° 23' 46.4"	2	0.4	0.1	1.3
CM035	Discovery Hill	N55° 51' 34.3"	W63° 26' 11.9"	0.4	0.60	0.4	0.5
CM036	Discovery Hill	N55° 51' 29.6"	W63° 25' 58.0"	5.6	0.38	0.1	3.0
CM037	Discovery Hill	N55° 51' 37.1"	W63° 26' 06.5"	0.6	0.24	0.1	0.4
CM042	Discovery Hill	N55° 51' 26.5"	W63° 26' 04.1"	0	0.62	0.2	0.3
CM043	Discovery Hill	N55° 51' 25.1"	W63° 26' 07.3"	2.5	0.26	0.3	1.4
CM044a	Discovery Hill	N55° 51' 25.1"	W63° 26' 07.3"	0	0.14	0.1	0.1
CM044B	Discovery Hill	N55° 51' 25.1"	W63° 26' 07.3"	0	0.50	0.1	0.25
CM051	North Shore	N55° 56' 21.6"	W63° 20' 36.1"	21	10.6	3.2	16.1
CM064	South Ridge	N55° 49' 54.0"	W63° 22' 49.8"	10	3.0	0.0	6.3
CM065	South Ridge	N55° 49' 53.9"	W63° 22' 53.4"	0	3.3	0.0	1.7
CM066	South Ridge	N55° 49' 49.0"	W63° 22' 53.4"	2	1.7	0.1	1.8
CM067	South Shore	N55° 49' 55.6.0"	W63° 21' 48.1"	20	23.6	0.0	22
W05-65s	South Shore	N55° 49' 55.7"	W63° 21' 17.4"	30	26.5	12.6	28
W05-65L	South Shore	N55° 49' 55.7"	W63° 21' 17.4"	26	26.5	12.6	26

Arch. = Archimedes' method; uncertainty of ±2%.

I.S. = Image Scan Method; relative uncertainty of 5-50% based on analyses of two different slab faces of each sample.

Table 3. Example crystallization data for each representative location

	Discovery Hill		Coté Creek		South Shore		North Shore	
	n=2	n=2	n=1	n=2	n=1	n=1	n=1	n=1
	Matrix	Plag.	Matrix	Plag.	Matrix	Plag.	Matrix	Plag.
SiO_2	56.38	53.72	52.57	55.56	53.95	51.43	58.25	52.78
TiO2	0.66		0.92		0.33		0.173	
Al_2O_3	22.36	28.49	25.59	25.24	26.64	30.42	25.63	29.41
FeO	4.43	0.61	2.55	1.52	2.80	0.34	0.79	0.49
MnO	0.05		0.07		0.04		0.02	
MgO	0.84		0.34		0.84		0.14	
CaO	7.06	12.54	9.12	10.48	8.68	14.05	6.69	13.16
Na_2O	4.39	4.04	5.11	4.96	4.90	3.47	6.15	4.27
K_2O	2.71	0.33	1.03	0.62	1.16	0.24	1.67	0.27
Total	98.87	99.73	97.30	98.38	99.33	99.95	99.51	100.38
An		61.95		51.90		68.15		62.04
Ab		36.11		44.45		30.46		36.43
Or		1.94		3.65		1.39		1.53
P (kbar)	0.02		0.0035		0.001		0.0035	
Temp. °C $_{H2O=0.2}$	1230		1291		1313		1259	
Temp.° C $_{H2O=0.4}$	1220		1281		1302		1249	

Plag. = Plagioclase, Temp. = temperature, P = pressure

Note: Temperature used in Putirka's (2005) equation is in Kelvin. Errors on temperatures are discussed in the text.

Data is from microprobe analysis. Pressure is calculated using equation (1).

n=number of analysis

Chapter 3

Composition and Heterogeneity of Impact Melt at Mistastin Lake Crater, Labrador

3.1 ABSTRACT

Anorthositic impact melt rocks, their target rocks (principally anorthosite, mangerite, granodiorite) and zircon clasts from the ~36 Ma-old, 28 km-wide Mistastin Lake crater of northern Labrador (55°53'N; 63°18'W) have been examined in order to evaluate the scale and origin of compositional heterogeneities in impact melts produced in craters of moderate size. In particular we assess whether mineral clasts entrained from the underlying rocks into the melt sheet have significantly modified the initial composition of the anorthositic melt that had formed upon impact. A secondary goal was to determine if zircon clasts in the impact melts are present in the proportions of their target rock sources and/or the substrate lithologies over which they flowed. Chemical compositions of bulk samples of thirty-three melt rocks and fourteen target rocks were measured by XRF and SN-ICPMS. Matrix compositions of nine samples of impact melt rocks were determined by EPMA and LA-ICPMS. Zircon grains from four samples of target rock and zircon clasts from three samples of impact melt rock were measured for multi-element composition, U-Pb age and Hf-isotopic composition by LA-(MC)-ICPMS.

The data reveal compositional heterogeneities in the impact melts on the scales of both bulk samples and matrices. Bulk samples can be divided into compositions with

high and low concentrations of high-field strength elements (HFSE; Ti, Zr, Nb) and Fe, Ba, Ce and Y. High HFSE-type melt rocks formed when impact melt entrained large quantities of clasts from mangerite, which is rich in HFSE. Matrix compositions of bulk samples do not show the HFSE distinction but are affected by the introduction of low-temperature melts from the clasts to form dispersed, micron-scale silica-rich heterogeneities. Both clast entrainment and melting are more extensive for the thicker flow units, which had a higher heat capacity for melting and cooled more slowly than thinner flows.

The best estimate of the sources of the initial impact melt is ~73% anorthosite, ~7% mangerite and ~20% granodiorite, based on least-squares modeling of major element compositions of the matrices of thinner flows. Zircon derived from anorthosite can be distinguished from zircon from mangerite and granodiorite on the basis of higher Nb/Ta and Eu/Eu* ratios and more negative initial ε Hf values. Zircon clasts greater than 40 microns in size in the impact melt rocks are dominantly or exclusively derived from mangerite and granodiorite. Hence zircon may be a poor provenance indicator for target rock contributors to impact melts.

3.2 INTRODUCTION

In meteorite impacts on the Earth and Moon, and almost certainly Venus and Mars, melts are commonly produced by total melting of the target rocks into which the projectile collides (Pierazzo et al., 1997). The composition of the melt is thus a function of the compositions of the target rocks and their relative abundances in the zone of melting. However the composition of the melt may be modified significantly as it flows outward radially from the centre of the impact. The melt sheet may pick up clasts from the underlying impact-derived breccias and basement rocks over which it flows (McCormick et al., 1989; Ryder et al., 1997). The clasts may be completely or partially digested into the melt, depending on their size and melting temperature, and the thermal budget of the melt sheet. Partial melts from the underlying breccias or basement rocks may be mixed into the melt, further changing its composition (Grieve, 1975). In very thick melt sheets, such as at Sudbury, internal differentiation of the melt into discrete layers may occur during slow cooling (Zieg and Marsh, 2005)

This paper is concerned with distinguishing between the initial and final compositions of impact melts that did not undergo significant internal differentiation during slow cooling. Target rock constituents that melted to form impact melts are commonly reconstructed using mass balance mixing models for the bulk composition of the melt rocks and the compositions of possible target rocks (Grieve, 2006). If the final, bulk composition of the melt rock does not faithfully reflect the initial melt composition, however, the model results will be incorrect.

The study area is the Mistastin Lake crater of northern Labrador, where the impact melt rocks form sheets of variable, but only modest thickness (80 to <1 m) and thus

cooled quickly (Marion et al., in revision). The melt rocks are associated with shocked anorthosite, mangerite (quartz-bearing pyroxene monzonite) and granodiorite (adamellite) basement rocks. Based on major element modelling, Grieve (1975) found that the most abundant type of melt rock at Mistastin, which has a very fine grained granular to fine-medium-grained poikilitic texture, had formed from total melting of a target composed of ~54-71% anorthosite, ~13-14% mangerite and ~14-33% granodiorite. Based on trace element modelling, however, Marchand and Crockett (1977) argued that the average melt rock composition at Mistastin formed from much less granodiorite, only ~2%, with 60% anorthosite and 38% mangerite.

We also examine the scale of heterogeneity in the impact melts at Mistastin in this study. It has long been recognized that the bulk chemical compositions of impact melt rocks at Mistastin (Grieve, 1975) and in many other impact structures such as Manicouagan (Floran et al., 1978), Clearwater West (Simonds et al., 1978) and Boltysh (Grieve et al., 1978), are remarkably homogeneous. This implies that impact melts are well-mixed by the energy of the impact (Grieve and Floran, 1978). However some compositions of impact melt rocks are heterogeneous on the macroscopic scale, as are many impact glasses on the microscopic scale (Dressler and Reimold, 2001). Thus, the origins of heterogeneities in impact melt rocks remain poorly explained.

Finally, a third aspect of this study relates to the relative abundances of undigested clasts in impact melt rocks, and their significance for defining the proportions of target rocks that formed impact melts. At Mistastin, McCormick et al. (1989) showed that *both* anorthosite and mangerite/granodiorite contributed feldspar clasts to the impact melt, but with a greater proportion of anorthosite-derived feldspar where the impact melt rocks now

overlie anorthosite basement, along the northwest shore of the lake. This suggests that a majority of the feldspar clasts were picked up by the melt sheet after it had spread out some distance from the melting zone in the centre of the crater. We instead examined accessory zircon, found in all target rocks, to determine if anorthosite-derived zircon is also preferentially enriched in melt rocks along the northwest shore of the lake. Because zircon is able to survive shock deformation and superheated conditions somewhat better than feldspar (Wittmann et al., 2006), we wondered if the provenance of zircon clasts in impact melt might be a better guide than feldspar to the proportions of the target rocks that melted during impact.

The principal goals of this study are thus: (1) to describe and understand the origins of compositions and heterogeneities of Mistastin melt rocks on both macroscopic and microscopic scales; and (2) to define the genetic relationship between zircon in the melt rocks and their source rocks. For (1), the compositions of hand-sized samples of melt rocks were determined by bulk analytical methods, x-ray fluorescence (XRF) and solution nebulisation-inductively coupled plasma mass spectrometry (SN-ICPMS), and compared to the compositions of the glassy to fine-grained matrix in the same samples, determined by microbeam methods, electron probe microanalysis (EPMA) and laser ablation (LA)-ICPMS. For (2), the uranium-lead age, trace element composition and hafnium-isotopic composition of zircon in target and melt rocks were determined by LA-ICPMS.

Mistastin is an exceptional study area for analogue cratering studies of impact melt genesis because geological relationships between impactite units and basement rocks are well-exposed. Also, it is perhaps the only impact structure on Earth in which anorthosite was the principal source of impact melt and it therefore may be the best terrestrial

analogue for lunar impact melt genesis. Studies of terrestrial impact craters like Mistastin can help constrain the genetic relationships between impact melts and target rocks where geological relationships are poorly known, as is the case at present for all planetary bodies except Earth.

3.3 GEOLOGICAL SETTING AND PREVIOUS WORK

Mistastin Lake impact crater (55°53'N; 63°18'W) is 28 km in diametre with an age of 36 ± 4 Ma, based on Ar-Ar dating of impact melt rocks (Mak et al., 1976; Grieve, 2006). A nearly circular lake occupies the inner ~16 km diametre portion of the crater. Two islands, Horseshoe Island and Bullseye Island, located in the centre of the lake represent the central uplift of the crater. Preserved impactites include a variety of impact melt rocks distributed nearly equidistant from the centre of the lake, around the western two thirds of the shoreline (Fig. 3.1). The distribution of the impactites has been mapped by Currie (1971) and Marion et al. (in revision).

The crater is located in the northeast end of the Mesoproterozoic Mistastin Batholith, which consists of a series of intrusive bodies including anorthositic and granitic rocks together with lesser gabbroic rocks (Emslie et al., 1980). The batholith is surrounded by a variety of Proterozoic amphibolite, granitic and migmatitic gneisses, including reworked Archean rocks. Granodiorite crops out all around the lake but is most well exposed on the east and northeast shores. It consists of augen potassium feldspar, plagioclase, quartz, hornblende and biotite. Notable heterogeneity and gradational contacts including inclusions of gneiss and transitions to equigranular granite are not uncommon (Currie,

1971; Marion et al., in revision). These inclusions have not been differentiated from the granodiorite as possible contributors to the impact melt in previous studies.

Anorthosite and mangerite occur in bands that extend from southeast of the lake to northwest of the lake. The exposed central uplift in particular consists of about 75 % anorthosite and 25% mangerite, both of which are highly shocked and, in places, brecciated. The mangerite is very similar in appearance to the granodiorite; it also contains augen feldspars but less quartz, and can be distinguished easily from granodiorite by its higher iron and titanium contents (Currie, 1971; Marion et al., in revision). Small outcrops of meta-quartz gabbro were also identified recently on Horseshoe Island (Marion et al., in revision).

Studies by Grieve (1975) and Marchand and Crocket (1977) indicated that the impact melt rock at Mistastin is remarkably homogeneous with, for example, a mean SiO_2 content of 57.8 wt% and a standard deviation of only 1.9 wt%, for 40 whole rock samples. Grieve (1975) concluded that differential shock effects and velocities in addition to the highly turbulent state of the melt resulted in its homogenization. He identified, however, three different types of impact melt rock compositions formed by total melting of the target rocks, categorized as low, intermediate and high SiO_2 and K_2O, a common classification for andesites (Gill, 1981). The principal melt rock composition of Grieve (1975) ranges from the upper part of the low $SiO_2 - K_2O$ group (~55 wt% SiO_2 and ~1.5 wt% K_2O) to the intermediate $SiO_2 - K_2O$ group (~58 wt% SiO_2 and ~2.3 wt% K_2O) and represents the fairly well mixed impact melt. Melt rock compositions with silica-potassium concentrations that are both lower (~53 wt% SiO_2 and ~1.1 wt% K_2O)

and higher (~62-65 wt% SiO_2 and ~3.6-4.6 wt% K_2O) are rarer, isolated pockets and veins of more poorly mixed melt (Grieve, 1975).

Grieve (1975) also identified heterogeneities on the microscopic scale in the matrix of some Mistastin impact melt rocks; in particular, irregular and diffused patches of glass coronas and more discrete glass globules (up to 1 mm in diametre). Both types of glasses are silica and potassium rich (~67-76 wt% SiO_2 and ~5.4-7.3 wt% K_2O). Grieve (1975) interpreted the glass globules as mangerite-derived partial melt that became entrained in the impact melt during outflow of the melt sheet. They were not able to become homogenized into the impact melt before it cooled and crystallized.

3.4 FIELD SAMPLING

Fourteen samples of basement rocks were collected from surface outcrops around Mistastin Lake, consisting of 4 anorthosites, 4 mangerites, 4 granodiorites, 1 granodiorite gneiss, 1 meta-quartz gabbro and 1 granite. Three of the anorthosites, 2 of the mangerites and the gabbro were sampled from Horseshoe Island. The anorthosite samples exhibited shock metamorphic features, such as planar features, and all of these samples exhibited intense fracturing. The granodiorites, gneiss and granite were sampled mainly from Steep Creek and the northeast shore. None of these samples display strongly shocked metamorphic features.

Thirty-three melt rock samples were collected from major outcrops around Mistastin Lake, in counter-clockwise order, Steep Creek, North Shore, Coté Creek, Discovery Hill, South Ridge and South Shore, as well as from smaller exposures in between. Melt unit thicknesses exposed at these locations probably reflect original variations in melt sheet

thickness, controlled by topographic variations on the floor of the transient crater (Marion et al., in revision). Much of the melt rock is clast-rich, and the clast content and size generally increases with increasing proximity to the underlying breccias. Melt rock texture varies with unit thickness, vertical position within the thicker melt units and clast abundance. In thin units and toward the base of the thicker units, the melt rock is more glassy and clast-rich, whereas within the thicker units, the melt rock texture is more crystalline and clast-poor. In the more crystalline melt rocks, textures typically are fine grained poikilitic with dendritic pyroxene (augite or pigeonite) and blocky Fe-Ti oxides (titanomagnetite or ilmenite) set in a matrix of plagioclase microlites and interstitial glass (Fig. 3.2A). In medium grained crystalline samples, the dendritic pyroxene and Fe-Ti oxides appear as microphenocrysts (Fig. 3.2B).

3.5 ANALYTICAL METHODS

3.5.1 Rationale

Bulk analyses of impactites have been used traditionally to determine the composition and target rock sources of impact melts. This approach does not factor in the effect of large clast populations included in the analysis. Conceivably, centimetre- to metre-scale clasts can be separated from the igneous groundmass by hand picking prior to bulk analysis, but the majority of clasts in many melt rocks are millimetre- to micrometre in size and these are extremely difficult to separate physically from the matrix. Bulk analyses of the rocks may therefore not be representative of the melt composition formed initially upon impact. An alternative method is to avoid clasts during analysis of impact

melts by making *in situ* analyses using microbeam techniques (e.g., Tuchscherer et al., 2006). The *in situ* analyses may be used in conjunction with bulk analyses to derive estimates of impact melt composition both before and after it picked up clasts during outflow.

3.5.2 Whole rock analyses of target and melt rocks

Bulk samples of 14 target rocks and 33 melt rocks were hand crushed and powdered in a Siebtechnik puck mill with a tungsten carbide bowl. Major and trace elements were determined using a Fisons/Applied Research Laboratories XRF (model 8420+ sequential wavelength-dispersive x-ray spectrometre). For major elements, fused glass disks were made by combining approximately 1.5 grams of rock powder with 6.0 grams of lithium metaborate, 1.5 grams of lithium tetraborate flux and heated at ~850°C for 8.5 minutes and fused at ~1050°C for 11.5 minutes in a muffle furnace. For trace elements, pressed powder pellets were made from approximately 5 grams of rock powder and 0.7 grams of a phenolic resin binder. After mixing, this powder was placed in a Herzog Pellet Press and pressed for 10 seconds at 20 ton/in^2 pressure. The pellet is then baked at 200°C for 15 minutes.

Additional trace elements, including the rare earth elements, were measured by SN-ICPMS using an Agilent (formerly HP) 4500*plus* quadrupole instrument. Samples were dissolved and analyzed in nitric acid following a sodium peroxide sinter decomposition procedure using approximately 100 milligrams of rock powder. Both the XRF and SN-ICPMS analyses were done at Memorial University.

3.5.3 Matrix analyses of melt rocks

Polished thin sections were prepared from all of the melt rock samples and inspected by optical microscopy to quantify hand sample descriptions of melt rock textures and to distinguish the melt matrix from the clasts. To confirm the optical interpretations and extend them to the μm-scale in each section, automated scanning election microscopy was also carried out at Memorial using a FEI Quanta 400 Scanning Electron Microscope/JKMRC Mineral Liberation Analyzer (SEM/MLA), operated at a working distance of 14 mm, 25kV and 2nA. The instrument utilizes both backscattered electron (BSE) and x-ray mapping to quantify mineral distributions and abundances.

Identified clast-free areas of the matrix in nine samples were then analyzed for chemical composition by EPMA and LA-ICPMS. Major elements were analyzed by EPMA in wavelength-dispersive mode. Large numbers of analyses (approximately 65 analyses per thin section) were made on four of the nine impact melt samples (CM023, CM071, CM042, CM055) on a 20 x 20 μm area using a Cameca SX-50 microprobe at Memorial. The instrument was controlled by SAMx microanalysis software, and was operated at 15 kV and 20 nA. The five other samples (CM088, W05-65, CM067, CM025, CM035) were analyzed on far fewer spots (approximately 5 each) using a JEOL JXA-733 Superprobe at the University of New Brunswick, Canada, with a 11 x 17μm scanning area and at 15kV and 20nA.

LA-ICPMS was employed for the analyses of major and trace elements in the matrix of all of the nine melt rock samples. A Thermo-Finnigan Element XR magnetic sector ICPMS coupled to a Lamda Physik Geolas 193 nm ArF excimer laser ablation system was used at Memorial. The laser was set for an energy density of 5 J/cm^2 and repetition

rate of 10 Hz. Ten to fourteen analyses were made on 40 micron diametre spots in the clast-free parts of the matrix in each sample. Raw data were converted to concentrations using the LAMTRACE software program of S. Jackson, with NIST 612 as the calibration standard, and by normalizing all major oxides and trace elements to 100% (Guillong et al., 2005). Potassium could not be measured accurately because of isobaric interferences from argon that could not be resolved in low resolution mode of the ICPMS, so the K_2O value derived from the EPMA was used instead.

Careful attention was taken when placing the probe or laser beam to avoid clasts. The BSE images produced by the SEM/MLA provided the means to select appropriate spot locations within the thin sections (Fig. 3.3). Many mineral clasts are obvious as they are larger than the matrix grain size and are different in colour, but the most difficult task is to differentiate plagioclase microlites from plagioclase clasts in a BSE image. Both are abundant, represented by the same colour and can be similar in size. To improve the identification and avoidance of these clasts, a series of visual inspections was conducted where each suggested beam location was scrutinized for the shape, texture and consistency of surrounding grains. Plagioclase microlites tend to be euhedral, lath or rectangular in shape whereas plagioclase clasts are typically subhedral to anhedral, rounded due to partial melting and have visible reaction rims (Fig. 3.3). With this in mind, we are confident that any clast larger than ~15 microns was avoided.

3.5.4 Analysis of microphenocrysts and matrix glass in melt rocks

As noted above, some of the more coarse-grained crystalline melt rocks at Mistastin contain microphenocrysts of dendritic pyroxene and Fe-Ti oxides. Thus, the composition of the clast-free melt in these samples is not represented accurately by the fine-grained matrix alone, and the compositions of the microphenocrysts must be included as well. This is the case for two (CM023, CM042) of the nine melt rock samples whose matrix compositions were analyzed by EPMA and LA-ICPMS. For these two samples, the abundances of dendritic pyroxene and Fe-Ti oxides relative to the fine-grained matrix were determined from the SEM/MLA data described above. Compositions of the dendritic pyroxene and Fe-Ti oxides were analyzed for major elements by EPMA, and for trace elements by LA-ICPMS. The EPMA were carried out using the electron probe at Memorial on a 3 μm beam, at 15 kV and 20 nA. LA-ICPMS analyses were made at Memorial on a 20 μm spot, with external calibration against NIST612 and using internal standardization for ablation yield corrections. The laser was operated at 5 J/cm^2 and 10 Hz. Si and Ti concentrations from the EPMA data were used as the internal standard element for pyroxene and Fe-Ti oxide, respectively. Using the compositions and proportions of the fine-grained matrix, pyroxene and Fe-Ti oxides, a reintegrated composition for the melt could be calculated by mass balance.

Like Grieve (1975), we noted discrete accumulations of glass dispersed throughout the matrices of some melt rock samples (Fig. 3.3). The major element composition of this glass was analyzed in six samples (CM044, CM067, CM088, CM015, CM039 and CM052) by EPMA at the University of New Brunswick on 3 μm spots, at 15 kV and 20 nA.

3.5.5 Zircon analyses

Zircon was studied in four target rocks and three impact melt rocks. Among the target rocks, CM003 is a mildly weathered granodiorite from the northeast shore of Mistastin Lake; CM032 is a shocked, light pink anorthosite from the centre of Horseshoe Island; W05-45 is a weathered mangerite sample from the western tip of Horseshoe Island; and CM001 is a granodioritic gneiss from the northeast shore of the lake. For impact melt rocks, one sample (CM023) is from the anorthosite basement-rich northwest shore of the lake and two others (CM005, CM065) from anorthosite basement-poor locations. Sample CM023 is from western bank of Coté Creek, approximately 10 m from the basal contact of the unit with underlying breccias. Sample CM005 is a unit of massive melt rock of unknown thickness from Steep Creek. CM065 is from a larger unit of melt (at least 25 m thick, though the basal contact is not exposed) from the South Ridge on the south western bay of Mistastin Lake.

To recover zircons from each of these samples, heavy minerals were separated by crushing, Wilfley table, heavy liquid separation, Frantz magnetic separation and hand picking. Picking criteria for the zircons consisted of: (1) a minimum size of 40 μm for each zircon crystal or fragment, restricted by the minimum size of the laser spot that can comfortably fit inside the grain and still achieve suitable analysis sensitivities; (2) the absence of very large (>15 μm) inclusions or contaminants; and (3) a representative range in grain size and shape for each sample. Also, intact crystals were favored over grain fragments, where possible. In the case of the anorthosite, zircons proved too difficult to find through normal picking procedures so the heavy mineral separate was mounted in

epoxy and zircons were identified using BSE imaging on the SEM at Memorial University. The anorthosite sample contained very few intact grains, and so most of the zircon inventory contained fragments. The mangerite and granodiorite samples, in contrast, contained many intact crystals and so very few fragments were picked. There were, however, zircon fragments in the impact melt rocks that were picked and analyzed, e.g. a dozen from sample CM065.

Picked zircons were mounted into polished epoxy pucks and imaged by BSE on the SEM at Memorial at a working distance of 10 mm, and 25kV and 2nA. The goal of the BSE imaging was to characterize the small-scale physical properties of the zircon such as zoning, shape, size and texture and to identify potential inclusions. U-Pb dating of the zircon grains was done by LA-ICPMS at Memorial using the Element XR and Geolas 193 nm laser, with a 40x40 μm raster. The laser was set for an energy density of 3 - 5 J/cm^2 with a repetition rate of 10 Hz. The U-Pb dating method broadly follows that presented in Košler and Sylvester (2003). The Plešovice and Harvard 91500 zircons were run as secondary standards for quality control purposes.

Major and trace element concentrations of the zircon were determined with the same LA-ICPMS instrumentation using a 40 to 49 μm spot that was carefully placed atop of the U-Pb raster position to correlate age and trace element data for each grain. NIST 612 was used for external calibration and USGS BCR2G was run as a quality control reference material. The elemental concentration data was processed with LAMTRACE and normalized to totals of 100%, as in the elemental analyses of the matrix made by LA-ICPMS.

A dozen zircons from each of the 3 main target rocks (anorthosite, mangerite and granodiorite), another 6 grains from the granodioritic gneiss, and 20 zircons from the three impact melt rock samples were analysed for $^{176}Hf/^{177}Hf$ isotope ratios by laser ablation ICP multicollector mass spectrometry using a Finnigan Neptune at Memorial. For these analyses, the Geolas 193 nm laser ablated either a 40 or 49 μm spot, on top of the U-Pb raster and trace element laser spot positions, with an energy density of 5 J/cm^2 and a laser frequency of 10 Hz for 600 pulses per analysis. Plesõvice zircon was used as the quality control standard. Present day Hf ratios were back calculated to obtain the initial $^{176}Hf/^{177}Hf$ using the measured Lu/Hf ratios, the Lu decay constant of 1.865×10^{-11} (Scherer et al. 2001) and the U-Pb concordia age of each grain of zircon in the impact melt rocks, and the U-Pb concordia age of each rock sample for target rock zircons. Epsilon Hf values are calculated with $^{176}Hf/^{177}Hf$ and $^{176}Lu/^{177}Hf$ (CHUR) values of 0.282772 and 0.0332, respectively (Blichert-Toft and Albarède, 1997).

3.6 RESULTS

3.6.1 Compositions of target rocks

Major and trace element concentrations of the target rocks determined in this study are compared to the earlier results of Currie (1971) and Marchand and Crocket (1977) in Table 3.1. The new results are similar to the previous data but there are some subtle differences. In particular, for anorthosite, the newly determined concentrations for MgO and Na_2O are somewhat higher and lower respectively than the older ones. For mangerite, there is slightly higher CaO and a much lower Na_2O concentrations than in the

previous results. Granodiorite has slightly lower K_2O and distinctly higher FeO contents in the new results. Some of the differences between these datasets may be attributed to the fact that major elements in this study were analyzed by fused bead XRF whereas Marchand and Crocket (1977) used pressed pellet XRF analysis. Fused bead XRF is now known to be more accurate for the light major elements because of matrix and mineralogical effects resulting from the nature of the x-ray excitation (Potts, 1987).

The gneiss has a major element composition that is very similar to the granodiorite save for higher K_2O. Compared to all other target rocks, the granite has the highest SiO_2 (75.6 wt%) and lowest Al_2O_3 (11.6 wt%) contents, whereas the quartz gabbro has the highest FeO_T (17.7 wt%) and MgO (4.0 wt%) contents.

Chondrite normalized trace elements for target rocks are plotted in Fig. 3.4. The trace element patterns have very similar shapes but elemental abundance varies from one target rock to another. The mangerite and meta-quartz gabbro are the most enriched sources for the trace elements; the anorthosite is a very depleted source, and the granodiorite, granite and gneiss fall in between. The anorthosite consists almost entirely of plagioclase which results in a large positive Eu anomaly, very high Sr contents, and very low Y, Zr, Nb, Ba and Ce contents, as a function of these elements in plagioclase..

3.6.2 Compositions of impact melt rocks

3.6.2.1 Bulk analyses

Table 3.2 presents the results for the average bulk melt rock compositions for each of the major outcrop locations at Mistastin analyzed in this study. The bulk analysis of each

sample is given in Table D1 (Appendix D). Outcrop locations are divided into melt rocks with low and high field strength elements (HFSE). Specifically, the high HFSE type has higher TiO_2 (~1.1 vs 0.8 wt%), Zr (~410 vs 240 ppm) and Nb (~16 vs 9 ppm), as well as higher FeO_T (~6.3 vs 4.6 wt%), Ba (~1190 vs 880 ppm), Ce (~150 vs 100 ppm) and Y (~30 vs 16 ppm) and somewhat lower Al_2O_3 (19.6 vs 22.0 wt%). Coté Creek, Steep Creek, North Shore, South Shore and the South Ridge consist of low HFSE melt rocks whereas Discovery Hill and individual samples from the North Shore and the far west side of Coté Creek are enriched in HFSE. Sample CM008, a suevite from Steep Creek, is also enriched in high HFSE.

Silica and total alkali concentrations of the low and high HFSE melt rocks are similar to each other, and both would be classified as having trachy-andesitic compositions in terms of endogenous volcanic rock terminology (Fig. 3.5). The average major element concentrations for the high HFSE melt rocks are most similar to those for melt rock at Mistastin given by Currie (1971) and Marchand and Crocket (1977). In particular the earlier averages gave high TiO_2 (~1.0 wt%), FeO_T (~5.9 wt%) and low Al_2O_3 (~19.5 wt%) contents. This may be the result of a large proportion of samples in the earlier averages being from Discovery Hill, the thickest unit at Mistastin.

3.6.2.2 Matrix analyses

Table 3.3 gives the average matrix compositions for the six impact melt rocks studied from Coté Creek and South Shore, which have low HFSE bulk compositions, and from the three from Discovery Hill and North Shore, which have high HFSE bulk

compositions. Detailed results can be found in Table D2 and D3 (Appendix D). For most samples in the low HFSE bulk melt group, there is little difference between the bulk and matrix compositions, but for samples in the high HFSE bulk melt group, the matrix compositions are distinctly different than the whole rock compositions. Indeed it is not possible to recognize the distinction between low and high HFSE samples on the basis of matrix compositions as we could do for bulk rock compositions. For instance, mean matrix compositions of samples from both the low and high HFSE bulk rock groups have overlapping concentrations of TiO_2 (~0.3-0.8 wt%), Zr (~100-270 ppm) and Nb (~6-10 ppm), FeO_T (~1.6-5.2 wt%), Ba (~610-1100 ppm), Ce (~50-120 ppm), Y (~13-28 ppm) and Al_2O_3 (19.6 vs 24.6 wt%).

The mean major element composition for the matrices of all nine samples in Table 3.3 is 58.6 ± 2.0 wt% SiO_2, 21.6 ± 1.6 wt% Al_2O_3, 3.5 ± 1.1 wt% FeO_T, 4.5 ± 0.4 wt% Na_2O, and 2.3 ± 1.0 wt% K_2O. This compares favorably to the dominant "intermediate SiO_2 – K_2O" matrix melt composition measured by broad beam EPMA by Grieve (1975), which contains 58.4 ± 0.9 wt% SiO_2, 20.6 ± 0.7 wt% Al_2O_3, 4.5 ± 0.6 wt% FeO_T, 4.8 ± 0.3 wt% Na_2O, and 2.3 ± 0.4 wt% K_2O. The chondrite normalized trace element composition for the average matrix of the nine samples is plotted in Fig. 3.4. The pattern for the average matrix composition tends to plot in between, and parallel to, those for the anorthosites, mangerite and granodiorite target rocks.

A striking characteristic of matrix data is the spot to spot heterogeneity on the 20 – 40 micron scale of the EPMA and LA-ICPMS analyses within individual petrographic thin sections (27 x 46 mm). The heterogeneities exist for both major and trace elements. Representative examples of matrix analyses from thicker (CM023, CM042) and thinner

(CM071, CM055) outcrop units of both low and high HFSE bulk melt rocks are plotted in Figs. 3.6 – 3.9. (The same scales were used for all plots to facilitate visual comparisons between samples.) All samples show significant variations in elemental concentrations within the matrix; for instance, at least 10 wt% for SiO_2 and Al_2O_3. However, chemical compositions of matrix from the thicker melt units of both low and high HFSE melt rocks (Figs. 3.6-3.7) are much more heterogeneous than those from the thinner melt units (Figs. 3.8-3.9). In particular the thicker units exhibit a significant number of matrix spots with silica-rich (~ 65-90 wt%) compositions.

The fine (3 micron) beam EPMA data for the discrete accumulations of glass dispersed in the matrices of the melt rock samples is given in Table D4 (Appendix D). The matrix glasses range in composition from ~57 to 98 wt% silica, with most of the analyses from the thicker Discovery Hill and Coté Creek units having > 75 wt% silica. The glass analyses are similar to those reported by Grieve (1975), but with a significantly greater range in composition.

3.6.4 Zircon characteristics

3.6.4.1 Physical data

Zircon crystals and crystal fragments, 15 microns in size or greater, were recovered from the three principal target rocks in the relative proportions: 110 grains in anorthosite/350 grains in mangerite/500 grains in granodiorite (normalized to the abundance of the rock sample processed for each lithology). If grains only 40 microns or greater in size are considered, which are those that could be analysed by LA-ICPMS

using the 40 micron spot routinely employed at Memorial, the recovered proportions were 80 grains in anorthosite/200 grains in mangerite/350 grains in granodiorite. The vast majority of zircons in the anorthosite are fragmental, most commonly ranging in length from 40-250 μm. The grains are poorly zoned in BSE images; some crystals and crystal fragments display planar deformation features as evidence of shock metamorphism (Figs. 3.10A-B). Zircon in the granodiorite and mangerite are similar in appearance. They are commonly 80 – 350 μm in size, have prismatic to rounded shapes and exhibit oscillatory zoning in BSE images (Figs. 3.10C-D).

Zircon is as plentiful in the granodiorite gneiss as it is in the granodiorite. The grains commonly range from 100 – 300 μm long, and are zoned in BSE images (Fig. 3.10E). Distinct cores and overgrowth mantles are evident in the BSE images of five zircon grains (Fig. 3.10F).

Zircon clasts in the three impact melt rocks examined here show a significant range in size (< 40 to 350 μm) and shape, and are a combination of intact crystals and crystal fragments (Figs. 3.10G-I). Some grains are very short and rounded, others are narrow and elongate. Many of the crystals and fragments exhibit irregular wavy grain boundaries, suggesting dissolution in the impact melt. There is no obvious difference in size, shape and zoning in the zircon grains from Coté Creek sample CM023, located along the anorthosite-basement-rich northwest shore of the lake, and South Ridge CM065 sample, situated along the anorthosite-basement-poor southwest shore of the lake. Steep Creek CM005 sample, from the anorthosite-basement-poor northeast shore of the lake, generally has smaller, stubby and rounded, and more fragmental grains than both CM023

and CM065. The most zircon grains were recovered from sample CM065 and the least from sample CM005.

Nearly all of the zircons in the impact melt and target rocks contain a variety of mineral inclusions up to 15 μm wide, most commonly apatite and potassium feldspar.

3.6.4.2 U-Pb geochronology

Figures 3.11 and 3.12 plot the results of the LA-ICPMS zircon geochronology for the target and impact melt rocks, respectively, on U-Pb concordia diagrams. Age histograms are also plotted for the impact melt rock samples in Fig. 3.12. The detailed data including those for the reference zircons Harvard 91500 and Plešovice are given in Tables D5, D6 and D7 (Appendix D).

The zircon ages of all four of the target rocks are within 2σ of each other and therefore are too close in age to differentiate from one another on the basis of the LA-ICPMS measurements. The concordia age of the mangerite is 1451 ± 12 Ma (2σ); the granodiorite gneiss is 1440 ± 13 Ma (2σ); the anorthosite is 1438.7 ± 8.9 Ma (2σ); and the granodiorite is 1429 ±10 Ma (2σ). Five grains in the gneiss, with distinct cores in the BSE images (Fig. 3.10F) give U-Pb ages between 2100 and 2400 Ma. The data suggest that the cores are inherited from an older source. Rb-Sr isochron ages for the target rocks have been previously reported by Marchand and Crocket (1977): the anorthosite had too small a range of $^{86}Rb/^{87}Sr$ ratios to calculate an isochron but the mangerite was determined to be 1409 ± 57 Ma and the granodiorite to be 1318 ± 17 Ma, significantly younger than the magmatic ages determined here by U-Pb zircon dating.

U-Pb ages of the zircon clasts in the three impact melt rocks overlap with those in the target rocks, and each other: Peaks in the age histograms are at 1435 ± 13 Ma for CM023, 1431 ± 21 Ma for CM005, and 1413 ± 13 Ma for CM065. In CM023, two significantly older, but strongly discordant grains, give apparent ages of ~1730 and 2190 Ma.

3.6.4.3 Elemental concentrations

Multi-elemental analyses of zircons in the target and impact melt rocks by LA-ICP-MS are presented in Table D8 and D9 respectively (Appendix D). Data for the reference zircon Harvard 91500 are given in Table D10 (Appendix D).

There are only subtle elemental differences between zircons from the various target rocks (Fig. 3.13). Zircons from the anorthosite tend to have higher Nb/Ta (~1.1-3.2) and Eu/Eu* (~ 0.13-1.7) ratios than zircons from the mangerite, granodiorite and gneiss (Nb/Ta ~1.0-2.2; Eu/Eu*~0.01-0.4). Zircons from anorthosite and granodiorite tend to have smaller differences between ZrO_2 and SiO_2 (~17-29 wt%) than zircons from mangerite and gneiss (~19-36 wt%) Some analyses of zircon grains exhibit anomalous enrichments in elements normally incompatible in the mineral such as barium and the light rare earth elements. We suspect that these ablations intersected small melt inclusions in the zircon.

Zircon clasts in the impact melt rocks have elemental compositions that overlap with one another, suggesting that they were derived from the same sources in all three samples (Fig. 3.13). None of the zircon clasts have Nb/Ta ratios greater than 2.5 where the

difference between ZrO_2 and SiO_2 is less than 27 wt%, and Eu/Eu* greater than 0.3, as is the case for many zircons from anorthosite.

3.6.4.4 Hf-isotopes

Results for Hf isotope analysis of zircons from the target and impact melt rocks, and quality control data for the reference Plešovice zircon are summarized in Tables D11, D12 and D13 respectively (Appendix D). Average initial ε Hf values for target rock zircons are –12.9±1.1 in the anorthosite, –10.8±1.3 in the granodiorite, –8.5±2.2 in the mangerite, and –8.7±1.0 in the gneiss for magmatic grains and +6.0 for a single analysis of an inherited grain. Initial ε Hf values for zircon clasts range from –16 to –4 and, as for elemental concentrations, exhibit substantial overlap in the three melt rock samples. Only one of the zircon clasts has the combination of initial ε Hf more negative than –11 and Eu/Eu* greater than 0.1, suggesting that anorthosite-derived zircon is very rare or absent in the melt rocks (Fig. 3.13).

3.7 DISCUSSION

3.7.1 Sources of Mistastin impact melts

It is a non-trivial task to determine the compositions and proportions of target rocks that were melted and mixed to form an impact melt sheet. Bulk samples of impact melt rocks are the product not only of the rocks that were melted totally upon impact, but also exogenous components added to the melt sheet as it subsequently spread away from the melting zone – in particular clasts and partial melts derived from the underlying impact

breccias and basement rocks. Target rock source models based on bulk compositions of impact melt rock samples alone may be incorrect if clasts and partial melts incorporated into melt rocks are volumetrically significant and/or differ substantially in composition compared to the target rocks. Analyses of just the matrix of melt rocks, avoiding clasts, may better reflect the initial, pre-outflow composition of the impact melt.

At Mistastin, several attempts have been made to determine the sources of the impact melts. All attempts recognized anorthosite as the dominant source but the principal secondary source – mangerite or granodiorite – has remained unclear. Currie (1971) modeled the SiO_2, Al_2O_3 and CaO contents of an average bulk composition of six melt rocks and found that they could have formed from a melt mixture of 51% anorthosite, 40% mangerite and 9% granodiorite. Marchand and Crockett (1977) also modeled an average bulk composition for melt rocks at Mistastin, but based on more melt rock samples (40) and ten trace elements (Nb, Zr, Y, Sr, Rb, Th, Pb, Zn, Cu, Ni) rather than major elements. The model result however was similar: 60% anorthosite, 38% mangerite and 2% granodiorite. Grieve (2006) re-modeled both the major and trace element whole rock data of Marchand and Crockett (1977) and found a result of 62% anorthosite, 38% mangerite and 0.1% granodiorite.

Grieve (1975) used a different approach from the others, modeling matrix compositions (measured by EPMA using a defocused electron beam) rather than bulk compositions for the melt rocks, and subdividing the compositions based on the petrographic textures of the samples. He reported that the major element composition of the matrix that made up the volumetric bulk of the impact melt formed from 54% anorthosite, 13% mangerite and 34% granodiorite, with a subordinate composition

derived from 71% anorthosite, 14% mangerite and 15% granodiorite. Although Grieve (1975) also reported two minor matrix melt compositions that formed solely from anorthosite (63-68%) + mangerite (32-37%), one just from mangerite (33%) + granodiorite (67%) and another solely from a mixture of total and partials melts of mangerite, the implication was that the vast majority of melt rocks at Mistastin formed from far more granodiorite and less mangerite than was indicated by the bulk (clast-bearing) compositions of the melt rocks.

Our study directly addresses the discrepancy between models for bulk vs matrix compositions of the melt rocks at Mistastin by comparing analyses of whole rocks and matrices on the same samples. Following on from our recent geological studies that recognized that impact melt flows at Mistastin varied in thickness from location to location within the crater (Marion et al., in revision), we examine our geochemical results in the context of key exposures of units that formed from either thick or thin melt flows. To determine the proportions of each target rock contribution to the impact melts, measured chemical compositions are calculated using least-squares mixing models after Bryan et al. (1969) and Wright and Doherty (1970). These calculations were assisted by MATLAB® (The MathWorks, Inc.) software where the common inverse least squares function x=inv(A'*A)*A'*b was converted to a MATLAB function where $x \geq 0$ as [x, lambda]=lsqnonneg(A,b) to avoid a negative proportion.

Table 3.4 presents the results of the least-squares mixing models for various major element compositions of the melt rocks derived from both bulk (Table 3.2) and matrix (Table 3.3) analyses, using the target rock compositions determined in this study (Table

3.1). For all models based on the three principal basement rocks alone (anorthosite, mangerite, granodiorite), the totals of the calculated proportions of the target rocks are close to 100% (97.5 to 104%). We ascribe the small deviations from 100% to variations from the mean oxide concentrations of the target rocks, which have standard deviations of up to ~2 wt% for each of SiO_2, Al_2O_3 and CaO in particular (Table 3.1). The total proportions are not improved significantly by including any or all of the target rocks (gneiss, gabbro, granite) that are volumetrically minor in the field area. However, we cannot rule out the presence of a small (<5%) proportion of the target containing gneiss, gabbro or granite, on the basis of the model calculations.

Trace element modeling results (Table D14 Appendix D) are broadly comparable with the major element results but are considered less reliable because the totals of source components for some samples deviate significantly from 100%. We ascribe the poor model results to the large variation in trace element concentrations of the target rocks. For instance the relative standard deviations on the means of Zr, Nb and Y in the anorthosite, mangerite and granodiorite are 46, 20 and 23% for Zr; 78, 40 and 21% for Nb; and 67, 30 and 29% for Y, respectively (Table 3.1). Also, the model calculations do not include the presence of minor amounts of mangerite partial melt that may have become entrained in some melt units (Grieve 1975). We did not analyze the compositions of the mangerite partial melts but it is likely that they would possess high and variable concentrations of incompatible trace elements, depending on the degree of melting, and thus much more strongly affect the mixing model results for trace elements than major elements.

Examples of the systematics of impact melt rock compositions and mixing models are shown graphically for pairs of major elements (SiO_2, FeO_{total}) and trace elements (Rb, Nb) in Figure 3.14.

Our modeling results are consistent with anorthosite as the primary source of the impact melt rocks, as argued by Grieve (1975) and Marchand and Crockett (1977), but suggest that the principal secondary sources are mangerite in the bulk rocks, and granodiorite in the matrices of the bulk rocks. Impact melt rocks with bulk compositions of the low HFSE type tend to have formed from more anorthosite (relative to mangerite and granodiorite) than those of the high HFSE type. The mean low and high HFSE bulk rocks are calculated to be derived from ~74% and 51% anorthosite respectively (Table 3.4). High HFSE bulk rocks include a substantial component of mangerite compared to low HFSE bulk rocks (means of ~42% vs ~8%).

Our model results for the matrix compositions of the bulk rocks give strikingly different results. For bulk rocks with *both* low and high HFSE compositions, the matrix compositions tend to have formed mainly from anorthosite and granodiorite, with significant mangerite calculated for the matrix of only one of the nine samples modeled (Table 3.4). The calculated sources of the nine matrix compositions have a mean of ~66% anorthosite, ~3% mangerite and ~31% granodiorite. The results suggest that the melt rocks with high HFSE bulk compositions formed on impact with initial, anorthosite-rich compositions similar to those with low HFSE bulk compositions but were subsequently enriched in mangerite relative to anorthosite. The mangerite enrichment in the high HFSE bulk rocks does not seem to have been incorporated into the matrix of most samples.

3.7.2 Mangerite enrichment in high HFSE bulk-melt rocks

Nine of eleven samples of melt rocks with high HFSE bulk compositions identified in this study are from Discovery Hill, a prominent butte that is the thickest preserved melt unit at Mistastin. The other two samples come from isolated outcrops of probably thinner units along the North Shore of Mistastin Lake (CM027) and just west of Coté Creek (CM055). Marion et al. (in revision) argued that the Discovery Hill unit represents impact melt that became thickened by flow along a topographically controlled channel along the transient crater floor, unlike most other preserved melt units at Mistastin, which formed thinner, sheet flows over more open plains. Using this model, the anomalous enrichment of mangerite in the thicker Discovery Hill flow can be explained as a consequence of its ability to incorporate large amounts of mangerite from underlying breccia and basement rock relative to the thinner melt units. Thicker, larger volume flows would tend to be more turbulent and have a greater heat capacity for thermally eroding the underlying substrate compared to thinner, smaller volume, more laminar flows. Comparison of ratios of anorthosite/(mangerite + granodiorite) in the bulk melt as a function of unit thicknesses indicates that the thin South Shore flows are the most anorthosite-rich, whereas the thick Discovery Hill flow is the most anorthosite-poor (Fig. 3.15). The bulk composition of the Coté Creek flow of intermediate thickness tends to consist of anorthosite in proportions that fall in between those of the South Shore and Discovery Hill flows. These relationships appear to be largely independent of stratigraphic position within the melt units.

The melt rocks at Discovery Hill contain 10 to 30% clasts, mostly plagioclase, perthite and quartz. Although feldspar in the mangerite and granodiorite has similar

compositions (McCormick et al. 1989), the clasts almost certainly are derived largely from mangerite. This is because large, metre-scale mangerite boulders that may represent the dislodged and disruptured remnants of the valley walls along which the Discovery Hill melt flowed are found protruding from the melt rock on the top and north side of the butte. Grieve (1975) noted evidence of partial melting of the mangerite boulders at Discovery Hill and suggested that silica and potash-rich globules (≤1mm) preserved in some melt rocks represent mangerite partial melts that became entrained in the anorthositic magma. These mangerite melt globules would have been included in the material analyzed for the bulk compositions of the melt rocks, also increasing the calculated proportion of mangerite relative to anorthosite at Discovery Hill.

3.7.3 Initial composition of Mistastin impact melt

The composition of the impact melt at Mistastin is not well-represented by the bulk compositions of the impact melt rocks because the bulk rocks include clasts. Impact melt composition more closely approximates by the composition of the matrices of impact melt rocks because they are free of all but the most minute clasts. Even in the matrices, however, it is likely that composition of the initial melt, formed immediately after impact, has been modified by the addition of melts derived from the partial or complete digestion of clasts entrained during outflow.

As noted above, the compositions of the matrices of impact melt rocks can be modeled as a mixture of anorthosite with subordinate granodiorite and in some cases, minor mangerite (Table 3.4). It is the matrix compositions of melt rocks in the thinner

units however that probably best approximate the initial composition of the impact melt at Mistastin.

This is indicated by two lines of evidence. First, as shown in Figs. 3.6 – 3.9, although both thick and thin impact melt rock units are heterogeneous on the 20 – 40 micron scale of the EPMA and LA-ICPMS analyses of the matrix compositions, the thicker units include a significant number of matrix spots with silica-rich (~ 65-90 wt%) compositions not seen in the thinner units. On an even finer scale (3 micron), silica-rich glasses in the matrix of the thick Discovery Hill flow have compositions approaching pure silica (Table D4 Appendix D). The simplest interpretation is that the silica-rich matrix areas and their constituent silica-rich glasses in the thicker flows represent a low melting point fraction of incorporated clasts that had sufficient time to become mingled with the initial anorthosite-rich impact melt during cooling. Thinner flows would have less heat capacity for partially melting of the clasts and cooled too quickly to allow significant mingling of any clast-derived melts that may have formed.

A second observation supporting this interpretation is that the proportions of anorthosite in the matrices, as in the bulk rocks, tend to vary as a function of unit thickness: lowest in Discovery Hill, and highest in South Shore (Fig. 3.15). This is consistent with the idea that the matrix compositions of the thicker flows, like the bulk compositions, have been affected by incorporation of clasts. Unlike the bulk compositions however, which reflect the addition of undigested clasts, the matrix compositions reflect mingling of the low temperature melt fraction of the clasts. Thus, even in the case of Discovery Hill, where clasts were mainly derived from mangerite, the

calculated silica-rich component for the matrix is granodiorite, which has a composition similar to that expected for low temperature crustal melts.

According to this model, the three matrix compositions (W05-65, CM071, CM067) determined from the thin South Shore melt units, and a fourth (CM055) from the likely thin North Shore units should be the best approximation to the initial melt composition at Mistastin. The average composition of these 4 matrix compositions is (wt.%): 57.2 ±1.5 SiO_2, 0.65±0.14 TiO_2, 22.4±1.9 Al_2O_3, 3.9±1.6 FeO_T, 0.98±0.59 MgO, 7.6±0.3 CaO, 4.5±0.5 Na_2O, 2.0±0.9 K_2O and 0.17±0.04 P_2O_5. The average calculated proportion of their target rock sources is: 73±13% anorthosite, 7±11% mangerite and 20±7% granodiorite.

3.7.4 Significance of zircon clasts in melt rocks

McCormick et al. (1989) examined the clasts of quartz and feldspar in nine samples of impact melt rocks from Mistastin. They found that the sources of the clasts were much more variable from sample to sample than the bulk compositions of the samples. Melt rock samples overlying basement containing significant anorthosite, from the north and northwest of Mistastin Lake, contained clasts with sources almost exclusively from anorthosite (~90–100%). In contrast, all but one of the melt rocks overlying mangerite and granodiorite, in the west and south of the lake, had clasts derived from more mangerite + granodiorite (~54-65%) than anorthosite (~46-35%). Thus, McCormick et al. (1989) concluded that the clast population reflected the nature of the rock in the

substrate over which the impact melt flowed, rather than the proportions of target rock sources in the impact melting zone.

Our results for the sources of zircon clasts in the impact melt rocks are dramatically different from those of McCormick et al. (1989) for the quartz and feldspar clasts, in that all or almost all of the zircon clasts are derived from mangerite + granodiorite (including granodiorite gneiss) rather than anorthosite, independent of substrate lithology (Fig. 3.13). This result was unexpected in that zircon, although less abundant in anorthosite than in mangerite and granodiorite, is still present in significant quantities (~1 grain in anorthosite for every 7 grains in mangerite + granodiorite). In addition, if zircon was able to survive the high temperatures and pressures of the impact melt zone, we might have expected enrichment in zircon clasts from anorthosite relative to mangerite + granodiorite, given that anorthosite was the predominant source of impact melt.

The most likely explanation for the apparent lack of anorthositic zircon in the melt rocks is that it was preferentially comminuted to a size smaller than the 40 micron spot size of the LA-ICPMS measurements. Zircon in the anorthosite tends to be somewhat smaller in size than zircon in the mangerite and granodiorite, but, more importantly it tends to be more fragmental and shocked. It is probable that anorthositic zircon simply fractured and splintered more easily along planar deformation features (Fig. 3.10A, B) than zircon in the mangerite and granodiorite. Thus zircon clasts may not be a particularly useful indicator of impact melt provenance unless tiny zircon grains preserved in the matrix are analyzed along with larger zircon clasts.

3.7.5 Implications for studies of impact melts on the Moon and beyond

Impact cratering has profoundly affected the Moon and other planets of our solar system but understanding their bombardment records is difficult because geological relationships are poorly known. On the Moon, in particular, billions of years of bombardment have destroyed or obscured the links of impact melt rock samples to their parent craters, adding uncertainty to a range of first-order questions such as cratering rates in the inner solar system and the structure of the lunar crust (e.g., Neal, in press). The Mistastin impact is similar to lunar impacts in that melt produced was anorthositic in both cases. But at Mistastin, unlike on the Moon, the field relationships of the impact melts in the crater are well-preserved and accessible for detailed examination.

Impact melt rocks at Mistastin consist of an initial impact melt formed mainly from anorthosite with subordinate granodiorite and mangerite; millimetre to micrometre-size clasts picked up from the brecciated anorthosite, mangerite and granodiorite substrate over which the initial melt spread outward from the impact site; and micrometre-scale melts formed from partially and completely digested clasts. The sources of the clasts vary in proportion from sample to sample and the extent of clast digestion is related to flow unit thickness. Nonetheless, when bulk analyses are made of hand-sized specimens of the impact melt rocks, the small-scale heterogeneities tend to become homogenized to give the false impression that the impact melt was well-mixed. Zircon clasts derived from anorthosite in impact melt rocks seem to have been preferentially comminuted compared to zircon from mangerite and granodiorite during impact and entrainment. Although the initial impact melt included a granodiorite source, no evidence of it remains in the central uplift, the likely region of melt production. Presumably the granodiorite

was present as a thin cover overlying anorthosite and mangerite at the time of impact, which is plausible given that granodiorite is the predominant lithology surrounding Mistastin Lake.

Similar complexities should be expected for lunar impact melts. For instance lunar impact melt breccias related to a single cratering event may have diverse clast inventories. The clasts may produce distinctive variations in the bulk chemical compositions of the melt rocks. Target rocks that formed lunar impact melt may no longer be present at the centre of craters.

3.8 CONCLUSIONS

Impact melt at Mistastin formed from ~73% anorthosite, ~7% mangerite and ~20% granodiorite. This estimate is based on matrix compositions of thin flow units which likely have been the least affected by contamination by clast entrainment and melting due to more laminar flow and lower heat capacities. The new result is somewhat richer in anorthosite and poorer in mangerite than previous estimates based on bulk analyses of impact melt rocks, particularly those from Discovery Hill, a thick unit that incorporated numerous mangerite clasts. Caution is thus warranted when using bulk compositions of impact melt rocks to model the identity and proportions of target rock sources involved in the melting event, either in terrestrial impact craters or those on other solar system bodies.

Mistastin impact melts were heterogeneous in composition at all scales – from the metre-scale outcrops (e.g., Discovery Hill vs South Shore) to micrometre-scale matrices. The heterogeneities were largely produced after impact as the melts spread outward and

entrained clasts and partial to complete melts of the clasts. The micrometre-scale heterogeneities tend to be averaged out in bulk analyses of hand-sized samples of impact melt rocks.

There is no evidence that zircon derived from anorthosite target rocks survived impact and is preferentially enriched as clasts in the impact melts relative to zircon sourced from mangerite and granodiorite. In fact, if anorthosite-derived zircon is present as clasts in the impact melt rocks at all, the grains must have been comminuted to sizes less than 40 microns by fracturing and splintering.

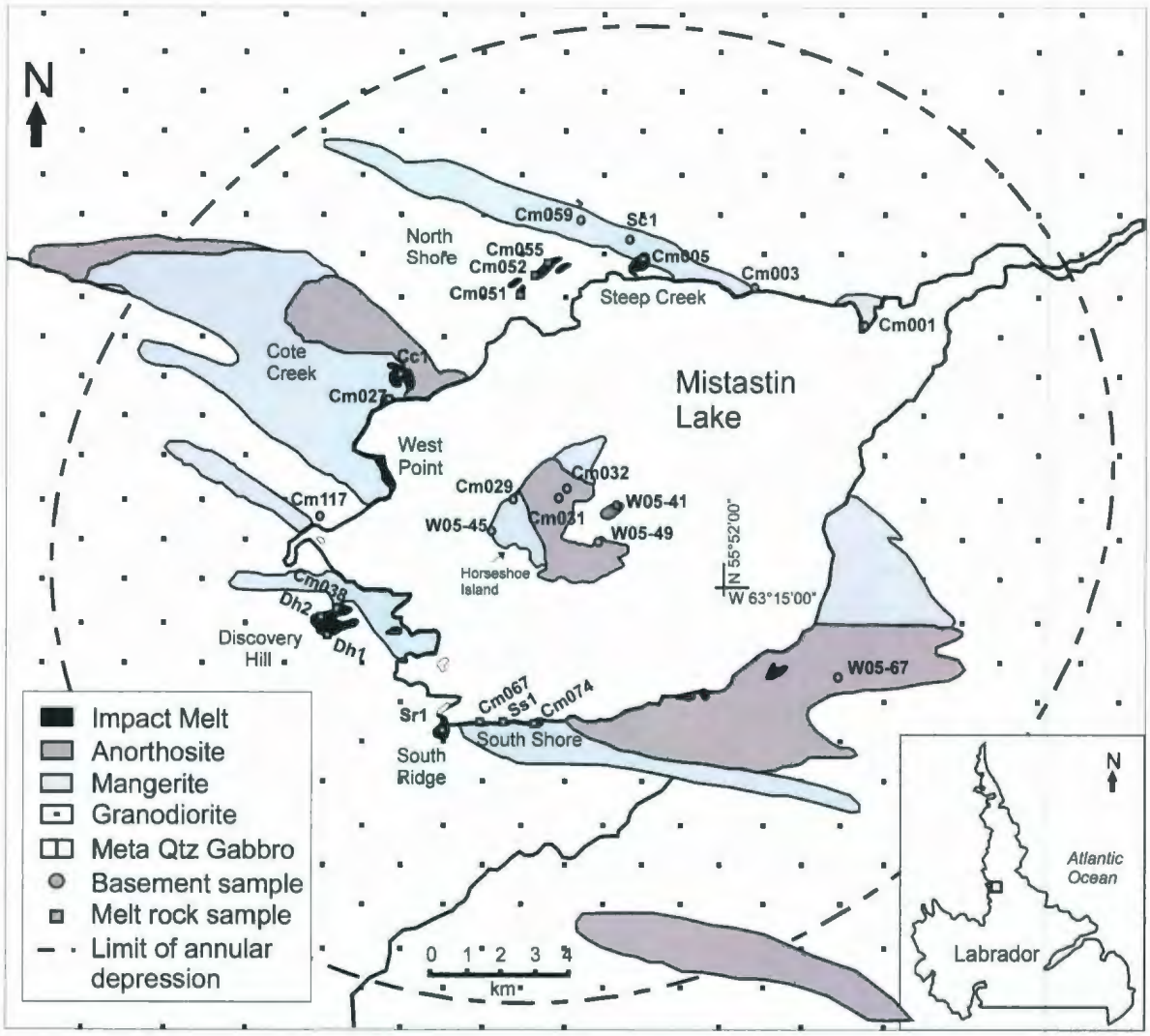

Figure 3.1. Generalized geology map of Mistastin impact structure, modified from Currie (1971) and Grieve (1975) based on new mapping (this study). The location of the map area is identified by the black box on the imbedded map Labrador. Dashed line indicates the approximate position of the inner face of the crater rim inferred by Grieve (1975).

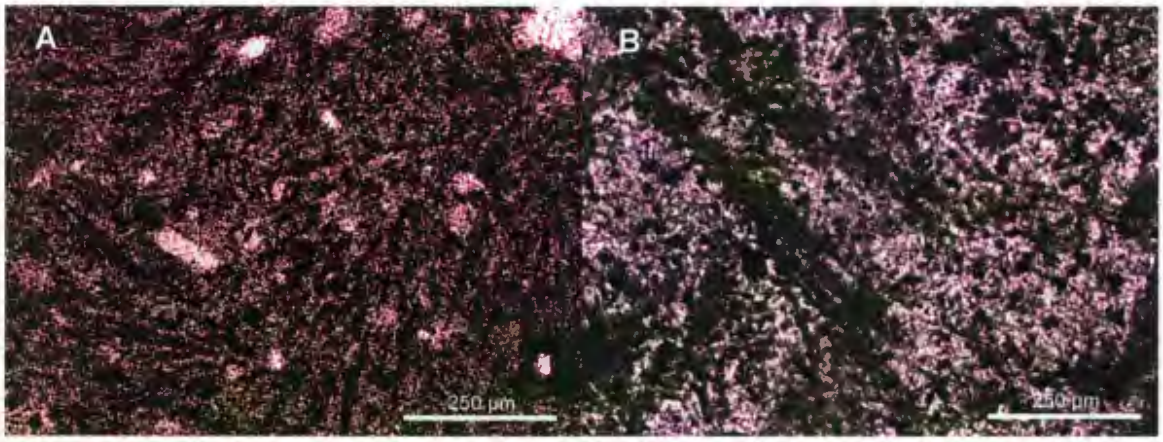

Figure 3.2. Photomicrographs of impact melt matrix for A) sample CM071 from the South Shore outcrops and B) sample CM042 from Discovery Hill. Compare the scale of the pyroxene crystals and interspersed plagioclase microlites in both samples.

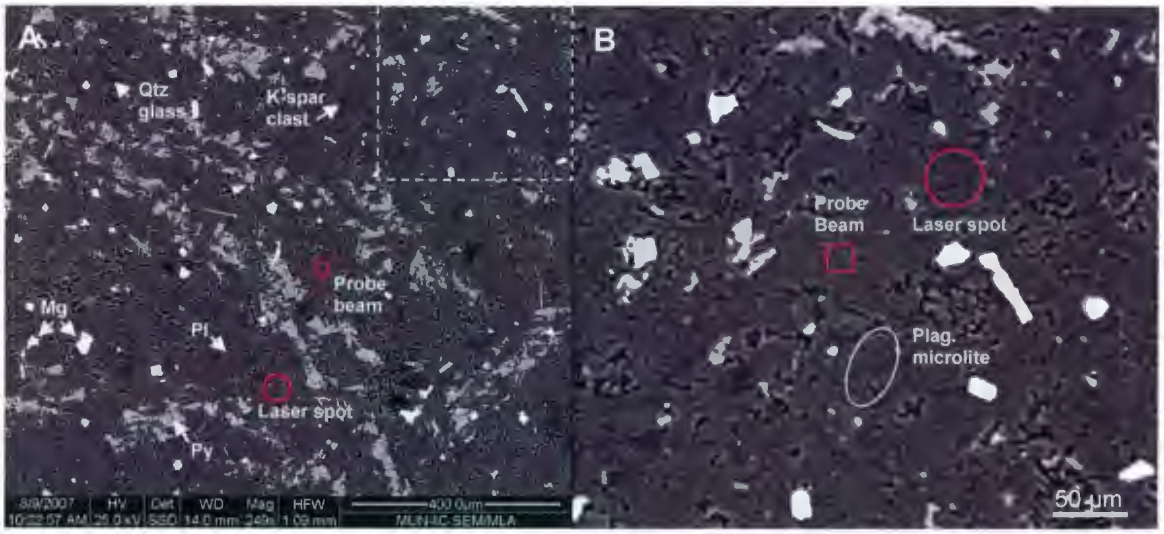

Figure 3.3. SEM/MLA backscatter electron images of the impact melt rock matrix of sample CM042 from Discovery Hill. Note the dendritic pyroxene crystals and interspersed plagioclase microlites. A) Micro-meter scale image of the melt matrix where the probe beam size (20 x 20µm) is identified by a red square and the laser spot by a red circle (40 x 40µm); B) is a magnification of the upper right corner of figure (A) where single microlites can be identified. This is similar to the image observed when using the microprobe. Note the euhedral shape of the plagioclase microlite in (B) and compare to the rounded and rimmed K-feldspar clast identified in (A). Please note that this is not the probe size used to analyze plagioclase microlites.

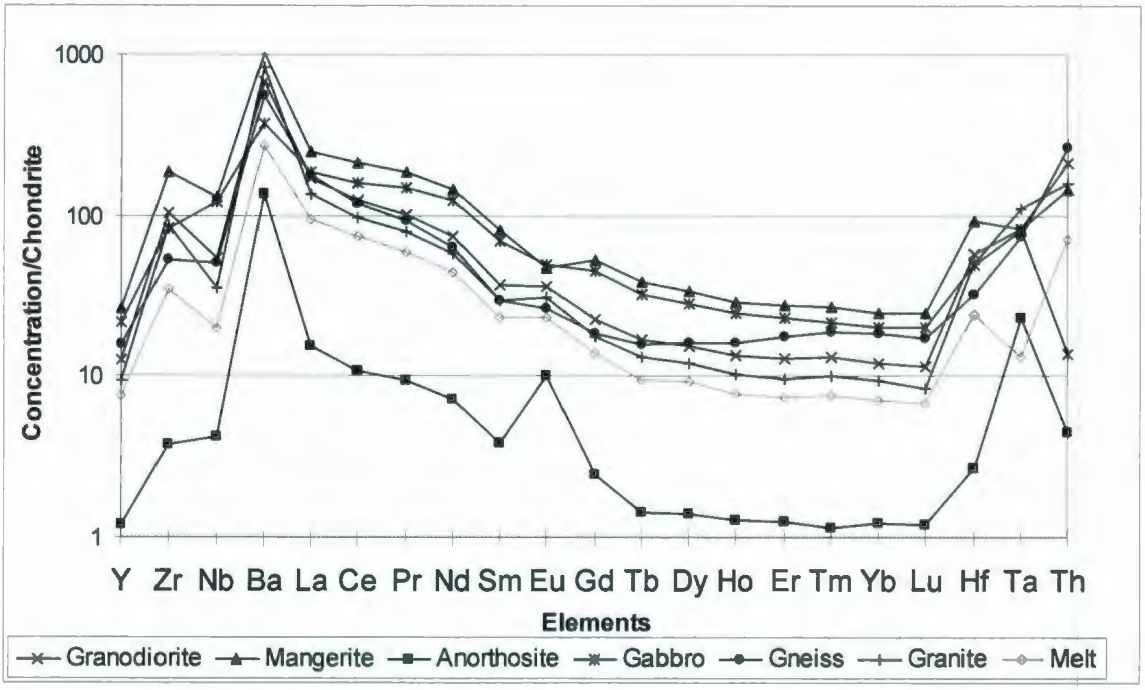

Figure 3.4. Chondrite normalized trace elements in the 5 possible target rocks and the average impact melt matrix of samples listed in Table 3.

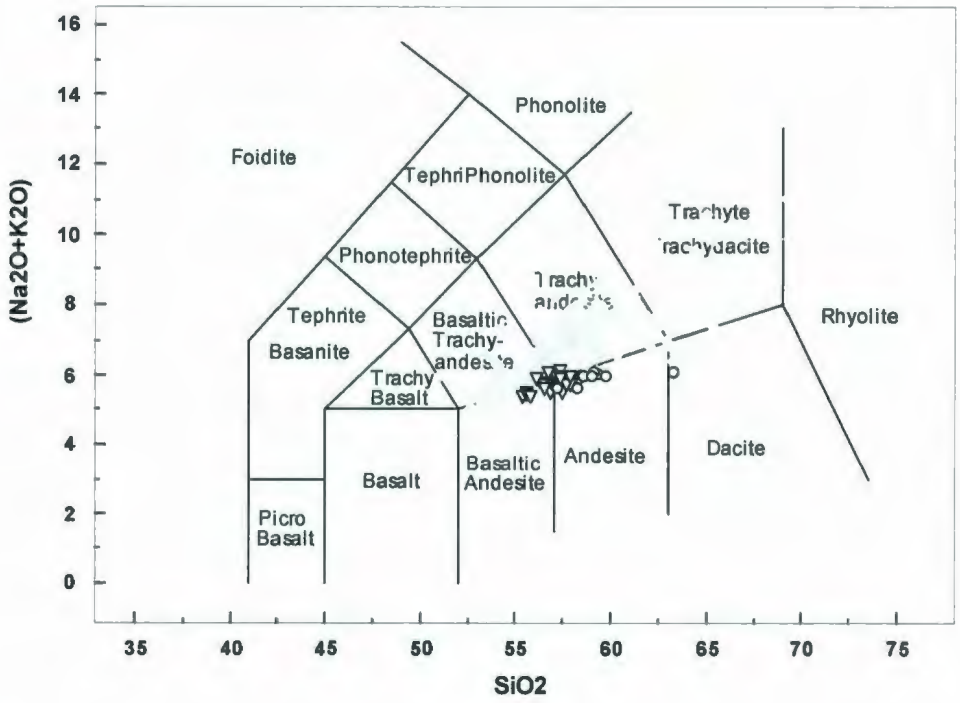

Figure 3.5. TAS alkalis-silica plot after Le Bas (1968), showing all microprobe analyses (gray diamonds) and bulk analyses (void upside down triangles = low HFSE; void circles = high HFSE) of the impact melt.

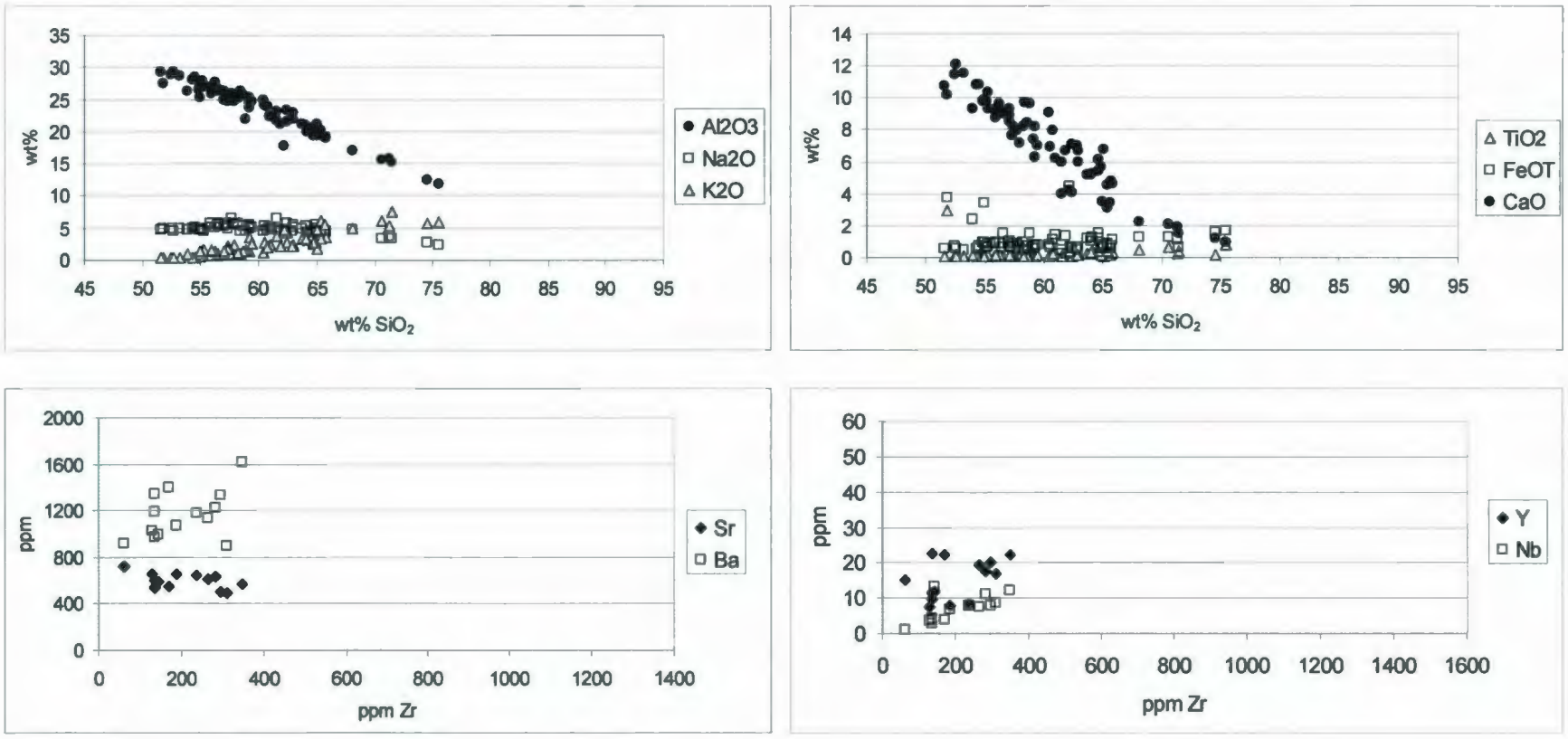

Figure 3.6. Compositional variation in sample CM023 (Coté Creek); EMPA (n=66) for major elements and LA-ICPMS analysis (n=14) for trace elements.

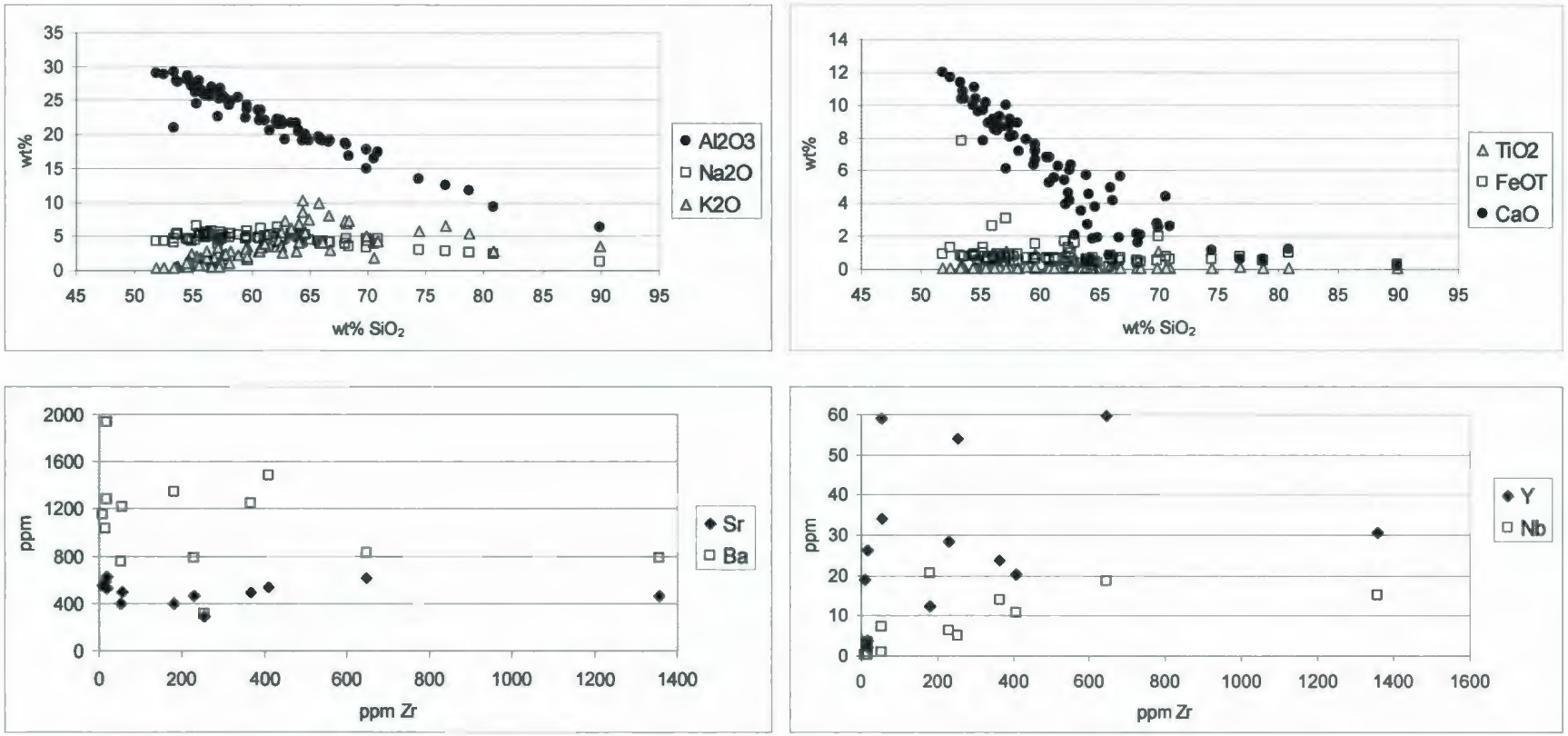

Figure 3.7. Compositional variation in sample CM042 (Discovery Hill); EMPA (n=71) for major elements and LA-ICPMS analysis (n=13) for trace elements.

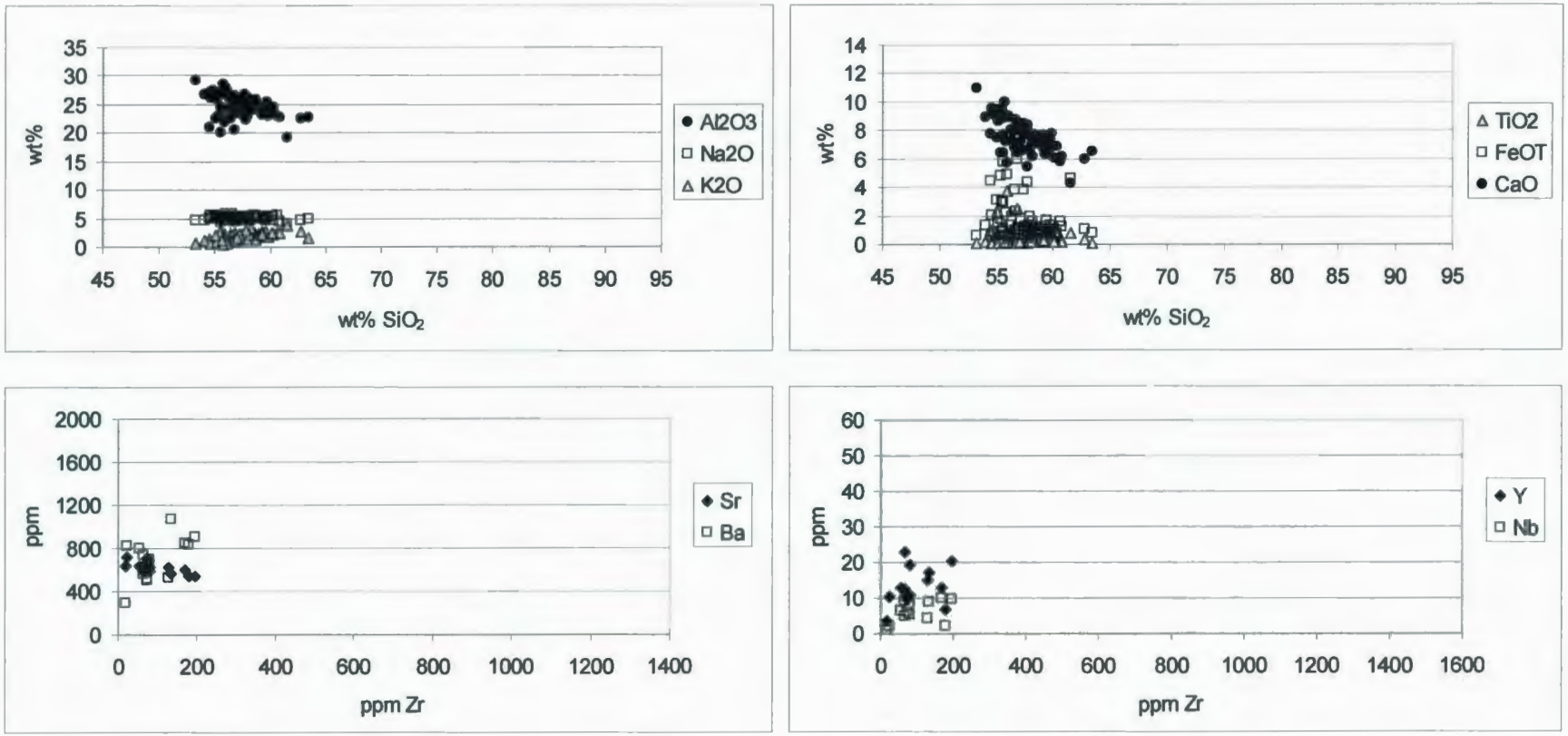

Figure 3.8. Compositional variation in sample CM071 (South Shore); EMPA (n=69) for major elements and LA-ICPMS analysis (n=14) for trace elements.

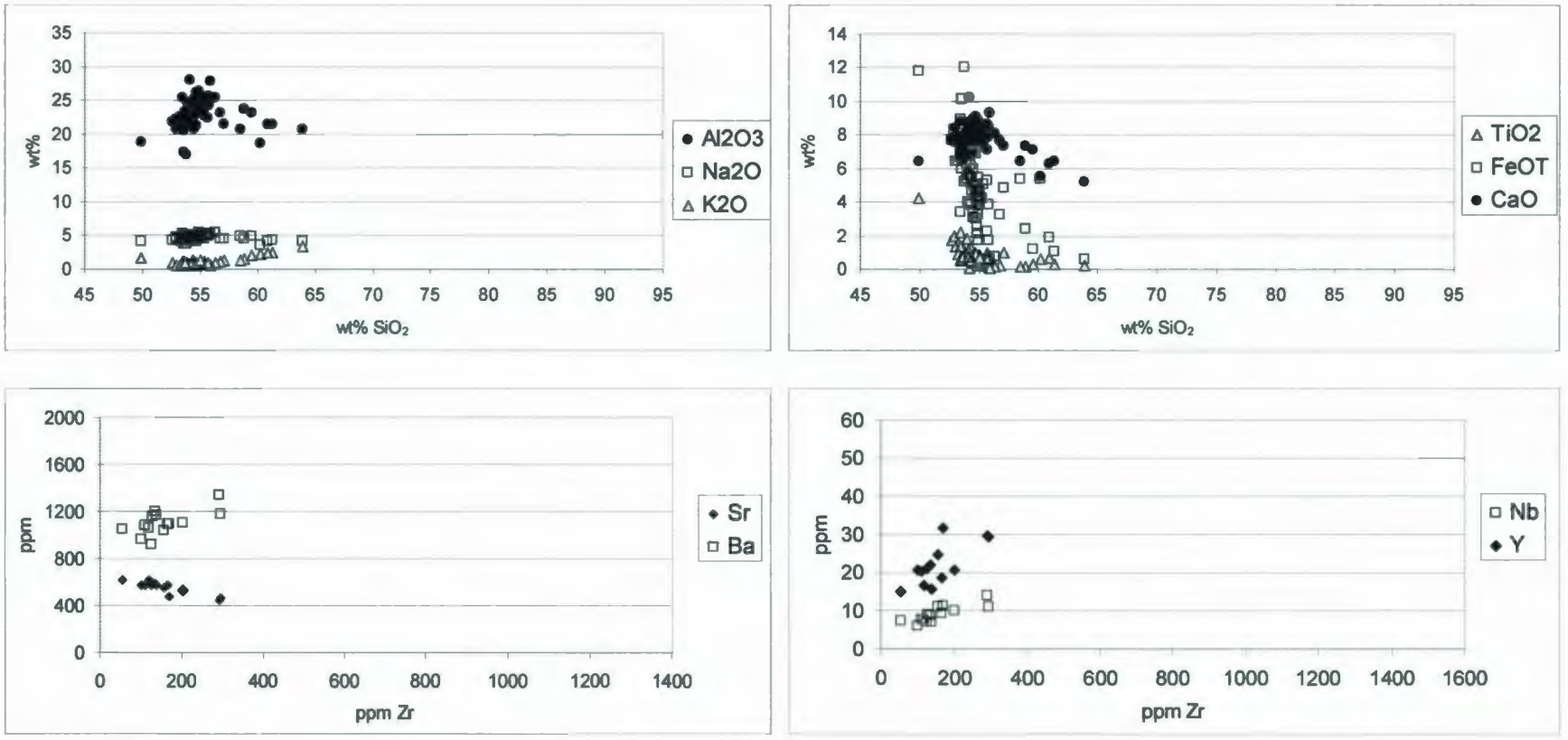

Figure 3.9. Compositional variation in sample CM055 (North Shore); EMPA (n=65) for major elements and LA-ICPMS analysis (n=13) for trace elements.

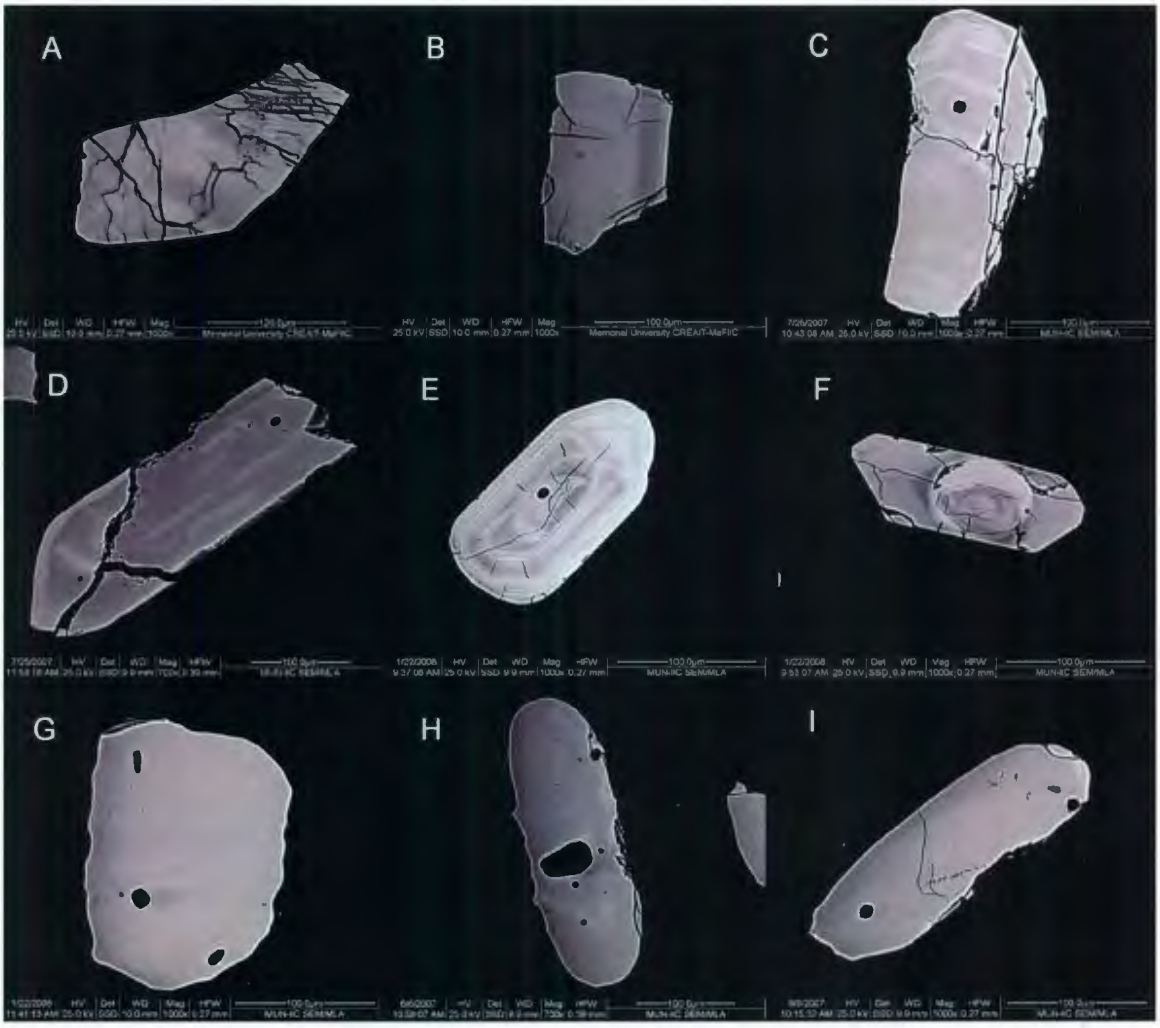

Figure 3.10. Target rock zircons. A) Shocked anorthosite zircon from sample CM032, note the planar deformation features and fractures; B) shocked anorthosite zircon fragment from sample CM032; C) mildly shocked mangerite zircon from sample W05-45; D) granodiorite zircon from sample CM003; E) granodiorite gneiss magmatic zircon; F) granodiorite gneiss zircon with inherited core; G) melt rock zircon clast from sample CM065, grain125; H) melt rock zircon clast from sample CM023, grain 14; and I) melt rock zircon clast from sample CM005, grain 1.

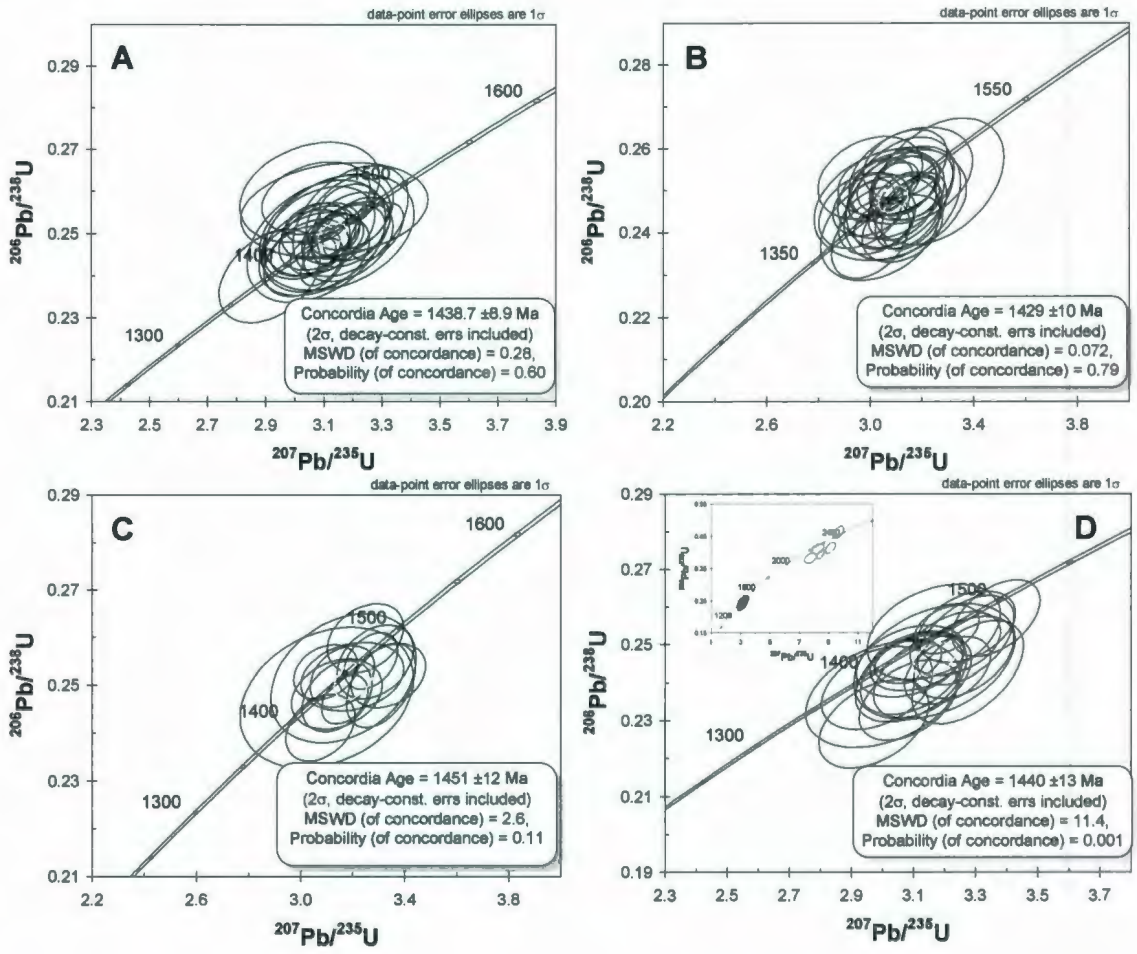

Figure 3.11. Concordia plots for A) sample CM032, anorthosite from Horseshoe Island; B) sample CM003, granodiorite from East shore; C) sample W05-45, mangerite from Horseshoe Island; and D) sample CM001, granodiorite gneiss showing magmatic ages. The insert plot shows magmatic and older inherited ages.

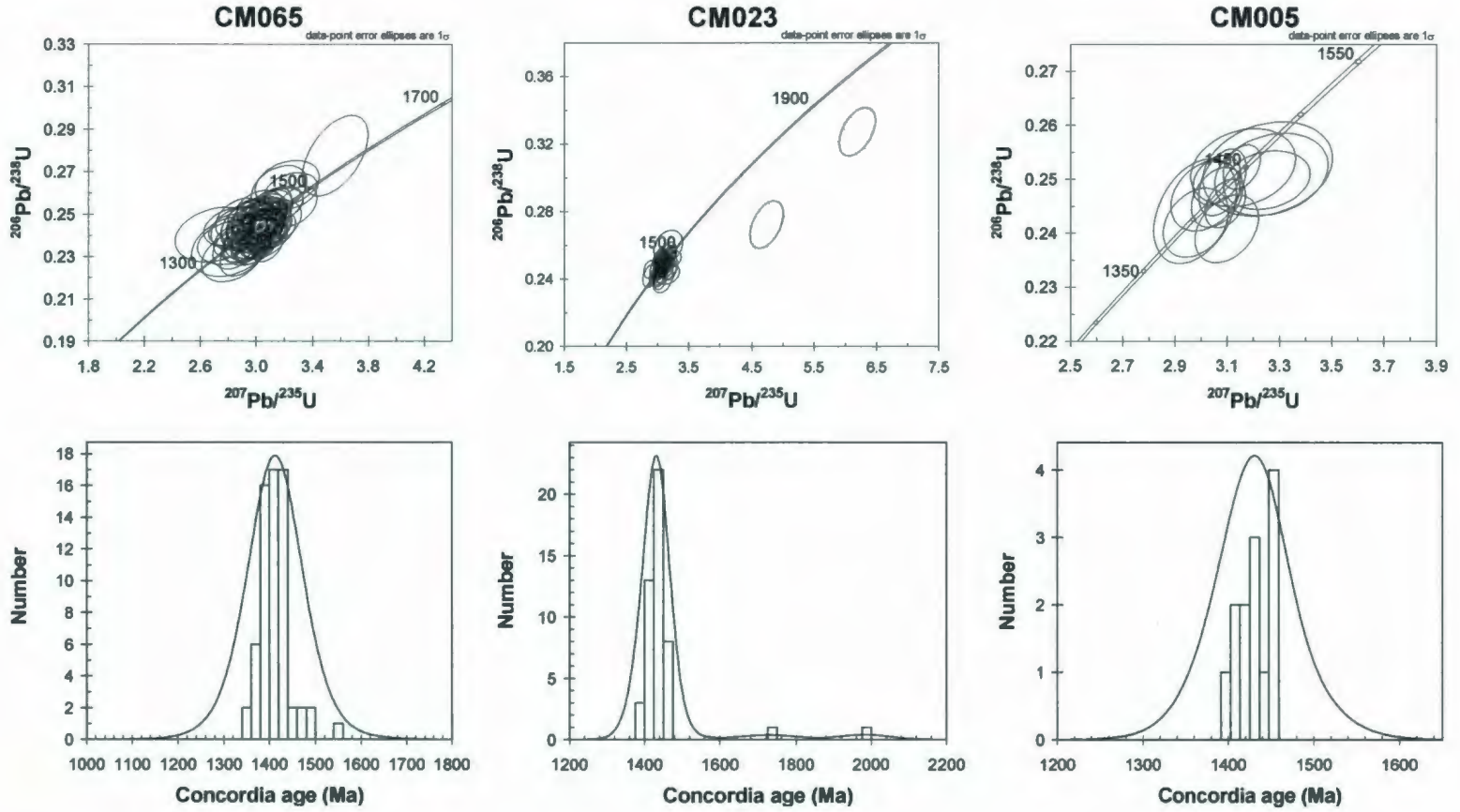

Figure 3.12. Concordia plots and histograms showing concordia ages for zircon clasts in impact melt rocks from samples CM065, CM023 and CM005. Average peak ages from the histogrammes are 1413 Ma ± 13, 1435 Ma ± 13 and 1431 Ma ± 21, respectively.

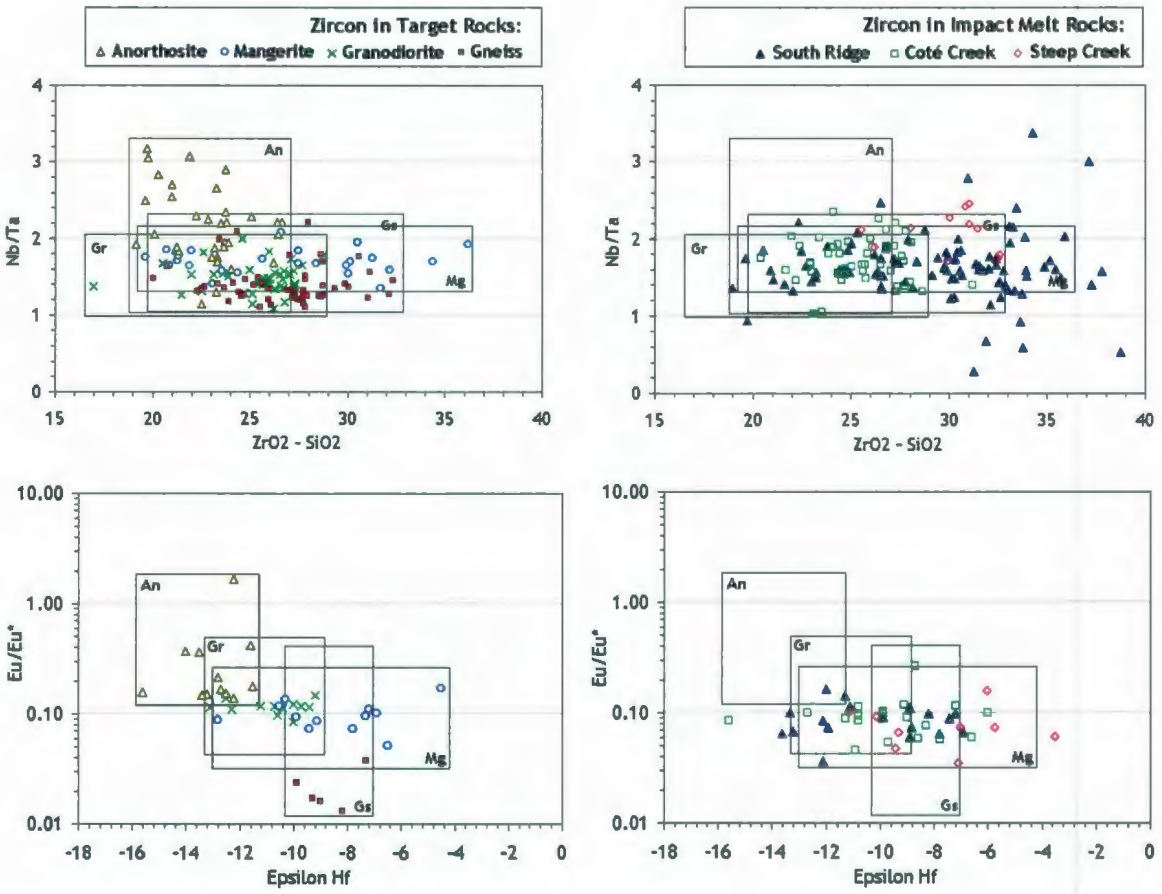

Figure 3.13. Zircon discrimination plots comparing Nb/Ta against $ZrO_2 - SiO_2$ and Eu/Eu* against Epsilon Hf for target rock zircons and zircons in the impact melt rocks. Note how few zircon compositions plot within the anorthosite fields. The granodiorite, mangerite and gneiss fields overlap as they are too close in composition.

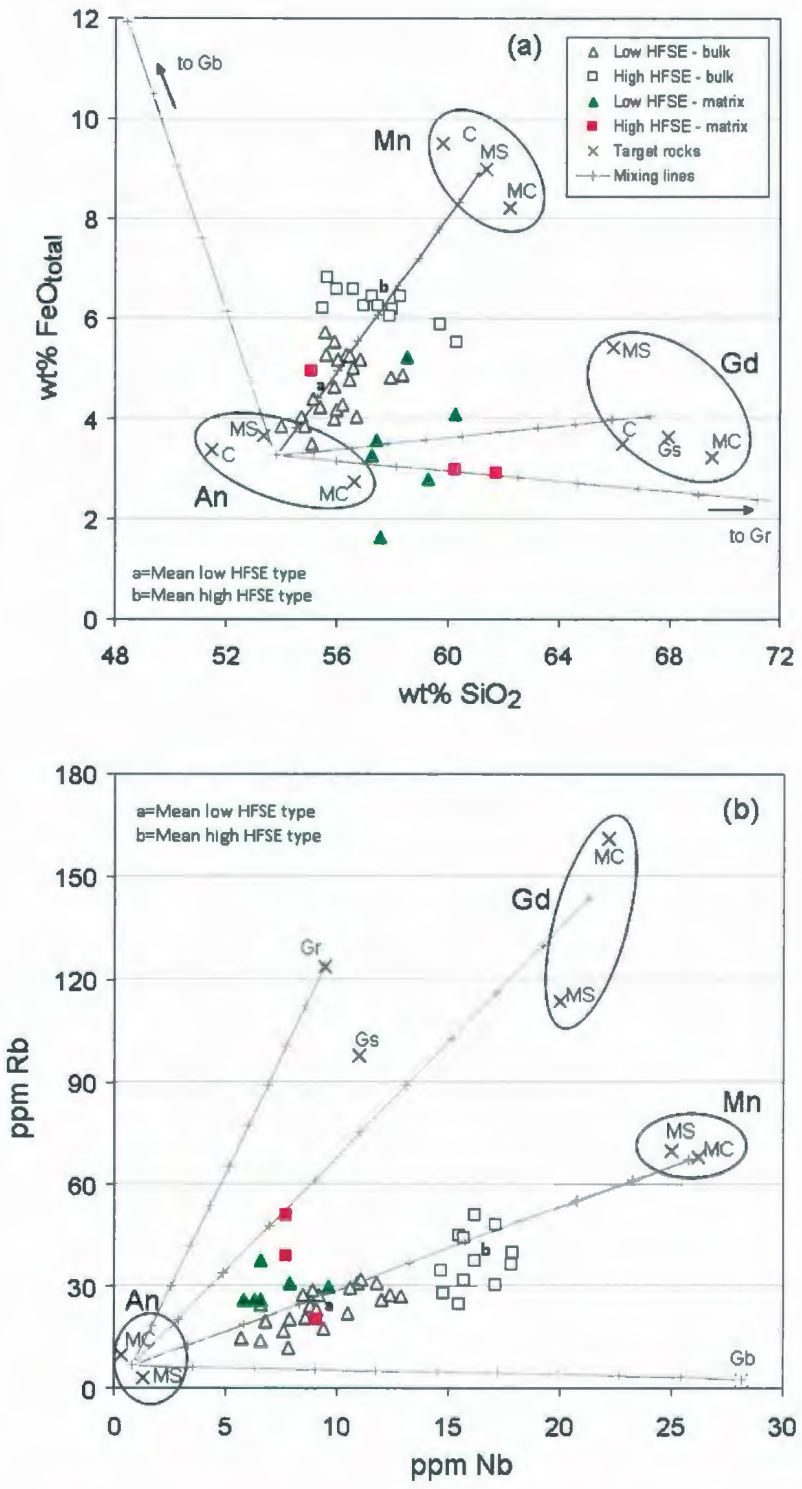

Figure 3.14. Mixing relationships between average anorthosite (An) and mangerite (Mn), granodiorite (Gd), gabbro (Gb), or granite (Gr) for impact melt rocks in (a) SiO2 vs FeOtotal, and (b) Nb vs Rb. Target rock means are from Currie (1971) (C), Marchand and Crockett (1977) (MC) and Marion and Sylvester (MS, this study). Gs=granodiorite gneiss (this study). Hash marks along mixing lines are increments of 10%.

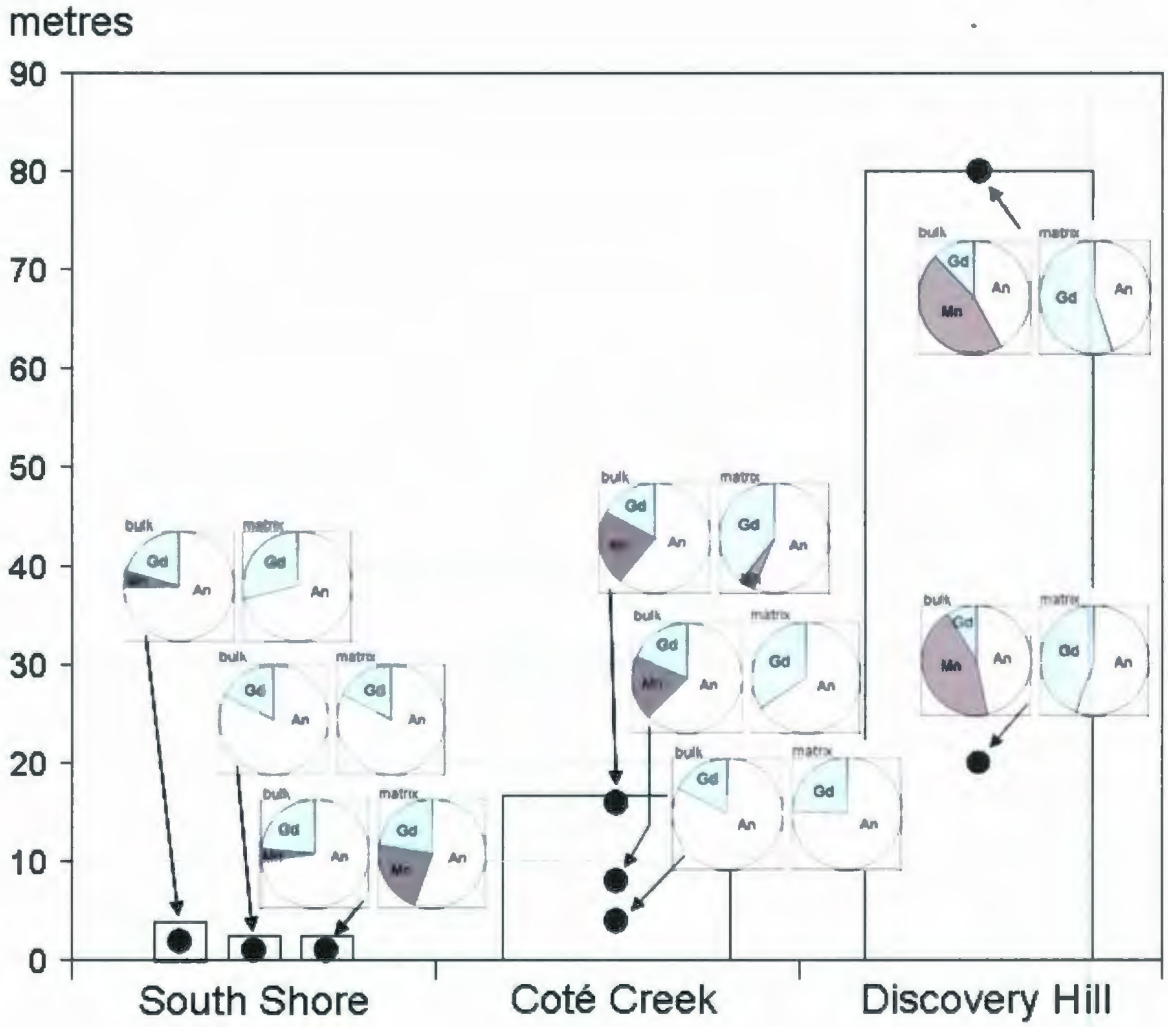

Figure 3.15. Modeled proportions of target rocks in bulk and matrix compositions of impact melt rock samples as a function of melt unit thickness and stratigraphic position. An=anorthosite, Mn=mangerite, Gd= granodiorite.

Table 3.1. Average chemical compositions of target rock units at Mistastin Lake

	Anorthosite						Mangerite						Granodiorite						Minor Rocks (This Study)		
	(This study)		(Marchand & Crockett 1977)		(Curie 1971)		(This study)		(Marchand & Crockett 1977)		(Curie 1971)		(This study)		(Marchand & Crockett 1977)		(Curie 1971)		Gneiss	Meta-Qtz Gabbro	Granite
	mean n=3	S.D.	mean n=7	S.D.	mean n=4	S.D.	mean n=4	S.D.	mean n=19	S.D.	mean n=2	S.D.	mean n=4	S.D.	mean n=27	S.D.	mean n=4	S.D.	n=1	n=1	n=1
SiO2 (wt%	53.36	0.81	56.62	1.71	51.5	0.5	61.37	2.11	62.23	2.92	59.8	0.6	65.98	2.42	69.54	4.1	66.3	1.9	67.96	44.86	75.56
TiO2	0.32	0.10	0.40	0.14	0.34	0.22	1.25	0.26	1.18	1.00	1.32	0.05	0.66	0.14	0.43	0.23	0.44	0.20	0.33	4.06	0.32
Al2O3	24.60	2.33	22.78	0.46	26.2	2.0	13.74	2.01	14.36	0.22	14.2	0.9	14.49	0.53	14.82	2.12	15.1	1.8	14.19	12.32	11.59
FeOT	3.66	1.69	2.75	1.26	3.4	1.6	8.99	0.67	8.22	2.23	9.5	0.7	5.42	1.10	3.24	1.386	3.5	1.4	3.65	17.71	2.15
MnO	0.06	0.02	0.08	0.01	0.05	0.03	0.17	0.05	0.10	0.06	0.12	0.02	0.09	0.04	0.07	0.02	0.04	0.02	0.07	0.29	0.03
MgO	2.73	1.30	1.64	1.53	1.7	0.9	1.09	0.19	0.98	0.37	0.9	0.0	0.54	0.13	0.33	0.19	0.6	0.1	0.84	3.98	0.22
CaO	9.28	0.77	10.09	0.91	8.9	0.5	5.36	2.27	4.53	0.83	4.4	0.1	2.15	0.86	1.95	1.06	1.7	0.5	1.52	8.05	1.14
Na2O	3.64	0.53	4.47	0.65	5.0	0.2	1.93	0.89	3.06	0.31	3.9	0.1	3.97	1.20	3.24	0.54	3.9	0.2	2.21	2.28	2.15
K2O	0.63	0.10	1.02	0.50	0.7	0.1	3.50	1.03	3.76	0.78	4.1	0.4	4.25	0.70	5.93	1.72	6.4	1.6	6.86	0.71	4.95
P2O5	0.12	0.09	0.15	0.07	0.16	0.10	0.41	0.11	0.09	0.31	0.33	0.04	0.20	0.06	0.13	0.08	0.13	0.07	0.08	1.30	0.07
LOI	2.57	1.98			0.9	0.5	3.00	1.50			1.3	0.8	0.88	0.39			0.5	0.1	0.66	0.18	0.75
Total	100.99		100.00		98.8		100.82		99.11		99.73		98.61		99.68		98.58		98.36	95.75	98.92
FeOT	3.66	1.69	2.75	1.26			8.09		8.22	2.23			4.88		3.24	1.39			3.65	17.71	2.15
Fe2O3T	4.07	1.88	3.06	1.40			8.99		9.13	2.48			5.42		3.60	1.54			4.06	19.68	2.39
S (ppm)	289	119					211	120					144	52					136	2759	93
Cl	183	142					152	110					360	115					88	113	379
Sc	9	3					20	7					15	6					14	34	<DL
V	28	10					41	13					21	11					45	266	<DL
Cr	56	47					13	11					17	14					17	22	<DL
Ni	23	18	23.6	16.7			7	1	20.6	7.4			4	2	26.3	13.1			0.6	28	2
Cu	18	12	19.3	15.9			13	4	1.5	4.9			6	2	<DL				6	41	<DL
Zn	15	*	24.5	12.7			48	21	139.0	37.2			10	13	64.4	34.9			<DL	116	<DL
Ga	22	3					18	3					21	4					16	20	23
As	<DL						6	10					7	14					<DL	4	5
Rb	3.1	1.9	10.0	9.7			70	22	68.3	23.7	63	4	114	20	161.4	58.0	155	20	98	2.7	124
Sr	736	16	736.1	25.4			314	91	315.7	62.2			228	61	246.6	96.5			302	519	245
Y	3.2	2.1	4.3	2.9			49	14	52.9	14.3			37	11	40.4	27.0			37	53	24
Zr	25	12	21.8	14.5			726	146	736.1	129.0			458	106	474.3	244.2			199	314	301
Nb	1.3	1.0	0.3	0.5			25	10	26.2	6.4			20	4	22.2	17.5			11	28	9.5
Ba	455	128					2505	861					2061	573					1759	1135	2550
Ce	24	*					257	51					184	40					148	182	87
Pb	7.1	*	4.6	2.2			22	1	24.0	4.1			24	5	38.4	10.8			25	8.7	25
Th	1.3	*	1.0	0.8			7	4	6.0	3.4			11	4	22.1	41.9			11	<DL	9.3
U	<DL						1	2					2	0					0.2	<DL	4.0
ICP-MS (ppm)	n=1						n=2						n=1						n=1	n=1	n=1
Y	2.7						43.9						28.5						35.3	49.1	21.4
Zr	20.8						835.7						580.5						294	464	477
Nb	1.6						29.4						20.5						18.8	45.4	13.2
Ba	463						2843.4						2311.0						1925	1268	2830
La	5.66						66.5						62.0						65.3	88.1	50.3
Ce	10.4						139.2						119.1						114.0	152.5	93.3
Pr	1.28						17.2						14.0						12.6	20.4	10.9
Nd	5.17						69.8						52.5						45.4	88.0	41.2
Sm	0.90						12.66						8.50						6.84	16.02	6.79
Eu	0.88						3.64						3.16						2.31	4.27	2.71
Gd	0.75						10.87						6.88						5.70	13.98	5.42
Tb	0.08						1.54						0.97						0.91	1.88	0.77
Dy	0.53						9.19						5.67						6.21	10.81	4.54
Ho	0.11						1.81						1.14						1.39	2.09	0.89
Er	0.31						5.11						3.24						4.35	5.75	2.40
Tm	0.04						0.73						0.47						0.67	0.77	0.36
Yb	0.30						4.79						3.01						4.56	5.06	2.31
Lu	0.05						0.73						0.44						0.66	0.78	0.32
Hf	0.48						15.00						10.41						5.85	8.62	8.99
Ta	0.60						1.91						2.16						1.93	2.10	2.88
Th	0.19						5.22						9.02						11.31	0.59	6.74

Notes: N = number of samples analysed. S.D. = standard deviation. * = only one analysis above detection limit. <DL = less than detection limit.

Analytical methods: This study - fused bead XRF for major elements, pressed powder pellet XRF and sinter-solution ICP-MS for trace elements. Marchand & Crockett (1977) - pressed powder pellet XRF for major and trace elements. Currie (1971) - X-ray spectrographic and partial wet-chemical analyses. Anorthosite is the average of samples W05-41, W05-49, W05-67; the mangerite of samples CM029, CM059, CM038 and W05-45; the granodiorite of samples CM006, CM007, CM117, CM003.

Table 3.2. Bulk (XRF) chemical compositions of melt rock units at Mistastin Lake

	Low HFSE melt rocks											High HFSE melt rocks						
	Cote Creek		Steep Creek	North Shore		South Ridge		South Shore			Mean	SD	Discovery Hill		Cote Creek West (3)	North Shore	Steep Creek (4)	Mean	SD
Sample	Mean	SD	CM005	Mean	SD	Mean	SD	Mean	SD	W05-65 (1)			Mean	SD	CM027	CM055	CM008		
	n=10		n=1	n=3		n=3		n=3		n=1	n=20 (2)		n=9		n=1	n=1	n=1	n=11 (5)	
SiO2 (wt%)	56.08	1.26	56.47	55.70	0.19	55.68	0.46	55.57	0.56	57.94	55.91	0.94	57.62	1.63	57.88	55.66	61.33	57.46	1.58
TiO2	0.79	0.12	0.77	0.89	0.03	0.69	0.03	0.64	0.05	0.81	0.77	0.11	1.04	0.06	1.13	1.06	0.97	1.05	0.06
Al2O3	21.86	1.25	20.93	21.91	1.26	22.14	0.20	23.12	1.45	22.97	22.05	1.18	19.55	1.03	20.45	19.05	15.94	19.59	0.98
FeOT	4.66	0.62	4.78	5.51	0.23	4.20	0.19	4.01	0.43	4.62	4.63	0.65	6.23	0.35	6.05	6.83	6.77	6.27	0.37
MnO	0.07	0.01	0.06	0.09	0.01	0.05	0.01	0.05	0.02	0.08	0.07	0.02	0.10	0.01	0.10	0.11	0.11	0.10	0.01
MgO	1.12	0.35	1.42	1.63	0.14	1.19	0.19	1.13	0.17	1.36	1.22	0.32	1.34	0.15	0.89	1.54	0.89	1.32	0.20
CaO	7.50	0.72	7.36	7.45	0.17	7.71	0.18	8.01	0.50	7.69	7.59	0.56	6.80	0.63	6.79	6.87	4.60	6.81	0.56
Na2O	4.08	0.27	3.87	3.92	0.11	4.18	0.08	4.30	0.06	4.42	4.09	0.23	3.61	0.16	3.59	3.51	2.90	3.60	0.14
K2O	1.55	0.33	1.86	1.49	0.04	1.45	0.07	1.26	0.28	1.71	1.49	0.27	2.14	0.20	1.93	1.77	2.94	2.09	0.22
P2O5	0.34	0.18	0.22	0.26	0.00	0.23	0.00	0.20	0.03	0.23	0.29	0.14	0.33	0.03	0.32	0.34	0.31	0.33	0.03
LOI	1.35	0.98	1.54	1.46	0.48	1.97	0.89	1.62	1.20	0.34	1.51	0.85	1.40	0.50	1.33	0.42	2.63	1.30	0.53
Total	99.40		99.08	100.31		99.49		99.91		102.37	99.81		100.16		100.45	97.18	99.39	99.92	
S (ppm)	147	98	79	113	91	47	5	119	120	226	120	91	160	177	211	50	172	154	183
Cl	54	35	27	50	21	52	6	53	26	107	52	27	74	23	80	103	114	77	23
Sc	14	7	11	14	1	8	1	16	3	10	13	6	16	7	18	18	14	16	6
V	46	7	44	53	7	43	5	45	7	46	46	7	52	5	63	59	25	53	8
Cr	23	14	22	23	5	16	3	28	12	22	23	11	13	5	19	19	0.3	15	5
Ni	13	3	16	20	5	13	4	13	2	14	14	4	10	3	9	14	7	10	3
Cu	12	2	10	12	5	13	5	13	1	13	12	3	13	2	18	15	10	13	2
Zn	16	7	28	17	2	15	9	16	7	10	17	7	29	7	24	46	52	30	8
Ga	21	2	24	23	2	22	2	20	1	21	21	2	21	2	20	23	23	21	2
As	10	8	4	9	3	0.4	0.2	7	4	<LD	7	6	8	4	<LD	7	5	8	4
Rb	24.5	7.4	24.3	20.3	2.4	26.8	1.6	20.3	7.7	27.3	23.5	6.2	39.7	7.9	31.6	24.6	44.5	37.6	8.6
Sr	598	38	601	597	6	636	20	637	46	587	609	38	519	29	542	558	452	525	29
Y	18.0	3.6	18.0	17.0	1.3	14.2	1.1	13.0	3.6	20.8	18.5	3.5	30.5	1.9	26.8	29.7	33.9	30.1	2.0
Zr	259	79	242	274	40	198	17	170	84	276	238	73	418	30	381	425	819	414	29
Nb	9.8	2.3	6.8	9.5	0.9	6.1	1.3	7.4	1.6	12.9	9.1	2.0	16.3	1.2	15.7	15.5	16.0	16.2	1.1
Ba	926	223	1093	988	116	743	29	674	159	879	879	207	1181	87	1237	1249	2503	1192	65
Ce	119	31	80	107	27	69	16	86	26	83	103	32	155	16	140	114	162	150	19
Pb	8	2	7	8	2	7	4	8	2	<LD	8	2	12	3	11	11	16	12	3
Th	6	2	5	2.1	0.3	4	2	4	2	<LD	4	2	5	2	<LD	2	5	5	2
U	1.1	1.0	<LD	1.4		0.8	-			<LD	1.1	0.6	0.2		<LD	0.9	<LD	0.6	0.5
Ratios																			
Mg no.	29	5	35	35	2	33	3	33	2	33	32	4	28	2	21	29	19	27	3
TiO2/Al2O3	0.037	0.007	0.037	0.041	0.003	0.031	0.001	0.028	0.003	0.035	0.035	0.006	0.053	0.003	0.055	0.057	0.061	0.054	0.003
FeOT/Al2O3	0.21	0.04	0.23	0.25	0.02	0.19	0.01	0.17	0.03	0.21	0.21	0.04	0.32	0.03	0.30	0.36	0.43	0.32	0.03
Y/Sr	0.031	0.007	0.030	0.028	0.002	0.022	0.002	0.021	0.007	0.036	0.028	0.007	0.059	0.006	0.049	0.053	0.075	0.058	0.006
Zr/Sr	0.44	0.15	0.40	0.46	0.07	0.31	0.04	0.27	0.15	0.47	0.40	0.14	0.80	0.08	0.70	0.76	1.37	0.79	0.06
Nb/Sr	0.017	0.005	0.015	0.016	0.002	0.013	0.002	0.012	0.003	0.022	0.015	0.004	0.032	0.003	0.029	0.028	0.035	0.031	0.003
Ba/Sr	1.57	0.44	1.82	1.66	0.21	1.17	0.08	1.07	0.32	1.50	1.46	0.41	2.28	0.18	2.26	2.24	5.53	2.28	0.16

Notes: S.D. = standard deviation. <LD = less than detection limit. (1)=melt breccia. (2) mean excludes melt breccia sample W05-65. (3)=shore 1.25 km west of Cote Creek. (4)=suevite. (5) mean excludes suevite sample CM008.

Table 3.3. Chemical compositions of matrix of melt rock units at Mistastin Lake

	Low HFSE bulk melt rocks												High HFSE bulk melt rocks					
	Coté Creek						South Shore						Discovery Hill				North Shore	
Sample No.	Near base of unit CM088		Middle of unit CM023		Top of unit CM025		Thin unit W05-65		Thin unit CM071		Thin unit CM067		Near base of unit CM042		Top of unit CM035		Thin unit CM055	
	mean	SD	mean	SD	mean	SD	mean	SD	mean	SD	mean	SD	mean	SD	mean	SD	mean	SD
	LA-ICPMS (n=13)		EPMA (n=66)		LA-ICPMS (n=14)		LA-ICPMS (n=10)		EPMA (n=69)		LA-ICPMS (n=14)		EPMA (n=71)		LA-ICPMS (n=12)		EPMA (n=85)	
(wt%)																		
SiO2	57.24	4.54	59.32	5.34	60.29	3.57	57.41	2.27	57.55	2.10	58.54	2.87	60.29	7.02	61.77	5.02	55.08	2.22
TiO2	0.75	0.29	0.56	0.88	0.44	0.52	0.62	0.36	0.48	0.66	0.69	0.56	0.39	0.50	0.25	0.17	0.81	0.62
Al2O3	22.09	6.00	22.06	3.66	20.28	3.28	22.19	1.84	24.56	1.95	20.00	2.19	20.81	4.47	19.59	3.26	22.93	2.18
FeOT	3.27	1.08	2.81	1.98	4.10	4.86	3.58	2.13	1.65	1.35	5.23	2.52	2.99	3.14	2.92	3.74	4.94	2.54
MnO	0.04	0.01	0.04	0.05	0.06	0.09	0.05	0.04	0.03	0.03	0.08	0.04	0.05	0.08	0.03	0.07	0.09	0.05
MgO	0.60	1.07	0.96	1.32	1.05	1.66	0.77	0.76	0.25	0.29	1.60	0.84	0.79	1.87	0.50	1.32	1.29	0.87
CaO	8.46	0.74	6.80	2.68	7.19	0.87	7.76	0.82	7.55	1.19	7.12	1.49	6.40	3.47	6.12	1.92	7.82	0.66
Na2O	5.24	2.45	4.63	0.68	4.23	0.90	3.87	0.42	5.09	0.33	4.30	0.47	4.35	0.82	4.37	0.67	4.68	0.39
K2O	1.35		2.32	1.83	1.95		3.29		1.60	0.70	2.02		3.19	2.30	4.17		0.98	0.52
P2O5	0.55	0.21	0.22	0.13	0.15	0.07	0.21	0.13	0.14	0.05	0.18	0.11	0.23	0.15	0.08	0.08		
Total	99.80		99.50		99.75		99.75		98.96		99.76		99.27		99.76		98.62	
(ppm)	LA-ICPMS (n=13)		LA-ICPMS (n=14)		LA-ICPMS (n=14)		LA-ICPMS (n=10)		LA-ICPMS (n=14)		LA-ICPMS (n=14)		LA-ICPMS (n=13)		LA-ICPMS (n=12)		LA-ICPMS (n=14)	
Sc	7	3	7	4	11	12	8	4	5	2	11	4	17	18	6	9	15.5	3.8
V	37	12	34	27	46	107	25	28	35	31	48	47	56	104	4	8	59.5	12.4
Cr	18	8	60	51	5	8	12	10	22	30	8	8	13	19	2	2	31.4	8.2
Co	5	2	9	7	10	14	6	5	9	5	12	7	14	15	3	8	15.3	2.7
Ni	31	40	14	18	10	19	13	18	65	132	15	11	12	21	3	5	24.6	7.5
Cu	11	3	9	4	13	10	32	24	11	12	14	14	14	8	7	3	4.8	1.5
Zn	49	15	56	53	55	57	65	45	80	60	73	40	115	115	36	38	105	15
Rb	26	4	35	11	26	14	30	10	26	13	31	21	48	20	39	25	20	12
Sr	584	159	542	59	519	91	606	92	606	52	517	115	447	85	503	132	552	54
Y	13	4	15	5	14	10	18	13	13	5	18	11	28	19	13	12	22	5
Zr	107	12	192	82	203	103	221	141	94	55	190	128	258	352	269	253	157	68
Nb	8.6	3.1	7.9	4.3	5.8	3.4	9.6	6.4	6.3	3.1	7.9	5.4	8.0	7.3	7.7	8.0	9.07	2.20
Ba	811	125	1062	188	985	302	967	217	685	198	760	139	985	369	1113	389	1103	105
La	34	11	29	10	25	14	39	27	33	9	34	22	55	37	28	18	33	4
Ce	69	21	60	24	49	31	83	59	62	21	73	47	115	62	54	42	72	10
Pr	6.0	2.5	8.8	2.9	5.5	3.7	9.4	8.9	6.9	2.8	8.2	5.7	13.1	9.3	6.1	5.3	9	1
Nd	30	10	25	11	22	16	37	27	26	11	32	23	50	35	22	20	36	6
Sm	4.8	1.5	4.7	2.4	3.8	2.7	6.0	4.4	4.4	1.9	5.8	3.8	8.6	5.9	3.8	3.6	8.3	1.1
Eu	1.5	0.4	1.9	0.2	1.9	0.3	2.1	0.3	1.6	0.4	1.8	0.2	2.2	0.4	2.5	0.3	2.3	0.2
Gd	4.1	1.3	3.8	1.4	3.1	2.4	4.7	3.5	3.3	2.0	4.4	3.2	8.8	4.8	2.7	2.7	5.1	1.2
Tb	0.50	0.15	0.40	0.20	0.42	0.32	0.62	0.49	0.41	0.17	0.57	0.39	0.86	0.56	0.40	0.41	0.71	0.16
Dy	2.9	1.0	2.9	1.2	2.8	2.0	3.7	2.7	2.8	1.1	3.6	2.4	5.7	4.0	2.5	2.4	4.5	1.1
Ho	0.50	0.16	0.58	0.23	0.54	0.40	0.73	0.51	0.49	0.18	0.66	0.41	1.05	0.68	0.51	0.50	0.68	0.21
Er	1.5	0.5	1.5	0.7	1.5	1.1	2.0	1.4	1.3	0.6	1.8	1.0	3.1	2.1	1.5	1.4	2.3	0.6
Tm	0.18	0.06	0.23	0.08	0.22	0.13	0.29	0.19	0.19	0.13	0.28	0.18	0.45	0.30	0.21	0.21	0.34	0.09
Yb	1.3	0.4	1.4	0.5	1.4	0.9	1.7	1.1	1.3	0.7	1.9	1.1	3.0	2.3	1.5	1.4	2.2	0.6
Lu	0.17	0.06	0.23	0.10	0.23	0.13	0.26	0.17	0.18	0.08	0.26	0.14	0.43	0.27	0.22	0.20	0.34	0.11
Hf	2.4	0.4	4.5	2.3	4.5	2.1	5.2	3.4	2.2	1.4	4.4	3.1	5.9	7.0	5.7	5.4	3.6	1.6
Ta	0.28	0.13	0.34	0.18	0.28	0.18	0.41	0.29	0.31	0.16	0.34	0.22	0.38	0.34	0.38	0.38	0.37	0.12
Pb	7.3	2.6	9.7	1.2	9.8	4.0	6.6	2.3	8.9	2.2	9.4	4.3	12.1	2.8	12.5	4.3	8.8	1.2
Th	2.6	0.8	2.8	1.2	2.3	1.3	3.5	2.5	3.2	1.4	3.2	2.3	4.0	2.4	3.6	3.7	1.7	0.8
U	0.25	0.03	0.36	0.16	0.38	0.37	0.39	0.24	0.42	0.21	0.43	0.30	0.34	0.27	0.49	0.43	0.22	0.11

EPMA matrix data collected using a broad (20 x 20 micron) beam. LA-ICPMS matrix data collected using a 40 x 40 micron spot and normalized to 100% total major oxides and trace elements, with K_2O taken from the average of the EPMA matrix analyses. P_2O_5 was determined by LA-ICPMS for all samples. Where LA-ICPMS data are shown for major elements, fewer than 7 analyses were made by EPMA using an 11 x 17 micron spot and thus the LA-ICPMS data are thought to be more representative. The matrix is predominantly glass in CM088, CM025, CM067 and CM055; and microcrystalline in the other samples. CM023 and CM042 have porphyritic textures and their EPMA matrix data have been recalculated to include the presence of pyroxene, titanomagnetite and ilmenite microphenocrysts (4.2% pigeonite, 0.9% titanomagnetite and 0.3% ilmenite in CM023; 5.6% augite and 1.2% titanomagnetite in CM042), which were analyzed by EPMA separately. CM088, CM023 and CM025 are located ~4, 8 and 16 metres respectively above the basal contact of the Coté Creek melt rock unit. CM042 and CM035 are located ~20 and 80 metres respectively above the basal contact of the Discovery Hill melt rock unit.

Table 3.4. Least squares modelling of sources to melt rock compositions at Mistastin Lake

	Low HFSE bulk melt rocks													High HFSE bulk melt rocks						
	All Bulk Rocks	Coté Creek						South Shore						All Bulk Rocks	Discovery Hill				North Shore	
	Mean n=20	CM088 bulk rock	CM088 matrix	CM023 bulk rock	CM023 matrix	CM025 bulk rock	CM025 matrix	W05-65 bulk rock	W05-65 matrix	CM071 bulk rock	CM071 matrix	CM067 bulk rock	CM067 matrix	Mean n=11	CM042 bulk rock	CM042 matrix	CM035 bulk rock	CM035 matrix	CM055 bulk rock	CM055 matrix
SiO_2, wt%	55.91	54.85	57.24	56.84	59.32	56.33	60.29	57.94	57.41	55.39	57.55	56.19	56.54	57.46	56.98	60.29	57.24	61.77	55.66	55.08
TiO_2	0.77	0.75	0.75	0.86	0.56	0.86	0.44	0.81	0.82	0.59	0.48	0.69	0.69	1.05	1.03	0.39	0.98	0.25	1.08	0.81
Al_2O_3	22.05	22.62	22.09	20.81	22.06	20.33	20.28	22.97	22.19	22.99	24.56	21.74	20.00	19.59	18.82	20.81	18.32	19.59	19.05	22.93
FeOT	4.63	3.86	3.27	5.18	2.81	5.27	4.10	4.82	3.56	4.24	1.65	4.29	5.23	6.27	6.25	2.99	6.44	2.92	6.83	4.94
MnO	0.07	0.05	0.04	0.08	0.04	0.08	0.06	0.08	0.05	0.04	0.03	0.07	0.08	0.10	0.08	0.05	0.10	0.03	0.11	0.09
MgO	1.22	0.88	0.80	1.31	0.98	1.42	1.05	1.36	0.77	1.08	0.25	1.33	1.60	1.32	1.38	0.79	1.33	0.50	1.54	1.29
CaO	7.59	8.32	6.46	6.93	6.80	6.91	7.19	7.69	7.76	7.69	7.55	7.58	7.12	6.81	6.47	6.40	6.04	6.12	6.87	7.82
Na_2O	4.09	4.40	5.24	3.84	4.63	3.94	4.23	4.42	3.87	4.26	5.09	4.25	4.30	3.60	3.48	4.35	3.46	4.37	3.51	4.68
K_2O	1.49	1.30	1.35	1.80	2.32	1.76	1.95	1.71	3.29	1.25	1.80	1.54	2.02	2.09	2.24	3.19	2.38	4.17	1.77	0.98
P_2O_5	0.29	0.84	0.55	0.26	0.22	0.25	0.15	0.23	0.21	0.19	0.14	0.23	0.18	0.33	0.36	0.23	0.32	0.08	0.34	0.13
Proportions, %																				
Anorthosite	73.9	61.7	76.5	62.1	67.4	59.9	57.6	77.0	71.8	61.8	85.7	72.6	56.0	50.8	45.8	58.6	41.0	46.0	49.3	61.4
Mangerite	7.9	0.0	0.0	18.5	0.0	21.6	4.4	4.8	0.0	0.0	0.0	3.2	22.3	42.5	43.8	0.0	45.0	0.0	48.2	5.6
Granodiorite	17.8	17.2	24.8	18.8	35.5	17.0	40.6	21.3	29.2	18.0	18.1	23.6	22.8	6.7	8.6	45.5	12.0	56.5	0.0	12.7
Total	99.6	98.9	101.3	99.5	102.8	98.5	102.6	103.1	101.0	99.8	103.7	99.4	101.1	100.0	98.4	102.3	98.0	102.5	97.5	99.7
Mixing model melt rock compositions																				
SiO_2	56.01	54.92	57.21	56.95	59.35	56.43	60.21	56.09	57.56	55.50	57.63	56.24	56.58	57.60	57.11	60.33	57.39	61.81	55.86	55.24
TiO_2	0.45	0.37	0.41	0.56	0.45	0.57	0.51	0.45	0.42	0.38	0.39	0.43	0.61	0.74	0.75	0.48	0.77	0.52	0.76	0.41
Al_2O_3	21.84	22.59	22.42	20.56	21.72	20.16	20.66	22.69	21.69	22.73	23.70	21.71	20.13	19.31	18.56	20.57	18.00	19.51	18.74	22.63
FeOT	4.21	3.83	4.01	4.69	4.20	4.77	4.44	4.25	4.05	3.87	4.02	4.07	4.98	5.62	5.65	4.30	5.73	4.44	5.70	4.05
MnO	0.07	0.06	0.07	0.06	0.07	0.09	0.06	0.07	0.07	0.06	0.07	0.07	0.09	0.11	0.11	0.07	0.11	0.06	0.11	0.07
MgO	2.20	2.33	2.23	2.00	2.03	1.98	1.84	2.27	2.12	2.33	2.44	2.15	1.90	1.89	1.78	1.80	1.67	1.56	1.87	2.36
CaO	7.67	7.95	7.64	7.17	7.02	7.06	6.46	7.86	7.29	7.98	8.34	7.42	6.88	7.14	6.79	6.25	6.47	5.49	7.16	8.13
Na_2O	3.55	3.65	3.77	3.37	3.86	3.27	3.79	3.74	3.77	3.69	3.84	3.84	3.37	2.94	2.86	3.87	2.84	3.92	2.72	3.57
K_2O	1.50	1.25	1.54	1.84	1.93	1.86	2.24	1.56	1.69	1.28	1.31	1.57	2.10	2.10	2.20	2.29	2.35	2.69	2.00	1.25
P_2O_5	0.16	0.13	0.14	0.19	0.15	0.19	0.17	0.15	0.14	0.13	0.14	0.15	0.20	0.25	0.25	0.16	0.26	0.17	0.26	0.15
Residuals	obs.-cal.	obs.-cal.	obs.-cal.	obs.-cal.	obs.-cal.	obs.-cal.	obs.-cal.	obs.-cal.	obs.-cal.	obs.-cal.	obs.-cal.	obs.-cal.	obs.-cal.	obs.-cal.	obs.-cal.	obs.-cal.	obs.-cal.	obs.-cal.	obs.-cal.	obs.-cal.
SiO_2	-0.11	-0.06	0.03	-0.11	-0.03	-0.10	0.09	-0.15	-0.15	-0.11	-0.08	-0.05	-0.04	-0.14	-0.14	-0.03	-0.15	-0.04	-0.21	-0.16
TiO_2	0.31	0.37	0.34	0.31	0.11	0.26	-0.07	0.36	0.20	0.21	0.09	0.26	0.08	0.31	0.28	-0.09	0.21	-0.27	0.32	0.40
Al_2O_3	0.21	0.04	-0.33	0.25	0.34	0.16	-0.38	0.29	0.30	0.26	0.86	0.03	-0.13	0.26	0.26	0.24	0.32	0.08	0.30	0.30
FeOT	0.41	0.03	-0.74	0.49	-1.38	0.50	-0.34	0.57	-0.46	0.37	-2.37	0.22	0.26	0.65	0.60	-1.31	0.71	-1.52	1.13	0.88
MnO	-0.01	-0.01	-0.03	-0.02	-0.03	0.00	-0.01	0.01	-0.02	-0.02	-0.04	0.01	-0.01	-0.01	-0.02	-0.03	-0.01	-0.04	0.01	0.02
MgO	-0.98	-1.44	-1.42	-0.70	-1.07	-0.54	-0.79	-0.91	-1.35	-1.28	-2.19	-0.82	-0.30	-0.57	-0.39	-1.01	-0.35	-1.06	-0.33	-1.07
CaO	-0.07	0.37	0.83	-0.24	-0.22	-0.17	0.73	-0.17	0.46	-0.09	-0.79	0.16	0.24	-0.33	-0.32	0.14	-0.43	0.63	-0.29	-0.31
Na_2O	0.54	0.74	1.47	0.47	0.77	0.66	0.43	0.68	0.10	0.59	1.25	0.61	0.93	0.66	0.62	0.47	0.62	0.45	0.79	1.10
K_2O	-0.01	0.05	-0.19	-0.04	0.39	-0.10	-0.29	0.15	1.60	-0.03	0.49	-0.03	-0.08	-0.01	0.04	0.90	0.03	1.48	-0.23	-0.27
P_2O_5	0.13	0.51	0.41	0.07	0.07	0.06	-0.01	0.06	0.07	0.05	0.00	0.06	-0.02	0.06	0.11	0.06	0.06	-0.11	0.08	-0.02

Chapter 4

Summary and Conclusion

4.1 INTRODUCTION

The principle objectives of this thesis, as presented in Chapter One, were to define and characterize the impact melt rocks at the Mistastin Lake impact crater in Labrador; by (a) an evaluation of the significance of preserved melt rock thicknesses and the relationship between preserved melt thickness, vesicularity and crystallization temperature; (b) re-evaluation of the scale of heterogeneities in the impact melt and the relationship between entrained mineral clasts and melt composition; and (c) determination of the origin and target rock contributions of zircon clasts in the impact melt. To achieve these goals, several conditions were met, which included: a stratigraphic analysis of the impactites, petrology, geochemistry and vesicularity measurements of impact melt rocks, geochemistry and U-Pb zircon geochronology of target rocks, in addition to geochemistry, Hf-isotope geochemistry and U-Pb geochronology of zircon inclusions in the melt rocks.

4.2 SUMMARY

In order to fulfill the principle objectives of this research project, detailed field observations of impactites were completed in conjunction with, (1) major and trace element geochemistry of melt rocks and target rocks, (2) vesicularity measurements and calculations of plagioclase crystallization temperatures in melts rocks, (3) U-Pb LA-

ICPMS and isotopic chemistry of target zircon and zircon clasts in melt rocks. This section is designed to provide an overview of the principle points and conclusions in the two papers presented in chapters 2 and 3.

4.2.1 Chapter 2 – Geology and impact melt thickness of Mistastin Lake crater, Labrador.

This paper focuses on the significance of preserved impact melt at the Mistastin Lake impact crater, Labrador and its relationship with melt matrix textures through the application of field observations, petrography, vesicularity measurements and plagioclase crystallization temperature calculations. This study is important as it provides an additional method, apart from numerical modeling and experiments to estimate and understand shock induced melt production in medium-size craters with crystalline targets.

Impact melt rocks at Mistastin are preserved in discontinuous patchy outcrops distributed around the edge of the lake, which fills the inner 12 x 19 km of the 28-km wide crater. These outcrops range in thickness from <1m to 80 m. Generally the impact melt rocks overlie a series of impactites which consist of: suevite, underlain by a polymict lithic breccia, followed by a monomict breccia and, finally, a basement of shocked and fractured target rocks. Five principle melt outcrops represent a variety of melt thickness and textures. Impact melt in the thick units, such as at the 80 m-thick Discovery Hill outcrop, display crystalline, non-vesicular rocks, whereas at thinner units such as the 1-2m South Shore outcrops, display glassy, very vesicular melt rocks. These field observations define a relationship between distribution, thickness and vesicularity of melt rock units.

Measured vesicularities vary from 0.1 to 31 % and follow an empirical relationship ($\varphi = 30 \pm 2\ h^{-0.8 \pm 0.1}$) whereby vesicularity φ increases with decreasing melt rock thickness *h*. Plagioclase microlite crystallization temperatures of thin melt rock outcrops such as the South Shore are very high (>1300 °C), indicating rapid cooling rates. Lower crystallization temperatures (~1245 °C) for the Discovery Hill melt are consistent with slower cooling rates. Crystallization temperatures from moderately thick melt units fall in between the two extremes.

The main conclusions of this study are summarized below. The inter-relationships of melt rock vesicularity, crystallization temperature, and outcrop thickness documented in this study are evidence that some near-original melt thicknesses are preserved at Mistastin. This implies (1) that a coherent melt sheet of near-uniform thickness may not have formed; (2) the total volume of impact melt produced in this crater may be significantly less than the previous estimates of ~ 20 km^3, which were based on assumptions of a single coherent melt sheet that was 200 meters thick prior to erosion; and (3) that the level of glacial erosion at Mistastin (>100 m) may have been overestimated in some areas and that differential erosion did indeed occur.

4.2.2 Chapter 3 – Composition and heterogeneity of impact melt at Mistastin lake crater, Labrador.

The main focus of this paper was to consider the scale of heterogeneities in impact melt rocks and their relationship to entrained target rocks clasts at the 28 km-wide Mistastin Lake impact crater, Labrador. In addition, to determine if the origin of zircon

clasts in the impact melts can be used to estimate target rock contributions to impact melts. This study is important because compositional variations in impact melt, as well as clast distribution, help describe the intensity and extent of mixing in melt sheets and therefore help explain impact melt formation and depositional processes, all of which are not well understood.

Chemical compositions of bulk samples of thirty-three melt rocks and fourteen target rocks were measured by XRF and SN-ICPMS. Matrix compositions of nine samples of impact melt rocks were determined by EPMA and LA-ICPMS. Zircon grains from four samples of target rock and zircon clasts from three samples of impact melt rock were measured for multi-element composition, U-Pb age and Hf-isotopic composition by LA-(MC)-ICPMS.

Three principle target rocks contributed to the melt: anorthosite, mangerite and granodiorite. Impact melt rocks at Mistastin are generally anorthositic in composition. The data suggest compositional heterogeneities in the impact melts on the scales of both bulk samples and matrices. Bulk samples can be divided into compositions with high and low concentrations of high-field strength elements (HFSE; Ti, Zr, Nb) and Fe, Ba, Ce and Y. Matrix compositions of bulk samples do not show the HFSE distinction. Zircon derived from anorthosite can be distinguished from zircon from mangerite and granodiorite on the basis of higher Nb/Ta and Eu/Eu* ratios and more negative initial ε Hf values.

The main conclusions of this study are summarized below. Impact melt at Mistastin formed from ~73% anorthosite, ~7% mangerite and ~20% granodiorite, based on least-squares modeling of major element compositions of the matrices of thinner flows. This

estimate is based on matrix compositions of thin flow units that likely have been the least affected by contamination by clast entrainment and melting due to more laminar flow and lower heat capacities. We discovered that using bulk compositions to model original target rock proportions is not an accurate method. Mistastin impact melts were heterogeneous in composition at all scales – from the metre-scale outcrops (e.g., Discovery Hill vs South Shore) to micrometre-scale matrices. The heterogeneities were largely produced after impact as the melts spread outward and entrained clasts and partial to complete melts of the clasts. The micrometre-scale heterogeneities tend to be averaged out in bulk analyses of hand-sized samples of impact melt rocks. High HFSE-type melt rocks formed when impact melt entrained large quantities of clasts from mangerite, which is rich in HFSE, whereas the low HFSE melts are only affected by the introduction of low-temperature melts from the clasts to form dispersed, micron-scale silica-rich heterogeneities.

Zircon clasts greater than 40 microns in size in the impact melt rocks are dominantly or exclusively derived from mangerite and granodiorite. Hence zircon may be a poor provenance indicator for target rock contributors to impact melts.

4.3 DIRECTIONS FOR FURTHER STUDY

This thesis covers a lot of ground in terms of impact melt studies, but there is always room for improvement. To provide a more detailed analysis of melt composition and distribution, outcrops not sampled in this study, such as those inward from the southeast shore and West Point could be examined to confirm results. An absolute must to further understand the extent of the melt and impact processes at Mistastin, is a drilling

program in which several strategically placed cores are recovered from the crater floor beneath the lake to include lake sediments, breccias and melt rocks. Primarily, the aim would be determine if the impact melt is still intact with an upper vesicular zone, which would support the conclusions in chapter 2.

A structural analysis, both of the crater rim and central uplift, where possible, would be an asset to the understanding of complex crater collapse and perhaps the distribution of impactites at Mistastin. To date, no studies along or outside the crater rim have been completed to discover possible ejecta material, including fallout breccias, melt or meteorite particles.

A more precise age for the Mistastin impact event is a fundamental requirement to confirm or refute an association to other craters such as Chesapeake Bay and Popigai and the possibility at these being responsible for late Eocene extinction. This could be accomplished through U-Th/He thermochronology or fossil fission track dating in apatite or zircons.

A bathymetric study of the crater floor is essential in understanding the topography of the crater in addition to a study of glacial erosion in the area. Both would provide key evidence for the preservation of impactites and cratering processes.

References

Andrews J.T. 1982. Letters to the Editor: Comment on "New evidence from Beneath the Western North Atlantic for the Depth of Glacial Erosion in Greenland and North America" by E.P. Laine. *Quaternary Research* 17: 123-124.

Artemieva N.A.and Ivanov B.A. 2001. Numerical simulation of obliue impacts: impact melt and transient cavity size. *Lunar and Planetary Science* XXXII abstract #3021.

Best M.G. and Christiansen E.H. 2001. *Igneous Petrology*, Blackwell Science. 458 p.

Bintanja R. and van de Wal R.S.W. 2008. North American ice-sheet dynamics and the onset of 100,000-year glacial cycles. *Nature* 454: 869-872.

Bischoff A. 1981. Verhalten von Feldsplten unterschiedlither Stosswellenmetamorphose in der Impaktschmelze von Lappajärvi, Finnland. Diploma Thesis, Westf. Wilh.Universitlt, Mtinster, FRG.

Blichert-Toft J. and Albarède F. 1997. The Lu-Hf isotope geochemistry of chondrites and the evolution of the mantle-crust system. *Earth and Planetary Science Letters* 148(1-2): 243-258.

Blower J.D., Mader H.M. and Wilson S.D.R. 2001. Coupling of viscous and diffusive controls on bubble growth during explosive volcanic eruptions. *Earth and Planetary Science Letters* 193:47-56.

Boamah D. and Koeberl C. 2006. Petrographic studies of "fallout" suevite from outside the Bosumtwi impact structure, Ghana. *Meteoritics & Planetary Science* 41(11): 1761-1774.

Bottinga Y. and Weill D.F. 1970. Densities of liquid silicate systems calculated from partial molar volumes of oxide components. *American Journal of Science* 269:169-182.

Bringemeier D. 1994. Petrofabric examination of the main suevite of the Otting Quarry, Nördlinger Ries, Germany. *Meteoritics* 29(3): 417-422.

Bryan W.B., Finger L.W. and Chayes F. 1969. Estimating proportions in petrographic mixing equations by least-squares approximation. *Science* 163: 926-927.

Carslaw H.S. and Jaeger J.C. 1959. *Conduction of heat in solids*, 2nd ed., Oxford: Clarendon Press. 510 p.

Chen M. and El Goresy A. 2000. The nature of maskelynite in shocked meteorites; not diaplectic glass but a glass quenched from shock-induced dense melt at high pressures. *Earth and Planetary Science Letters* 179(3-4): 489-502.

Cheng H.C., and Lemlich R. 1983. Errors in measurement of bubble size distribution in foam. *Industrial Engineering Chemistry Fundamentals* 22: 105-109.

Cintala M.J. and Grieve R.A.F. 1994. The effects of differential scaling of impact melt and crater dimensions on lunar and terrestrial craters: Some brief examples. In *Large Meteorite Impacts and Planetary Evolution.* (Dressler B.O., Grieve R.A.F and Sharpton V.L., eds.)*Geological Society of America* Special Paper 293, 51-59.

Cluzel N., Laporte D., Provost A., and Kannewischer I. 2006. An experimental study of heterogeneous bubble nucleation in oxide-bearing rhyolitic magmas. *Geophysical Research Abstracts* 8, 06111.

Croft S.K. 1985. The scaling of complex impact craters. *Proceedings in Lunar and Planetary Science Conference* 15: 828-842.

Currie K. L. 1971. Geology of the resurgent cryptoexplosion crater at Mistastin Lake, Labrador. *Bulletin - Geological Survey of Canada* 207, 62 p.

Delmas M., Calvet M. and Gunnell Y. 2009. Variability of Quaternary glcial erosion rates – A global perspective with special reference to the Eastern Pyrenees. *Quaternary Science Reviews* 28: 484-498.

Dence M.R. 1968. Dence M. R. 1968. Shock zoning at Canadian craters: Petrography and structural implications. In *Shock Metamorphism of Natural Materials* (B. M. French and N. M. Short, eds.), Mono Book Corp., Baltimore pp. 169–184.

Dence M.R. 1971. Impact melts. *Journal of Geophysical Research.* 76(23): 5552-5565.

Dence M.R., Grieve R.A.F and Robertson P.B. 1977. Terrestrial impact structures: Principle characteristics and energy considerations. In *Impact and Explosion Cratering* (eds. D.J. Roddy, R.O. Pepin and R.B.Merrill) pp.247-275. Pregamon Press, New York.

Deutsch, A., Grieve, R. A. F., Avermann, M., Bischoff, L., Brockmeyer, P., Buhl, D., Lakomy, R., Müller-Mohr, V., Ostermann, M., and Stöffler, D. 1995. The Sudbury Structure (Ontario, Canada): a tectonically deformed multi-ring impact basin: Geologische Rundschau 84: 697-709.

Dressler, B.O. and Reimold, M.U., 2001. Terrestrial impact melt rocks and glasses. *Earth-Science Reviews* 56: 205-284.

Dubé B., Dunning G.R., Lauziere K. and Roddick J.C. 1996. New in-sights into the Appalachian orogen from geology and geochronology along the Cape Ray fault zone southwest Newfoundland. *Geol. Soc. Am. Bull.,* 108: 101-116.

Eldrett J.S., Harding, I.C., Wilson P.A., Butler E. and Roberts A.P. 2007. Continental ice in Greenland during the Eocene and Oligocene. *Nature* 446: 176-179.

Emslie R.F., Cousens B., Hamblin C. and Bielecki J. 1980. The Mistastin batholith, Labrador-Quebec: An Elsonian composite rapakivi suite; in Current Research Part A, Geological Survey of Canada paper 80-1A: 95-100.

von Engelhardt W. 1997. Suevite breccia of the Ries impact crater, Germany: Petrography, chemistry and shock metamorphism of crystalline rock clasts. *Meteoritics* 32: 454-554.

Floran, R.J., Grieve, R.A.F., Phinney, W.C., Warner, J.L., Simonds, C.H., Blanchard, D.P. and Dence, M.R., 1978. Manicouagan impact melt, Quebec, 1, Stratigraphy, Petrology, and Chemistry. Journal of geophysical Research. 83 (B6), 2737-2759.

French, B. M. 1998. *Traces of Catastrophe: A Handbook of Shock-Metamorphic Effects in Terrestrial Meteorite Impact Structures*. LPI Contribution No. 954, Lunar and Planetary Institute, Houston 120p.

Gardner J. E. 2007. Heterogeneous bubble nucleation in highly viscous silicate melts during instantaneous decompression from high pressure. *Chemical Geology* 236: 1-12.

Gardner J. E., Thomas R. M. F., Jaupart C., and Tait S. 1996. Fragmentation of magma during volcanic plinian eruptions. *Bulletin Volcanology* 58: 144-162.

Gardner J. E., Hilton M., and Carroll M. R. 2000. Bubble growth in highly viscous silicate melts during continuous decompression from high pressure. *Earth and Planetary Science Letters* 168: 201-218.

Gerdes, A. and Zeh, A., 2008. Zircon formation versus zircon alteration – New insights from combined U-Pb and Lu-Hf in-situ LA-ICP-MS analyses, and consequences for the interpretation of Archean zircon from the Central Zone of the Limpopo Belt. Chemical Geology (in press).

Gill J.B., 1981. Orogenic Andesites and Plate Tectonics. Berlin: Springer

Grieve R. A. F. 1975. Petrology and chemistry of impact melt at Mistastin Lake crater, Labrador. *Geological Society of America Bulletin* 86:1617-1629.

Grieve R. A. F., Dence M. R., and Robertson P. B. 1977. Cratering process: As interpreted from the occurrence of impact melts. In *Impact and Explosion Cratering: Planetary and Terrestria Implications* (D. J. Roddy, R. O. Pepin, and R. B. Merrill, eds.), pp. 791–814. Pergamon, New York.

Grieve R. A. F. and Cintala M. J. 1981. A method for estimating the initial impact conditions of terrestrial cratering events, exemplified by its application to Brent crater, Ontaio. Proceedings in Lunar and Planetary Science Conf. 12:1607-1621.

Grieve R. A. F. and Cintala M. J. 1992. An analysis of differential impact melt-crater scaling and implications for the terrestrial impact record. *Meteoritics* 27: 526-538.

Grieve R. A. F. 2006. Mistastin, Chapter 16. In *Impact Structures in Canada*, Earth Sciences Sector Natural Resources Canada, Geological Association of Canada, pp.115-120.

Grieve R.A.F. 1978. Terrestrial Impact Structures. Annual Review in *Earth and Planetary Science* 15: 245-270.

Grieve R.A.F., Reny1 G., Gurov E.P. and Ryabenko V.A., 1987. The melt rocks of the Boltysh impact crater, Ukraine, USSR. Contributions to mineralogy and petrology 96(1), 56-62.

Guillong M., Hametner K., Reusser E., Wilson S.A. and Günther D. 2005. Preliminary characterisation of new glass reference materials (GSA-1G, GSC-1G, GSD-1G and GSE-1G) by laser ablation-inductively coupled plasma-mass spectrometry using 193 nm, 213 nm and 266 nm wavelengths. *Geostandards and Geoanalytical Research* 29: 315-331.

Gurov E.P., Gurova E.P. and Sokur T.M. 2002. Petrography of the Zapadnaya impact crater in the Ukranian Shield. In *Impact in Precambrian Shields*. (Plato J. and Pesonene L.J., eds.), Springer.

Gurov E.P., Kelly S.P., Koeberl C. and Dykan N.I. 2006. Sediments and impact rocks filling the Boltysh impact crater. In *Biological Processes with Impact Events* (eds. Cockell C., Koeberl C. and Gilmour, L.) Impact Studies, Springer p.335-358.

Hallet B., Hunter L. and Bogen J. 1996. Rates of erosion and sediment evacuation by glaciers: A review of field data and their implications. *Global and Planetary Change* 12: 213-235.

Hartmann W. K., Quantin C. and Mangold N. 2007. Possible long-term decline in impact rates 2. Lunar impact-melt data regarding impact history. *Icarus* 186: 11–23.

Heiken G.H., Vaniman D.T. and French B.M. 1991. The Lunar Sourcebook: A User's Guide to the Moon. Cambridge University Press, Lunar and Planetary Institute. pp.736.

Hiesinger H. and Head III J.W. 2006. New Views of Lunar Geoscience: An Introduction and Overview. *Reviews in Mineralogy & Geochemistry* 60: 1-81.

Holsapple K.A. and Schmidt R.M. 1987. Point Source Solutions and Coupling Parameters in Cratering Mechanics. *Journal of Geophysical Research* 92 (B7): 6350-6376.

Hurwitz S. and Navon O. 1994. Bubble nucleation in rhyolitic melts: Experiments at high pressure, temperature and water content. *Earth Planet Sci. Lett.* 122: 267-280.

Irvine T.N. and Baragar W.R.A. 1971. A guide to the chemical classification of the common volcanic rocks. *Canadian Journal of Earth Sciences* 8: 523-548.

Keil K., Stöffler D., Love S.G., Scott R.D. 1997. Constrains on the role of impact heating and melting in asteroids. *Meteoritics and Planetary Science* 32: 349–363.

Kieffer S.W. and Simonds C.H. 1980. The role of volatiles and lithology in the impact cratering process. *Reviews of Geophysics and Space Physics* 18: 143–181.

Klassen R.A. and Thompson F. J. 1990. Glacial history, drift composition, and till geochemistry, Labrador; Geological Survey of Canada. Open File 2170.

Košler, J., Fonneland, H., Sylvester, P., Tubrett, M. and Pederson, R., 2002. U-Pb dating of detrital zircons for sediment provenance studies: a comparison of laser-ablation ICPMS and SIMS techniques. *Chemical Geology* 182: 605-618.

Krogh T.E. 1982. Improved accuracy of U-Pb ages by the creation of more concordant systems using an air abrasion technique. *Geochimica et Cosmochimica Acta* 46: 617-649.

Laine E.P. 1980. New evidence from beneath the western North Atlantic for the depth of glacial erosion in Greenland and North America, 1980. *Quaternary Research.* 14: 188-198.

Lambert P. 1981. Reflectivity applied to peak pressure estimates in silicates of shocked rocks, *J. Geophys. Res.* 86: 6187-6204.

Lambert P. and Grieve R.A.F. 1984. Shock experiments on maskelynite-bearing anorthosites. *Earth and Planetary Science Letters,* 68(159): 171-159

Lambert P. 2008. Impact deposits at Rochechouart-Chassenon. Proceedings, Large Meteorite Impacts and Planetary Evolution IV. (abstract #3034)

Lana C., Romano R., Reimold U. and Hippertt J. 2006. Collapse of large complex impact craters: Implications from the Araguainha impact structure, central Brazil. *Geological Society of America* 34 (1): 9-12.

Langenhorst F. and Deutsch A. 1994. Shock experiments on pre-heated α- and β-quartz: I. Optical and density data. Earth and Planetary Science Letters. 125: 407-420.

Le Bas M.J., Le Maitre, R.W., Streckeisen, A. and Zanettin, B.A., 1986. Chemical classification of volcanic rocks based on the total alkali-silica diagram. Journal of Petrology. 27(3), 745-750.

Lensky N.G. Navon O., and Lyakhovsky V. 2004. Bubble growth during decompression of magma: experimental and theoretical investigation. *Journal of Volcanology and Geothermal Research* 129: 7-22.

Ludwig, K.R. 2003. User's manual for Isoplot 3.00. A Geochronological Toolkit for Microsoft Excel. Berkeley Geochronology Center Special Publication, vol. 4a. Berkeley, California 70. (www.bgc.org/isoplot_etc/software.html).

Mak E. K., York D., Grieve R. A. F., and Dence M. R. 1976. The age of the Mistastin Lake crater, Labrador, Canada. *Earth and Planetary Science Letters* 31(3): 345-357.

Mangan M.T. and Cashman K.V. 1996. The structure of basaltic scoria and reticulate and inferences for vesiculation, foam formation, and fragmentation in lava fountains. *Journal of Volcanology and Geothermal Research* 73:1-18.

Marchand, M. and Crocket, J.H. 1977. Sr isotope and trace element geochemistry of the impact melt and target rocks at the Mistastin Lake crater, Labrador. *Geochimica et Cosmochimica Acta* 41: 1487-1495.

Marine Geoscience Data System, Geomapapp. A data exploration and visualization tool. Accessed August 27, 2008. http://www.geomapapp.org/

Marion C.L. and Sylvester P.J. (submitted). Composition and heterogeneity of impact melt at Mistastin Crater, Labrador. *Planetary and Space Science*.

Marion C.L., Sylvester P.J. and Leitch A.M. (in revision): Geology and impact melt thickness of Mistastin Lake crater, Labrador. Meteoritics and Planetary Science

Marvin U.B. 1990. Impact and its revolutionary implications for geology. In *Global Catastrophes in Earth's History*, (Sharpton V.L. and Ward P.D., eds.) Geological Society of America, Special Paper 247, 147-154.

Masaitis, V. L., 1994, Impactites from Popigai crater, In *Large meteorite impacts and planetary evolution* (Dressler, B. O., Grieve, R. A. F., and Sharpton, V. L., eds.) Geological Society of America Special Paper, 293:153-162.

Masaitis V.L. 1999. Impact structures of northeastern Eurasia: the territories of Russia and adjacent countries. *Meteoritics and Planetary Science* 34: 691–711.

Masaitis V.L., Naumov M.V. and Mashchak M.S. 1999. Anatomy of the Popigai impact crater, Russia. In *Large Meteorite Impacts and Planetary Evolution II* (B.O. Dressler and V.L. Sharpton, eds.), *Geological Society of America*, Special Paper 339: 1–17.

Masaitis V.L., Naumov M.V. and Mashchak M.S. 2005. Original diameter and depth of erosion of the Popigai impact crater, Russia. In *Large Meteorite Impacts III* (eds. Kenkman T., Hörz F. and Deutsch A.) Geological Society of American Special Paper 384: 131-140.

Melosh H.J. 1989. Impact Cratering: A Geologic Process: Oxford University Press, New York, 245p.

McCormick, K.A., Taylor, G.J., and Keil, K., 1989. Sources of Clasts in Terrestrial Impact Melts: Clues to the Origin of LKFM. Proceedings of the 19th Lunar and Planetary Science Conference. 691-696.

Morgan J.W., Higuchi H., Ganapathy R. and Anders E. 1975. Meteoritic material in four terrestrial meteorite craters. *Proceedings Lunar and Planetary Conference*. 6: 1609-1623.

Morris A. R., Head J.W., Margot J.-L. and Donald B.C. 2000. Impact melt distribution and emplacement on Tycho: a new look at an old question. *Lunar and Planetary Science* 31. abstract #1828.

Murase T. and McBirney A.R. 1973. Properties of some common igneous rocks and their melts at high temperatures. *Geological Society of America Bulletin* 84:3563-3592.

Neal C.R. (in press) The Moon 35 years after Apollo: What's left to learn? Chemie der Erde - Geochemistry, In Press, Corrected Proof, Available online 6 December 2008

Newsom H. E. and Hagerty J. J. 2003. Evidence for impact-induced hydrothermal alteration at the Lonar Crater, India, and Mistastin Lake, Canada (abstract #4116). Third International Conference on Large Meteorite Impacts, Nördlingen.

O'Keefe J.D. and Ahrens T.J. 1977. Impact-induced energy partitioning, melting, and vaporization on terrestrial planets. *Proceedings in Lunar and Planetary Science Conference*. 8: 3357-3374.

O'Keefe J.D. and Ahrens T.J. 1993. Planetary Cratering Mechanics. *Journal of Geophysical Research* 98(E9): 17011-17028.

Onorato P.I.K., Uhlman D.R. and Simonds C.H. 1978. The Thermal History of the Manicouagan Melt Sheet, Quebec. *Journal of geophysical Research*. 83 (B6): 2789-2798.

Osinski G.R. 2004. Impact melt rocks from the Ries structure, Germany: an origin as impact melt flows? *Earth and Planetary Science Letters* 226: 529– 543.

Osinski G.R., Spray J.G., Grieve R.A.F. 2008. Impact melting in sedimentary target rocks: An assessment. In: Evans, K., Horton,W., King, D., Morrow, J.,Warme, J. (Eds.), *The Sedimentary record of meteorite impacts*. Geological Society of America, Special Paper 437. doi:10.1130/2008.2437(01).

Palme H., Göbel E. and Grieve R.A.F. 1979. The distribution of volatile and siderophile elements in the impact melt of East Clearwater (Québec). *Proceedings Lunar and Planetary Science Conference* 10: 2465-2492.

Palme, H., Grieve, R.A.F. and Wolf R. 1981. Identification of the projectile at Brent crater, and further considerations of projectile types at terrestrial craters. *Geochimica et Cosmochimica Acta* 45: 2417-2424.

Palme H., Janssens M.-J., Takahashi H., Anders E. and Hertogen J. 1978. Meteoritic material at five large impact craters. *Geochimica et Cosmochimica Acta* 42: 313-323

Parrish, R.R. 1987. An improved micro-capsule for zircon dissolution in U-Pb geochronology. *Chemical Geology* 66: 99-102.

Pearce, N.J.G., Perkins, W., Westgate, J.A., Gorton, M.P., Jackson, S.E., Neal, R.N., and Chenery, S.P., 1996. A compilation of new and published major and trace element data for NIST SRM 610 and NIST SRM 612 Glass Reference Materials. Geostandards Newsletter 21(1): 115-144.

Peck D.L., Hamilton M.S. and Shaw H.B. 1977. Numerical analysis of lava lake cooling models, I, Description of the method. *American Journal of Science* 277: 384-414.

Phinney W. C., Simonds C. H., Cochran A. and McGee P.E. 1978. West Clearwater, Québec impact structure, Part II: Petrology. *Proceedings of Lunar and Planetary Science Conference* 9: 2659-2693.

Phinney W. C. and Simonds C. H. 1977. Dynamical implications of the petrology and distribution of impact melt rocks. In *Impact and Explosion Cratering* (eds D.J. Roddy, R.O. Pepin and R.B. Merrill), pp.771-790. Pergamon Press, New York.

Pierazzo E. and Melosh H.J. 2000. Understanding oblique impacts from experiments, observations and modeling. *Annual Reviews of Earth and Planetary Science* 28:141-167.

Pierazzo, E., Vickery, A.M., and Melosh H.J., 1997. A reevaluation of impact melt production. *Icarus* 127, 408–423.

Pipping F. and Lehtinen M. 1992. Geology, stratigraphy and structure of the Lappajärvi meteorite crater, western Finland: preliminary results of deep drilling. *Tectonophysics* extended abstract 216: 91-97.

Potts, P.J., 1987: X-ray Fluorescence analysis: Principles and practice of wavelength dispersive spectrometry, chapter 8 in A Handbook of silicate rock analysis. Blackie Academic & Professional, Chapman Hall, Great Britain.

Putirka K. 2005. Igneous thermometers and barometers based on plagioclase + liquid equilibria: Tests of some existing models and new calibrations. *American Mineralogist* 90: 336-346.

Raup D.M. 1991. Extinction: Bad genes or bad luck? Norton, New York 210 p.

Reimold W.U. 1982. The Lappajärvi meteorite crater, Finland: petrography, Rb-Sr, major and trace element geochemistry of the impact melt and basement rocks. *Geochimrca et Cosmochimica Acta* 46: 1203-1225

Reimold W.U., Grieve R.A.F. and Palme H. 1981. Rb-Sr dating of the impact melt from East Clearwater, Québec: *Contributions to Mineralogy and Petrology* 76: 73-76.

Rollinson H.R. 1993. Using Geochemical Data: Evaluation, Presentation, Interpretation. Longman Scientific & Technical, UK.

Ryan B. and James D. 2004. The Mesoproterozoic Nain Plutonic Suite and its country rocks in the Kingurutik LakeFraser River area, Labrador (NTS 14D/9 and 16), in Current Research, Newfoundland Department of Mines and Energy, Geological Survey, Report 04-1, p. 235-258.

Ryder G., Norman M.D., and Taylor G.J., 1997. The complex stratigraphy of the highland crust in the Serenitatis region of the Moon inferred from mineral fragment chemistry. Geochimica et Cosmochimica Acta, 61, 1083-1105.

Sato M. 1976. Oxygen fugacity and other thermochemical parameters of Apollo 17 high Ti basalts and their implications on the reduction mechanism. Proc. Lunar Science Conference 7th. pp.1323-44.

Scherer, E.,* Münker, C., Mezger, K., 2001. Calibration of the Lutetium-Hafnium Clock. Science 27 July 2001: 293(5530), 683 – 687.

Schlichting H. 1968. *Boundary layer theory*, New York: McGraw Hill. 817p.

Schmidt R.M. and Holsapple K.A. 1982. Estimates of crater size for large-body impact: Gravity scaling results. *Geological Society of America* Special paper 190: 93-102.

Schmidt R.M. and Housen K.R. 1987. Some recent advances in the scaling of impact and explosion cratering. *International Journal of Impact Engineering*. 5: 543-560.

Schuraytz B.C., Sharpton V.L. and Marin L.E., 1994. Petrology of the impact melt rocks at the Chicxulub multiring basin, Yucatán, Mexico. Geology 22: 868-872.

Shah A.K., Brozena J., Vogt P., Daniels D. and Plescia J. 2005. New surveys of the Chesapeake Bay impact structure suggest melt pockets and target-structure effect. *Geology* 33: 417-420.

Simonds, C. H., Phinney, W. C., McGee, P. E., and Cochran, A., 1978. West Clearwater, Quebec impact structure, Part I: Field geology, structure and bulk chemistry: Lunar and Planetary Science Conference, 9th, Proceedings 2: 2633-2658.

Spray J.G. and Thompson L.M. 2008. Constraints on central uplift structure from the Manicouagan impact crater. *Meteoritics and Planetary Science* 43(12): 2049-2057.

Stacey, J.S. and Kramer, J.D. 1975. Approximation of terrestrial lead isotope evolution by a two stage model. *Earth Planetary Sciences Letters* 26: 207-221.

Stöffler D., Artemieva N., Ivanov B.A., Hecht L., Kenkmann T., Schmitt R.-T., Tagle R.A. and Wittmann A. 2004. Prigin and emplacement of the impact formations at Chicxulub, Mexico, as revealied but the ICDP deep drilling at Yaxcopoil-1 and by numerical modelling. *Meteoritics and Planetary Science* 39(7): 1035-1067.

Stöffler D., Bischoff L., Oskierski W., and Wiest B. 1988. Structural deformation, breccia formation, and shock metamorphism in the basement of complex terrestrial impact craters: implications for the cratering process. In *Deep Drilling in Crystalline Bedrock, Vol. 1: The Deep Gas Drilling in the Siljan Impact Structure, Sweden and Astroblemes*. (A. Bodén and K.G. Eriksson eds.), pp. 277-297. Springer-Verlag, New York.

Stöffler D. and Grieve R. A. F. 2007a. Impactites. In *Metamorphic Rocks: A Classification and Glossary of Terms.* D. Fettes and J. Desmons ed. Cambridge University Press. p.82.

Stöffler D. and Grieve R. A. F. 2007b. Impactites: Recommendations by the IUGS Subcommission on the Systematics of Metamorphic Rocks: Web version 01.02.07. http://www.bgs.ac.uk/SCMR/docs/papers/paper_11.pdf

Sugden, D. E. 1976a. Glacial Erosion by the Laurentide Ice Sheet and its relationships to ice, topographic and bedrock conditions. Department of Geography, University of Aberdeen, Aberdeen.

Sugden D.E. 1976b. A case against deep erosion of shields by ice sheets. *Geology*. 4: 580-582

Taylor F.C. 1975. Geology, Mistastin Lake area, Newfoundland-Quebec; Geological Survey of Canada, Map 1442A.

Taylor F.C. and Dence M.R.1969. A probable meteorite origin for Mistastin Lake, Labrador, *Canadian Journal of Earth Sciences* 6: 39-45.

Tuchscherer, M.G., Reimold, W.U., Gibson, R.L., de Bruin, D., Späth, A., 2006. Major and trace element compositions of melt particles and associated phases from the Yaxcopoil-1 drill core, Chicxulub impact structure, Mexico. Meteoritics & Planetary Science 41: 1361-1379.

Weaire D. and Hutzler S. 1999. *The physics of foams*, Oxford: Clarendon Press.246p.

White W.A., 1972. Deep erosion by continental ice sheets. *Geological Society of America Bulletin* 83: 1037-1056.

Whitehead J., Spray, J.G., and Grieve R.A.F. 2002. Origin of "toasted" quartz in terrestrial impact structures. *Geology* 30(5): 431-434.

Witmann, A., Kenkmann, T., Schmitt, R.T., and Stöffler D. 2006. Shock-metamorphosed zircons in terrestrial impact craters. Meteoritics and Planetary Science 41(3): 433-454.

Wohletz K. H.1999. MAGMA: Calculates IUGS Volcanic Rock Classification, Densities, and Viscosities. Los Alamos National Laboratory computer code LA-CC 99-28, Los Alamos New Mexico. URL http://geont1.lanl.gov/Wohletz/Magma.htm.

Wright T.L. and Doherty P.C. 1970. A linear-programming and least-squares computer method for solving petrologic mixing problems. *Geological Society of America Bulletin* 81: 1995-2008

Zieg M.J. and Marsh B.D. 2005. The Sudbury Igneous Complex: Viscous emulsion differentiation of superheated impact melt sheet. *Geological Society of America Bulletin* 117: 1427-1450.

Appendix A

Analytical Methods and Additional Geochemical Data

A.1 ARCHIMEDES METHOD

The following is a detailed description of the Archimedes method applied to determine the vesicularity of the bulk melt rock in Chapter 2.

Step One: Weigh dry rocks

The dry melt rocks and various 'counterweight' rocks (see below) were weighed on a benchtop electrical scale (Denver Instruments TR8102D) which has an accuracy and precision of ±0.01 g.

Ex: $M_R = 781.05g$

$M_{CW} = 3707.70g$

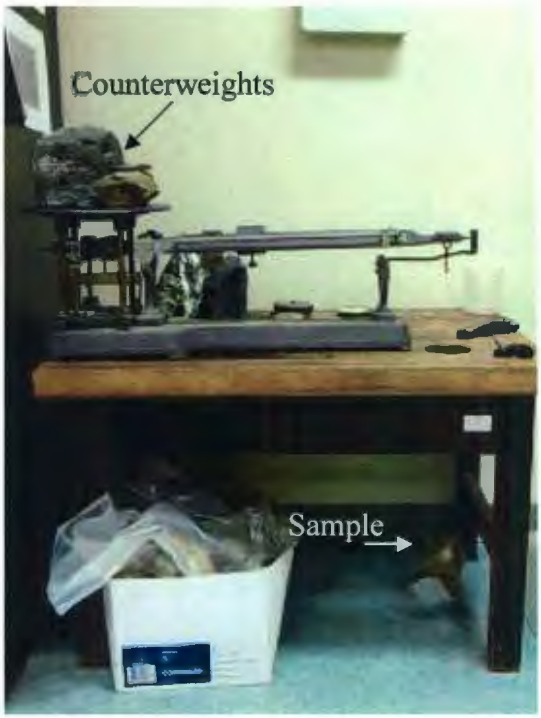

Figure A.1. Ohaus triple beam balance showing the setting for the Archimedes method.

Step Two: Find the balance factor F for the manual triple beam balance.

In simple terms, the balance consists of a bar balanced on a fulcrum. The two arms of the bar on either side of the fulcrum are of unequal length. The unknown weight is normally placed on the pan, on the short arm of the bar. The weight is then determined by sliding calibrated weights along a scale on the long arm until balance is achieved. To extend the range of the balance, extra calibrated counterweights can be suspended from the end of the long arm. Because the arms are of unequal length, the nominal value of the counterweight (e.g., "1 kg", required to balance a 1 kg load on the pan) is less than its actual weight. The ratio of the actual to the nominal weight, the "balance factor" F, is related to the ratio of the lengths of the long and the short arms.

For practical reasons, our measurements are made by suspending the unknown weight from the long arm of the bar instead of placing it on the pan. In a sense we are using the balance backwards, and so we need to determine F.

First, we place one known weight M1 on the balance pan and tie another known weight M2 on a string to hang on the end of the long arm. We then level the balance and record the measurement Msc on the sliding scales. The difference, M1', is the effective weight (in grams) on the short arm of the balance.

Ex:	M1 (on balance pan)	3707.70g
	Msc (Scale measurement)	- 297.25g
	M1'	= 2410.45g

We then take this number and divide it by the balancing known weight M2 to find F.

Ex:	M1' (effective pan weight)	2410.45g
	M2 (weight hanging from long arm)	÷ 781.05g

$F = M1'/M2 \qquad = 4.37$

F can then be used to find M2 when it is unknown (see below).

Step Three: Measure the weight of the rock in water.

We hang the rock from the end of the long arm by thin fishing line, add known counterweight (M1) onto the pan, and submerge the rock into water (in a bucket lying beneath the scale) making sure that the line and rock do not touch the sides of the bucket. We then balance the scale. The weight of the submerged rock plus the string is equal to the effective pan weight M1' (counterweight M1 minus scale measurement Msc) divided by the factor F.

Ex:

M1 (counterweight on balance pan)	= 2082.58g
Msc (scale measurement)	- 109g
M1' (effective pan weight)	1973.58g
Factor F	÷ 4.37

Weight of the submerged rock+string = 451.62g

We then make a correction for the weights of the string and water absorbed by the rock (e.g. by lichen). An estimate of the water absorbed by the rock is found by weighing the wet rock after it has been removed from the bucket, shaken and patted dry to remove surface wetness.

Ex:

Weight of the submerged rock+string	= 451.62g
Different between wet and dry rock	- 7.42g
Weight of the string	- 0.12g

Corrected weight of submerged rock, M_w: 444.08g

Note that the difference between the weights of the rock in air and water is equal to the weight of the displaced water (Archimedes Principle). The displaced volume is the

volume as the rock. Since the density of water is $1 g/cm^3$, this measurement yields the volume of the rock in cm^3.

Step Four:

Determine the volume V, density ρ and vesicularity φ of the rock by using the following equations:

(1) Volume, V = Weight in air, M_a – Weight in water, M_w

(2) Density, $\rho = M_a/V$

(3) Vesicularity, φ = the volume of vesicles divided by the total volume V.

This becomes:

$$\varphi = 1-(\rho_{rock} / \rho_{matrix})$$

where ρ_{matrix} is ascertained using Magma software and XRF data of each particular rock sample.

Ex: (1) $V_t = M_a - M_w = 781.05 - 444.08 = 336.97$

(2) $\rho = M_a / V_{total} = 781.05 / 336.97 = 2.32$

(3) Vesicularity $\varphi = 1-(\rho_{rock} / \rho_{matrix}) = 1-(2.32/2.5) = 0.073$

To convert to %, φ is multiplied by 100. In this example, the vesicularity is 7.3%.

A.2 U-Pb DATING OF ZIRCONS BY THERMAL IONIZATION MASS SPECTROMETRY (TIMS)

Introduction

Sample W05-57 was collected by Derek Wilton in a field excursion to Mistastin in 2005. Large blocks of this rock type are observed in a subvertical sequence on the east and west side of Cote Creek in the polymict lithic breccias. The sample is a highly shocked fragment of one of the main target rocks. No bulk chemical analysis were completed on this sample but microprobe analyses of the irregular matrix reveals plagioclase compositions (Appendix C). As mentioned in chapter 2 (Fig. 2.8A), the quartz and feldspar have been converted to diaplectic glasses (lechatelierite and maskelynite, respectively) which indicates shock pressures of >35 GPa (Stöffler and Grieve, 2007). Planar deformation features have also been observed in several zircon grains (Fig 2.5A).

Analytical Method

Isotope Dilution-Thermal Ionization Mass Spectrometre (ID-TIMS) analyses were performed at Memorial University of Newfoundland, Canada. Normal transmitted and reflected light microscopy as well as SEM back-scattered imagery were used to determine the zircon internal structures prior to analysis. Zircons were separated first by crushing in a disc mill, followed by the use of a Wilfley table to discard fine particles and light minerals. Further separation was completed with heavy liquids and a Frantz magnetic separator. Zircons were handpicked from the heavy mineral separate and were abraded (Krogh, 1982) and then washed in dilute nitric acid and ultra-pure acetone. Single grains

or small populations of zircons were then placed into 0.35 ml Teflon vials together with 30 µl HF and a mixed ^{205}Pb-^{235}U spike. Eight of these Teflon vials were then placed in a Parr Container for 2 days at 210°C (Parrish, 1987).

After two days in the oven, the Teflon vials were cooled down, then their content was dried out on a hot plate. Once dried, 10 drops of 3.1N HCl was added to each vial. All the vials were put back inside the Parr Container and left in the oven at 210 °C overnight. The vials were then cooled down. Separation of Pb and U was performed with micro-columns and ion-exchange resin AG1X8 following the technique described in Dubé *et al.* (1996).

The samples were measured on a Finnigan MAT262 mass spectrometre equipped with an ion-counting secondary electron multiplier. The calculation of common Pb was made by subtracting blanks and then assuming that the remaining common Pb has a Proterozoic composition determined from the model of Stacey and Kramers (1975). Data were reduced using PbDat (Ludwig, 2003). Analytical uncertainties are listed at 2σ and age determinations were processed using Isoplot/Ex (Ludwig, 2000).

Results

Reversely discordant grains, grains with very large errors and contaminant grains from mineral separation were discarded. The remaining three analyses show a discordant age of 1382 ± 16 Ma (2σ) (Fig. A.1A).

Discussion

The granodiorite target zircons have an age of 1429 ±10 Ma (2σ) (Chapter 3 by U-Pb LA-ICPMS) so clearly there is a discrepancy. This may be due to whole grain age averaging of zircons with the TIMS compared to spot analysis by LA-ICPMS if the rims of the grains are much younger. Other possibilities include a partial resetting of the U-Pb system by the heat of the Mistastin impact or that shock metamorphism causes additional lead loss. A second concordia plot (Fig A.1B below), anchored to the age of the impact, however, gives almost exactly the same result as when the discordia is forced through the origin. If a simple least squares line is fit to the three data points from the TIMS data however, the data show an upper intercept age of 1417 ± 230 Ma and a meaningless lower intercept age of 955 ± 1800 Ma. Unfortunately this data can't be used given the large errors.

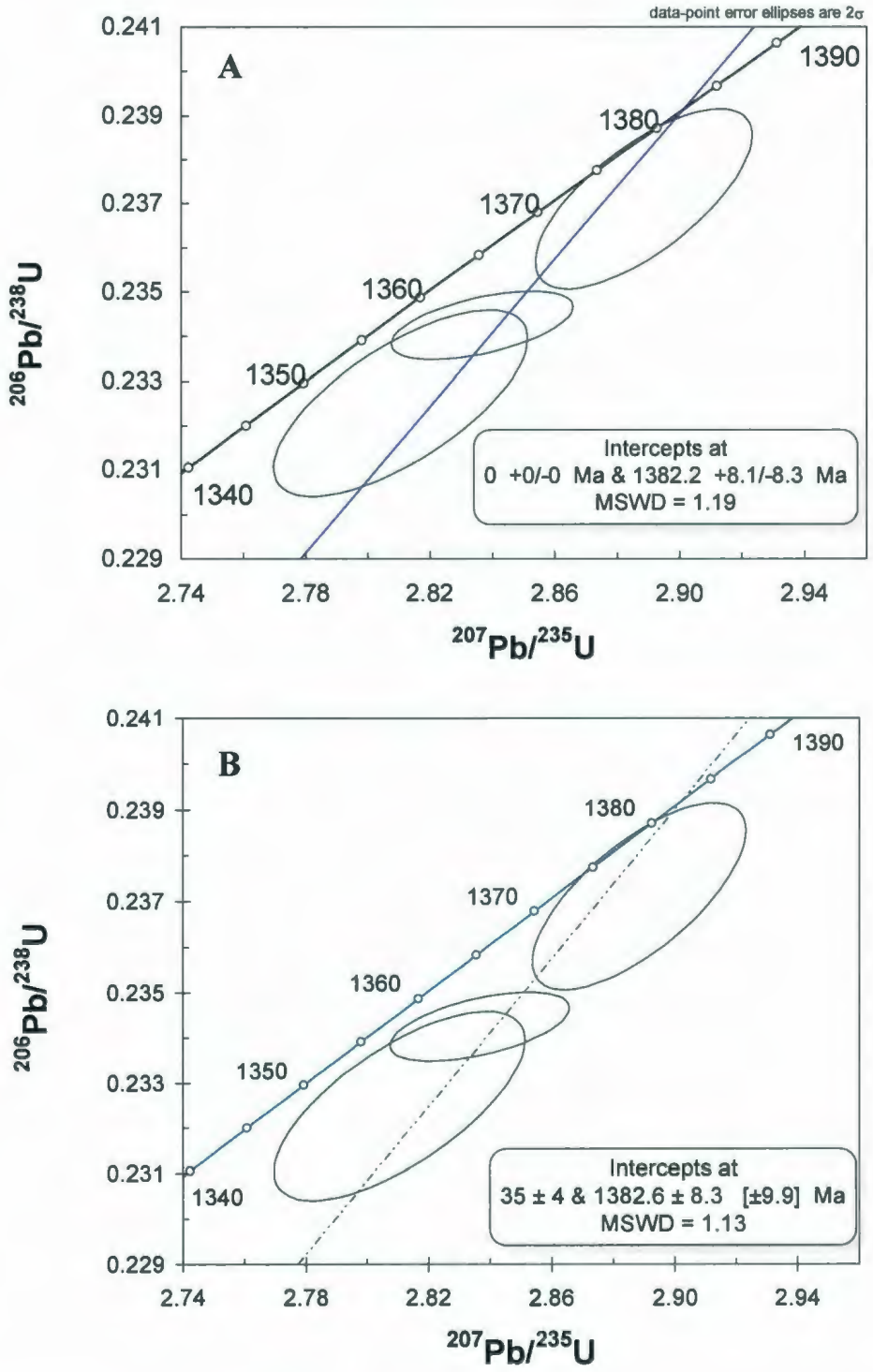

Figure A.2. Concordia plots for zircons from sample W05-57, a polymict lithic breccia at Coté Creek. A) Shows a discordant age with an intercept at the origin where B) shows a discordant age with the intercept at 35± 4 Ma, the age of the impact (Mak et al. 1976).

A.3 MICROPROBE ANALYSIS OF FELDSPARS

To help determine the role of clasts in impact melts, feldspar minerals in the target rocks and as clasts in melt rocks were analyzed. Analyses were completed on the JEOL JXA-733 Superprobe at the University of New Brunswick, Canada, with a 3 μm beam at 15kV and 20nA. The resulting data from these analyses were not detailed in this study as McCormick et al. (1989) completed a much more comprehensive analysis and conclusions. Which are that the clast proportions do not necessarily represent target rock contributions in impact melts. This is in agreement with zircon results in chapter 3.

Table A.1. Microprobe analysis of target rock feldspar.

Sample	SiO_2	Al_2O_3	FeO	CaO	Na_2O	K_2O
CM004	60.24	24.53	0.03	6.55	7.83	0.23
CM004	60.62	24.19	0.05	6.18	8.00	0.18
CM004	64.63	18.40	0.01	0.05	1.17	14.79
CM004	64.75	18.34	0.05	0.03	1.54	14.28
CM004	65.12	18.40	0.05	0.02	1.46	14.48
CM031	58.28	26.08	0.12	8.40	6.64	0.40
CM031	58.98	25.44	0.17	7.69	6.97	0.40
CM031	58.42	26.55	0.17	8.82	6.44	0.43
CM031	58.37	25.98	0.16	8.38	6.53	0.44
CM010	64.54	18.46	0.00	0.03	0.85	15.25
CM010	62.34	23.94	0.08	5.49	8.58	0.24
CM010	61.16	24.50	0.14	6.26	8.07	0.31
CM010	61.27	24.46	0.09	6.23	8.24	0.35
CM010	60.61	24.33	0.14	6.28	8.09	0.27
W05-45A	60.75	24.60	0.16	6.65	7.66	0.55
W05-45A	60.20	24.29	0.10	6.45	7.77	0.53
W05-45A	60.45	24.29	0.22	6.48	7.70	0.46
W05-45A	60.10	24.50	0.36	6.62	7.72	0.40
W05-45A	63.75	18.20	0.94	0.10	1.84	12.99
CM007	65.44	18.65	0.06	0.00	1.00	15.36
CM007	69.45	19.39	0.00	0.04	12.13	0.12
CM007	69.81	19.48	0.18	0.10	12.01	0.07
CM007	69.75	19.37	0.00	0.05	12.04	0.04
CM007	66.62	21.40	0.07	0.32	10.26	1.38
W05-41	56.95	26.93	0.32	9.57	6.05	0.33
W05-41	57.09	26.95	0.34	9.53	6.23	0.28
W05-41	57.69	27.37	0.31	9.76	5.90	0.44
W05-41	57.69	27.48	0.32	9.66	5.62	0.42
W05-49	56.29	26.99	0.39	10.09	5.47	0.51
W05-49	56.90	26.88	0.33	9.62	5.29	1.28
W05-49	56.41	26.85	0.35	9.92	5.81	0.41
W05-49	57.33	27.26	0.36	10.07	5.69	0.51
CM058	60.98	24.42	0.23	6.61	7.66	0.57
CM058	60.50	24.46	0.11	6.74	7.64	0.47
CM058	60.91	24.73	0.14	6.73	7.65	0.50
CM058	60.96	24.85	0.06	6.69	7.76	0.46
CM058	65.28	18.68	0.01	0.06	1.34	14.75
W05-65	61.01	24.99	0.13	6.68	7.79	0.41
W05-65	60.97	24.79	0.09	6.66	7.79	0.44
W05-65	61.05	24.30	0.20	6.37	7.89	0.47
W05-65	60.59	24.74	0.24	6.69	7.87	0.47
W05-65	67.11	18.69	0.17	0.04	1.72	13.92
W05-57	58.87	26.81	0.30	5.47	4.25	6.03
W05-57	68.57	19.28	0.11	0.75	3.81	8.36
CM003	61.93	23.98	0.10	5.76	8.55	0.25
CM003	62.42	24.17	0.00	5.60	8.78	0.16
CM003	60.82	25.16	0.12	6.86	7.79	0.40
CM003	62.38	24.29	0.10	5.85	8.52	0.24

Table A.2. Microprobe analysis of feldspar clasts in impact melt.

Sample	SiO_2	Al_2O_3	FeO	CaO	Na_2O	K_2O
CM052	53.72	29.33	0.53	12.76	4.39	0.27
CM052	53.28	29.17	0.57	12.73	4.38	0.27
CM052	50.95	30.93	0.42	14.80	3.11	0.16
CM052	51.74	30.24	0.30	14.14	3.68	0.20
CM085	60.56	25.40	0.17	7.52	6.75	0.84
CM085	61.27	25.13	0.10	7.07	7.17	1.02
CM085	50.57	30.69	0.42	14.29	3.35	0.19
CM085	55.81	27.55	0.34	10.40	5.56	0.44
W05-61	55.00	27.96	0.42	10.95	4.88	0.70
W05-61	55.33	28.02	0.37	10.90	4.91	0.70
W05-61	56.25	27.52	0.34	10.33	5.15	0.77
W05-61	56.30	27.46	0.37	10.29	5.28	0.77
W05-65	54.43	27.90	0.25	11.02	4.95	0.41
W05-65	54.86	27.48	0.56	10.50	5.04	1.05
W05-65	55.43	27.45	0.78	10.66	4.48	1.57
W05-65	52.15	29.84	0.60	12.91	4.19	0.28
CM051	57.07	27.12	0.34	9.75	5.39	0.87
CM051	56.57	27.04	0.35	9.71	5.48	0.76
CM051	61.57	24.77	0.36	6.69	7.01	1.03
CM051	61.65	24.84	0.10	6.91	6.90	1.23
CM044B	55.32	27.57	0.65	10.56	5.05	0.49
CM044B	56.24	27.09	0.62	10.13	5.52	0.55
CM044B	56.02	26.70	0.89	10.27	5.25	0.60
CM044B	56.29	27.01	0.60	10.20	5.41	0.59

Appendix B. Sample Locations

	Rock Type	Location	Latitude	Longitude
Target rock samples				
CM001	Gneiss	North East shore	N55° 55' 43.0"	W63° 10' 44.0"
CM003	Granodiorite	North East shore	N55° 56' 18.9"	W63° 14' 06.7"
CM004	Gneiss	North East shore	N55° 56' 16.6"	W63° 14' 12.0"
CM006	Granodiorite	Steep Creek	N55° 57' 00.5"	W63° 17' 08.0"
CM007	Granodiorite	Steep Creek	N55° 57' 00.9"	W63° 17' 12.7"
CM010	Mangerite	Steep Creek	N55° 57' 00.2"	W63° 17' 11.1"
CM029	Mangerite	Steep Creek	N55° 53' 23.2"	W63° 20' 48.8"
CM057	Mangerite	Steep Creek	N55° 57' 04.7"	W63° 17' 23.5"
CM059	Mangerite	Steep Creek	N55° 57' 04.6"	W63° 17' 23.0"
CM117	Granodiorite	north West shore	N55° 53' 08.2"	W63° 26' 17.4"
W05-45	Mangerite	Horseshoe Island	N55° 52' 51.6"	W63° 21' 29.1"
W05-49	anorthosite	Horseshoe Island	N55° 52' 43.3"	W63° 18' 19.2"
W05-41	anorthosite	Horseshoe Island	N55° 53' 08.0"	W63° 18' 11.2"
W05-67	anorthosite	South East (3km from shore)	N55° 50' 28.6"	W63° 10' 09.0"
CM031	Meta-Qtz gabbro	Horseshoe Island	N55° 53' 14.0"	W63° 19' 50.7"
CM038	Mangerite	Discovery Hill	N55° 51' 37.1"	W63° 26' 06.5"
Melt rock samples				
CM005	Melt rock	Steep Creek	N55° 56' 45.2"	W63° 17' 04.8"
CM008	Suevite	Steep Creek	N55° 57' 00.8"	W63° 17' 12.4"
CM015	Melt rock	Coté Creek	N55° 55' 07.7"	W63° 23' 37.2"
CM020	Melt rock	Coté Creek	N55° 55' 09.4"	W63° 23' 38.4"
CM021	Melt rock	Coté Creek	N55° 55' 09.3"	W63° 23' 39.5"
CM023	Melt rock	Coté Creek	N55° 55' 14.4"	W63° 23' 51.8"
CM024B	Melt rock	Coté Creek	N55° 55' 14.4"	W63° 23' 51.8"
CM025	Melt rock	Coté Creek	N55° 55' 07.1"	W63° 23' 29.0"
CM027	Melt rock	Coté Creek	N55° 54' 47.0"	W63° 24' 36.3"
CM028	Melt rock	Coté Creek	N55° 55' 08.8"	W63° 24' 01.2"
CM035	Melt rock	Discovery Hill	N55° 51' 34.3"	W63° 26' 11.9"
CM036	Melt rock	Discovery Hill	N55° 51' 29.6"	W63° 25' 58.0"
CM037	Melt rock	Discovery Hill	N55° 51' 37.1"	W63° 26' 06.5"
CM039	Melt rock	Discovery Hill	N55° 51' 37.1"	W63° 26' 06.5"
CM042	Melt rock	Discovery Hill	N55° 51' 26.5"	W63° 26' 04.1"
CM043	Melt rock	Discovery Hill	N55° 51' 25.1"	W63° 26' 07.3"
CM044C	Melt rock	Discovery Hill	N55° 51' 25.1"	W63° 26' 07.3"
CM051	Melt rock	North Shore	N55° 56' 21.6"	W63° 20' 36.1"
CM052	Melt rock	North Shore	N55° 56' 44.0"	W63° 19' 47.7"
CM053	Melt rock	North Shore	N55° 56' 45.3"	W63° 19' 47.3"
CM055	Melt rock	North Shore	N55° 56' 50.1"	W63° 19' 40.4"
CM064	Melt rock	South Ridge	N55° 49' 54.0"	W63° 22' 49.8"
CM065	Melt rock	South Ridge	N55° 49' 53.9"	W63° 22' 53.4"
CM066	Melt rock	South Ridge	N55° 49' 49.0"	W63° 22' 53.4"
CM067	Melt rock	South Shore	N55° 49' 55.6.0"	W63° 21' 48.1"
CM071	Melt rock	South Shore	N55° 49' 55.7"	W63° 21' 16.3"
CM074	Melt rock	South Shore	N55° 49' 54.0"	W63° 20' 15.1"
CM084	Melt rock	Coté Creek	N55° 49' 54.0"	W63° 20' 15.1"
CM088	Melt rock	Coté Creek	N55° 55' 15.3"	W63° 23' 46.6"
W05-60	Melt rock	Coté Creek	N55° 55' 15.0"	W63° 23' 46.4"
W05-61	Melt rock	Discovery Hill	N55° 51' 30.4"	W63° 26' 13.1"
W05-63	Melt rock	Discovery Hill	N55° 51' 29.8"	W63° 25' 58.0"
W05-65	Melt rock	South Shore	N55° 49' 55.7"	W63° 21' 17.4"

Appendix C

Additional Photos and Sample Descriptions

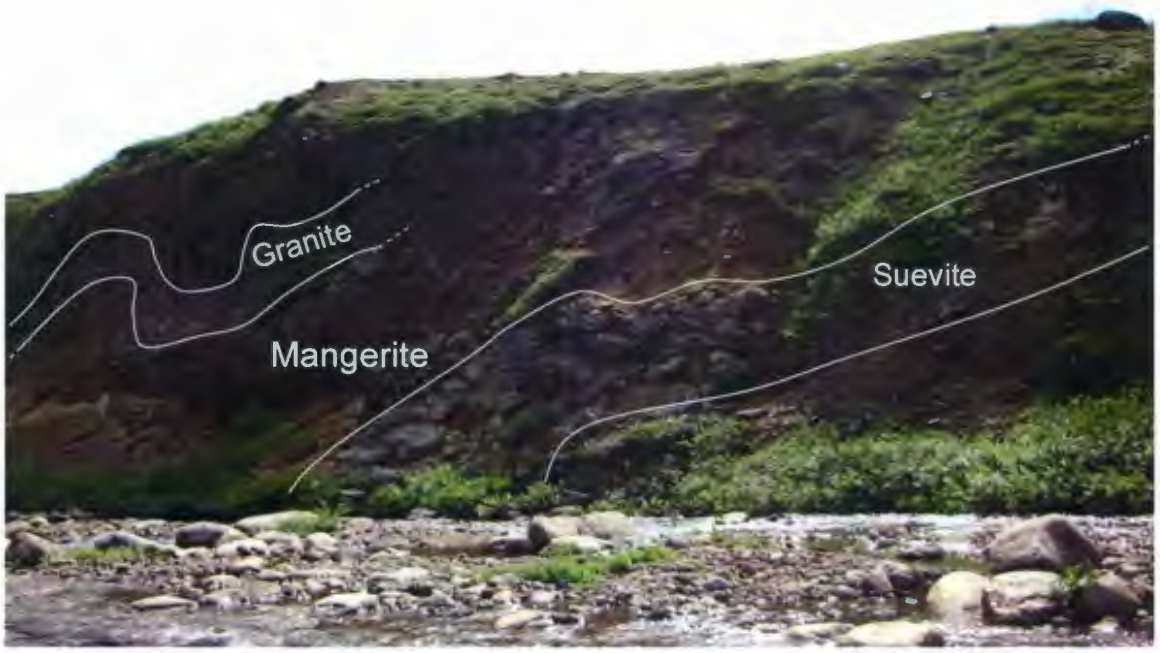

Figure C.1. Impactite outcrop at Steep Creek. This exposure consists of intrusions of suevite (sample CM008) and granite (sample CM010) into mildly brecciated mangerite. These units are described in chapter 2. Note the angle of intrusion.

Figure C.2. Outcrop of monomict anorthosite breccia along the South Creek (a creek on the far west side of the southern shore of Mistastin Lake). The breccia is approximately 2.5 m thick and is overlain by 2-4 m of regolith. This area along the South Creek has a variety of anorthosite breccias and exotic deposits. Unfortunately little time was devoted to these outcrops but there is a lot of potential for further study here. Note that a pair of rubber boots would be helpful.

Figure C.3. Pseudotachylite veins in mangerite at the South Shore. Pseudotachylite is formed by frictional melting of the target rock. The veins have weathered to a light brown and contain a pebbly mangerite breccia.

Figure C.4. Vesicular melt rocks at the South Shore. A) South Shore beach with Discovery Hill in the background. Note the higher elevation of Discovery Hill relative to the beach outcrops. B) A South Shore beach outcrop. Sledgehammer for scale in both photos.

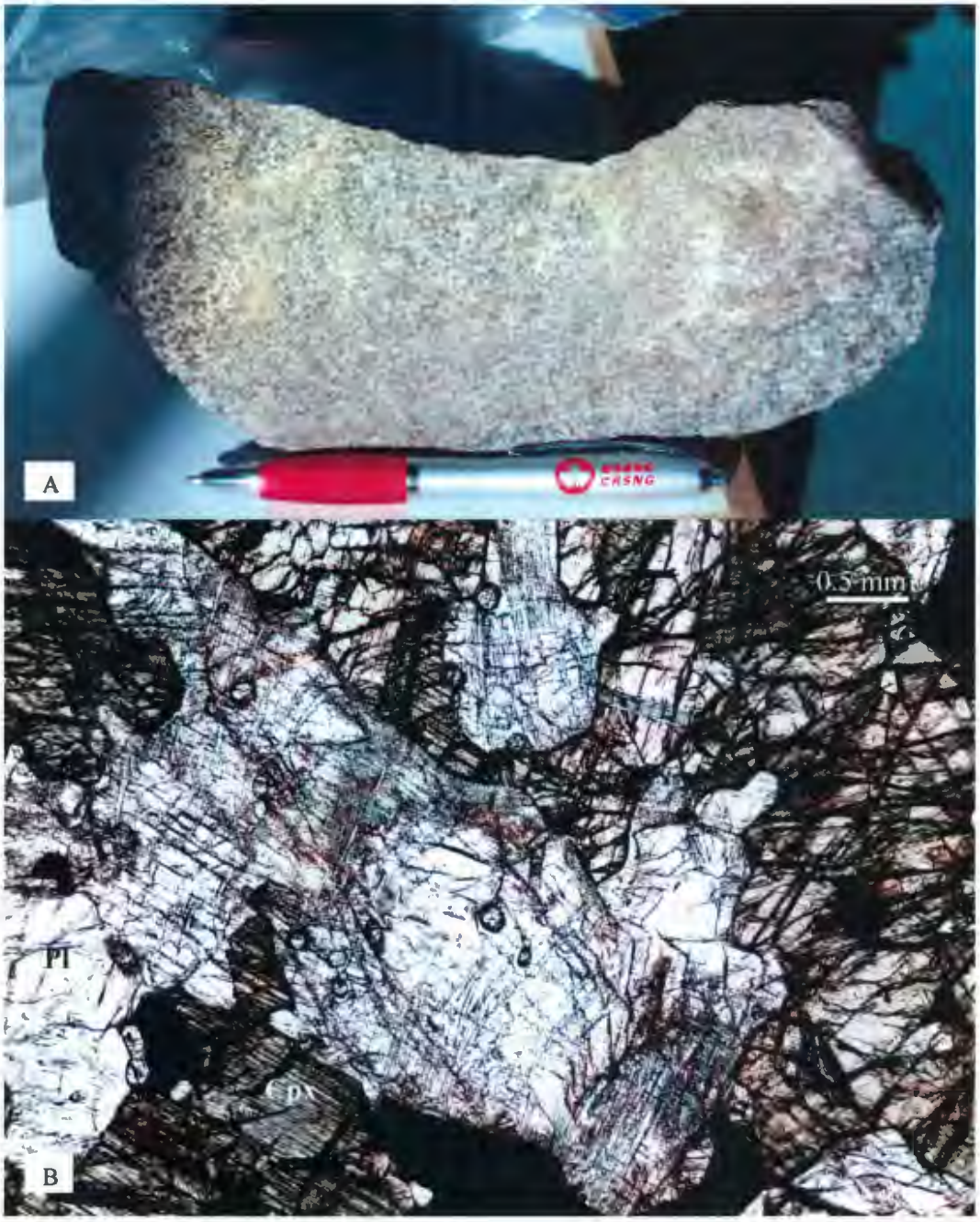

Figure C.5. Sample CM031 of meta-quartz gabbro from Horseshoe Island. A) Hand sample photo; B) photomicrograph in plane polarized light showing micro-fractures, planar features, plagioclase and clinopyroxene with hornblende exsolution. Pl = plagioclase, Cpx = clinopyroxene.

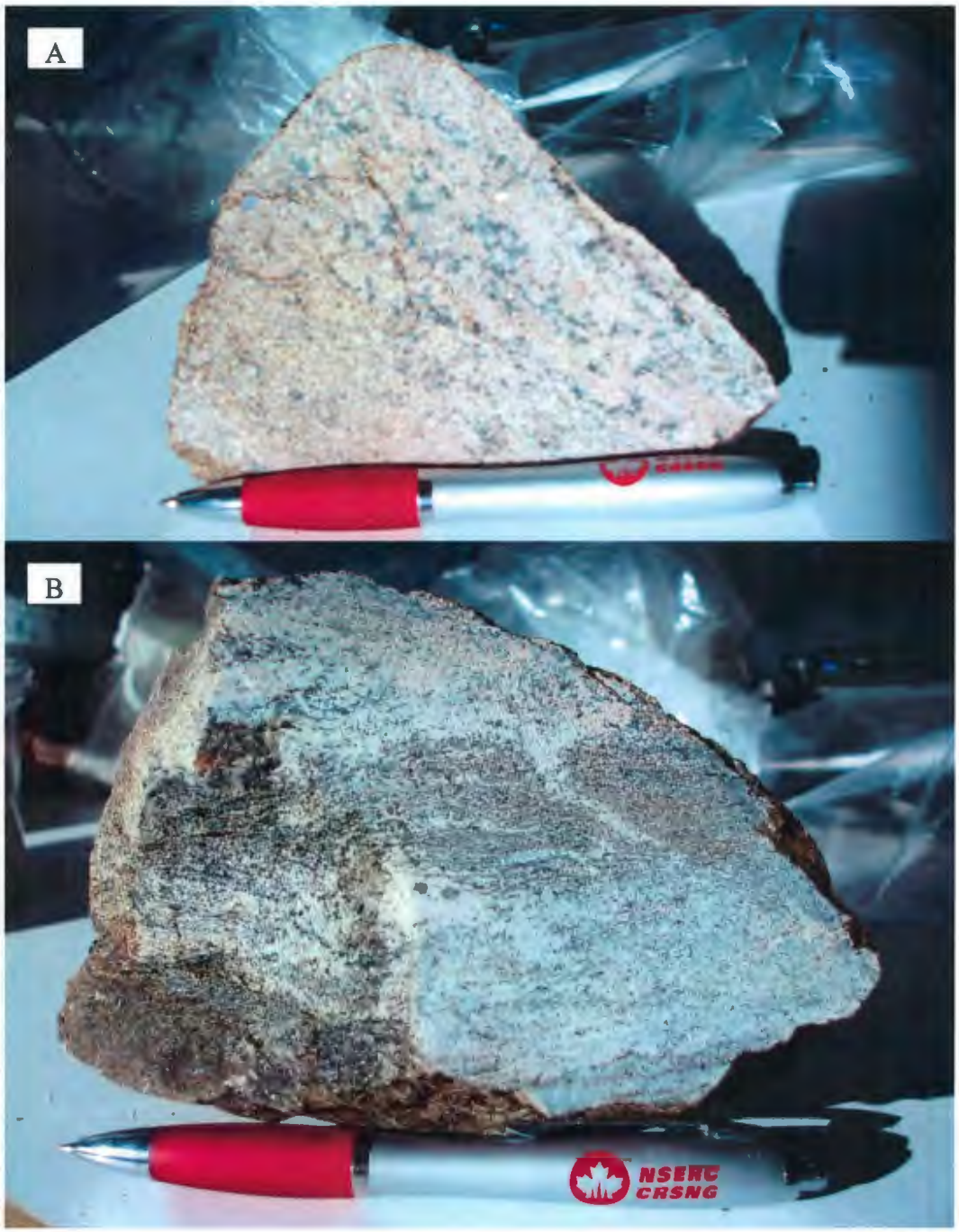

Figure C.6. Gneisses from the northeast shore of Mistastin Lake. A) Sample CM001 is a granodioritic gneiss similar in composition to the granodiorite discussed in Chapter 3. B) sample CM004, a granite gneiss. The gneisses occur as masses within the granodiorite and mangerite. These samples were observed within the granodiorite but many globules of gneiss are identified in outcrop on Horseshoe Island and along the South Shore within the mangerite.

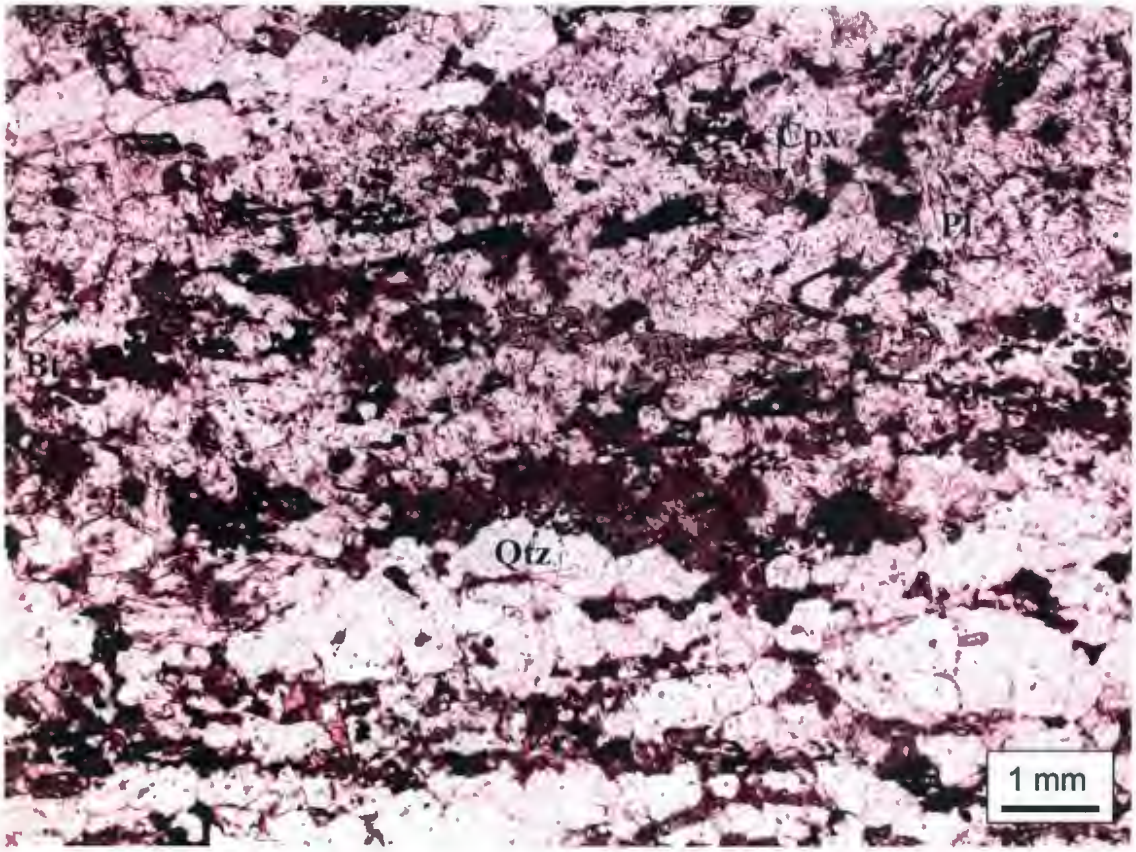

Figure C.7. Photomicrograph of the sample CM004 gneiss (Fig. C.6) in plane polarized light. Clinopyroxene is altering to hornblende.

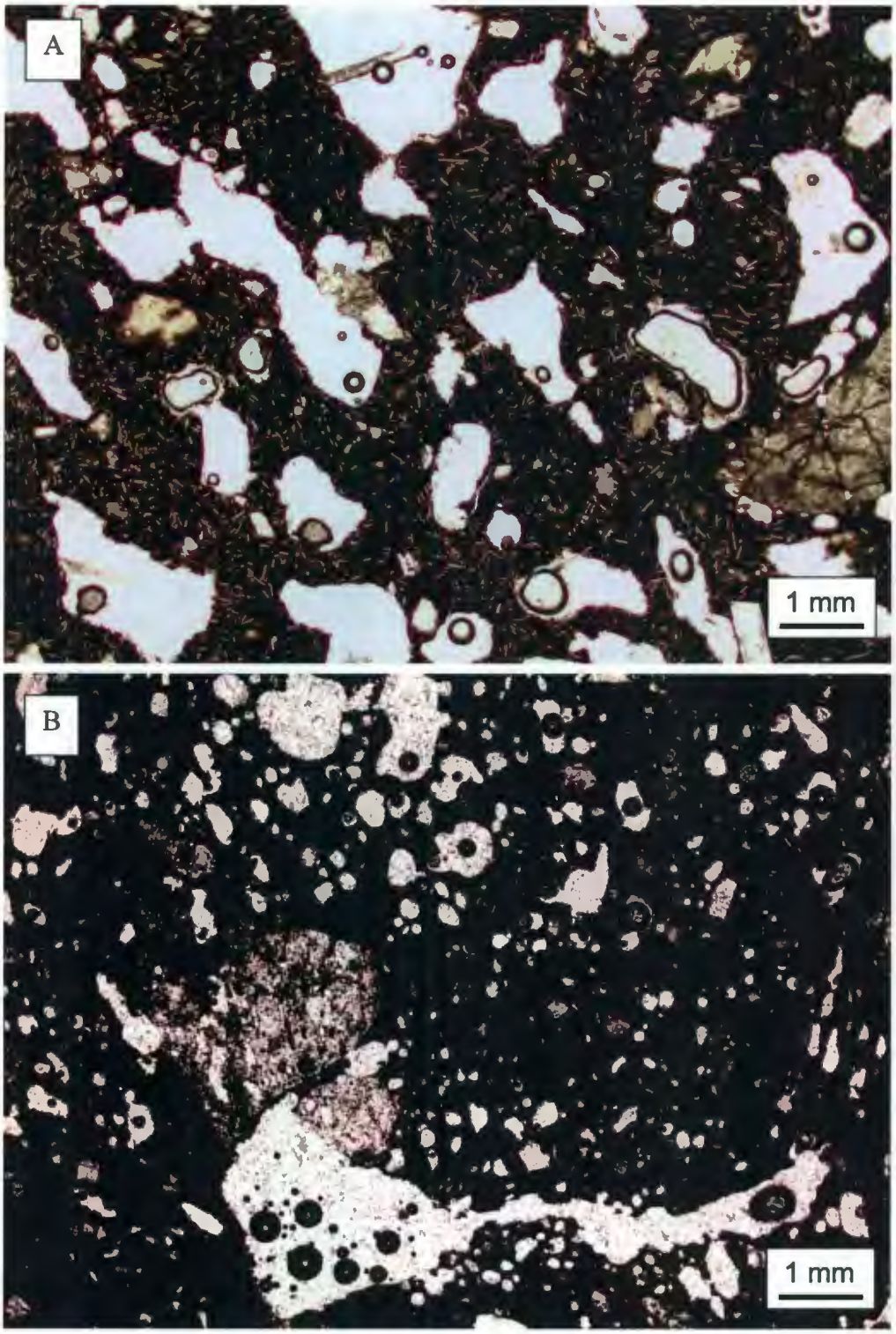

Figure C.8. Vesicular, glassy melt rocks from Mistastin Lake. A) Sample CM_Scuba_1, a boulder collected at 15 ft depth along the northern shallows of Horseshoe Island. This sample may have been airborne. B) Sample CM055 from the North Shore, collected *insitu*. Note the irregular shape of vesicles in each sample.

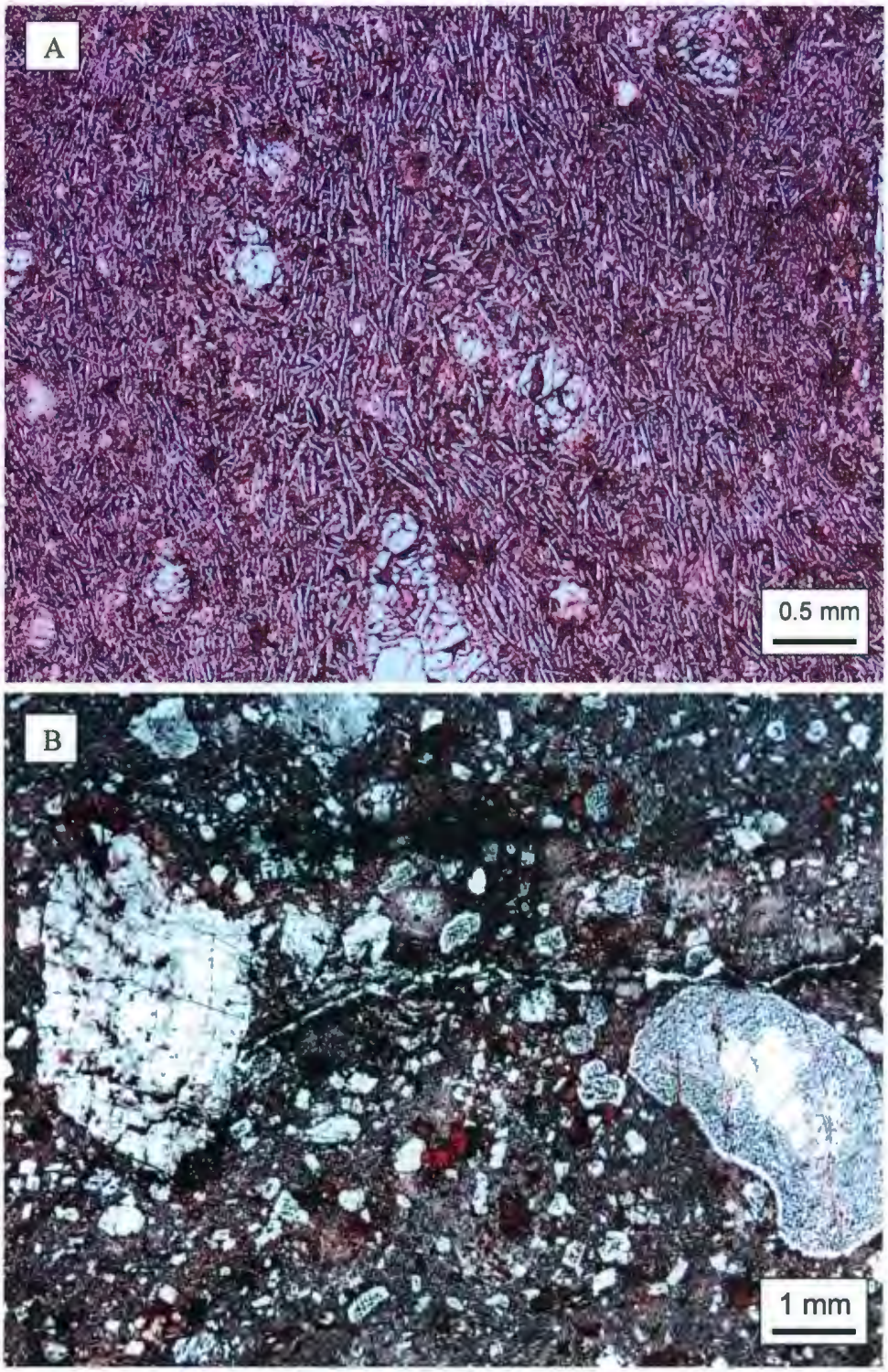

Figure C.9. Melt rock textures in thick melt units. A) Sample CM039, collected approximately 1.5 m from a large mangerite boulder at Discovery Hill shows well developed plagioclase microlites with preferred orientation. B) Clast-rich sample from the top of the South Ridge outcrop. This sample clearly shows that partially digested and melted clasts are found adjacent to nearly unaffected clasts. This outcrop has irregular zones of more clast-rich rocks.

Appendix D: Additional Data Tables for Chapter 3

Table D1. Bulk (XRF) chemical compositions of melt rock units at Mistastin Lake

Low HFSE melt rocks

	Cote Creek												Steep Creek	North Shore			
File name	M30618G	M29567S	M29585RE	M30606X	M29569N	M29571G	M30612A	M29568P	M28145H	M30611E			M28143D	M29578X	M30616N	M29579	
Sample	CM084	CM015	CM088	W05-60	CM025	CM028	CM024B	CM021	CM023	CM020	Mean	SD	CM005	CM051	CM053	CM052	Mean
SiO2 (wt%)	53.99	54.71	54.85	56.03	56.33	56.47	56.56	56.69	56.84	56.35	56.06	1.26	56.47	55.58	55.59	55.92	55.70
TiO2	0.74	0.53	0.75	0.83	0.86	0.85	0.90	0.71	0.86	0.91	0.79	0.12	0.77	0.89	0.86	0.91	0.89
Al2O3	23.05	23.96	22.62	20.74	20.33	20.51	21.68	22.68	20.81	22.00	21.86	1.25	20.93	20.96	23.35	21.39	21.91
FeOT	3.85	4.05	3.86	5.18	5.27	5.24	5.01	4.04	5.18	4.86	4.66	0.62	4.78	5.72	5.26	5.54	5.51
MnO	0.06	0.05	0.05	0.07	0.06	0.06	0.07	0.06	0.06	0.07	0.07	0.01	0.06	0.11	0.09	0.08	0.09
MgO	0.69	1.04	0.88	1.60	1.42	1.43	1.16	0.47	1.31	1.16	1.12	0.35	1.42	1.60	1.51	1.78	1.63
CaO	8.42	8.76	8.32	6.93	6.91	6.96	7.11	7.46	6.93	7.18	7.50	0.72	7.36	7.29	7.64	7.43	7.45
Na2O	4.10	4.28	4.40	3.76	3.94	3.78	3.98	4.54	3.84	4.14	4.08	0.27	3.87	3.80	3.93	4.03	3.92
K2O	1.04	1.00	1.30	1.76	1.76	1.83	1.78	1.46	1.80	1.84	1.55	0.33	1.66	1.51	1.52	1.45	1.49
P2O5	0.71	0.27	0.64	0.23	0.25	0.26	0.24	0.34	0.26	0.24	0.34	0.18	0.22	0.26	0.26	0.27	0.26
LOI	2.42	2.06	1.80	0.88	0.43	0.38	0.96	3.26	0.83	0.50	1.35	0.98	1.54	1.63	0.92	1.64	1.46
Total	99.05	100.72	99.47	98.00	97.56	97.81	99.46	101.93	98.72	101.26	99.40		99.08	99.57	100.93	100.44	100.31
S (ppm)	224	131	119	298	45	58	201	62	51	285	147	98	79	79	216	45	113
Cl	124	47	92	67	15	19	61	27	22	85	54	35	27	36	40	74	50
Sc	<LD	25	10	12	21	2	13	8	14	16	14	7	11	<LD	13	15	14
V	43	39	46	49	37	43	59	42	53	52	46	7	44	47	61	50	53
Cr	8	26	60	21	16	17	22	13	20	23	23	14	22	22	29	19	23
Ni	8	20	13	11	14	15	14	17	9	11	13	3	16	17	16	26	20
Cu	14	14	11	12	10	14	12	12	9	12	12	2	10	17	7	12	12
Zn	21	12	15	16	6	11	22	18	30	13	16	7	28	17	19	15	17
Ga	21	21	20	19	22	21	16	24	22	22	21	2	24	21	24	24	23
As	<LD	1.0	1.3	<LD	15	15	<LD	17	<LD	<LD	10	8	4	7	<LD	11	9
Rb	11.9	14.1	20.5	31.1	26.3	29.7	31.2	19.9	32.2	27.6	24.5	7.4	24.3	22.3	17.6	21.0	20.3
Sr	645	666	637	565	580	560	587	604	577	576	598	38	601	592	603	595	597
Y	16.9	11.6	14.9	18.3	23.5	21.3	19.8	14.1	20.1	19.9	18.0	3.6	16.0	16.4	16.1	18.4	17.0
Zr	201	147	166	312	338	322	308	166	304	328	259	79	242	309	230	283	274
Nb	7.8	6.6	7.9	10.9	12.0	10.6	11.8	6.8	11.1	12.4	9.8	2.3	6.8	10.5	9.4	8.6	9.5
Ba	962	581	642	1115	1099	1057	1052	642	984	1147	926	223	1093	1121	902	942	988
Ce	86	103	135	111	105	153	98	185	126	88	119	31	80	130	78	113	107
Pb	<LD	5	7	8	13	8	9	9	8	9	8	2	7	9	6	9	8
Th	<LD	5	5	<LD	4	<LD	5	9	6	<LD	6	2	5	2	<LD	2	2.1
U	<LD	<LD	<LD	<LD	<LD	0.4	<LD	2	<LD	<LD	1.1	1.0	<LD	<LD	<LD	1.4	1.4
Total ppm	2393	1855	2023	2676	2399	2378	2526	1896	2297	2711	2325		2345	2476	2290	2285	2360
Total wt%	99.29	100.90	99.67	98.27	97.82	98.05	99.71	102.12	98.95	101.53	99.63		99.32	99.82	101.16	100.67	100.55
Ratios																	
Mg no.	24	31	29	35	32	33	29	17	31	30	29	5	35	33	34	36	35
TiO2/Al2O3	0.032	0.022	0.033	0.040	0.042	0.042	0.042	0.031	0.041	0.041	0.037	0.007	0.037	0.043	0.037	0.043	0.041
FeOT/Al2O3	0.17	0.17	0.17	0.25	0.26	0.26	0.23	0.18	0.25	0.22	0.21	0.04	0.23	0.27	0.23	0.26	0.25
Y/Sr	0.026	0.018	0.023	0.032	0.040	0.038	0.035	0.023	0.035	0.034	0.031	0.007	0.030	0.028	0.027	0.031	0.026
Zr/Sr	0.31	0.22	0.26	0.55	0.58	0.57	0.54	0.28	0.53	0.57	0.44	0.15	0.40	0.52	0.38	0.48	0.46
Nb/Sr	0.012	0.010	0.012	0.019	0.021	0.019	0.021	0.011	0.019	0.022	0.017	0.005	0.015	0.018	0.016	0.014	0.016
Ba/Sr	1.49	0.84	1.01	1.97	1.89	1.89	1.86	1.06	1.71	1.99	1.57	0.44	1.82	1.89	1.50	1.58	1.66

Notes: S.D. = standard deviation. <LD = less than detection limit. (1)=melt breccia. (2)=shore 1.25 km west of Cote Creek. (3)=suevite melt clast.

Table D1 continued

	Low HFSE melt rocks														High HFSE melt rocks	
		South Ridge					South Shore						Mean	SD	Discovery Hill	
File name		M29582M	M29583T	M28149Q			M30617J	M28150E	M29584B			M30609R			M29577U	M30608T
Sample	SD	CM084	CM086	CM085	Mean	SD	CM074	CM071	CM087	Mean	SD	W05-65 (1)	n=20		CM043	W05-63
SiO2 (wt%)	0.19	55.15	55.91	55.97	55.68	0.46	55.11	55.39	56.19	55.57	0.56	57.94	55.91	0.94	55.46	56.00
TiO2	0.03	0.66	0.69	0.71	0.69	0.03	0.64	0.59	0.69	0.64	0.05	0.81	0.77	0.11	1.03	1.13
Al2O3	1.26	22.34	21.94	22.14	22.14	0.20	24.62	22.99	21.74	23.12	1.45	22.97	22.05	1.18	19.70	20.17
FeOT	0.23	4.40	4.01	4.20	4.20	0.19	3.51	4.24	4.29	4.01	0.43	4.62	4.63	0.65	6.21	6.60
MnO	0.01	0.07	0.04	0.05	0.05	0.01	0.04	0.04	0.07	0.05	0.02	0.08	0.07	0.02	0.10	0.10
MgO	0.14	1.26	0.98	1.34	1.19	0.19	1.01	1.08	1.33	1.13	0.17	1.36	1.22	0.32	1.47	1.29
CaO	0.17	7.90	7.62	7.62	7.71	0.16	8.55	7.89	7.58	8.01	0.50	7.69	7.59	0.56	8.10	6.65
Na2O	0.11	4.21	4.24	4.09	4.18	0.08	4.37	4.28	4.25	4.30	0.06	4.42	4.09	0.23	3.68	3.34
K2O	0.04	1.37	1.50	1.46	1.45	0.07	0.99	1.25	1.54	1.26	0.28	1.71	1.49	0.27	1.93	2.10
P2O5	0.00	0.23	0.23	0.22	0.23	0.00	0.18	0.19	0.23	0.20	0.03	0.23	0.29	0.14	0.35	0.32
LOI	0.48	2.26	2.47	1.18	1.97	0.69	1.53	2.86	0.47	1.62	1.20	0.34	1.51	0.85	0.99	1.97
Total		99.83	99.64	99.99	99.49		100.57	100.77	99.39	99.91		102.37	99.61		99.00	99.69
S (ppm)	91	43	47	53	47	5	257	49	51	119	120	226	120	91	36	536
Cl	21	45	57	55	52	6	61	24	74	53	26	107	52	27	73	59
Sc	1	7	7	9	8	1	<LD	14	18	16	3	10	13	6	13	19
V	7	46	37	45	43	5	50	37	48	45	7	46	46	7	61	58
Cr	5	17	19	13	18	3	18	27	40	28	12	22	23	11	24	11
Ni	5	16	9	15	13	4	10	14	14	13	2	14	14	4	9	10
Cu	5	14	8	18	13	5	12	12	14	13	1	13	12	3	12	12
Zn	2	7	13	25	15	9	10	24	13	16	7	10	17	7	17	36
Ga	2	23	23	20	22	2	20	21	19	20	1	21	21	2	23	20
As	3	<LD	0.3	0.5	0.4	0.2	<LD	4	9	7	4	<LD	7	6	<LD	<LD
Rb	2.4	24.9	27.7	27.6	26.8	1.6	14.8	16.9	29.1	20.3	7.7	27.3	23.5	6.2	28.1	36.4
Sr	8	657	617	635	636	20	690	616	606	637	46	587	609	36	559	513
Y	1.3	13.4	13.7	15.5	14.2	1.1	9.2	13.5	16.3	13.0	3.6	20.6	16.5	3.5	30.9	28.5
Zr	40	186	217	191	198	17	103	143	265	170	84	276	238	73	399	446
Nb	0.9	8.6	9.2	8.5	8.1	1.3	5.7	7.6	8.9	7.4	1.6	12.9	9.1	2.0	14.8	17.6
Ba	116	716	775	737	743	29	507	691	824	674	159	879	879	207	1127	1247
Ce	27	77	51	80	69	16	76	67	116	86	26	83	103	32	151	155
Pb	2	4	11	8	7	4	<LD	8	9	8	2	<LD	8	2	8	11
Th	0.3	<LD	2	5	4	2	<LD	2	5	4	2	<LD	4	2	2	6
U		<LD	0.8	<LD	0.8		<LD	<LD	<LD			<LD	1.1	0.6	0.2	<LD
Total ppm		1904	1945	1959	1938		1842	1791	2180	1949		2354	2216		2589	3222
Total wt%		100.02	99.84	99.18	99.68		100.75	100.94	98.81	100.10		102.61	99.83		99.26	100.01
Ratios																
Mg no.	2	34	30	36	33	3	34	31	36	33	2	33	32	4	30	26
TiO2/Al2O3	0.003	0.029	0.031	0.032	0.031	0.001	0.026	0.026	0.032	0.028	0.003	0.035	0.035	0.006	0.053	0.056
FeOT/Al2O3	0.02	0.20	0.18	0.19	0.19	0.01	0.14	0.18	0.20	0.17	0.03	0.21	0.21	0.04	0.32	0.33
Y/Sr	0.002	0.020	0.022	0.024	0.022	0.002	0.013	0.022	0.027	0.021	0.007	0.036	0.028	0.007	0.055	0.056
Zr/Sr	0.07	0.28	0.35	0.30	0.31	0.04	0.15	0.23	0.44	0.27	0.15	0.47	0.40	0.14	0.71	0.87
Nb/Sr	0.002	0.010	0.015	0.013	0.013	0.002	0.008	0.012	0.015	0.012	0.003	0.022	0.015	0.004	0.026	0.035
Ba/Sr	0.21	1.09	1.26	1.16	1.17	0.08	0.74	1.12	1.36	1.07	0.32	1.50	1.46	0.41	2.01	2.43

Table D1 continued

High HFSE melt rocks

	Discovery Hill									Cote Creek West (2)	North Shore	Steep Creek (3)	Mean	SD
File name	M29574N	M28147M	M28146W	M30607V	M29576S	M30614U	M30615Q			M30613X	M28148B	M28144S		
Sample	CM037	CM042	CM035	W05-61	CM039	CM036	CM044C	Mean	SD	CM027	CM055	CM008	n=11	
SiO2 (wt%)	56.59	56.98	57.24	58.00	58.27	59.71	60.33	57.62	1.63	57.88	55.66	61.33	57.46	1.58
TiO2	1.13	1.03	0.98	1.07	1.02	0.98	0.97	1.04	0.06	1.13	1.08	0.97	1.05	0.06
Al2O3	19.35	18.82	18.32	21.40	18.22	20.43	19.51	19.55	1.03	20.45	19.05	15.94	19.59	0.98
FeOT	6.59	6.25	6.44	6.16	6.45	5.88	5.51	6.23	0.35	6.05	6.83	6.77	6.27	0.37
MnO	0.11	0.06	0.10	0.11	0.11	0.07	0.10	0.10	0.01	0.10	0.11	0.11	0.10	0.01
MgO	1.59	1.38	1.33	1.14	1.47	1.16	1.27	1.34	0.15	0.89	1.54	0.89	1.32	0.20
CaO	6.93	6.47	6.04	7.41	6.24	6.61	6.77	6.80	0.63	6.79	6.87	4.60	6.81	0.56
Na2O	3.68	3.45	3.46	3.88	3.65	3.66	3.66	3.61	0.16	3.59	3.51	2.90	3.60	0.14
K2O	1.92	2.24	2.38	1.83	2.22	2.34	2.29	2.14	0.20	1.93	1.77	2.94	2.09	0.22
P2O5	0.38	0.38	0.32	0.28	0.34	0.28	0.35	0.33	0.03	0.32	0.34	0.31	0.33	0.03
LOI	1.82	1.35	1.14	0.79	1.83	1.91	0.76	1.40	0.50	1.33	0.42	2.63	1.30	0.53
Total	100.09	98.45	97.74	102.09	99.82	103.04	101.54	100.16		100.45	97.18	99.39	99.92	
S (ppm)	46	32	17	237	29	207	294	160	177	211	50	172	154	163
Cl	56	69	37	114	69	88	98	74	23	80	103	114	77	23
Sc	31	17	12	15	5	16	17	16	7	18	16	14	16	6
V	50	53	52	52	51	42	47	52	5	63	59	25	53	6
Cr	7	14	13	<LD	13	<LD	12	13	5	19	19	0.3	15	5
Ni	13	10	6	7	6	6	15	10	3	9	14	7	10	3
Cu	15	11	10	14	10	12	17	13	2	16	15	10	13	2
Zn	29	36	36	19	29	28	29	29	7	24	46	52	30	8
Ga	20	19	21	23	19	22	21	21	2	20	23	23	21	2
As	9	13	4	<LD	5	<LD	<LD	8	4	<LD	7	5	8	4
Rb	34.6	45.0	51.0	30.4	48.1	39.9	44.1	39.7	7.9	31.8	24.6	44.5	37.6	8.6
Sr	533	500	486	559	477	517	526	519	29	542	558	452	525	29
Y	27.7	29.6	30.7	31.2	34.4	30.8	30.2	30.5	1.9	26.6	29.7	33.9	30.1	2.0
Zr	367	396	424	453	444	432	386	416	30	381	425	619	414	29
Nb	14.7	15.5	16.2	17.1	17.1	17.9	15.7	16.3	1.2	15.7	15.5	16.0	16.2	1.1
Ba	1081	1172	1194	1256	1144	1261	1188	1181	87	1237	1249	2503	1192	65
Ce	138	158	176	146	179	163	131	155	16	140	114	162	150	19
Pb	7	11	17	13	17	14	12	12	3	11	11	16	12	3
Th	<LD	4	4	<LD	7	<LD	6	5	2	<LD	2	5	5	2
U	<LD	<LD	<LD	<LD	<LD	<LD	<LD	0.2		<LD	0.9	<LD	0.6	0.5
Total ppm	2462	2605	2609	2986	2605	2899	2868	2769		2845	2785	4274	2779	
Total wt%	100.34	98.71	98.00	102.39	100.08	103.33	101.83	100.44		100.73	97.46	99.82	100.20	
Ratios														
Mg no.	30	28	27	25	29	26	29	28	2	21	29	19	27	3
TiO2/Al2O3	0.058	0.055	0.054	0.050	0.056	0.048	0.050	0.053	0.003	0.055	0.057	0.061	0.054	0.003
FeOT/Al2O3	0.34	0.33	0.35	0.29	0.35	0.29	0.28	0.32	0.03	0.30	0.36	0.43	0.32	0.03
Y/Sr	0.052	0.060	0.063	0.056	0.072	0.060	0.057	0.059	0.006	0.049	0.053	0.075	0.058	0.006
Zr/Sr	0.69	0.79	0.87	0.81	0.93	0.84	0.73	0.80	0.06	0.70	0.76	1.37	0.79	0.06
Nb/Sr	0.028	0.031	0.033	0.031	0.036	0.035	0.030	0.032	0.003	0.029	0.026	0.035	0.031	0.003
Ba/Sr	1.99	2.34	2.46	2.24	2.40	2.44	2.22	2.28	0.16	2.28	2.24	5.53	2.28	0.16

Table D2. Electron Microprobe analyses of matrix and phenocryst minerals of melt rock units at Mistastin Lake

	Coté Creek CM088							Discovery Hill CM035				South Shore CM067			
Matrix															
SiO2	52.59	52.55	52.16	52.75	52.75			62.27	57.91			52.27	55.62	64.20	55.10
TiO2	0.71	1.13	0.91	0.84	0.97			0.33	0.22			0.47	0.16	0.56	1.09
Al2O3	25.79	25.39	25.46	25.76	24.92			20.68	23.23			25.97	27.30	18.46	19.01
FeOT	2.48	2.62	3.44	2.06	2.79			1.58	1.52			4.71	0.88	2.46	7.92
MnO	0.04	0.10	0.02	0.01	0.00			0.04	0.01			0.08	0.03	0.01	0.11
MgO	0.39	0.28	0.56	0.23	0.24			0.10	0.13			1.63	0.06	0.25	2.61
CaO	9.05	9.19	8.52	9.64	8.49			4.13	5.54			9.17	8.19	2.54	6.83
Na2O	5.14	5.07	4.88	4.95	5.05			4.01	4.80			4.12	5.68	5.67	4.33
K2O	0.92	1.14	1.50	1.16	2.04			4.64	3.69			0.85	1.48	3.96	1.81
Total	97.11	97.47	97.45	97.61	97.25			97.76	97.07			99.25	99.42	98.10	98.81
	Coté Creek CM023c														
Matrix															
SiO2	61.54	64.70	55.81	62.96	65.04	61.00	70.60	55.21	59.21	65.40	51.83	65.01	52.42	56.50	57.10
TiO2	0.10	0.22	0.11	0.17	0.11	0.21	0.67	0.09	0.14	0.23	2.93	0.14	0.09	0.08	0.11
Al2O3	23.12	20.33	26.91	22.01	21.21	22.34	15.64	27.83	25.26	20.21	27.47	19.35	28.79	26.70	25.63
FeOT	0.77	1.21	0.87	0.51	0.87	1.46	1.26	0.70	0.79	0.83	3.75	0.79	0.88	0.66	0.73
MnO	0.00	0.00	0.03	0.03	0.03	0.03	0.00	0.01	0.04	0.03	0.00	0.01	0.00	0.01	0.01
MgO	0.07	0.17	0.16	0.03	0.06	0.29	0.05	0.09	0.09	0.13	0.10	0.09	0.07	0.07	0.06
CaO	6.00	6.12	9.23	5.98	6.73	6.16	2.07	10.31	8.22	3.06	10.20	3.47	11.45	9.13	9.31
Na2O	4.70	4.27	5.72	5.59	4.50	5.04	3.45	5.04	5.37	4.38	4.94	4.99	4.86	5.66	5.64
K2O	3.77	2.65	0.84	2.11	1.75	2.46	6.14	0.75	1.32	6.22	0.46	4.84	0.36	0.88	0.96
Total	100.08	99.68	99.71	99.38	100.11	99.01	99.88	100.02	100.42	100.49	101.69	98.70	98.71	99.68	99.55
	South Shore CM071														
Matrix															
SiO2	57.46	63.43	55.14	58.99	55.65	58.97	57.54	54.64	56.89	53.30	57.40	56.69	55.55	56.62	57.80
TiO2	0.17	0.13	0.17	0.27	0.12	0.25	0.16	0.17	0.18	0.11	0.14	0.25	0.21	0.19	0.25
Al2O3	25.24	22.75	25.82	24.74	26.79	23.99	25.55	25.97	23.42	29.22	25.35	24.57	27.15	24.66	25.37
FeOT	1.29	0.83	1.55	1.09	1.18	0.94	0.74	2.01	1.11	0.59	0.86	2.32	0.92	0.80	1.06
MnO	0.02	0.05	0.03	0.02	0.05	0.00	0.00	0.02	0.01	0.00	0.01	0.05	0.01	0.04	0.01
MgO	0.33	0.12	0.69	0.20	0.25	0.16	0.15	0.82	0.18	0.07	0.15	0.82	0.09	0.10	0.17
CaO	7.70	6.55	9.45	7.33	8.86	6.98	7.74	9.57	8.28	10.95	6.49	6.77	9.48	7.24	7.65
Na2O	4.95	4.85	5.15	5.23	5.29	5.06	5.39	4.85	4.69	4.60	4.83	5.30	4.54	5.40	5.18
K2O	1.49	1.56	0.79	1.79	0.78	2.13	1.47	0.81	2.31	0.66	1.88	1.00	1.09	2.37	1.66
Total	98.64	100.28	98.79	99.66	98.98	98.50	98.74	98.67	97.07	99.50	99.11	99.77	99.04	99.42	99.14
	Discovery Hill CM042														
Matrix															
SiO2	57.14	64.01	89.93	61.53	56.41	65.92	68.19	68.10	62.10	66.60	59.64	57.50	55.64	78.73	60.59
TiO2	1.04	0.08	0.10	0.06	0.12	0.13	0.13	0.11	0.65	0.11	0.11	0.09	0.08	0.07	0.10
Al2O3	22.63	20.58	6.37	20.62	25.68	19.32	18.52	18.65	21.96	18.85	24.29	25.72	26.61	11.86	23.62
FeOT	3.10	0.44	0.33	0.65	0.96	0.82	0.36	0.51	1.71	0.53	0.58	0.94	0.73	0.52	0.67
MnO	0.01	0.00	0.04	0.00	0.00	0.00	0.07	0.00	0.00	0.00	0.00	0.00	0.00	0.00	0.00
MgO	0.14	0.02	0.05	0.08	0.15	0.18	0.06	0.05	0.12	0.05	0.11	0.14	0.07	0.13	0.09
CaO	6.12	2.69	0.25	6.25	8.45	4.91	1.60	2.17	5.42	1.97	8.82	8.08	8.90	0.62	6.80
Na2O	3.86	4.93	1.24	5.15	5.40	3.89	4.77	3.89	4.63	4.04	5.09	5.16	4.96	2.68	4.91
K2O	3.37	6.94	3.51	3.60	1.47	4.12	6.94	7.35	3.48	7.99	3.48	2.24	1.86	5.51	2.81
Total	97.42	99.69	101.83	97.95	98.64	99.28	100.64	100.83	100.27	100.13	99.93	99.89	98.64	100.12	99.59
	North Shore CM055														
Matrix															
SiO2	58.86	57.09	54.02	59.50	53.79	58.48	60.22	54.36	55.30	54.85	52.99	49.91	63.91	56.73	54.51
TiO2	0.18	0.97	1.82	0.29	0.74	0.15	0.61	1.13	0.61	0.23	1.32	4.26	0.24	0.25	0.97
Al2O3	23.74	21.44	22.00	23.07	16.87	20.74	18.60	21.27	23.47	25.19	22.14	18.73	20.63	23.15	22.53
FeOT	2.41	4.63	8.01	1.22	12.02	5.40	5.37	5.44	4.23	2.60	6.40	11.83	0.80	3.25	6.01
MnO	0.10	0.10	0.12	0.01	0.23	0.10	0.15	0.12	0.03	0.07	0.14	0.19	0.03	0.07	0.06
MgO	0.64	1.05	1.54	0.13	4.34	1.93	1.41	1.22	1.03	0.78	2.26	0.51	0.03	1.01	1.60
CaO	7.32	7.31	7.50	7.11	6.57	6.44	5.55	7.88	6.10	8.65	8.38	6.46	5.19	7.66	7.62
Na2O	4.53	4.50	4.55	4.80	3.71	4.90	3.51	4.27	4.59	4.94	4.62	4.20	4.10	4.53	4.70
K2O	1.52	1.32	0.84	2.01	0.92	1.34	2.24	1.34	1.05	0.79	0.55	1.63	3.36	1.14	0.90
Total	99.32	98.61	100.41	98.14	99.19	99.48	97.64	97.02	98.41	98.29	98.81	97.74	98.09	97.76	98.90

Table D2 continued

Matrix	South Shore W05-65					Coté Creek CM025				
SiO2	54.75	59.66	60.09	59.65	62.09	56.97	57.00	62.74	60.19	51.28
TiO2	0.16	0.41	0.32	0.32	0.87	0.17	0.16	0.48	0.31	0.08
Al2O3	26.34	22.31	22.68	22.67	19.49	26.52	26.71	20.14	23.34	31.72
FeOT	1.15	1.61	1.13	1.54	2.00	0.86	0.58	1.82	1.40	0.57
MnO	0.08	0.00	0.00	0.03	0.00	0.06	0.02	0.06	0.01	0.00
MgO	0.17	0.15	0.10	0.16	0.17	0.04	0.02	0.12	0.16	0.08
CaO	8.25	6.08	5.58	4.43	4.66	8.34	8.34	5.20	6.44	12.30
Na2O	4.28	4.08	5.42	5.32	3.87	4.56	5.61	4.11	5.18	4.42
K2O	2.00	3.14	2.62	4.15	4.53	2.46	1.35	3.60	2.04	0.32
Total	97.17	97.62	97.94	98.28	97.67	99.98	99.79	98.27	99.07	100.76

Matrix	Coté Creek CM023c															
SiO2	54.51	56.52	56.24	60.50	54.98	59.17	64.90	63.73	62.34	60.44	59.26	53.20	65.77	71.31	57.06	51.61
TiO2	0.10	0.09	0.14	0.14	0.18	0.13	0.13	0.21	0.12	0.10	0.11	0.06	0.22	0.21	0.08	0.10
Al2O3	28.56	26.34	27.63	24.09	25.22	23.71	20.97	21.19	23.34	24.92	24.43	28.76	19.16	15.79	26.35	29.24
FeOT	0.72	1.50	0.90	0.66	3.45	0.69	0.57	1.16	0.54	0.79	0.55	0.44	0.75	1.13	0.61	0.54
MnO	0.02	0.02	0.02	0.03	0.08	0.01	0.00	0.02	0.00	0.01	0.00	0.03	0.00	0.02	0.04	0.00
MgO	0.06	0.39	0.11	0.05	1.10	0.04	0.07	0.19	0.04	0.08	0.08	0.04	0.08	0.23	0.06	0.06
CaO	10.78	8.99	9.66	6.92	9.83	7.42	5.67	5.16	7.11	9.09	6.28	11.51	4.75	1.90	8.92	10.76
Na2O	5.19	5.49	5.14	5.30	4.79	4.90	5.58	5.02	4.63	4.47	5.50	4.91	4.27	3.86	5.71	4.79
K2O	0.36	0.97	1.31	2.82	0.59	3.64	2.81	3.37	2.72	1.16	3.59	0.46	3.63	5.28	1.09	0.40
Total	100.29	100.33	101.16	100.49	100.22	99.71	100.69	100.04	100.85	101.05	99.80	99.42	98.61	99.73	99.89	97.51

Matrix	South Shore CM071															
SiO2	59.71	58.44	59.68	59.71	57.39	62.60	59.40	60.63	57.70	54.84	59.59	55.49	59.39	57.68	60.26	56.01
TiO2	0.20	0.16	0.18	1.02	1.33	0.33	0.16	0.45	0.11	0.12	0.23	0.22	0.48	0.14	0.22	0.06
Al2O3	25.40	25.05	25.06	23.99	23.23	22.57	23.80	22.94	26.73	27.36	23.43	24.62	24.20	25.38	23.74	27.87
FeOT	0.78	0.91	0.95	1.30	3.79	1.10	0.95	1.60	0.47	0.79	1.05	0.89	1.73	0.61	0.79	0.33
MnO	0.04	0.05	0.04	0.00	0.05	0.06	0.03	0.00	0.00	0.01	0.08	0.00	0.06	0.01	0.00	0.00
MgO	0.11	0.15	0.13	0.12	0.18	0.19	0.17	0.18	0.04	0.11	0.19	0.18	0.16	0.08	0.09	0.05
CaO	7.39	7.66	7.26	6.79	6.56	5.93	6.70	5.80	8.34	9.14	6.66	9.14	7.22	8.30	6.86	9.04
Na2O	5.24	5.53	5.13	5.19	4.68	4.74	5.17	5.54	5.48	5.36	4.71	5.21	4.92	5.26	4.63	5.70
K2O	1.95	1.40	2.06	1.96	2.29	2.60	2.42	2.36	1.33	0.80	2.74	1.31	2.28	1.47	2.31	0.66
Total	100.83	99.34	100.50	100.08	99.51	100.32	98.81	99.50	100.16	98.53	98.69	97.06	100.44	98.93	98.90	99.72

Matrix	Discovery Hill CM042															
SiO2	64.59	56.05	55.22	70.67	51.78	64.07	59.62	60.73	64.88	53.37	64.41	62.52	60.81	59.55	64.34	62.19
TiO2	0.10	0.14	0.16	0.12	0.11	0.10	0.97	0.07	0.08	0.30	0.16	0.08	0.08	0.14	0.04	0.07
Al2O3	20.07	26.28	26.12	17.32	29.06	20.48	23.72	22.04	19.18	20.87	19.14	21.88	23.53	22.49	19.03	22.27
FeOT	0.45	0.80	1.28	0.62	0.91	0.64	1.51	0.60	0.35	7.83	0.69	0.45	0.52	0.64	0.25	0.70
MnO	0.00	0.00	0.02	0.01	0.02	0.00	0.00	0.00	0.01	0.18	0.00	0.04	0.00	0.01	0.00	0.01
MgO	0.05	0.08	0.19	0.17	0.17	0.10	0.20	0.15	0.05	3.27	0.05	0.06	0.04	0.16	0.04	0.09
CaO	3.80	9.15	9.66	2.59	12.01	4.53	7.61	6.84	1.94	10.40	1.86	4.19	5.27	6.35	0.59	3.96
Na2O	5.20	4.92	4.47	4.77	4.31	5.28	4.88	4.65	4.55	4.08	4.82	4.93	6.24	4.69	4.11	6.31
K2O	5.61	1.68	0.98	4.27	0.35	4.20	1.75	2.82	7.51	0.33	8.67	5.56	3.38	3.28	10.38	4.30
Total	99.86	99.09	98.11	100.72	98.71	99.40	100.25	97.90	98.54	100.60	99.60	99.71	99.87	97.29	98.77	99.90

Matrix	North Shore CM055															
SiO2	53.76	52.66	53.39	55.00	55.76	54.74	54.96	54.96	53.51	54.53	53.59	53.96	54.37	54.97	55.69	54.54
TiO2	1.04	1.73	0.53	0.84	0.18	0.40	0.84	0.40	1.22	0.95	1.32	0.54	0.81	0.73	0.97	0.85
Al2O3	23.33	21.86	20.73	23.95	25.54	23.53	23.28	23.66	22.31	20.67	20.54	24.64	24.22	23.43	22.30	24.61
FeOT	5.23	7.72	8.92	4.32	1.76	4.77	5.44	4.01	5.99	7.57	8.66	5.34	4.71	4.72	5.26	3.43
MnO	0.07	0.16	0.20	0.04	0.05	0.10	0.06	0.10	0.09	0.11	0.17	0.07	0.08	0.07	0.06	0.06
MgO	1.13	1.52	3.50	0.92	0.42	1.79	1.35	1.37	1.36	2.20	2.09	1.65	1.21	1.47	1.29	0.72
CaO	8.01	7.62	7.86	7.99	8.58	8.09	7.94	8.20	7.81	6.88	6.87	8.74	8.20	7.98	7.13	8.48
Na2O	4.72	4.37	4.07	5.07	5.27	4.62	4.68	4.57	5.03	4.48	4.34	4.52	4.97	4.68	4.81	4.92
K2O	0.98	0.97	0.52	0.83	0.84	0.82	0.84	0.94	0.77	1.05	1.17	0.56	0.69	0.79	1.01	0.83
Total	98.27	98.61	99.71	98.97	98.40	98.85	99.41	98.21	98.10	98.42	98.53	100.03	99.27	98.85	98.52	98.26

Table D2 continued

Matrix																
SiO2																
TiO2																
Al2O3																
FeOT																
MnO																
MgO																
CaO																
Na2O																
K2O																
Total																

Coté Creek CM023c

Matrix																
SiO2	58.44	58.85	65.65	57.74	54.80	57.93	55.20	62.38	61.56	55.28	62.91	74.58	54.34	54.93	57.39	61.82
TiO2	0.10	0.55	0.16	0.11	0.11	0.10	0.13	0.08	0.10	0.19	0.17	0.19	0.09	0.11	0.14	0.28
Al2O3	26.21	21.90	19.23	25.87	26.55	24.81	26.97	21.48	21.80	27.30	22.87	12.38	28.18	27.21	25.22	21.10
FeOT	0.51	1.52	0.55	0.84	0.95	0.70	0.63	0.87	0.51	0.88	0.62	1.56	0.57	0.98	0.90	1.31
MnO	0.00	0.00	0.02	0.00	0.00	0.02	0.00	0.02	0.05	0.00	0.00	0.00	0.00	0.01	0.00	0.03
MgO	0.04	0.11	0.03	0.11	0.18	0.11	0.05	0.15	0.06	0.07	0.07	0.27	0.04	0.11	0.12	0.12
CaO	9.68	9.81	3.43	7.98	9.79	7.19	9.82	4.07	4.01	9.33	6.65	1.16	10.82	9.81	8.22	6.64
Na2O	4.60	4.55	4.38	6.56	4.68	5.63	4.70	5.82	6.61	4.63	5.20	2.81	5.04	4.85	5.01	4.62
K2O	1.04	1.50	5.51	1.02	1.05	2.38	1.66	4.35	3.67	1.49	2.32	5.69	0.43	1.31	2.17	2.09
Total	100.62	98.58	98.96	100.24	98.09	98.86	99.16	99.00	98.38	99.18	100.80	98.64	99.51	99.33	99.18	98.02

South Shore CM071

Matrix																
SiO2	58.04	55.55	57.93	56.38	58.68	57.86	55.89	58.78	56.57	55.85	59.21	55.51	58.28	55.42	56.93	56.33
TiO2	0.18	1.40	1.22	0.91	0.18	0.20	3.71	2.50	1.34	0.21	0.40	1.22	0.34	1.85	0.17	0.20
Al2O3	25.52	19.95	22.66	22.80	25.92	26.23	21.80	20.42	24.22	24.39	24.35	24.46	24.28	23.26	26.19	26.02
FeOT	0.74	5.80	1.97	2.00	0.95	1.06	4.90	6.02	3.61	2.24	1.10	2.99	1.26	4.77	0.66	1.31
MnO	0.00	0.06	0.02	0.00	0.00	0.02	0.09	0.11	0.03	0.03	0.04	0.02	0.03	0.06	0.02	0.00
MgO	0.06	0.14	0.25	0.77	0.17	0.19	0.37	0.65	0.11	0.40	0.14	0.20	0.26	0.32	0.07	0.44
CaO	7.50	6.41	6.60	7.29	7.43	7.84	5.75	6.41	6.78	7.25	7.65	7.47	7.02	6.40	8.44	8.07
Na2O	5.20	5.07	5.04	5.45	5.64	5.28	4.68	4.38	4.95	5.17	4.89	5.15	5.17	4.95	5.17	5.26
K2O	2.16	2.89	2.39	2.15	1.33	1.37	2.27	2.54	2.07	1.51	2.00	1.74	2.13	2.49	1.53	1.20
Total	99.40	97.30	98.07	97.54	100.30	100.06	99.48	99.81	99.89	97.04	99.78	98.76	98.78	99.51	99.17	98.84

Discovery Hill CM042

Matrix																
SiO2	55.29	53.61	58.76	55.93	56.63	65.77	66.09	61.17	58.21	66.78	54.83	53.56	63.41	68.43	74.43	54.47
TiO2	0.20	0.07	0.06	0.13	0.09	0.07	0.09	0.09	0.08	0.09	0.08	0.08	0.07	0.07	0.10	0.09
Al2O3	24.57	27.70	26.60	25.79	26.95	19.57	19.12	22.02	24.87	19.16	27.16	27.91	21.65	18.78	13.49	28.59
FeOT	1.04	0.78	0.76	2.80	0.98	0.19	0.61	0.87	0.57	0.71	0.54	0.75	0.37	0.47	0.61	0.90
MnO	0.00	0.00	0.01	0.03	0.00	0.02	0.00	0.00	0.04	0.01	0.04	0.00	0.02	0.01	0.01	0.00
MgO	0.13	0.12	0.15	0.74	0.13	0.05	0.13	0.06	0.02	0.15	0.07	0.07	0.04	0.10	0.14	0.15
CaO	7.84	10.39	8.64	9.00	9.27	0.66	4.17	5.55	7.22	5.66	9.61	10.86	3.53	2.06	1.19	11.03
Na2O	8.57	5.43	5.14	5.32	5.74	4.23	4.38	5.08	5.45	4.05	4.36	5.19	5.38	3.62	2.98	4.67
K2O	2.15	0.48	1.96	0.72	0.50	9.98	4.20	3.98	2.87	3.03	2.41	0.51	6.18	7.27	5.87	0.60
Total	97.79	98.58	100.12	100.27	100.27	100.73	98.79	98.60	99.31	99.65	99.09	98.93	100.84	98.82	98.80	100.51

North Shore CM055

Matrix																
SiO2	54.72	55.74	54.47	54.34	54.98	53.54	54.25	54.14	52.93	53.49	55.07	56.30	54.88	54.80	55.32	54.55
TiO2	0.62	0.77	0.67	1.29	0.42	1.02	0.69	0.11	1.96	2.21	0.61	0.14	0.58	0.45	0.61	0.36
Al2O3	26.09	24.20	21.35	22.28	24.80	21.78	21.86	28.03	20.78	21.92	23.81	25.38	25.57	23.70	22.69	25.31
FeOT	3.06	3.86	7.25	5.50	3.23	7.28	6.20	0.66	8.36	8.70	4.79	0.74	2.10	4.16	5.04	3.09
MnO	0.06	0.06	0.17	0.07	0.06	0.10	0.12	0.00	0.12	0.13	0.06	0.00	0.05	0.06	0.15	0.03
MgO	0.87	0.64	2.35	1.75	0.79	1.92	1.97	0.04	2.51	0.70	1.29	0.06	0.26	1.33	1.47	1.15
CaO	9.10	7.91	7.79	7.73	8.27	7.66	7.72	10.20	7.55	7.00	8.31	8.06	8.58	8.32	7.48	8.96
Na2O	5.08	5.11	4.51	4.49	5.04	4.88	4.65	4.91	4.52	4.77	4.75	5.39	5.41	4.95	4.93	4.86
K2O	0.60	0.82	0.70	0.72	0.72	0.79	0.74	0.54	0.61	1.12	0.69	0.97	0.71	0.87	0.76	0.54
Total	100.00	99.31	99.26	98.18	98.31	98.77	98.20	98.64	99.35	98.03	99.40	97.04	98.14	98.44	98.45	98.85

Table D2 continued

Matrix																
SiO2																
TiO2																
Al2O3																
FeOT																
MnO																
MgO																
CaO																
Na2O																
K2O																
Total																

Coté Creek CM023c

Matrix																
SiO2	64.71	52.61	57.36	57.05	65.81	71.45	59.43	53.92	75.49	55.94	64.09	68.08	60.78	58.63	65.37	64.04
TiO2	0.41	0.10	0.11	0.14	0.35	0.36	0.15	0.12	0.77	0.12	0.43	0.51	0.28	0.08	0.42	0.34
Al2O3	19.40	29.31	24.80	24.89	18.97	15.18	24.89	26.28	11.82	25.83	19.90	16.98	23.84	25.89	19.47	21.05
FeOT	1.51	0.56	0.87	1.04	1.09	0.68	0.76	2.41	1.70	0.97	1.30	1.24	1.10	0.73	0.84	1.02
MnO	0.01	0.04	0.00	0.01	0.01	0.00	0.04	0.08	0.00	0.00	0.00	0.00	0.03	0.02	0.03	0.05
MgO	0.18	0.08	0.15	0.11	0.10	0.08	0.10	0.66	0.14	0.14	0.11	0.19	0.08	0.09	0.08	0.07
CaO	5.39	12.05	7.67	8.49	4.58	1.51	7.03	9.31	0.94	8.73	5.26	2.19	7.98	8.43	4.52	5.18
Na2O	4.58	4.62	5.73	5.36	4.60	3.39	5.16	4.82	2.34	5.09	4.44	4.76	4.66	5.27	4.64	5.30
K2O	2.69	0.39	1.82	1.46	3.55	7.44	2.58	1.02	5.85	1.57	3.23	5.00	1.93	1.33	3.30	3.26
Total	98.88	99.74	98.50	98.55	99.07	100.09	99.92	98.59	99.08	98.39	98.78	98.95	100.67	100.27	98.67	100.32

South Shore CM071

Matrix																
SiO2	56.58	54.49	57.17	60.78	61.54	59.81	56.09	56.75	60.23	56.21	58.10	59.26	57.01	53.99	54.58	55.17
TiO2	0.24	0.98	0.12	0.21	0.82	0.14	0.09	0.09	0.17	0.32	0.20	0.29	0.17	0.14	0.13	0.11
Al2O3	26.13	20.88	24.18	22.81	19.14	23.01	27.46	26.44	24.55	23.76	24.35	23.24	24.95	26.85	27.30	26.64
FeOT	1.02	4.45	1.77	1.23	4.67	0.91	0.56	0.80	0.64	1.60	1.19	1.26	1.00	1.36	0.66	0.67
MnO	0.00	0.10	0.04	0.01	0.03	0.01	0.04	0.05	0.03	0.01	0.03	0.00	0.03	0.03	0.01	0.02
MgO	0.18	1.98	0.47	0.21	0.19	0.17	0.10	0.12	0.08	0.27	0.17	0.18	0.15	0.25	0.08	0.04
CaO	7.93	7.76	7.26	6.20	4.29	7.75	8.95	8.29	6.67	6.14	6.93	6.31	7.95	8.96	9.20	8.65
Na2O	5.76	5.03	5.13	4.55	4.10	5.11	5.45	5.44	5.30	4.58	4.81	4.81	5.03	4.71	5.52	5.53
K2O	1.22	1.38	2.19	2.46	3.84	1.82	0.75	1.18	2.20	3.30	2.25	2.61	1.49	1.21	0.60	0.94
Total	99.07	97.05	98.32	98.46	98.83	98.72	99.51	99.16	100.07	98.19	98.02	97.95	97.78	97.51	98.07	97.78

Discovery Hill CM042

Matrix																
SiO2	69.89	62.37	56.14	70.56	76.75	53.31	59.59	80.83	52.46	57.33	56.15	62.90	58.87	57.76	69.93	54.61
TiO2	0.10	0.38	0.10	0.10	0.17	0.07	0.12	0.10	0.09	0.08	0.08	0.65	0.12	0.10	1.05	0.10
Al2O3	17.82	21.46	25.83	18.47	12.60	29.18	24.36	9.29	26.81	26.73	26.27	19.36	25.53	25.26	14.91	26.16
FeOT	0.56	1.31	0.59	0.77	0.75	0.85	0.73	1.01	1.29	0.75	0.69	1.61	0.67	0.80	1.99	0.76
MnO	0.00	0.03	0.00	0.03	0.03	0.04	0.02	0.04	0.03	0.00	0.02	0.02	0.01	0.02	0.00	0.00
MgO	0.06	0.09	0.05	0.15	0.16	0.12	0.11	0.22	0.22	0.11	0.06	0.20	0.12	0.11	0.12	0.09
CaO	2.81	4.63	8.52	4.39	0.60	11.41	7.17	1.22	11.67	8.63	8.58	2.11	7.87	6.12	2.56	10.35
Na2O	4.75	5.40	5.52	3.89	2.75	4.66	5.87	2.49	4.26	5.56	4.96	4.65	5.22	4.61	3.28	4.47
K2O	4.43	4.42	1.86	1.91	6.57	0.31	2.01	2.61	0.38	1.50	2.76	7.32	2.30	2.44	4.96	1.31
Total	100.42	100.11	98.62	98.28	100.37	99.95	100.00	98.02	99.21	100.70	99.59	98.82	100.69	99.41	98.80	99.86

North Shore CM055

Matrix																
SiO2	54.57	55.93	53.58	54.06	54.91	53.49	53.97	54.10	54.26	53.24	54.97	55.72	54.69	55.01	53.40	53.67
TiO2	0.98	0.07	1.29	1.11	0.38	1.39	0.93	0.67	0.55	0.68	0.55	0.58	0.93	0.71	0.61	0.79
Al2O3	23.85	27.92	17.40	24.60	26.35	25.48	22.44	22.57	24.44	22.59	24.48	25.60	21.29	23.50	21.88	21.38
FeOT	5.03	0.58	10.15	3.97	1.75	3.42	8.30	5.57	3.83	6.45	4.18	2.27	6.88	3.84	7.15	7.20
MnO	0.05	0.00	0.18	0.08	0.00	0.04	0.09	0.11	0.10	0.13	0.08	0.07	0.14	0.06	0.14	0.14
MgO	1.01	0.04	3.63	1.00	0.17	0.44	1.76	1.70	1.04	1.85	1.06	0.21	1.98	0.66	2.14	2.13
CaO	8.12	9.28	6.67	8.49	8.84	8.81	7.76	7.99	8.26	7.98	8.29	8.63	7.75	8.34	7.89	7.90
Na2O	4.90	5.30	3.79	4.73	5.33	5.23	4.75	4.66	5.11	4.74	4.67	4.82	4.19	4.62	4.37	4.35
K2O	0.72	0.62	0.90	0.68	0.73	0.65	0.71	0.75	0.83	0.54	0.60	1.03	1.01	1.37	0.83	0.86
Total	99.22	99.74	97.59	98.69	98.46	98.95	96.72	98.11	98.43	98.41	99.07	98.92	98.67	98.10	98.40	98.43

Table D2 continued

Matrix	
SiO2	
TiO2	
Al2O3	
FeOT	
MnO	
MgO	
CaO	
Na2O	
K2O	
Total	

Coté Creek CM023c

Matrix				Pigeonite						Titanomagnetite				
SiO2	58.28	62.81	62.13	SiO2	52.50	51.84	52.67	49.81	50.06	0.14	0.19	0.16	0.15	0.13
TiO2	0.11	0.18	0.37	TiO2	0.47	0.44	0.56	0.51	0.52	14.64	14.80	20.64	19.99	20.29
Al2O3	25.18	22.02	17.76	Al2O3	0.93	0.93	1.32	1.04	1.21	1.59	1.65	1.68	1.70	1.68
FeOT	0.92	0.80	4.47	FeOT	23.08	23.45	22.44	26.43	27.01	77.03	76.82	71.25	72.09	72.81
MnO	0.01	0.05	0.08	MnO	0.44	0.46	0.46	0.57	0.60	0.26	0.38	0.42	0.39	0.38
MgO	0.12	0.04	1.15	MgO	21.24	20.50	21.69	17.20	17.52	0.31	0.29	0.30	0.28	0.32
CaO	8.16	6.98	4.20	CaO	1.74	1.74	1.62	1.86	1.78	0.13	0.18	0.08	0.08	0.05
Na2O	5.70	4.83	4.81	Na2O										
K2O	1.19	2.21	4.69	K2O										
Total	99.87	99.51	99.65	Total	100.41	99.36	100.96	97.41	98.68	94.10	94.29	94.53	94.68	95.65

South Shore CM071

Matrix						
SiO2	55.70	57.76	55.02	60.11	55.65	59.20
TiO2	0.15	1.22	2.34	0.22	0.41	0.30
Al2O3	28.58	22.31	22.45	23.49	23.59	24.40
FeOT	0.63	4.36	3.09	1.09	2.90	1.05
MnO	0.00	0.14	0.11	0.01	0.07	0.00
MgO	0.09	0.18	0.23	0.12	0.97	0.15
CaO	10.02	5.45	7.47	6.05	7.70	6.72
Na2O	5.07	5.01	4.80	5.35	5.38	5.34
K2O	0.51	2.87	1.99	2.44	1.06	2.17
Total	100.74	99.31	97.49	98.87	97.74	99.34

Discovery Hill CM042

Matrix									Augite		Titanomagnetite		
SiO2	57.43	57.18	55.48	54.43	63.87	58.10	62.51	62.64	49.20	48.92	0.21	1.20	0.16
TiO2	0.11	0.10	0.08	0.10	0.12	0.11	0.15	0.15	0.80	0.81	16.45	15.97	16.54
Al2O3	25.79	25.31	27.81	28.04	21.65	24.38	22.12	21.50	1.11	1.23	1.12	1.25	1.14
FeOT	0.61	0.69	0.58	0.84	0.80	0.91	0.67	1.00	23.95	21.51	71.48	71.92	73.47
MnO	0.01	0.01	0.01	0.00	0.00	0.02	0.03	0.07	0.56	0.49	0.39	0.45	0.32
MgO	0.10	0.16	0.04	0.16	0.10	0.15	0.10	0.29	12.22	10.51	0.40	0.49	0.41
CaO	9.12	9.99	10.15	9.97	5.75	8.90	6.03	6.36	10.15	14.06	0.10	0.21	0.10
Na2O	4.63	4.52	5.34	4.74	5.09	4.93	4.44	4.52					
K2O	1.13	0.49	0.72	1.07	2.72	1.10	3.64	2.71					
Total	99.12	98.46	100.21	99.34	99.91	98.59	99.70	99.23	97.96	97.54	90.16	91.49	92.16

North Shore CM055

Matrix		
SiO2	61.37	60.93
TiO2	0.29	0.67
Al2O3	21.46	21.44
FeOT	1.08	1.92
MnO	0.00	0.00
MgO	0.13	0.10
CaO	6.40	6.31
Na2O	4.37	4.13
K2O	2.41	2.52
Total	97.52	98.02

Table D3. Laser Ablation-ICPMS Analyses of the matrix in the melt rock units at Mistastin Lake

SiO2	TiO2	Al2O3	FeOT	MnO	MgO	CaO	Na2O	P2O5	Total	Sc	V	Cr	Co	Ni	Cu	Zn	Rb	Sr	Y	Zr	Nb
Coté Creek CM088																					
57.83	0.80	23.75	3.61	0.04	0.63	7.73	5.00	0.39	99.78	7.6	46.5	19.8	6.3	46.2	16.2	46.8	32.7	628.2	15.0	97.7	7.2
56.14	0.77	23.64	4.66	0.06	1.23	8.80	4.01	0.48	99.78	11.0	51.7	25.2	9.4	0.0	12.5	55.5	23.3	611.0	14.1	121.1	5.6
56.05	0.79	23.50	4.23	0.06	1.17	8.52	4.95	0.52	99.79	9.7	46.8	22.0	8.7	28.3	11.4	51.9	26.2	623.5	13.6	113.9	6.5
56.45	0.74	24.42	3.57	0.04	0.85	8.67	4.66	0.40	99.79	7.1	40.2	16.2	5.5	93.1	12.0	48.0	24.7	668.2	12.2	106.3	6.6
56.87	0.66	24.52	3.18	0.03	0.36	9.00	4.53	0.65	99.80	6.6	33.7	17.7	4.8	28.2	12.8	45.7	24.5	662.1	13.1	97.1	5.9
56.68	0.74	24.83	2.59	0.03	0.18	9.25	4.82	0.68	99.80	6.4	32.4	9.2	2.9	25.8	8.7	54.2	22.3	659.9	17.4	99.8	6.5
56.07	0.75	24.67	3.29	0.03	0.19	9.52	4.30	0.97	99.78	9.2	32.1	15.6	3.7	0.0	14.6	51.8	24.8	661.1	18.6	116.2	6.1
56.29	1.48	24.35	3.52	0.04	0.17	8.80	4.49	0.65	99.78	8.0	48.2	21.9	3.7	19.8	7.1	72.5	24.2	652.2	17.3	109.0	15.8
57.56	0.79	23.51	4.22	0.04	0.72	8.39	3.98	0.56	99.77	8.9	45.6	24.5	6.6	0.0	12.9	60.3	34.9	613.2	13.3	109.0	6.8
56.29	0.75	24.08	3.80	0.03	0.24	9.11	4.83	0.67	99.79	8.4	34.9	11.8	3.8	38.2	9.6	56.1	20.5	636.3	13.3	94.0	5.4
57.09	0.79	24.27	2.83	0.03	0.32	8.91	4.90	0.66	99.80	6.9	37.8	14.6	4.1	14.9	7.1	47.4	24.5	633.6	14.7	109.1	7.2
57.44	0.98	23.26	3.62	0.04	0.43	8.50	4.78	0.71	99.76	9.3	46.8	20.5	4.5	142.6	15.7	51.2	30.7	605.5	16.2	141.2	8.6
57.71	0.59	23.42	3.30	0.04	0.52	8.45	5.27	0.52	99.80	7.1	34.2	28.7	5.6	0.0	10.0	48.2	20.5	603.0	11.2	109.9	4.7
73.87	0.02	1.33	0.01	0.00	4.38	6.47	13.86	0.01	99.96	0.0	0.7	6.0	0.2	0.0	4.2	1.6	30.0	36.5	1.3	98.2	0.5
Coté Creek CM023c																					
58.98	0.21	21.55	2.36	0.03	3.74	7.47	4.80	0.59	99.73	6.5	4.8	0.0	5.1	0.0	8.1	25.2	42.8	551.0	22.6	135.9	4.0
61.10	0.44	23.24	1.62	0.01	0.53	7.31	5.33	0.17	99.74	4.5	9.7	4.4	4.1	0.0	13.1	141.0	33.9	613.1	19.2	265.5	7.6
62.39	0.27	23.22	1.00	0.01	0.09	7.26	5.25	0.26	99.75	3.7	2.0	0.0	2.6	0.0	14.8	25.9	34.0	630.1	17.6	282.4	11.2
61.67	0.21	24.22	0.78	0.01	0.10	7.76	4.93	0.12	99.78	3.0	1.7	0.4	0.6	0.0	10.7	19.0	27.8	656.7	7.9	186.9	6.8
64.28	0.17	22.73	1.05	0.01	0.06	6.47	4.76	0.22	99.75	3.8	2.0	0.0	1.4	0.0	6.3	14.6	53.7	545.8	22.1	169.5	4.0
57.86	0.10	25.58	1.93	0.01	0.19	9.13	4.81	0.17	99.79	2.3	3.1	3.7	1.9	0.0	10.2	24.0	28.0	725.6	15.1	62.4	1.2
63.57	0.12	23.17	1.11	0.01	0.27	7.04	4.41	0.11	99.81	2.6	1.8	5.0	2.1	0.0	3.8	15.2	40.1	538.1	9.6	135.4	2.8
59.72	0.13	25.54	0.87	0.01	0.24	8.39	4.81	0.08	99.79	3.0	1.0	6.2	0.2	22.8	3.6	17.8	30.1	651.3	7.6	129.7	3.5
66.24	0.18	21.30	0.99	0.01	0.08	5.80	4.90	0.25	99.74	3.9	1.8	3.3	1.7	12.7	8.9	14.8	58.6	507.5	20.1	295.8	7.8
62.14	0.21	24.12	0.97	0.01	0.16	7.77	4.23	0.16	99.77	2.6	3.2	9.1	1.5	30.3	5.1	20.4	33.4	601.3	11.5	136.0	4.2
61.10	0.24	22.89	2.91	0.05	0.09	8.03	4.32	0.12	99.74	9.5	5.2	8.1	5.1	22.9	13.0	36.3	29.7	645.6	8.1	238.7	7.7
59.21	1.15	23.18	2.76	0.03	0.74	7.66	4.82	0.24	99.77	5.4	12.3	0.5	5.5	15.5	12.2	59.5	30.9	594.3	12.0	143.8	13.2
62.09	0.40	21.91	4.03	0.06	0.32	7.11	3.61	0.23	99.76	12.1	8.7	5.1	8.4	0.0	8.0	46.6	33.9	496.4	17.0	311.9	8.7
63.83	0.38	21.35	1.50	0.01	1.24	6.37	4.62	0.40	99.70	5.1	3.1	8.4	4.2	16.9	10.6	27.7	63.9	566.3	22.2	349.7	12.3
Coté Creek CM025																					
54.33	0.36	16.78	11.38	0.22	5.00	8.35	3.07	0.22	99.71	33.2	32.8	7.6	26.2	44.1	7.8	142.5	9.0	453.9	34.6	72.4	2.15
55.96	0.37	19.49	8.13	0.16	3.77	7.99	3.67	0.20	99.74	20.6	36.9	8.8	22.1	17.5	23.9	124.4	11.3	524.5	28.8	87.7	2.40
58.07	2.28	13.08	12.78	0.19	3.32	6.66	3.05	0.26	99.69	31.6	416.9	7.8	36.4	7.7	15.0	136.1	47.7	295.6	29.7	159.4	10.59
58.10	0.30	15.78	13.66	0.24	1.64	7.16	2.80	0.05	99.73	28.2	53.2	29.6	39.0	65.8	4.8	172.1	2.0	447.9	11.4	33.0	0.65
59.95	0.19	24.40	1.16	0.01	0.16	9.08	4.77	0.10	99.81	2.3	2.9	3.7	1.2	0.6	3.6	14.6	11.9	677.7	5.9	176.4	3.26
61.51	0.24	24.10	1.07	0.01	0.05	8.13	4.53	0.13	99.78	3.6	11.1	0.0	0.9	0.8	12.1	16.1	28.5	604.5	11.1	259.7	5.36
62.65	0.44	22.75	1.23	0.01	0.08	7.72	4.66	0.22	99.76	4.6	4.1	1.6	1.1	0.0	9.2	23.4	21.1	598.1	14.6	304.6	9.56
63.17	0.32	23.22	0.91	0.01	0.05	7.07	4.84	0.16	99.75	3.5	2.5	1.5	0.7	0.0	19.6	15.7	28.9	586.4	12.0	231.3	7.32
63.47	0.28	22.74	0.91	0.01	0.05	7.73	4.45	0.15	99.79	3.3	2.0	0.6	0.8	0.0	5.3	16.9	29.3	598.2	8.0	219.8	6.98
63.73	0.13	20.37	2.88	0.02	0.56	5.65	6.38	0.04	99.76	3.6	87.8	1.2	4.0	4.1	42.2	36.9	28.2	469.7	4.4	100.9	1.46
64.11	0.37	22.26	1.15	0.01	0.09	6.88	4.78	0.12	99.77	3.7	2.3	1.6	1.3	8.5	18.0	35.7	33.4	536.9	7.3	334.6	8.48
64.70	0.28	22.09	0.98	0.01	0.06	6.97	4.51	0.17	99.77	3.7	2.3	0.0	0.7	0.0	7.0	17.8	27.8	552.2	11.6	236.9	7.07
64.96	0.31	22.00	1.08	0.01	0.11	6.74	4.46	0.11	99.78	3.2	2.2	0.0	1.3	0.0	6.1	15.9	53.3	554.7	6.3	308.4	7.19
66.23	0.41	20.56	1.27	0.01	0.07	6.50	4.38	0.29	99.73	5.9	3.2	2.6	1.1	0.0	13.9	24.3	35.4	512.6	20.2	367.2	11.03

Table D3 continued

Ba	La	Ce	Pr	Nd	Sm	Eu	Gd	Tb	Dy	Ho	Er	Tm	Yb	Lu	Hf	Ta	Pb	Th	U
Coté Creek CM088																			
684	40.8	82.6	9.3	33.6	4.18	1.46	4.77	0.55	3.37	0.59	1.52	0.23	1.02	0.14	2.80	0.18	8.1	3.47	0.25
644	33.3	67.4	7.8	32.1	5.14	1.46	3.92	0.43	3.64	0.49	1.86	0.23	1.34	0.23	2.40	0.24	6.6	2.80	0.24
605	33.8	67.7	7.8	26.6	5.32	1.71	4.83	0.50	3.12	0.60	1.60	0.21	1.49	0.26	2.37	0.27	5.3	2.36	0.24
575	33.0	66.6	7.2	29.0	4.48	1.43	3.95	0.49	2.54	0.43	1.09	0.14	1.13	0.07	2.33	0.28	5.7	2.51	0.23
616	33.7	68.2	7.7	29.8	4.28	1.52	3.74	0.53	2.43	0.42	1.50	0.12	1.02	0.17	2.31	0.26	6.6	2.67	0.19
657	40.8	81.2	9.3	34.5	6.36	1.76	4.74	0.60	3.43	0.60	1.65	0.24	1.53	0.20	2.69	0.27	6.7	2.98	0.30
679	44.1	84.7	10.1	36.9	5.57	1.69	3.59	0.61	3.75	0.74	2.29	0.30	1.58	0.21	2.24	0.31	14.9	2.48	0.28
633	42.7	85.1	10.0	38.8	6.34	1.48	4.90	0.66	3.39	0.68	1.90	0.26	1.66	0.28	2.27	0.66	6.3	2.69	0.29
747	36.0	73.0	8.7	33.2	5.24	1.79	3.92	0.44	3.05	0.61	1.28	0.20	1.45	0.12	2.21	0.26	11.4	2.87	0.32
636	32.5	61.9	7.2	29.2	4.43	1.73	4.74	0.54	2.59	0.37	1.60	0.12	1.22	0.22	1.82	0.23	4.8	2.12	0.22
616	39.9	80.8	9.5	38.2	6.00	1.75	4.90	0.55	3.10	0.55	1.32	0.15	1.47	0.26	2.85	0.30	7.4	2.99	0.25
713	45.6	93.2	10.9	41.2	5.70	1.87	5.66	0.67	4.26	0.54	1.82	0.17	1.53	0.17	3.25	0.43	7.2	3.79	0.25
655	30.8	58.7	7.1	26.1	4.53	1.59	4.17	0.44	2.48	0.48	1.36	0.17	1.76	0.08	2.14	0.19	7.6	2.31	0.25
207	1.9	3.1	0.3	1.2	0.17	0.13	0.01	0.04	0.15	0.05	0.13	0.06	0.16	0.03	2.47	0.06	5.6	0.35	0.29
Coté Creek CM023c																			
1346	55.3	130.9	15.3	58.1	11.48	2.63	6.91	0.93	5.83	0.94	2.14	0.29	1.80	0.31	3.66	0.16	11.6	2.97	0.28
1133	37.7	78.0	9.0	33.3	6.43	2.12	4.22	0.41	3.85	0.72	2.02	0.25	1.93	0.19	6.20	0.26	11.1	3.58	0.33
1227	33.3	65.1	7.3	28.5	4.74	2.21	4.21	0.47	3.14	0.79	2.09	0.24	1.97	0.29	6.75	0.45	9.5	4.99	0.43
1067	19.0	37.3	4.1	14.0	1.81	1.88	1.87	0.19	1.71	0.27	0.91	0.13	1.13	0.16	4.52	0.30	9.7	2.62	0.45
1402	42.7	89.1	11.2	38.5	7.69	1.95	5.21	0.50	4.07	0.92	2.11	0.31	1.33	0.28	3.34	0.29	11.4	2.64	0.29
918	30.8	59.5	6.9	27.3	5.11	2.49	3.84	0.53	2.65	0.71	1.83	0.20	1.25	0.20	0.92	0.09	8.9	1.47	0.12
976	21.6	42.1	4.5	16.6	2.57	1.78	2.29	0.22	2.14	0.30	0.87	0.17	1.04	0.21	2.98	0.16	10.8	2.26	0.21
1023	20.6	39.9	4.5	15.9	2.02	2.30	1.95	0.24	1.38	0.28	0.72	0.08	0.76	0.19	2.57	0.29	12.0	2.34	0.30
1329	34.3	71.3	8.3	32.3	6.20	2.06	5.22	0.55	4.15	0.92	2.57	0.34	2.05	0.37	7.62	0.42	12.3	4.50	0.68
1190	27.5	56.4	6.7	24.6	4.10	2.09	3.42	0.31	2.40	0.47	1.06	0.20	1.09	0.12	2.18	0.21	10.8	1.98	0.27
1186	17.2	35.2	3.9	13.3	3.38	2.13	2.60	0.18	1.29	0.41	0.73	0.16	0.85	0.15	4.42	0.25	10.3	2.11	0.39
991	24.8	47.7	5.1	18.0	3.19	1.96	2.48	0.32	2.41	0.51	1.04	0.28	0.93	0.24	3.53	0.50	10.6	2.78	0.38
893	36.4	80.2	9.3	32.9	5.99	2.24	5.42	0.32	3.17	0.56	1.55	0.26	1.39	0.15	8.61	0.59	7.4	2.06	0.45
1614	35.4	75.5	8.2	32.2	6.19	1.84	4.12	0.70	4.16	0.68	2.68	0.38	1.88	0.47	7.85	0.49	11.6	5.92	0.76
Coté Creek CM025																			
653	56.78	119.80	13.95	59.89	10.20	2.26	8.79	1.12	7.32	1.46	3.82	0.46	3.23	0.51	1.99	0.11	5.91	2.16	0.16
670	51.93	112.28	13.55	55.03	9.18	2.36	7.40	0.98	5.92	1.11	3.31	0.39	2.55	0.39	1.96	0.13	7.12	1.86	0.14
597	22.30	48.22	5.81	25.03	5.60	1.67	5.70	0.85	5.76	1.15	3.00	0.46	2.97	0.46	4.43	0.69	10.20	5.26	1.57
463	9.77	16.80	1.95	8.17	1.43	1.47	1.80	0.23	1.94	0.42	1.23	0.22	1.60	0.25	1.24	0.01	2.89	0.23	0.04
825	16.62	31.42	3.36	12.45	2.22	2.16	1.37	0.16	1.14	0.21	0.57	0.09	0.51	0.09	3.89	0.10	7.57	1.08	0.17
1056	24.07	45.13	5.06	17.73	3.01	2.13	2.56	0.33	1.82	0.36	1.07	0.18	1.00	0.17	5.83	0.34	9.87	2.77	0.37
1152	26.37	48.78	5.31	19.97	3.57	2.05	2.97	0.38	2.50	0.47	1.40	0.25	1.51	0.24	6.58	0.37	11.14	3.13	0.44
1429	24.00	46.40	5.07	19.76	2.99	2.00	2.45	0.34	2.22	0.45	1.25	0.19	1.10	0.19	4.98	0.32	10.04	2.61	0.36
1069	18.56	35.90	3.94	14.40	2.31	2.20	1.84	0.23	1.59	0.27	0.74	0.12	0.81	0.14	4.80	0.33	9.45	2.15	0.34
1307	11.97	17.28	1.76	7.35	0.97	1.62	0.76	0.09	0.55	0.15	0.33	0.05	0.22	0.06	2.38	0.11	21.02	0.44	0.13
1160	15.05	28.39	3.09	10.53	1.94	1.88	1.41	0.22	1.38	0.29	0.90	0.13	0.99	0.13	7.87	0.43	11.13	2.80	0.53
1231	22.91	44.12	4.84	18.58	3.21	1.84	2.44	0.32	2.11	0.39	1.17	0.17	1.21	0.19	4.84	0.31	10.67	2.36	0.35
1086	15.84	31.52	3.14	12.18	2.01	2.01	1.13	0.23	1.16	0.26	0.71	0.12	0.70	0.14	6.17	0.31	10.79	1.84	0.30
1360	35.81	71.80	7.94	30.36	4.97	1.96	4.09	0.56	3.89	0.71	2.12	0.31	2.04	0.30	7.87	0.46	12.72	4.12	0.55

Table D3 continued

SiO2	TiO2	Al2O3	FeOT	MnO	MgO	CaO	Na2O	P2O5	Total	Sc	V	Cr	Co	Ni	Cu	Zn	Rb	Sr	Y	Zr	Nb
60.95	0.39	24.00	2.16	0.01	0.34	7.38	4.21	0.27	99.73	7.2	5.7	10.2	2.4	0.0	46.3	53.0	42.7	609.7	18.3	324.8	11.03
59.15	0.35	23.63	2.97	0.03	0.55	8.34	4.54	0.19	99.75	7.2	10.6	11.6	5.4	0.0	32.0	72.3	32.5	656.1	16.1	250.6	6.65
59.81	0.70	23.94	3.13	0.02	0.51	7.78	3.62	0.23	99.74	8.0	17.7	9.3	5.0	26.1	97.1	75.8	36.3	600.5	20.9	178.2	9.71
61.58	0.43	23.61	1.76	0.02	0.21	7.83	4.08	0.24	99.75	5.0	6.1	6.2	1.7	0.0	19.0	22.6	37.1	622.1	16.6	308.0	9.96
61.01	1.14	22.28	2.73	0.04	0.31	7.69	4.13	0.36	99.68	9.6	14.0	4.2	2.2	2.1	34.2	31.2	27.3	594.8	41.8	483.2	21.47
57.98	0.50	19.07	8.18	0.13	2.61	7.50	3.52	0.24	99.73	18.2	40.8	22.8	16.9	35.3	21.9	118.2	32.5	490.8	19.4	181.6	6.27
57.29	0.21	26.25	1.55	0.02	0.27	9.71	4.46	0.04	99.78	2.1	7.2	5.3	3.0	49.6	17.8	14.4	10.2	817.4	1.7	15.8	1.35
62.98	0.86	21.45	2.67	0.03	0.39	6.68	4.17	0.47	99.68	8.2	13.3	0.9	2.2	0.0	33.1	25.5	37.5	507.6	39.8	368.7	21.09
55.23	1.35	23.14	5.73	0.09	1.11	8.87	4.14	0.09	99.75	8.1	98.1	24.3	11.2	0.0	16.5	154.0	13.4	716.6	6.1	68.0	7.34
57.65	0.50	22.06	6.09	0.09	1.69	8.43	3.15	0.10	99.76	11.1	45.6	30.5	13.2	16.8	8.4	100.8	38.5	651.6	6.7	109.6	4.38
South Shore CM071																					
60.15	0.64	23.22	2.58	0.04	0.28	7.77	4.92	0.18	99.78	5.9	56.1	52.4	16.0	0.0	14.2	197.5	24.2	634.3	12.8	54.5	6.5
60.06	0.38	25.06	1.21	0.01	0.19	8.28	4.47	0.17	99.83	1.7	16.9	9.1	4.0	101.2	3.5	20.8	17.7	648.0	10.2	72.8	6.1
61.10	0.64	22.61	3.22	0.03	0.45	6.90	4.73	0.13	99.80	5.8	57.7	33.2	9.5	0.0	5.4	52.4	21.6	586.2	10.8	81.0	5.3
56.59	1.48	23.71	3.81	0.04	0.54	8.38	5.07	0.17	99.79	6.4	101.0	49.3	9.7	35.3	13.3	81.6	18.4	702.1	9.8	73.3	10.2
61.63	0.85	23.09	2.13	0.03	0.28	7.00	4.58	0.18	99.79	4.2	49.2	37.3	9.5	0.0	6.1	25.1	33.9	597.1	12.9	169.1	10.0
58.08	0.13	26.03	0.99	0.01	0.09	9.21	5.16	0.09	99.81	1.3	6.4	3.5	4.5	40.0	4.6	14.1	8.3	720.0	10.5	24.0	2.2
64.18	0.15	21.90	1.78	0.02	0.42	6.73	4.52	0.07	99.76	3.5	4.8	1.4	4.2	514.1	1.2	23.8	42.7	540.7	6.7	178.4	2.3
63.71	0.48	23.06	1.48	0.02	0.19	6.38	4.29	0.16	99.78	6.7	15.8	0.0	13.8	97.9	12.0	21.1	49.4	541.4	20.4	195.2	9.5
58.38	0.87	23.66	3.06	0.04	0.37	7.97	5.25	0.16	99.77	7.8	86.2	104.9	17.9	0.0	20.2	92.1	32.4	623.8	19.4	81.0	8.5
60.45	0.25	24.45	1.42	0.02	0.35	8.30	4.38	0.20	99.82	4.6	9.2	3.8	7.0	83.2	5.4	33.0	27.6	620.9	15.0	129.4	4.2
58.72	0.06	25.79	0.56	0.01	0.10	8.06	6.53	0.06	99.89	0.6	2.1	0.1	3.0	0.0	3.8	35.3	9.7	633.4	3.6	17.9	1.2
59.39	0.73	23.76	3.06	0.04	0.57	7.66	4.38	0.18	99.77	7.8	19.9	2.2	17.8	0.0	49.6	192.7	23.2	589.2	23.0	64.8	9.2
63.59	0.40	23.12	1.69	0.02	0.19	6.05	4.61	0.11	99.77	5.7	15.1	0.0	8.9	52.8	10.3	34.3	48.9	566.9	17.1	133.9	9.1
58.15	0.67	24.70	2.46	0.03	0.23	8.06	5.34	0.18	99.82	3.7	54.0	22.7	6.0	0.0	4.9	34.0	17.2	630.5	12.4	65.5	5.0
South Shore CM067																					
62.29	0.84	17.70	6.41	0.09	1.72	5.76	4.40	0.48	99.69	14.4	28.8	3.5	14.3	0.0	58.7	89.2	47.7	362.5	43.0	319.4	13.8
65.32	0.73	19.66	2.86	0.04	0.42	5.75	4.64	0.33	99.74	9.5	7.6	0.0	3.7	5.7	22.1	46.1	78.9	410.7	37.4	491.4	18.6
57.32	0.72	21.90	5.34	0.08	1.76	8.33	4.18	0.14	99.79	10.1	51.7	14.7	12.8	22.1	5.8	68.1	14.9	605.6	10.6	134.5	6.1
60.53	0.50	19.83	5.34	0.08	1.94	7.27	3.97	0.29	99.76	13.4	26.8	9.0	13.2	14.3	13.0	69.1	42.0	529.5	26.2	240.4	8.4
58.66	0.68	20.97	5.59	0.09	1.85	7.38	4.41	0.13	99.75	10.4	73.7	8.5	14.0	20.3	8.2	80.7	30.2	537.6	13.9	165.4	5.3
59.16	0.90	19.56	6.73	0.11	1.93	6.76	4.39	0.20	99.75	12.2	69.9	20.4	15.1	16.7	10.2	92.5	33.1	474.5	16.8	187.4	8.6
58.60	0.19	22.98	3.31	0.05	1.15	8.92	4.51	0.09	99.81	7.7	18.8	2.6	8.4	11.2	5.4	32.8	10.7	639.1	7.4	58.5	2.3
56.40	1.35	19.10	8.89	0.14	2.39	7.50	3.81	0.15	99.74	15.1	109.6	16.6	20.4	19.8	11.1	140.6	32.1	498.4	15.6	157.0	8.5
57.02	0.23	24.61	2.93	0.05	0.99	9.87	4.02	0.08	99.81	6.0	16.9	0.2	7.8	0.0	8.0	39.7	17.3	737.2	7.6	90.0	3.1
59.90	2.33	15.61	10.59	0.17	2.53	4.10	4.22	0.22	99.66	18.3	178.7	20.2	26.7	36.1	20.1	165.8	68.0	297.3	25.7	377.5	18.2
61.40	0.27	22.36	2.13	0.03	0.63	7.06	5.76	0.14	99.77	6.4	9.7	0.8	3.8	21.6	11.1	33.2	20.4	600.3	12.3	169.3	5.8
56.06	0.23	20.41	6.81	0.12	3.10	9.06	3.92	0.06	99.77	18.6	43.6	3.2	20.4	28.3	6.5	85.3	5.0	634.7	9.2	27.1	1.3
65.12	0.47	21.16	1.69	0.02	0.14	6.21	4.78	0.20	99.79	3.9	7.3	1.8	1.8	0.0	12.2	24.2	33.7	499.5	17.5	232.2	9.6
58.75	0.36	19.96	6.08	0.10	2.28	7.77	4.40	0.08	99.78	15.1	37.7	17.9	14.9	17.9	5.4	71.4	13.6	564.2	10.4	67.5	2.5

Table D3 continued

Ba	La	Ce	Pr	Nd	Sm	Eu	Gd	Tb	Dy	Ho	Er	Tm	Yb	Lu	Hf	Ta	Pb	Th	U
1173	37.01	76.58	8.95	32.21	5.95	2.57	4.65	0.58	3.40	0.74	2.12	0.28	2.18	0.30	7.87	0.52	10.80	4.37	0.51
963	32.73	68.15	7.40	32.26	4.78	2.26	4.33	0.48	2.71	0.63	1.69	0.25	1.55	0.22	7.33	0.31	8.77	3.06	0.40
960	48.61	102.87	11.37	43.80	6.90	2.19	4.36	0.79	5.48	0.92	1.92	0.32	2.01	0.28	3.84	0.39	11.00	3.50	0.44
1055	33.81	68.99	7.76	29.65	4.48	2.07	3.63	0.51	3.34	0.63	1.83	0.30	1.75	0.27	7.17	0.40	9.18	3.95	0.39
1203	91.46	196.44	23.34	89.58	14.88	2.78	10.16	1.70	8.94	1.54	4.60	0.60	3.86	0.51	11.71	1.09	10.15	7.22	0.72
738	33.75	74.28	8.60	35.86	6.09	2.24	5.88	0.71	3.39	0.82	2.53	0.29	1.71	0.27	3.94	0.33	9.05	2.89	0.31
1050	9.84	16.98	1.67	6.90	0.81	2.22	0.72	0.08	0.44	0.07	0.12	0.01	0.23	0.04	0.43	0.02	4.65	0.26	0.03
1397	84.75	185.59	20.78	86.36	13.01	1.96	11.66	1.23	7.68	1.69	4.07	0.65	3.26	0.60	7.09	0.74	12.38	8.48	0.82
711	19.08	38.58	4.09	16.08	2.76	2.13	1.64	0.16	1.57	0.25	0.72	0.11	0.70	0.12	1.73	0.26	6.39	1.38	0.15
746	16.34	32.75	3.48	14.33	2.10	1.60	1.68	0.21	1.44	0.28	0.79	0.16	0.84	0.08	2.20	0.20	6.88	1.47	0.19
South Shore CM071																			
797	23.7	44.1	5.04	20.1	3.86	2.10	3.37	0.52	2.45	0.50	1.37	0.19	1.25	0.23	1.60	0.40	9.09	1.93	0.34
517	32.4	60.6	7.03	26.1	3.90	1.27	1.75	0.41	2.18	0.42	1.05	0.23	0.89	0.23	1.75	0.20	6.94	2.82	0.27
641	33.7	64.6	6.75	25.9	3.82	1.15	3.89	0.38	1.81	0.55	1.17	0.12	0.82	0.13	1.67	0.28	8.23	2.89	0.30
510	29.0	54.0	5.58	21.0	3.50	1.29	2.04	0.35	1.53	0.22	1.20	0.07	1.05	0.13	2.02	0.63	5.95	2.16	0.30
841	29.6	57.3	6.34	22.8	4.90	1.57	2.50	0.31	2.50	0.53	0.94	0.10	0.87	0.14	4.16	0.48	8.23	5.24	0.54
827	35.4	63.0	6.94	24.8	3.71	2.42	2.30	0.33	1.74	0.39	0.84	0.10	1.00	0.09	0.58	0.17	9.44	1.80	0.29
837	18.4	31.1	2.99	10.8	2.14	1.47	1.03	0.19	1.26	0.32	1.01	0.15	1.30	0.13	4.83	0.23	10.34	4.23	0.63
905	42.1	82.3	9.53	36.8	6.08	1.90	4.28	0.66	4.04	0.93	2.22	0.40	2.74	0.21	4.63	0.49	12.33	6.17	0.93
691	37.8	81.7	8.86	35.4	6.97	1.74	4.96	0.52	4.31	0.66	1.63	0.23	1.73	0.15	1.85	0.32	8.17	3.62	0.62
528	32.6	64.9	7.14	28.4	4.58	1.36	4.07	0.45	2.93	0.45	1.46	0.20	1.20	0.20	2.90	0.18	6.95	3.32	0.36
293	23.5	33.8	2.92	10.3	0.73	2.64	1.15	0.09	1.01	0.23	0.21	0.00	0.19	0.10	0.25	0.00	13.97	0.90	0.17
739	55.9	114.6	14.36	53.0	8.78	1.53	8.93	0.78	4.47	0.64	2.37	0.37	2.52	0.22	1.62	0.35	8.96	2.79	0.40
1069	34.5	69.5	7.43	27.1	5.63	1.61	3.98	0.36	3.62	0.62	2.16	0.43	1.74	0.41	2.24	0.43	10.70	4.72	0.69
567	36.0	68.3	8.00	28.8	4.27	1.47	3.19	0.51	2.78	0.48	1.61	0.16	1.57	0.16	1.41	0.21	7.28	3.16	0.22
South Shore CM067																			
1041	84.1	182.0	21.7	92.0	15.70	1.55	13.34	1.62	9.76	1.60	4.07	0.72	4.39	0.57	7.23	0.60	17.87	6.52	0.94
803	74.3	161.5	18.5	71.7	11.60	1.75	9.28	1.16	7.83	1.37	3.82	0.55	3.46	0.51	11.27	0.86	17.74	8.81	1.03
599	17.5	34.1	3.9	14.5	2.97	1.68	2.02	0.26	1.92	0.33	1.39	0.13	1.49	0.14	3.18	0.17	5.77	1.22	0.18
703	44.1	94.2	10.3	42.1	7.56	1.56	4.79	0.79	4.58	0.96	2.70	0.51	2.36	0.37	5.75	0.37	10.33	3.70	0.45
816	29.7	65.0	7.4	28.3	4.22	1.71	3.75	0.47	3.37	0.48	1.83	0.22	1.67	0.20	3.65	0.30	7.98	2.39	0.80
801	31.0	63.4	7.3	26.5	4.55	1.38	3.88	0.62	3.08	0.64	1.59	0.21	1.78	0.27	4.05	0.34	9.62	3.48	0.33
694	15.3	30.3	3.6	12.6	2.16	1.51	1.85	0.20	1.62	0.26	0.70	0.09	0.55	0.12	1.11	0.08	5.89	1.16	0.14
615	27.7	57.4	6.3	26.3	4.99	1.39	3.36	0.55	3.19	0.67	1.60	0.27	1.89	0.26	3.73	0.35	8.50	2.36	0.26
642	17.9	36.9	4.1	15.4	3.18	1.69	1.66	0.30	1.40	0.28	0.83	0.15	1.10	0.08	2.07	0.22	6.53	1.58	0.26
868	48.6	101.4	12.5	44.9	9.07	1.80	5.93	0.84	5.11	0.96	2.54	0.32	3.28	0.39	9.52	0.64	13.31	5.86	0.65
1026	27.1	68.1	5.7	21.9	4.95	2.28	3.37	0.31	2.34	0.56	1.31	0.23	0.99	0.20	4.03	0.34	8.79	2.60	0.39
675	14.5	30.3	3.2	13.4	2.42	1.49	2.05	0.30	2.18	0.29	1.21	0.18	1.07	0.19	0.50	0.06	3.82	0.49	0.08
886	40.6	87.8	9.9	37.3	6.23	1.71	4.82	0.51	3.50	0.65	1.76	0.25	1.78	0.24	5.16	0.45	12.30	3.79	0.51
686	13.3	28.5	3.2	12.9	2.71	1.38	2.06	0.27	1.88	0.41	1.07	0.14	1.15	0.21	1.52	0.13	5.65	1.08	0.15

Table D3 continued

SiO2	TiO2	Al2O3	FeOT	MnO	MgO	CaO	Na2O	P2O5	Total	Sc	V	Cr	Co	Ni	Cu	Zn	Rb	Sr	Y	Zr	Nb
Discovery Hill CM042																					
53.08	1.81	16.95	14.69	0.19	2.08	6.81	3.57	0.43	99.61	30.2	196.9	27.6	23.6	0.0	15.8	261.2	19.2	402.8	59.0	52.6	7.3
66.43	0.23	21.82	0.89	0.01	0.10	5.81	4.28	0.15	99.72	3.5	1.3	0.0	0.7	0.0	9.0	16.6	66.6	533.5	20.2	408.3	10.8
61.40	1.09	21.11	4.65	0.04	0.55	6.13	4.59	0.14	99.69	7.4	16.6	0.0	7.4	0.0	19.7	93.4	51.0	496.7	23.8	366.0	13.8
61.71	0.56	18.92	6.10	0.10	1.80	6.65	3.61	0.20	99.63	19.8	24.6	4.5	10.0	49.6	17.2	69.2	64.2	461.8	30.7	1358.5	15.1
59.24	0.30	23.41	3.54	0.03	0.87	8.28	3.64	0.38	99.67	12.1	3.8	0.0	4.8	0.0	35.3	50.2	41.1	614.0	59.7	646.7	18.7
63.75	0.25	22.96	1.46	0.01	0.32	5.80	5.18	0.06	99.78	0.9	3.4	3.7	2.8	0.0	12.0	20.2	67.9	522.3	3.8	16.9	3.4
66.41	0.09	20.29	1.37	0.01	0.36	6.70	4.01	0.52	99.76	2.3	2.1	2.1	2.0	0.0	9.1	16.7	50.1	491.5	34.1	53.8	1.0
63.16	0.09	22.96	1.37	0.01	0.36	6.75	4.83	0.26	99.78	0.7	3.1	2.0	2.7	0.0	10.6	24.0	54.8	543.8	18.9	8.5	0.3
52.98	0.55	12.84	17.62	0.31	5.73	7.42	1.95	0.27	99.67	46.2	64.8	15.1	34.3	22.2	15.1	221.1	13.3	285.2	54.0	252.8	5.0
60.88	0.07	24.91	1.09	0.01	0.27	7.83	4.72	0.03	99.81	1.0	1.5	0.6	1.9	1.7	10.3	20.1	58.6	579.2	2.3	15.6	0.3
56.66	0.68	17.12	10.33	0.17	3.31	7.33	3.77	0.32	99.70	23.0	31.2	6.7	22.2	24.6	11.2	143.4	36.8	457.3	28.4	229.6	6.3
64.99	0.09	22.60	0.86	0.00	0.21	5.75	4.81	0.37	99.69	1.3	1.0	0.0	1.0	0.0	9.3	11.4	99.2	620.0	26.2	17.3	0.3
64.19	1.83	16.70	8.50	0.12	1.03	3.86	3.43	0.02	99.69	19.7	23.6	12.3	12.9	9.1	7.0	154.5	66.0	397.6	12.3	181.5	20.5
Discovery Hill CM035																					
72.55	0.35	17.35	1.90	0.01	0.08	3.18	4.26	0.04	99.72	5.2	1.0	1.6	0.7	0.0	8.3	16.8	54.7	342.3	21.2	470.6	12.4
67.12	0.24	20.05	1.78	0.01	0.08	5.10	5.29	0.02	99.69	3.5	1.1	1.6	0.8	0.0	6.0	21.8	40.6	520.4	14.2	342.8	8.4
62.17	0.15	23.03	1.72	0.01	0.07	7.61	4.96	0.07	99.78	1.3	1.5	1.2	0.4	0.4	4.6	18.9	43.8	576.9	7.3	168.2	4.5
54.68	0.24	14.55	15.20	0.26	4.90	6.92	2.95	0.02	99.72	34.9	29.9	2.2	29.8	13.2	3.7	157.0	5.6	458.3	18.6	12.8	0.2
57.83	0.07	25.82	0.97	0.00	0.05	10.34	4.71	0.05	99.84	0.5	2.1	0.0	0.2	14.7	3.3	18.0	3.2	810.0	1.1	5.7	0.1
67.40	0.19	20.17	2.05	0.01	0.12	4.84	4.92	0.02	99.72	2.1	1.1	0.0	0.9	7.8	6.5	16.9	75.4	488.0	7.7	216.3	5.8
63.11	0.19	22.57	1.47	0.01	0.07	7.28	5.06	0.02	99.79	1.2	1.0	0.0	0.6	0.0	4.2	22.3	22.7	576.5	7.3	159.8	5.6
60.37	0.31	23.96	1.74	0.01	0.10	8.52	4.76	0.03	99.80	1.4	2.1	6.6	1.0	0.0	6.0	29.0	8.7	708.7	4.0	61.7	5.8
66.81	0.25	20.61	1.56	0.01	0.11	5.49	4.86	0.02	99.73	2.1	0.9	0.3	0.7	0.0	6.1	20.4	76.4	498.4	10.8	305.7	9.7
65.28	0.26	20.41	2.61	0.02	0.23	6.83	4.07	0.08	99.79	4.0	1.8	5.3	2.0	0.1	9.2	32.8	53.3	481.3	15.6	300.9	9.7
64.54	0.08	21.65	1.51	0.01	0.21	6.56	5.16	0.01	99.74	2.5	1.3	0.0	1.6	0.0	13.8	28.8	39.7	519.3	2.6	332.7	2.9
71.59	0.77	15.09	4.02	0.04	0.20	3.95	3.67	0.33	99.66	13.1	2.3	1.3	3.1	0.0	10.0	66.5	68.8	312.4	47.1	986.2	31.6
North Shore CM055																					
57.09	0.80	21.33	6.09	0.11	1.87	8.35	3.97	0.12	99.73	12.8	51.8	43.6	14.1	15.7	8.6	89.5	5.6	614.0	14.9	56.2	7.2
56.36	0.92	20.22	7.65	0.13	2.20	7.90	4.18	0.14	99.72	15.6	69.4	29.3	19.1	24.8	4.1	123.8	10.0	575.1	20.7	100.6	6.1
57.43	0.89	21.49	5.77	0.10	1.59	8.12	4.21	0.13	99.73	11.4	60.7	31.4	13.3	24.5	3.3	85.7	9.0	612.1	16.8	119.0	7.6
56.69	1.03	20.66	7.35	0.13	2.01	7.89	3.81	0.14	99.72	14.8	77.5	38.2	17.8	26.2	1.8	107.9	11.1	571.7	21.1	126.3	6.9
58.03	1.09	20.40	7.03	0.12	1.55	7.66	3.69	0.14	99.71	16.1	73.3	42.2	15.1	16.0	4.4	98.3	18.8	547.1	24.6	157.5	11.1
58.93	1.14	17.60	9.10	0.16	2.38	6.78	3.40	0.19	99.68	23.4	81.1	44.1	19.9	24.4	6.0	129.5	26.8	474.9	31.7	170.5	11.5
60.94	0.74	17.27	8.14	0.15	2.58	6.48	3.25	0.13	99.68	23.1	44.5	19.6	18.8	44.0	5.6	123.9	31.6	463.6	29.3	295.4	10.9
64.24	0.81	17.60	6.07	0.11	1.59	5.85	3.33	0.10	99.68	15.8	41.8	20.9	12.7	28.4	4.8	93.4	51.4	447.5	29.7	293.3	13.9
57.87	1.07	20.42	6.81	0.11	1.55	7.90	3.82	0.15	99.70	13.9	63.6	34.1	15.2	20.6	5.3	105.6	13.4	594.2	21.4	128.3	9.2
60.08	0.80	20.46	5.58	0.10	1.41	7.43	3.75	0.11	99.72	11.5	51.7	25.3	12.5	19.4	4.5	90.9	20.6	567.7	15.6	139.8	7.1
58.63	0.86	19.96	6.95	0.12	1.78	7.72	3.57	0.10	99.69	16.4	54.6	28.7	15.1	29.5	5.6	115.1	16.1	586.9	21.9	134.9	8.6
57.81	0.90	19.54	7.60	0.14	2.09	7.90	3.61	0.12	99.70	17.0	62.0	30.5	17.0	32.2	5.3	122.6	12.9	575.5	20.2	109.6	7.7
59.66	0.89	20.09	5.87	0.10	1.35	7.68	3.96	0.12	99.72	11.8	54.2	30.8	12.4	19.4	3.9	98.4	20.5	570.5	18.8	166.6	9.2
61.15	0.81	19.47	5.72	0.10	1.40	7.30	3.66	0.11	99.72	13.2	46.4	21.4	11.9	19.2	4.7	91.5	26.7	533.3	20.6	202.1	10.0

Table D3 continued

Ba	La	Ce	Pr	Nd	Sm	Eu	Gd	Tb	Dy	Ho	Er	Tm	Yb	Lu	Hf	Ta	Pb	Th	U
Discovery Hill CM042																			
750	129.6	287.6	33.2	124.1	19.78	2.53	15.67	2.10	12.67	2.19	5.50	0.93	6.49	0.64	1.05	0.22	9.38	4.34	0.25
1479	34.0	72.2	8.7	34.2	5.82	2.64	3.90	0.68	4.19	0.78	2.00	0.30	2.24	0.38	9.48	0.88	14.17	7.75	0.87
1248	61.0	113.6	12.3	47.4	8.06	2.31	6.51	0.76	5.40	0.99	3.41	0.35	2.08	0.49	9.07	0.58	13.97	5.30	0.45
785	40.1	91.7	11.6	42.8	7.84	2.37	5.83	0.91	6.45	1.07	3.24	0.53	3.56	0.56	26.99	1.07	11.84	7.09	0.83
827	143.1	298.1	32.4	115.2	20.26	2.45	14.63	1.55	13.15	1.72	6.28	1.05	5.99	0.90	11.18	0.61	10.03	7.76	0.76
1279	20.4	36.3	3.6	10.6	1.29	2.13	1.36	0.08	0.64	0.11	0.32	0.02	0.28	0.09	0.39	0.13	14.97	0.50	0.03
1212	84.2	181.4	21.3	80.0	12.67	2.62	9.91	1.10	6.68	1.56	3.39	0.42	2.29	0.27	1.66	0.15	13.38	4.40	0.36
1155	53.4	107.7	12.0	44.6	7.04	2.54	4.18	0.62	3.82	0.61	1.81	0.27	0.97	0.20	0.55	0.00	15.10	3.67	0.18
307	56.3	129.3	15.2	68.6	12.99	1.76	13.11	1.46	10.94	2.22	7.12	0.80	7.67	0.83	7.51	0.30	6.79	7.08	0.49
1031	17.5	25.3	2.4	8.4	0.98	2.46	0.81	0.09	0.54	0.05	0.31	0.07	0.38	0.06	0.81	0.05	15.47	0.57	0.05
783	48.9	105.5	12.0	49.8	8.66	2.16	6.76	0.81	5.67	1.08	2.69	0.47	2.85	0.56	6.09	0.39	10.89	2.00	0.16
1930	70.5	147.3	15.6	62.9	10.14	3.43	7.91	1.02	4.71	0.99	2.96	0.29	2.05	0.20	0.71	0.01	17.60	4.13	0.20
1342	13.8	21.7	2.2	8.2	2.30	1.70	1.83	0.37	1.84	0.50	1.65	0.45	2.02	0.39	5.01	0.59	13.79	2.21	0.21
Discovery Hill CM035																			
1497	42.5	86.1	9.3	32.2	5.56	2.29	4.45	0.58	4.02	0.91	2.53	0.38	2.42	0.28	10.08	0.54	18.71	5.99	0.94
1806	28.4	53.6	5.9	20.5	3.65	3.00	2.74	0.41	2.58	0.53	1.48	0.23	1.74	0.28	7.83	0.50	13.81	5.12	0.62
1065	23.3	46.3	4.7	17.5	2.54	2.92	1.62	0.27	1.31	0.25	0.89	0.11	0.83	0.10	3.81	0.25	12.63	2.47	0.34
591	9.5	17.8	2.1	9.1	2.33	1.96	2.66	0.46	3.31	0.76	2.23	0.37	3.03	0.47	0.41	0.00	5.42	0.11	0.02
621	10.7	19.1	1.9	6.7	0.84	2.81	0.48	0.06	0.30	0.07	0.09	0.02	0.16	0.03	0.08	0.00	5.41	0.13	0.03
1682	24.2	40.8	4.0	13.8	2.19	2.68	1.34	0.21	1.58	0.29	1.06	0.14	0.90	0.15	4.19	0.28	17.25	2.31	0.64
1085	24.4	44.0	4.7	16.3	2.90	2.94	1.57	0.23	1.54	0.31	0.77	0.11	0.84	0.11	3.38	0.24	13.11	2.34	0.31
944	15.5	28.7	3.1	11.4	1.55	2.74	1.11	0.15	0.90	0.14	0.41	0.05	0.54	0.06	1.25	0.24	8.62	1.00	0.15
1458	39.4	68.1	8.0	27.0	4.31	2.54	2.63	0.36	2.31	0.45	1.29	0.19	1.12	0.18	6.49	0.55	17.70	4.74	0.59
736	33.6	64.1	8.0	28.7	5.49	2.53	3.31	0.50	3.25	0.63	1.62	0.25	2.04	0.25	6.10	0.43	13.39	4.26	0.72
1389	20.2	27.7	3.0	9.7	1.14	2.55	0.64	0.08	0.57	0.12	0.50	0.03	0.34	0.05	6.21	0.22	16.56	1.87	0.22
1065	77.5	178.7	22.1	84.6	14.89	2.01	10.82	1.66	9.71	1.97	5.52	0.79	5.31	0.76	21.13	1.51	14.16	14.37	1.61
North Shore CM055																			
1050	26.6	54.6	6.4	27.0	4.33	2.14	3.66	0.45	3.06	0.60	1.66	0.23	1.58	0.23	1.28	0.26	7.22	0.61	0.08
965	30.1	64.0	7.7	32.4	5.85	2.23	4.53	0.66	4.40	0.74	2.09	0.30	2.01	0.27	2.15	0.23	7.14	1.27	0.12
1057	29.6	61.3	7.0	29.7	5.41	2.34	4.05	0.51	3.43	0.70	1.68	0.24	1.67	0.24	2.60	0.27	7.57	1.09	0.14
916	31.0	67.6	8.2	34.7	6.32	1.87	5.23	0.74	4.22	0.88	2.20	0.31	1.79	0.27	2.69	0.30	7.29	1.57	0.13
1038	35.6	76.2	9.2	39.1	6.91	2.24	5.87	0.81	5.03	0.98	2.49	0.37	2.68	0.34	3.57	0.47	9.23	1.50	0.20
1088	38.5	85.6	10.8	47.5	8.47	2.24	8.19	1.07	6.95	1.34	3.40	0.47	3.07	0.54	3.78	0.43	9.09	1.53	0.21
1178	34.0	74.8	9.1	38.6	6.76	2.05	5.98	0.90	5.77	1.16	3.14	0.47	3.25	0.52	7.14	0.49	8.77	2.46	0.34
1341	41.6	91.2	10.9	42.6	8.15	2.05	5.88	0.89	6.13	1.19	3.23	0.51	3.12	0.49	6.51	0.66	11.47	3.16	0.41
1153	34.8	76.5	9.1	39.9	6.65	2.54	5.22	0.69	4.52	0.75	2.25	0.32	1.93	0.33	2.99	0.32	8.87	1.37	0.47
1169	30.6	62.9	7.2	29.0	5.15	2.40	4.00	0.54	2.95	0.65	1.53	0.20	1.29	0.26	3.40	0.30	9.09	2.29	0.18
1197	33.6	69.1	8.2	34.4	6.28	2.66	4.90	0.69	4.23	0.86	2.46	0.35	2.48	0.39	3.33	0.28	9.66	1.59	0.19
1083	31.6	69.2	8.1	33.2	5.70	2.44	4.71	0.67	4.28	0.79	2.33	0.33	2.18	0.27	2.49	0.31	8.85	1.73	0.19
1096	35.5	77.3	8.7	36.3	6.08	2.45	4.50	0.65	4.13	0.85	1.89	0.31	2.02	0.25	3.73	0.40	9.00	1.96	0.23
1107	35.4	77.3	9.0	36.4	5.66	2.29	4.38	0.69	4.53	0.82	2.43	0.34	2.07	0.34	4.59	0.44	9.77	2.20	0.24

Table D4. Glass compositions (wt%) in the impact melt matrix measured by EPMA (3 micron beam)

Sample Name	Unit	SiO2	Al2O3	FeO	CaO	Na2O	K2O	Total
CM044	Discovery Hill	98.44	1.26	0.94	0.18	0.18	0.27	101.27
CM044	Discovery Hill	96.80	1.42	2.18	0.27	0.24	0.23	101.15
CM044	Discovery Hill	97.47	2.36	0.48	0.37	0.49	0.11	101.28
CM039	Discovery Hill	76.55	13.39	0.72	3.54	3.60	1.69	99.49
CM039	Discovery Hill	83.38	8.29	1.04	1.98	2.23	2.37	99.30
CM039	Discovery Hill	62.50	22.83	0.64	5.45	5.43	4.23	101.08
CM088	Coté Creek	57.26	23.02	3.20	8.63	3.94	1.05	97.10
CM088	Coté Creek	58.23	23.81	0.98	9.17	5.07	1.17	98.43
CM015	Coté Creek	76.90	13.01	1.93	2.89	2.72	1.96	99.41
CM015	Coté Creek	75.59	15.81	0.34	0.60	3.01	8.54	103.90
CM052	North Shore	81.40	11.28	1.17	0.63	3.17	4.34	101.99
CM052	North Shore	81.51	10.76	1.58	0.50	2.78	4.58	101.72
CM052	North Shore	82.09	10.38	1.05	0.44	2.08	5.78	101.83
CM052	North Shore	68.16	16.82	0.33	1.41	8.05	1.75	96.52
CM067	South Shore	57.13	26.95	0.56	10.08	5.36	0.79	100.87
CM067	South Shore	61.95	23.51	0.47	6.08	7.49	1.24	100.75
CM067	South Shore	64.54	20.83	0.60	2.80	7.54	3.68	100.00

Table D5. LA-ICP-MS U-Pb isotopic analyses of zircons from target rocks at Mistastin Lake Crater

File name	Grain/spot Number	Concentrations			Measured Isotopic Ratios							Calculated Ages										
		U (ppm)	Th (ppm)	Th/U	207Pb/235U	1s error	206Pb/238U	1s error	Rho	207Pb/206Pb	1s error	207Pb/235U Ma	1s error Ma	206Pb/238U Ma	1s error Ma	207Pb/206Pb Ma	1s error Ma	U-Pb/Pb-Pb concordancy (%)	U-Pb Concordia age (Ma)	2s error Ma	MSWD	Probability (of concordance)
Granodiorite, North East shore (CM063)																						
au22A12	2	80	81	1.02	3.0776	0.2403	0.2469	0.0109	0.28	0.0901	0.0009	1427.1	59.8	1422.5	56.4	1427.7	18.2	100	1425	93	0.00	0.95
au22A13	5	76	86	1.13	3.1894	0.1027	0.2450	0.0074	0.47	0.0895	0.0008	1449.7	25.0	1412.7	38.5	1415.9	13.3	100	1444	49	1.14	0.29
au22A16	8	49	54	1.11	3.0716	0.1606	0.2519	0.0065	0.25	0.0907	0.0010	1425.6	40.1	1448.1	33.3	1439.8	20.4	101	1439	57	0.25	0.62
au22A19	11	36	34	0.94	3.0803	0.1681	0.2489	0.0083	0.31	0.0895	0.0008	1427.8	41.8	1432.6	43.0	1415.8	17.8	101	1430	69	0.01	0.92
au22A20	12	45	31	0.68	3.0970	0.0744	0.2517	0.0041	0.34	0.0893	0.0008	1431.9	18.4	1447.2	21.0	1409.9	17.0	103	1438	32	0.45	0.50
au22A29	17	83	42	0.67	3.1356	0.1323	0.2564	0.0067	0.31	0.0905	0.0007	1441.5	32.5	1471.2	34.3	1435.2	15.8	103	1455	54	0.57	0.45
au22A33	34	54	42	0.78	3.0000	0.1648	0.2531	0.0080	0.29	0.0883	0.0007	1407.8	41.8	1454.2	41.3	1388.0	16.2	105	1431	66	0.89	0.35
au22A34	37	83	67	0.80	2.9637	0.1325	0.2452	0.0073	0.33	0.0885	0.0006	1398.4	34.0	1413.8	37.7	1393.9	13.8	101	1405	58	0.14	0.71
au22A36	39	152	115	0.76	3.1150	0.1699	0.2496	0.0108	0.40	0.0889	0.0005	1438.4	41.9	1436.3	55.6	1401.5	11.1	102	1438	78	0.00	1.00
au23A68	41	59	60	1.03	3.1239	0.1269	0.2410	0.0065	0.33	0.0912	0.0009	1438.6	31.3	1392.1	33.5	1450.7	19.4	96	1417	53	1.52	0.22
au23A69	41	41	32	0.76	3.0420	0.1019	0.2508	0.0056	0.33	0.0877	0.0008	1418.2	25.6	1442.6	28.9	1376.3	20.7	105	1428	44	0.80	0.44
au23A70	45	47	35	0.74	3.1579	0.1314	0.2513	0.0089	0.33	0.0891	0.0009	1446.9	32.1	1445.0	35.7	1408.9	19.0	103	1446	55	0.00	0.96
au23A73	48	44	40	0.93	3.1039	0.1281	0.2512	0.0057	0.28	0.0907	0.0010	1433.7	31.2	1444.8	29.3	1441.4	21.0	100	1440	46	0.09	0.76
au23A74	49	66	84	1.27	3.1554	0.0920	0.2465	0.0044	0.31	0.0892	0.0008	1446.3	22.5	1430.7	22.9	1408.6	17.5	102	1439	37	0.34	0.56
au23A75	52	35	35	0.98	3.0048	0.0721	0.2475	0.0041	0.35	0.0879	0.0009	1406.8	18.3	1425.8	21.3	1380.8	18.8	103	1415	32	0.56	0.45
au23A76	53	57	44	0.76	3.0534	0.0933	0.2419	0.0047	0.32	0.0882	0.0009	1421.1	23.4	1396.4	24.4	1386.6	19.4	101	1409	39	0.76	0.38
au23A78	55	111	103	0.93	3.1236	0.1076	0.2463	0.0066	0.39	0.0897	0.0008	1438.6	26.5	1419.4	34.1	1416.8	12.2	100	1433	46	0.31	0.58
au23A79	58	55	50	0.90	3.0263	0.1208	0.2430	0.0065	0.34	0.0899	0.0008	1414.3	30.5	1402.2	33.8	1401.7	17.5	100	1409	52	0.11	0.74
au23A80	59	64	70	1.09	3.0040	0.1206	0.2466	0.0061	0.31	0.0890	0.0007	1408.6	30.6	1421.1	31.4	1403.7	15.5	101	1415	50	0.12	0.73
au23A81	60	61	75	1.24	3.0010	0.1232	0.2386	0.0076	0.39	0.0890	0.0007	1407.9	31.3	1379.5	39.8	1404.9	15.6	98	1399	58	0.51	0.48
au23A83	62	61	50	0.82	3.1565	0.1953	0.2535	0.0094	0.30	0.0903	0.0009	1446.6	47.7	1458.7	48.4	1432.4	18.9	102	1452	77	0.03	0.86
au23A84	65	71	65	0.92	3.1484	0.1047	0.2446	0.0069	0.43	0.0908	0.0007	1444.6	25.6	1410.8	35.9	1441.8	15.1	98	1437	49	0.99	0.32
au22A18	10	67	62	0.94	3.2612	0.2088	0.2522	0.0123	0.38	0.0919	0.0007	1471.8	49.8	1448.8	63.5	1464.9	14.4	99	1465	92	0.12	0.73
au23A82	62	42	32	0.78	3.1314	0.1012	0.2511	0.0058	0.36	0.0882	0.0010	1440.4	24.9	1444.4	29.9	1387.8	21.4	104	1442	44	0.02	0.90
au22A26	19	75	50	0.67	3.1241	0.1838	0.2471	0.0110	0.39	0.0914	0.0007	1438.6	45.3	1423.3	66.8	1455.2	14.5	98	1434	83	0.07	0.79
au22A11	2	49	46	0.93	3.0395	0.1886	0.2412	0.0101	0.34	0.0913	0.0008	1417.8	47.5	1392.7	52.7	1452.7	18.9	96	1407	82	0.18	0.67
Anorthosite, Horseshoe Island (CM032)																						
au01a21	10 84-8				3.0515	0.1954	0.2598	0.0098	0.29	0.0901	0.0010	1420.6	49.2	1488.9	49.9	1427.1	21.1	104	1453	79	1.40	0.24
au01a23	10 75-12				3.0737	0.1527	0.2584	0.0070	0.27	0.0920	0.0010	1426.2	38.1	1481.7	36.1	1456.1	21.2	101	1455	58	1.60	0.21
au01a25	10 58-8				3.0751	0.1952	0.2482	0.0119	0.38	0.0894	0.0009	1426.5	48.6	1429.2	61.3	1412.8	19.4	101	1427	89	0.00	0.97
au01a29	10 38-9				3.0873	0.1540	0.2508	0.0086	0.35	0.0891	0.0009	1429.5	38.3	1441.8	44.5	1405.8	19.5	103	1434	67	0.06	0.80
au01a30	10 35-13				3.0791	0.1081	0.2490	0.0062	0.35	0.0897	0.0006	1427.5	26.9	1433.2	32.0	1418.2	12.7	101	1430	48	0.03	0.87
au01a34	10 33-2				3.1092	0.1813	0.2500	0.0113	0.39	0.0890	0.0009	1435.0	44.8	1438.4	58.3	1404.1	17.8	102	1436	83	0.00	0.95
au01a35	10 31-1				3.2130	0.0957	0.2511	0.0061	0.41	0.0904	0.0007	1460.3	23.1	1444.0	31.6	1433.3	14.9	101	1456	44	0.29	0.59
au01a36	10 31-11				3.1454	0.2177	0.2503	0.0113	0.33	0.0919	0.0011	1443.9	53.3	1440.0	58.2	1464.6	22.0	98	1442	91	0.00	0.95
au01a37	10 30-12				3.0903	0.1102	0.2507	0.0054	0.30	0.0895	0.0007	1430.3	27.4	1442.1	27.9	1416.9	14.5	102	1436	45	0.13	0.72
au01a38	10 30-6				3.1921	0.1620	0.2530	0.0107	0.42	0.0892	0.0009	1455.3	39.2	1454.0	55.2	1408.2	18.8	103	1455	75	0.00	0.98
au01a39	10 29-14				3.1372	0.2635	0.2557	0.0081	0.21	0.0908	0.0008	1441.9	64.7	1467.6	46.9	1442.1	17.0	102	1460	83	0.13	0.72
au01a43	10 24-29				3.0942	0.0595	0.2432	0.0045	0.46	0.0896	0.0003	1431.3	14.8	1403.3	23.5	1417.1	7.5	99	1428	29	1.80	0.18
au01a44	10 24-25				3.0377	0.0983	0.2459	0.0049	0.31	0.0915	0.0008	1417.1	24.7	1417.1	25.1	1457.8	16.5	97	1417	40	0.00	1.00
au01a49	10 20-8				3.0419	0.1212	0.2474	0.0057	0.34	0.0899	0.0007	1418.2	30.4	1425.2	34.8	1422.4	14.8	100	1421	53	0.03	0.85
au01a50	10 14-16				3.1834	0.1274	0.2481	0.0077	0.39	0.0914	0.0008	1453.1	30.9	1428.4	39.7	1455.7	16.8	98	1445	57	0.39	0.53
au01a51	10 14-15				3.2819	0.0756	0.2505	0.0055	0.46	0.0916	0.0008	1476.8	17.9	1441.3	28.4	1459.0	16.5	99	1472	35	2.00	0.16
au01a52	10 11-21				3.1942	0.1052	0.2529	0.0056	0.34	0.0902	0.0009	1455.8	25.5	1453.4	29.0	1429.3	18.7	102	1455	44	0.01	0.94
au01a53	10 11-11				3.1834	0.1048	0.2495	0.0060	0.37	0.0912	0.0007	1453.1	25.4	1435.9	31.0	1450.1	14.8	99	1447	46	0.29	0.59
au01a54	10 10-25				3.1697	0.1226	0.2543	0.0079	0.41	0.0892	0.0007	1454.7	29.7	1460.7	40.8	1407.8	15.2	104	1456	56	0.02	0.88
au01a55	10 8-24				3.1316	0.0872	0.2488	0.0048	0.34	0.0908	0.0007	1440.5	21.4	1432.1	24.6	1441.4	13.8	99	1437	37	0.10	0.75
au01a57	10 5-8				3.1405	0.0574	0.2492	0.0042	0.40	0.0893	0.0005	1442.7	16.5	1434.8	21.9	1411.8	10.4	102	1440	31	0.14	0.71
au01a58	10 5-7				3.0673	0.1554	0.2452	0.0061	0.33	0.0914	0.0008	1424.6	38.8	1413.7	41.9	1454.7	16.9	97	1420	66	0.05	0.82
au01a67	1 62-5				2.9131	0.1419	0.2399	0.0091	0.39	0.0904	0.0008	1385.3	38.8	1386.0	47.1	1434.5	17.1	97	1386	68	0.00	0.98
au01a68	1 54-1				3.0631	0.0645	0.2449	0.0037	0.38	0.0912	0.0005	1423.5	18.1	1412.3	19.0	1451.1	12.1	97	1419	29	0.31	0.58
au01a69	1 33-3				3.0752	0.0671	0.2524	0.0039	0.28	0.0904	0.0007	1426.5	21.7	1450.7	20.3	1434.7	15.4	101	1440	33	0.92	0.34
au01a70	1 7-8				3.1808	0.0786	0.2567	0.0041	0.32	0.0901	0.0008	1452.5	19.1	1472.9	21.0	1427.6	16.5	103	1461	32	0.77	0.38
au01a71	1 1-9				3.0409	0.1196	0.2442	0.0075	0.39	0.0897	0.0007	1418.0	30.1	1409.7	38.7	1419.0	15.6	99	1415	58	0.06	0.81

Table D5 continued

Number	U	Th	Th/U	207Pb/235U	1s error	206Pb/238U	1s error	Rho	207Pb/206Pb	1s error	207Pb/235U	1s error	206Pb/238U	1s error	207Pb/206Pb	1s error	U-Pb/Pb-Pb	U-Pb Concordia	2s error	MSWD	Probability
Manganite, Horseshoe Island (W06-45)																					
au24A05	1			3.3084	0.1080	0.2500	0.0072	0.44	0.0910	0.0007	1483.0	25.5	1438.4	37.0	1446.1	13.9	99	1474	49	1.70	0.20
au24A10	7			3.1391	0.1422	0.2481	0.0080	0.27	0.0913	0.0008	1442.3	34.9	1428.7	30.8	1451.9	18.4	98	1434	52	0.12	0.73
au24A11	8			3.1007	0.2721	0.2474	0.0120	0.28	0.0928	0.0016	1432.9	67.4	1425.1	62.0	1482.8	32.9	96	1429	100	0.01	0.92
au24A13	10			3.1651	0.2281	0.2515	0.0110	0.30	0.0920	0.0013	1448.7	55.6	1446.1	56.8	1467.7	26.5	99	1447	91	0.00	0.97
au24A14	12			3.2668	0.1200	0.2549	0.0063	0.34	0.0912	0.0009	1477.9	28.4	1463.9	32.2	1450.0	18.2	101	1472	49	0.16	0.69
au24A16	17			3.2492	0.1194	0.2598	0.0060	0.31	0.0916	0.0010	1469.0	28.5	1489.0	30.5	1458.9	20.9	102	1478	48	0.33	0.56
au24A18	18			3.0761	0.1081	0.2411	0.0057	0.34	0.0904	0.0007	1426.8	26.9	1392.7	29.8	1434.1	15.5	97	1412	47	1.08	0.30
au24A19	20			3.1694	0.0725	0.2470	0.0042	0.37	0.0912	0.0007	1449.7	17.7	1423.1	21.6	1451.8	14.3	98	1440	32	1.40	0.23
au24A23	30			3.1980	0.1613	0.2518	0.0058	0.23	0.0929	0.0011	1456.9	39.0	1447.8	29.9	1484.8	21.7	98	1451	53	0.04	0.83
au24A24	34			3.3373	0.1171	0.2520	0.0054	0.31	0.0917	0.0010	1489.8	27.4	1448.7	28.0	1460.3	20.8	99	1469	45	1.60	0.21
au24A26	33			3.1397	0.1094	0.2477	0.0050	0.35	0.0908	0.0008	1442.5	26.8	1426.5	31.2	1445.5	16.1	99	1436	47	0.23	0.63
au24A27	39			3.2704	0.0839	0.2551	0.0048	0.37	0.0910	0.0008	1474.0	19.9	1464.9	24.6	1445.8	16.2	101	1471	36	0.13	0.72
au24A28	44			3.1608	0.1007	0.2518	0.0052	0.33	0.0909	0.0009	1447.6	24.6	1447.9	27.0	1443.5	18.2	100	1448	42	0.00	0.91
au24A30	46			3.0959	0.1004	0.2526	0.0048	0.28	0.0918	0.0009	1431.7	24.9	1452.7	23.9	1463.5	18.0	99	1443	39	0.52	0.47
Granodiorite gneiss, North East shore (CA'001)																					
Magmatic grains																					
au28A08	1			3.2740	0.1465	0.2427	0.0111	0.51	0.0893	0.0005	1474.9	34.8	1400.7	57.7	1410.6	11.4	99	1469	70	2.20	0.13
au28A17	6			3.1671	0.2118	0.2456	0.0125	0.38	0.0897	0.0009	1449.2	51.6	1415.7	64.6	1419.6	16.4	100	1438	95	0.26	0.61
au28A18	9			3.1649	0.1754	0.2535	0.0103	0.37	0.0888	0.0008	1448.6	42.8	1456.3	52.9	1400.1	18.1	104	1451	77	0.02	0.89
au28A21	12			3.2344	0.1191	0.2503	0.0089	0.37	0.0909	0.0008	1465.5	28.6	1440.0	35.4	1443.5	16.6	100	1457	52	0.49	0.48
au28A23	14			3.2702	0.1280	0.2547	0.0078	0.39	0.0899	0.0007	1474.0	30.4	1462.7	39.9	1422.8	15.6	103	1471	57	0.08	0.78
au28A29	18			3.3655	0.1158	0.2570	0.0083	0.47	0.0913	0.0007	1496.4	26.9	1474.4	42.7	1453.9	15.1	101	1494	53	0.33	0.57
au28A30	19			3.2676	0.1271	0.2513	0.0096	0.49	0.0893	0.0007	1473.4	30.2	1445.0	49.5	1409.6	15.7	103	1471	60	0.43	0.51
au28A32	21			3.2090	0.1130	0.2432	0.0073	0.42	0.0909	0.0008	1459.3	27.3	1403.2	37.7	1444.5	16.9	97	1445	52	2.40	0.12
au28A35	24			3.0832	0.1290	0.2353	0.0086	0.44	0.0896	0.0005	1426.5	32.1	1362.4	45.0	1417.1	10.3	96	1413	62	2.40	0.12
au28A42	27			2.9821	0.1457	0.2385	0.0089	0.38	0.0894	0.0008	1403.1	37.2	1379.1	46.3	1413.7	13.2	98	1395	68	0.28	0.61
au28A43	28			3.0916	0.1459	0.2413	0.0096	0.42	0.0895	0.0008	1430.6	36.2	1393.7	49.8	1415.0	12.3	98	1421	69	0.60	0.44
au28A44	29			3.2822	0.1315	0.2467	0.0088	0.44	0.0901	0.0008	1472.1	31.3	1421.4	45.7	1428.0	12.8	100	1462	62	1.40	0.23
au28A46	31			3.0827	0.0977	0.2456	0.0047	0.34	0.0896	0.0007	1426.4	21.8	1415.7	24.4	1417.4	14.0	100	1423	38	0.22	0.64
au28A53	35			3.1110	0.1232	0.2457	0.0064	0.33	0.0913	0.0008	1435.4	30.4	1416.2	33.0	1452.6	16.7	97	1427	52	0.27	0.60
au28A60	43			3.1287	0.1283	0.2415	0.0088	0.44	0.0893	0.0005	1439.8	31.6	1394.2	45.6	1410.7	10.6	99	1430	61	1.18	0.28
au28A67	45			3.2054	0.0858	0.2540	0.0053	0.39	0.0885	0.0005	1458.5	20.7	1458.9	27.1	1382.7	11.8	105	1459	38	0.00	0.99
au28A70	49			2.9722	0.1445	0.2291	0.0095	0.43	0.0886	0.0008	1400.5	36.9	1329.9	50.0	1395.7	14.0	95	1382	71	2.20	0.14
au28A71	50			3.0932	0.1344	0.2421	0.0088	0.41	0.0891	0.0005	1431.0	33.3	1397.5	44.5	1405.8	11.4	99	1422	63	0.59	0.44
au28A72	51			3.0006	0.2028	0.2369	0.0114	0.38	0.0894	0.0005	1407.8	51.5	1370.6	58.6	1413.0	12.6	97	1393	91	0.34	0.56
au28A74	53			3.0892	0.1413	0.2457	0.0077	0.34	0.0907	0.0007	1430.0	35.1	1416.0	39.8	1440.9	14.3	98	1424	61	0.11	0.75
Inherited grains																					
au28A28	16			9.6885	0.2951	0.4626	0.0155	0.5602	0.1428	0.0010	2403.72	28.1	2451.1	68.5	2261.2	12.4	108	2400	56	0.66	0.42
au28A31	20			8.4554	0.1957	0.3943	0.0120	0.6548	0.1425	0.0006	2281.14	21.1	2142.9	55.5	2258.4	9.6	95	2303	39	9.80	0.00
au28A33	22			7.7574	0.3242	0.3822	0.0129	0.4049	0.1431	0.0009	2203.27	37.6	2086.7	60.3	2265.2	11.0	92	2183	74	4.30	0.04
au28A34	23			9.1265	0.2772	0.4139	0.0138	0.5502	0.1479	0.0007	2350.77	27.8	2232.9	63.1	2321.5	7.7	96	2358	55	5.00	0.03
au28A55	37			8.2734	0.3325	0.4110	0.0126	0.3802	0.1378	0.0009	2261.41	36.4	2219.6	57.4	2199.1	11.1	101	2254	71	0.58	0.45

Notes: Measured isotopic ratios determined using the LAMDATE data reduction program for LA-ICP-MS (Koller et al. 2008). "Rho" is the correlation coefficient between the two U/Pb isotope ratios calculated as the ratio of the covariance to the product of the standard deviations for each ratio. "U-Pb/Pb-Pb concordancy (%)" is a

Table D.6. LA-ICP-MS U-Pb isotopic analyses of zircon clasts from impact melt rocks at Mistastin Lake Crater

File name	Grain/spot Number	Concentrations			Measured Isotopic Ratios							Calculated Ages										
		U (ppm)	Th (ppm)	Th/U	$^{207}Pb/^{235}U$	1σ error	$^{206}Pb/^{238}U$	1σ error	Rho	$^{207}Pb/^{206}Pb$	1σ error	$^{207}Pb/^{235}U$ Ma	1σ error Ma	$^{206}Pb/^{238}U$ Ma	1σ error Ma	$^{207}Pb/^{206}Pb$ Ma	1σ error Ma	U-Pb/Pb-Pb concordancy (%)	U-Pb Concordia age (Ma)	2σ error Ma	MSWD	Probability (of concordance)
Cole Creek (CM923)																						
in13A08	1	527	81	0.15	6.1893	0.2373	0.3274	0.0117	0.47	0.1365	0.0004	2002.9	33.5	1825.9	57.0	2183.1	5.7	84	1993	67	12.39	0.00
in13A09	1	373	53	0.14	4.7382	0.2185	0.2723	0.0115	0.48	0.1265	0.0008	1773.7	38.7	1552.5	58.0	2049.8	10.6	76	1727	78	17.63	0.00
in13A10	3	79	73	0.93	3.0849	0.0437	0.2475	0.0027	0.38	0.0900	0.0005	1428.9	10.9	1425.5	13.9	1425.4	11.0	100	1428	20	0.05	0.80
in13A11	4	46	41	0.90	3.1805	0.0484	0.2539	0.0036	0.46	0.0929	0.0007	1449.0	11.8	1458.7	18.3	1488.6	14.5	98	1460	23	0.34	0.56
in13A12	5	26	23	0.88	3.0264	0.0753	0.2420	0.0047	0.39	0.0926	0.0009	1414.3	19.0	1397.2	24.2	1484.2	18.2	94	1409	35	0.49	0.48
in13A13	6	61	46	0.75	3.0305	0.0493	0.2478	0.0031	0.39	0.0895	0.0006	1415.3	12.4	1427.3	16.0	1414.7	12.1	101	1419	23	0.58	0.45
in13A14	6	49	45	0.92	2.8789	0.0804	0.2459	0.0043	0.31	0.0882	0.0007	1378.4	21.0	1417.1	22.4	1387.5	15.3	102	1394	35	2.58	0.11
in13A15	7	35	25	0.73	2.9498	0.0651	0.2412	0.0040	0.38	0.0897	0.0007	1394.8	16.7	1392.9	20.8	1420.1	14.7	98	1394	30	0.01	0.93
in13A16	8	69	68	0.97	3.1531	0.0864	0.2468	0.0049	0.37	0.0935	0.0008	1445.8	21.1	1421.7	25.6	1497.7	18.4	95	1437	38	0.82	0.37
in13A19	9	17	21	1.27	3.0723	0.0880	0.2485	0.0044	0.31	0.0928	0.0010	1425.8	22.0	1430.7	22.6	1484.4	21.1	96	1428	36	0.03	0.85
in13A20	11	101	95	0.94	3.1077	0.0802	0.2498	0.0043	0.44	0.0895	0.0005	1434.6	14.9	1437.3	22.1	1415.3	11.8	102	1435	29	0.02	0.89
in13A21	12	46	46	0.98	3.1751	0.1880	0.2594	0.0076	0.25	0.0932	0.0009	1451.1	45.7	1486.9	39.6	1492.8	17.7	100	1472	67	0.47	0.49
in13A22	13	39	44	1.15	2.8829	0.0955	0.2418	0.0055	0.35	0.0895	0.0008	1377.4	25.0	1396.0	28.7	1414.8	17.2	99	1385	43	0.36	0.55
in13A23	14	61	56	0.89	3.0416	0.0846	0.2478	0.0053	0.38	0.0884	0.0005	1418.1	21.3	1427.0	27.2	1390.9	11.9	103	1421	39	0.11	0.75
in13A24	15	59	47	0.79	3.0372	0.0678	0.2510	0.0036	0.32	0.0891	0.0007	1417.0	17.1	1443.6	18.7	1406.3	14.8	103	1428	29	1.53	0.20
in13A26	18	46	37	0.80	3.0672	0.0710	0.2512	0.0035	0.31	0.0910	0.0006	1432.0	17.8	1444.7	18.3	1447.1	13.0	100	1438	29	0.36	0.55
in13A31	19	35	36	1.02	3.1128	0.0580	0.2469	0.0033	0.35	0.0905	0.0007	1435.9	14.8	1436.0	16.9	1435.9	15.7	100	1437	26	0.01	0.91
in13A32	19	46	40	0.87	3.0705	0.1080	0.2484	0.0062	0.35	0.0900	0.0007	1425.4	27.0	1430.1	31.9	1425.9	15.1	100	1427	48	0.02	0.89
in13A33	20	50	37	0.73	3.2321	0.0599	0.2545	0.0040	0.42	0.0901	0.0006	1464.9	14.4	1461.8	20.5	1427.3	12.6	102	1464	28	0.03	0.87
in13A35	22	46	32	0.70	3.0686	0.1307	0.2401	0.0067	0.33	0.0938	0.0006	1429.9	32.5	1387.3	35.1	1503.4	18.7	92	1410	55	1.18	0.28
in13A35	23	39	28	0.71	3.2819	0.0797	0.2520	0.0035	0.30	0.0946	0.0009	1476.6	18.9	1448.7	18.7	1520.6	17.8	95	1462	30	1.58	0.21
in13A37	24	29	52	1.81	3.1586	0.1602	0.2432	0.0051	0.21	0.1001	0.0013	1446.6	39.1	1403.2	28.5	1626.5	24.8	86	1414	46	1.02	0.31
in13A35	25	44	39	0.88	3.1976	0.0689	0.2551	0.0040	0.37	0.0909	0.0008	1456.6	16.7	1464.5	20.7	1423.6	13.2	103	1459	30	0.14	0.71
in13A39	25	47	54	1.16	3.0810	0.0768	0.2522	0.0042	0.33	0.0895	0.0007	1423.0	19.2	1449.9	21.8	1414.3	15.1	103	1434	33	1.29	0.26
in13A40	26	55	40	0.71	3.0851	0.0702	0.2487	0.0041	0.37	0.0896	0.0007	1429.0	17.4	1431.7	21.3	1417.0	15.0	101	1430	31	0.02	0.90
in13A41	27	28	21	0.73	2.9883	0.0852	0.2484	0.0050	0.36	0.0882	0.0008	1404.8	21.7	1419.8	25.8	1387.5	18.7	102	1410	36	0.31	0.58
in13A42	28	76	58	0.73	3.0758	0.0524	0.2470	0.0033	0.39	0.0907	0.0005	1428.7	13.1	1423.1	18.5	1439.5	11.1	99	1428	24	0.04	0.83
in13A43	28	72	50	0.70	3.1081	0.0656	0.2467	0.0040	0.36	0.0899	0.0006	1434.7	16.2	1421.5	20.7	1422.9	11.5	100	1431	30	0.40	0.53
in13A44	29	17	16	0.93	3.2199	0.0941	0.2463	0.0056	0.44	0.0938	0.0011	1462.0	20.2	1419.4	29.1	1504.5	21.5	94	1453	39	2.45	0.12
in13A52	32	43	54	1.25	3.0583	0.0784	0.2517	0.0044	0.34	0.0897	0.0007	1422.3	19.8	1447.2	22.4	1418.7	15.8	102	1432	34	1.05	0.30
in13A53	33	47	39	0.83	3.0792	0.0673	0.2532	0.0038	0.35	0.0903	0.0007	1427.5	16.8	1454.9	19.8	1389.2	15.2	105	1438	29	1.70	0.19
in13A54	34	45	43	0.98	3.0620	0.0680	0.2487	0.0034	0.31	0.0921	0.0008	1426.2	16.9	1421.8	17.5	1468.7	15.8	97	1425	28	0.11	0.74
in13A55	35	42	35	0.83	3.1122	0.0680	0.2474	0.0044	0.40	0.0893	0.0007	1435.7	16.8	1425.2	22.6	1410.7	15.8	101	1433	32	0.23	0.63
in13A56	37	55	46	0.86	3.1784	0.0944	0.2549	0.0057	0.36	0.0895	0.0007	1451.9	22.9	1463.7	29.4	1414.3	14.3	103	1458	42	0.16	0.69
in13A57	38	37	39	1.07	3.0248	0.0843	0.2412	0.0048	0.34	0.0907	0.0007	1413.6	21.3	1392.8	23.9	1440.4	15.1	97	1406	37	0.65	0.42
in13A58	39	31	31	1.00	3.0371	0.0831	0.2518	0.0050	0.36	0.0882	0.0007	1417.0	20.9	1447.7	25.8	1387.3	15.3	104	1427	37	1.33	0.25
in13A59	42	37	25	0.68	3.0541	0.0849	0.2404	0.0054	0.40	0.0896	0.0007	1421.3	21.3	1388.8	28.1	1418.7	15.6	98	1412	40	1.39	0.24
in13A60	43	29	24	0.82	3.0803	0.0809	0.2456	0.0037	0.29	0.0921	0.0009	1427.6	20.1	1415.5	19.0	1469.6	18.4	96	1421	31	0.28	0.60
in13A61	44	26	19	0.74	3.1819	0.1012	0.2458	0.0049	0.31	0.0943	0.0010	1452.8	24.6	1416.9	25.5	1513.7	20.9	94	1435	41	1.49	0.22
in13A62	45	69	49	0.70	3.0635	0.0573	0.2466	0.0037	0.34	0.0895	0.0006	1423.6	16.8	1422.1	19.1	1415.3	13.0	100	1423	29	0.01	0.94
in13A63	46	24	21	0.88	3.1591	0.0739	0.2487	0.0046	0.40	0.0905	0.0009	1447.2	18.0	1431.6	23.8	1437.1	18.3	100	1443	34	0.44	0.51
in13A64	47	61	97	1.20	3.1686	0.0539	0.2469	0.0033	0.40	0.0904	0.0005	1453.9	13.1	1433.0	17.2	1434.6	11.3	100	1448	24	1.51	0.22
in13A65	47	77	99	1.29	3.1897	0.0722	0.2517	0.0045	0.40	0.0895	0.0006	1464.7	17.5	1447.4	23.3	1415.3	12.7	102	1453	33	0.10	0.75
in13A66	48	15	13	0.86	2.9947	0.0575	0.2471	0.0049	0.34	0.0879	0.0010	1408.3	22.2	1423.3	25.2	1379.4	21.2	103	1413	38	0.39	0.53
in13A67	50	110	61	0.73	3.0376	0.0656	0.2448	0.0042	0.40	0.0894	0.0004	1417.1	16.5	1410.7	21.9	1412.9	9.5	100	1415	31	0.09	0.76
in13A68	51	46	35	0.74	3.0948	0.0710	0.2462	0.0040	0.35	0.0901	0.0006	1431.4	17.6	1418.6	20.7	1427.3	13.5	99	1427	31	0.34	0.58
in13A69	52	32	34	1.07	3.0423	0.0804	0.2461	0.0051	0.35	0.0884	0.0009	1418.3	22.4	1418.2	28.3	1391.3	18.4	102	1418	40	0.00	1.00
in13A70	53	69	50	0.72	3.1353	0.0541	0.2542	0.0039	0.34	0.0903	0.0008	1441.4	13.3	1460.3	15.2	1431.5	12.3	102	1449	23	1.91	0.25
Steep Creek (CM906)																						
in13A75	1	41	36	0.87	2.9762	0.1295	0.2441	0.0079	0.37	0.0885	0.0008	1401.8	33.1	1407.9	41.1	1414.5	17.1	100	1404	60	0.02	0.88
in13A76	2	51	42	0.83	3.1552	0.0584	0.2523	0.0034	0.38	0.0921	0.0006	1446.3	14.3	1450.2	17.3	1468.5	13.0	99	1448	26	0.05	0.83
in13A77	3	43	40	0.93	3.0927	0.0630	0.2455	0.0037	0.37	0.0926	0.0007	1430.9	15.8	1415.4	19.0	1479.2	15.1	96	1425	28	0.62	0.43
in13A78	8	24	20	0.84	3.2858	0.1368	0.2200	0.0060	0.32	0.1089	0.0013	1472.9	32.8	1281.9	31.8	1746.4	21.8	73	discordant			
in13A79	7	45	30	0.65	3.0811	0.0804	0.2487	0.0045	0.35	0.0918	0.0007	1423.0	20.1	1421.3	23.4	1469.7	13.8	97	1422	35	0.00	0.95
in13A80	8	35	27	0.76	3.0606	0.0702	0.2525	0.0041	0.35	0.0892	0.0008	1422.9	17.8	1451.8	20.9	1407.6	16.8	103	1433	31	1.89	0.19
in13A81	9	122	151	1.23	3.0139	0.0700	0.2513	0.0046	0.39	0.0892	0.0005	1411.1	17.7	1445.0	23.7	1407.9	10.0	103	1430	33	2.11	0.15
in13A82	10	13	13	0.99	3.1606	0.1641	0.2522	0.0059	0.23	0.0969	0.0013	1447.8	40.0	1449.8	30.4	1565.8	24.9	93	1449	53	0.00	0.97
in13A63	17	37	24	0.66	2.9799	0.1026	0.2420	0.0052	0.31	0.0904	0.0008	1402.5	26.2	1396.9	27.2	1434.8	16.4	97	1400	43	0.03	0.86
in13A84	18	37	33	0.89	3.0592	0.0744	0.2489	0.0037	0.31	0.0912	0.0009	1422.5	18.8	1437.8	19.3	1450.9	18.4	99	1430	31	0.47	0.49
in13A85	20	46	37	0.81	3.0812	0.0742	0.2484	0.0051	0.42	0.0894	0.0007	1428.0	18.5	1435.5	26.1	1412.5	14.3	102	1430	35	0.09	0.76
in13A88	22	55	37	0.68	3.2544	0.2025	0.2519	0.0071	0.23	0.0936	0.0019	1470.2	48.3	1448.4	36.7	1540.3	37.1	94	1455	65	0.18	0.69
in13A87	26	26	22	0.77	3.2893	0.1769	0.2509	0.0062	0.23	0.0986	0.0014	1473.8	42.1	1443.2	32.1	1596.4	28.8	90	1453	57	0.42	0.52
in13A88	23	33	26	0.78	3.2509	0.1353	0.2499	0.0044	0.21	0.0975	0.0018	1469.4	32.3	1437.8	22.9	1578.4	34.4	91	1447	41	0.79	0.38
in13A89	12	46	53	1.12	3.0982	0.0992	0.2408	0.0051	0.33	0.0984	0.0010	1432.2	24.8	1391.1	28.7	1585.3	19.0	89	1414	42	1.92	0.17
in13A90	13	52	54	1.03	3.0166	0.1083	0.2470	0.0053	0.30	0.0974	0.0011	1411.8	27.4	1422.8	27.8	1575.1	21.8	90	1417	44	0.11	0.74

Table D.6. continued

File name	Number	U (ppm)	Th (ppm)	Th/U	207Pb/235U	1s error	206Pb/238U	1s error	Rho	207Pb/206Pb	1s error	207Pb/235U Ma	1s error Ma	206Pb/238U Ma	1s error Ma	207Pb/206Pb Ma	1s error Ma	U-Pb/Pb-Pb concordancy (%)	U-Pb Concordia age (Ma)	2s error Ma	MSWD	Probability (of concordance)
South Ridge (CM865)																						
sr29A09	1				3.1284	0.0922	0.2419	0.0073	0.51	0.0912	0.0009	1439.7	22.7	1396.8	38.1	1450.1	18.6	96	1437	45	1.72	0.19
sr29A103	100				3.0661	0.1009	0.2454	0.0057	0.35	0.0921	0.0010	1424.3	28.2	1414.9	29.5	1458.5	21.3	96	1421	44	0.09	0.77
sr29A104	102				3.2474	0.1536	0.2808	0.0070	0.28	0.0936	0.0013	1468.6	38.7	1494.0	36.7	1500.7	26.4	100	1482	58	0.35	0.56
sr29A105	105				3.0631	0.1083	0.2422	0.0065	0.38	0.0904	0.0010	1423.5	27.1	1398.3	33.9	1433.2	20.1	98	1415	50	0.54	0.46
sr29A108	109				3.0078	0.1151	0.2416	0.0065	0.30	0.0909	0.0024	1409.6	29.2	1395.0	28.4	1443.6	50.2	97	1422	46	0.18	0.67
sr29A109	111				2.7101	0.2367	0.2403	0.0105	0.25	0.0872	0.0012	1331.2	64.8	1388.1	54.6	1385.2	26.7	102	1365	82	0.61	0.44
sr29A11	3				3.0260	0.1350	0.2434	0.0077	0.35	0.0918	0.0012	1414.2	34.1	1404.2	39.8	1464.1	24.1	96	1410	60	0.08	0.81
sr29A110	115				3.0193	0.1576	0.2484	0.0081	0.31	0.0912	0.0011	1412.5	39.8	1430.2	41.7	1451.5	23.8	99	1421	66	0.14	0.71
sr29A111	116				3.0201	0.1192	0.2442	0.0084	0.33	0.0902	0.0010	1412.7	30.1	1408.3	33.4	1429.0	21.1	99	1411	52	0.01	0.90
sr29A113	119				3.0904	0.0969	0.2450	0.0058	0.38	0.0905	0.0009	1430.3	24.1	1412.8	30.1	1435.3	20.0	98	1424	44	0.34	0.56
sr29A115	121				3.1093	0.1177	0.2524	0.0081	0.43	0.0910	0.0011	1435.0	29.1	1450.6	41.9	1445.6	22.6	100	1436	56	0.16	0.69
sr29A116	124				3.0294	0.1225	0.2386	0.0079	0.41	0.0895	0.0011	1415.1	30.9	1379.5	40.9	1415.9	23.0	97	1408	58	0.79	0.37
sr29A12	4				3.1750	0.1284	0.2548	0.0087	0.32	0.0930	0.0012	1451.1	31.2	1463.4	34.3	1487.8	24.0	98	1456	53	0.10	0.75
sr29A121	125				3.0276	0.0972	0.2436	0.0065	0.42	0.0894	0.0008	1414.6	24.5	1405.4	34.0	1412.0	18.1	100	1412	47	0.08	0.78
sr29A123	128				3.0246	0.0649	0.2442	0.0047	0.45	0.0898	0.0008	1413.8	18.4	1408.5	24.3	1399.9	16.5	101	1413	32	0.08	0.81
sr29A124	129				2.8602	0.1029	0.2351	0.0064	0.36	0.0886	0.0010	1376.7	26.9	1361.0	33.3	1400.7	22.0	97	1371	49	0.21	0.64
sr29A125	131				3.0243	0.1354	0.2529	0.0057	0.30	0.0897	0.0009	1413.8	34.2	1453.5	34.5	1420.0	20.0	102	1433	55	0.96	0.33
sr29A127	135				2.9765	0.1288	0.2417	0.0061	0.39	0.0904	0.0012	1401.8	32.9	1395.6	42.3	1433.8	24.7	97	1400	61	0.02	0.89
sr29A129	139				2.8786	0.1652	0.2433	0.0083	0.30	0.0911	0.0013	1375.8	43.3	1403.6	43.2	1448.7	27.9	97	1389	69	0.30	0.59
sr29A130	142				2.9712	0.1208	0.2484	0.0074	0.37	0.0920	0.0013	1400.3	30.9	1419.9	38.0	1467.0	26.2	97	1407	56	0.25	0.62
sr29A131	143				3.0847	0.1424	0.2509	0.0086	0.37	0.0920	0.0012	1428.9	35.4	1443.1	44.2	1466.6	25.2	98	1434	64	0.10	0.75
sr29A132	144				3.1617	0.1614	0.2818	0.0090	0.34	0.0899	0.0012	1447.9	39.4	1599.0	46.1	1422.9	25.1	105	1467	68	1.07	0.30
sr29A15	7				2.9753	0.1546	0.2448	0.0074	0.29	0.0928	0.0016	1401.3	39.5	1411.8	38.4	1480.3	32.5	95	1407	62	0.05	0.82
sr29A16	8				3.0740	0.1382	0.2475	0.0070	0.31	0.0915	0.0012	1426.2	34.7	1425.8	35.9	1456.9	25.3	98	1426	57	0.00	0.99
sr29A17	9				3.0804	0.0880	0.2346	0.0058	0.43	0.0934	0.0007	1427.8	21.9	1358.4	30.3	1495.1	14.0	91	1411	42	5.85	0.02
sr29A22	11				2.9944	0.0872	0.2369	0.0061	0.45	0.0895	0.0008	1406.2	22.2	1370.8	32.0	1416.9	18.5	97	1399	43	1.42	0.23
sr29A24	14				2.9685	0.1678	0.2378	0.0088	0.36	0.0900	0.0010	1399.6	42.9	1375.4	50.9	1425.8	21.3	96	1390	77	0.21	0.65
sr29A25	16				2.8293	0.1800	0.2301	0.0099	0.34	0.0895	0.0008	1363.3	47.7	1335.2	51.7	1415.1	19.5	94	1351	82	0.24	0.62
sr29A26	18				2.9479	0.1241	0.2488	0.0066	0.32	0.0885	0.0010	1394.3	31.9	1431.3	34.2	1394.0	20.8	103	1411	53	0.92	0.34
sr29A27	19				3.0043	0.1204	0.2476	0.0065	0.33	0.0893	0.0010	1408.7	30.5	1426.2	33.5	1411.3	22.3	101	1418	52	0.22	0.64
sr29A28	20				3.0857	0.0971	0.2474	0.0064	0.41	0.0882	0.0009	1431.6	24.1	1424.9	32.8	1388.2	18.6	103	1430	45	0.04	0.83
sr29A32	26				2.8267	0.2026	0.2365	0.0085	0.25	0.0932	0.0014	1362.7	53.8	1368.8	44.3	1492.7	28.8	92	1366	76	0.01	0.92
sr29A33	27				2.9555	0.1472	0.2389	0.0087	0.38	0.0891	0.0007	1396.3	37.8	1381.2	46.1	1407.1	14.7	98	1391	66	0.10	0.75
sr29A39	29				3.1381	0.1490	0.2483	0.0083	0.35	0.0906	0.0007	1442.1	39.6	1419.5	43.1	1436.0	15.0	99	1433	65	0.24	0.62
sr29A40	30				2.9303	0.1179	0.2430	0.0057	0.29	0.0899	0.0010	1389.8	30.5	1402.5	29.7	1424.2	20.3	98	1396	48	0.13	0.72
sr29A41	32				3.0414	0.0902	0.2397	0.0072	0.50	0.0891	0.0009	1418.1	22.7	1385.4	37.2	1406.8	20.3	98	1415	45	1.02	0.31
sr29A42	33				2.8178	0.2306	0.2348	0.0116	0.30	0.0862	0.0009	1360.2	61.3	1359.8	60.8	1367.0	19.6	98	1360	99	0.00	0.99
sr29A43	34				3.1088	0.1398	0.2427	0.0076	0.35	0.0931	0.0016	1434.9	34.5	1400.7	39.3	1488.9	33.6	94	1421	60	0.85	0.42
sr29A44	36				2.8205	0.1313	0.2425	0.0061	0.27	0.0869	0.0010	1361.0	34.9	1399.9	31.7	1402.1	21.9	100	1382	52	0.94	0.33
sr29A45	37				2.8429	0.1788	0.2437	0.0077	0.25	0.0909	0.0012	1366.9	47.2	1405.9	39.9	1444.3	25.2	97	1390	67	0.54	0.46
sr29A46	38				3.0174	0.1644	0.2381	0.0079	0.30	0.0915	0.0019	1412.0	41.5	1377.1	40.9	1456.3	38.7	95	1394	67	0.51	0.47
sr29A54	42				3.0470	0.1325	0.2490	0.0063	0.29	0.0922	0.0014	1419.5	33.3	1433.5	32.6	1472.2	28.6	97	1427	53	0.13	0.72
sr29A55	44				2.9788	0.1048	0.2341	0.0085	0.40	0.0910	0.0010	1402.2	26.7	1356.0	34.0	1446.3	20.4	94	1387	50	1.85	0.17
sr29A58	50				3.1005	0.1244	0.2437	0.0074	0.38	0.0912	0.0012	1432.8	30.8	1406.1	38.4	1450.8	24.4	97	1424	56	0.47	0.49
sr29A59	51				2.8296	0.1098	0.2372	0.0061	0.33	0.0878	0.0009	1363.4	29.1	1372.4	31.9	1378.2	19.4	100	1367	50	0.08	0.80
sr29A60	53				2.9353	0.1216	0.2417	0.0064	0.32	0.0907	0.0009	1391.1	31.4	1395.3	33.5	1440.0	19.9	97	1393	53	0.01	0.91
sr29A61	54				3.2859	0.1194	0.2538	0.0076	0.41	0.0912	0.0010	1477.7	28.3	1457.9	39.2	1450.2	20.8	101	1473	54	0.28	0.60
sr29A62	55				3.1761	0.1282	0.2547	0.0062	0.30	0.0923	0.0012	1451.4	31.2	1462.5	31.8	1474.4	24.5	99	1457	51	0.09	0.77
sr29A63	56				3.0053	0.0814	0.2359	0.0054	0.42	0.0896	0.0008	1409.0	20.8	1365.3	27.9	1417.3	17.3	96	1397	39	2.64	0.10
sr29A70	59				2.9487	0.1640	0.2445	0.0097	0.35	0.0877	0.0011	1394.0	42.2	1410.0	50.1	1375.9	24.7	102	1400	75	0.09	0.76
sr29A71	61				3.0635	0.1278	0.2481	0.0080	0.39	0.0884	0.0010	1423.6	31.9	1428.6	41.3	1390.7	21.0	103	1425	59	0.01	0.90
sr29A72	62				2.8599	0.1411	0.2347	0.0087	0.37	0.0882	0.0012	1371.4	37.1	1359.2	45.3	1386.1	25.4	98	1367	67	0.07	0.79
sr29A73	63				3.5620	0.1921	0.2775	0.0155	0.52	0.0973	0.0018	1541.1	42.9	1578.8	78.1	1573.7	35.3	100	1542	85	0.31	0.58
sr29A74	64				3.2198	0.1852	0.2644	0.0096	0.29	0.0883	0.0015	1461.8	44.6	1512.5	44.8	1385.0	30.0	101	1488	71	0.91	0.34
sr29A75	65				2.9676	0.1763	0.2453	0.0100	0.34	0.0911	0.0014	1398.4	45.1	1414.2	51.9	1449.2	28.4	98	1405	79	0.07	0.79
sr29A76	67				3.0582	0.1148	0.2429	0.0083	0.48	0.0903	0.0012	1422.3	28.7	1401.5	43.3	1431.0	25.8	98	1419	56	0.28	0.60
sr29A79	73				3.0832	0.0825	0.2501	0.0062	0.48	0.0889	0.0008	1423.5	20.6	1439.0	32.1	1402.3	18.5	103	1426	40	0.28	0.59
sr29A80	75				2.9023	0.1309	0.2318	0.0090	0.43	0.0862	0.0009	1382.5	34.1	1343.7	47.2	1387.6	20.1	97	1373	65	0.75	0.39
sr29A80	75				2.9850	0.0847	0.2355	0.0089	0.51	0.0884	0.0009	1398.7	21.7	1363.3	35.8	1391.5	19.4	98	1396	43	1.31	0.25
sr29A87	76				2.9485	0.1057	0.2361	0.0066	0.39	0.0896	0.0010	1393.9	27.2	1366.5	34.2	1417.6	22.2	96	1385	50	0.63	0.43
sr29A88	79				2.8776	0.1370	0.2476	0.0080	0.34	0.0872	0.0011	1376.1	35.9	1426.2	41.1	1383.9	23.4	105	1395	62	1.27	0.28
sr29A90	83				3.0800	0.1094	0.2514	0.0086	0.37	0.0908	0.0012	1427.7	27.2	1445.7	34.1	1442.3	25.2	100	1434	49	0.27	0.61
sr29A94	90				3.0851	0.0894	0.2491	0.0061	0.35	0.0904	0.0010	1424.0	22.3	1433.9	28.5	1434.3	22.1	100	1428	40	0.12	0.72
sr29A96	95				3.0469	0.1310	0.2412	0.0071	0.34	0.0913	0.0010	1419.5	32.9	1393.1	37.0	1452.5	20.7	96	1408	57	0.43	0.51
sr29A97	98				3.0360	0.1522	0.2417	0.0083	0.34	0.0897	0.0010	1416.7	36.3	1395.6	43.1	1418.9	21.9	98	1408	67	0.20	0.65

Notes. Measured isotopic ratios determined using the LAMDATE data reduction program for LA-ICP-MS (Keller et al. 2008). "Rho" is the correlation coefficient between the two U/Pb isotope ratios calculated as the ratio of the covariance to the product of the standard deviations for each ratio. "U-Pb/Pb-Pb concordancy (%)" is a measure of U-Pb discordancy calculated as [(206Pb/238U age) / (207Pb/206Pb age)] x 100. U-Pb "concordia ages" calculated using Isoplot Ex/3.00 program (Ludwig 2003) with associated uncertainties given at 2 s, and decay constant errors included. MSWD (Mean Square of Weighted Deviates) of concordance is the ratio of the observed to expected deviation from the concordia based on the assigned errors and error correlations. If the assigned errors are the only cause of scatter, the MSWD will tend to be near unity. Probability of concordance of the concordia age is given as a fraction of 1 (100%); if less than 0.001 (0.1%), a concordia age could not be calculated and the analysis is labelled as "DISCORDANT", except for rare inherited ages. Common lead corrections were not made as 204Pb was below detection limits in all analyses. Concentrations for U and Th by external standardization against Harvard 91500 using the calibration values of U= 80 ppm and Th = 30ppm.

Table D.7. LA-ICP-MS U-Pb isotopic analyses of reference zircons Harvard 91500 and Plešovice

	Concentrations			Measured Isotopic Ratios							Calculated Ages										
File name	U (ppm)	Th (ppm)	Th/U	207Pb/235U	1s error	206Pb/238U	1s error	Rho	207Pb/206Pb	1s error	207Pb/235U Ma	1s error Ma	206Pb/238U Ma	1s error Ma	207Pb/206Pb Ma	1s error Ma	U-Pb/Pb-Pb concordancy (%)	U-Pb Concordia age (Ma)	2s error Ma	MSWD	Probability (of concordance)
Harvard 91500 zircon																					
au22A08				1.9383	0.0410	0.1848	0.0031	0.39	0.0736	0.0005	1094.4	14.2	1093.2	16.7	1036.3	14.4	105	1094	25	0.01	0.94
au22A38				1.9048	0.0700	0.1818	0.0046	0.35	0.0754	0.0008	1082.8	24.5	1075.6	25.1	1077.9	15.5	100	1079	41	0.06	0.80
au22A24				1.8828	0.0636	0.1805	0.0034	0.28	0.0754	0.0008	1075.0	22.5	1069.5	18.8	1078.3	15.3	99	1072	33	0.05	0.82
au22A07				1.8772	0.0551	0.1781	0.0033	0.32	0.0757	0.0008	1073.1	19.5	1056.4	18.0	1087.9	14.8	97	1064	30	0.57	0.45
au22A24				1.8643	0.0920	0.1809	0.0052	0.29	0.0751	0.0008	1068.5	32.6	1071.8	28.2	1071.1	18.1	100	1070	48	0.01	0.93
au22A23				1.8463	0.0561	0.1805	0.0031	0.28	0.0753	0.0008	1062.1	20.0	1069.7	16.9	1078.8	14.8	99	1067	29	0.12	0.73
au22A23				1.8398	0.0601	0.1789	0.0033	0.28	0.0754	0.0008	1059.7	21.5	1061.0	17.8	1078.2	14.9	98	1060	31	0.00	0.96
au22A02				1.7887	0.0489	0.1769	0.0029	0.30	0.0746	0.0008	1041.4	17.8	1050.0	15.9	1056.5	16.3	99	1046	27	0.18	0.66
au22A06				1.8193	0.0661	0.1774	0.0048	0.37	0.0727	0.0005	1052.4	23.8	1052.8	28.1	1005.3	14.8	105	1053	41	0.00	0.99
au22A01				1.8734	0.0454	0.1811	0.0032	0.36	0.0727	0.0008	1071.8	16.1	1073.0	17.2	1005.1	18.0	107	1072	27	0.00	0.95
au24A01				1.8467	0.0651	0.1751	0.0039	0.32	0.0744	0.0007	1062.3	23.2	1040.0	21.4	1052.4	17.7	99	1050	36	0.72	0.40
au24A02				1.8691	0.0796	0.1789	0.0042	0.28	0.0754	0.0007	1070.2	28.2	1049.9	23.1	1080.3	18.8	97	1057	40	0.42	0.51
au24A21				1.8837	0.0507	0.1783	0.0033	0.34	0.0746	0.0008	1068.3	18.0	1057.7	17.9	1057.2	16.4	100	1063	29	0.26	0.61
au24A33				1.8435	0.0646	0.1795	0.0031	0.25	0.0772	0.0007	1061.1	23.1	1064.1	17.1	1125.5	18.4	95	1063	30	0.01	0.91
au24A34				1.8565	0.0620	0.1822	0.0026	0.23	0.0755	0.0009	1065.7	22.1	1079.0	15.5	1083.1	24.8	100	1075	28	0.31	0.58
au01a59				1.7430	0.0646	0.1811	0.0042	0.24	0.0731	0.0007	1024.6	31.3	1072.8	22.8	1017.7	19.8	105	1058	40	2.05	0.15
au01a16				1.7833	0.1479	0.1775	0.0085	0.29	0.0751	0.0007	1039.4	54.0	1053.1	46.3	1071.4	18.0	98	1048	79	0.05	0.82
au01a31				1.8117	0.0560	0.1803	0.0033	0.30	0.0740	0.0008	1049.7	20.2	1068.5	18.0	1042.2	17.0	103	1061	30	0.69	0.41
au01a46				1.8164	0.0805	0.1798	0.0063	0.40	0.0723	0.0008	1051.4	29.0	1064.7	34.7	983.5	16.8	107	1056	52	0.14	0.70
au01a15				1.8183	0.0556	0.1811	0.0035	0.31	0.0757	0.0008	1052.1	20.0	1072.8	19.0	1087.1	15.9	99	1063	31	0.83	0.36
au01a83				1.8548	0.0484	0.1832	0.0034	0.37	0.0741	0.0006	1065.1	16.5	1084.6	18.6	1045.4	17.5	104	1073	29	0.96	0.32
au01a62				1.8810	0.0671	0.1786	0.0045	0.36	0.0770	0.0007	1077.9	23.6	1059.4	24.8	1122.1	18.0	94	1069	40	0.45	0.50
au01a75				1.9003	0.0700	0.1785	0.0057	0.43	0.0755	0.0007	1081.2	24.5	1058.9	31.2	1083.1	17.8	98	1074	46	0.55	0.46
ja28A50				1.7689	0.1196	0.1764	0.0068	0.28	0.0764	0.0009	1034.1	43.8	1047.4	38.3	1105.8	23.4	95	1042	63	0.08	0.78
ja28A50				1.7808	0.0641	0.1799	0.0049	0.29	0.0765	0.0009	1038.5	30.7	1066.6	28.8	1108.3	22.3	96	1055	45	0.68	0.41
ja28A14				1.7949	0.1158	0.1816	0.0056	0.24	0.0745	0.0007	1043.6	42.1	1075.5	30.3	1056.1	20.0	102	1066	54	0.49	0.48
ja28A76				1.8129	0.0785	0.1778	0.0050	0.33	0.0783	0.0007	1050.1	27.6	1054.8	27.5	1102.3	18.7	96	1052	45	0.02	0.88
ja28A15				1.8146	0.0889	0.1806	0.0049	0.28	0.0738	0.0007	1050.7	32.1	1070.0	26.9	1034.9	19.3	103	1063	46	0.30	0.59
ja28A01				1.8436	0.0851	0.1808	0.0068	0.44	0.0749	0.0008	1061.2	30.4	1069.9	37.6	1066.6	22.2	95	1044	57	1.88	0.16
ja28A83				1.8697	0.1499	0.1892	0.0079	0.27	0.0746	0.0008	1070.4	52.0	1117.2	43.0	1058.6	22.0	106	1099	74	0.86	0.42
ja28A49				1.9059	0.0885	0.1788	0.0043	0.33	0.0756	0.0007	1083.2	23.9	1049.7	23.3	1083.8	18.2	97	1065	39	1.50	0.22
ja28A75				1.9231	0.0720	0.1778	0.0048	0.36	0.0782	0.0006	1089.1	25.0	1053.7	28.0	1101.1	21.0	96	1072	42	1.49	0.22
ja28A49				1.9303	0.0694	0.1791	0.0043	0.33	0.0759	0.0007	1091.8	24.0	1062.1	23.5	1092.6	18.2	97	1076	39	1.15	0.28
ja28A62				1.9371	0.1481	0.1867	0.0077	0.27	0.0757	0.0009	1094.0	51.2	1114.2	41.8	1086.9	23.8	103	1107	72	0.13	0.72
ja28A02				2.0173	0.1434	0.1938	0.0064	0.23	0.0772	0.0014	1121.4	48.2	1141.7	34.8	1126.9	37.1	101	1135	62	0.15	0.70
je13A17	83	29	0.35	1.7952	0.0316	0.1771	0.0024	0.38	0.0733	0.0005	1043.7	11.5	1051.2	13.1	1022.8	13.4	103	1047	20	0.30	0.6
je13A04	82	28	0.34	1.7986	0.0544	0.1820	0.0025	0.23	0.0757	0.0006	1044.2	19.8	1077.8	13.8	1087.3	17.0	99	1068	25	2.52	0.1
je13A51	83	29	0.36	1.8190	0.0368	0.1813	0.0024	0.32	0.0750	0.0005	1052.3	13.2	1074.1	12.9	1068.9	14.2	100	1064	21	2.07	0.2
je13A01	77	29	0.39	1.8258	0.0682	0.1782	0.0047	0.35	0.0739	0.0006	1054.7	24.9	1057.1	25.7	1038.1	15.7	102	1056	41	0.01	0.9
je13A29	81	29	0.36	1.8391	0.0432	0.1798	0.0029	0.34	0.0746	0.0005	1059.6	15.5	1065.8	15.9	1058.4	13.1	101	1063	28	0.12	0.7
je13A02	80	31	0.38	1.8501	0.0516	0.1817	0.0029	0.29	0.0754	0.0006	1063.5	18.4	1076.5	15.9	1077.9	15.2	100	1071	27	0.41	0.5
je13A50	81	29	0.36	1.8568	0.0418	0.1792	0.0032	0.40	0.0732	0.0005	1066.6	14.8	1062.4	17.7	1020.5	14.7	104	1065	27	0.06	0.8
je13A74	86	31	0.36	1.8660	0.0512	0.1808	0.0037	0.37	0.0744	0.0005	1069.1	18.1	1071.6	20.0	1051.7	14.7	102	1070	31	0.01	0.9
je13A30	81	29	0.35	1.8663	0.0347	0.1795	0.0025	0.37	0.0740	0.0005	1069.2	12.3	1064.3	13.8	1041.6	13.1	102	1067	21	0.12	0.7
je13A03	85	30	0.35	1.8679	0.0447	0.1811	0.0029	0.33	0.0750	0.0005	1076.9	15.7	1073.1	15.7	1068.1	13.5	100	1075	28	0.04	0.8
je13A73	83	30	0.36	1.9606	0.0380	0.1792	0.0026	0.41	0.0765	0.0005	1102.1	13.0	1062.6	15.4	1109.4	13.6	96	1087	24	6.37	0.0
je13A73	82	29	0.36	1.9213	0.0531	0.1799	0.0042	0.42	0.0765	0.0008	1088.5	18.5	1066.3	22.9	1107.7	15.2	96	1081	34	0.97	0.3
je13A74	86	31	0.36	1.8660	0.0512	0.1806	0.0037	0.37	0.0744	0.0005	1069.1	18.1	1071.6	20.0	1051.7	14.7	102	1070	31	0.01	0.9
je13A93	80	28	0.35	1.8631	0.0358	0.1787	0.0029	0.42	0.0745	0.0004	1068.1	12.7	1060.0	15.9	1054.8	12.0	101	1066	24	0.27	0.6

Table D.7. continued

File name	U (ppm)	Th (ppm)	Th/U	207Pb/235U	1s error	206Pb/238U	1s error	Rho	207Pb/206Pb	1s error	207Pb/235U Ma	1s error Ma	206Pb/238U Ma	1s error Ma	207Pb/206Pb Ma	1s error Ma	U-Pb/Pb-Pb concordancy (%)	U-Pb Concordia age (Ma)	2s error Ma	MSWD	Probability (of concordance)
Harvard 91500 zircon																					
ja29A19				1.7464	0.1129	0.1851	0.0060	0.25	0.0729	0.0006	1025.8	41.7	1094.9	32.4	1010.1	23.4	108	1070	56	2.31	0.1
ja29A03				1.8093	0.0868	0.1797	0.0041	0.31	0.0748	0.0009	1048.8	24.2	1065.6	22.4	1082.9	24.7	100	1058	37	0.37	0.5
ja29A82				1.8288	0.1078	0.1789	0.0070	0.34	0.0751	0.0009	1055.8	38.7	1049.8	38.6	1071.7	24.8	98	1053	63	0.02	0.9
ja29A66				1.8301	0.0523	0.1806	0.0037	0.36	0.0727	0.0007	1056.3	18.8	1071.6	20.1	1008.4	20.5	106	1063	32	0.48	0.5
ja29A04				1.8342	0.0886	0.1754	0.0050	0.38	0.0746	0.0007	1057.8	24.6	1042.0	27.5	1058.7	19.8	99	1051	43	0.30	0.6
ja29A67				1.8370	0.0950	0.1867	0.0051	0.27	0.0744	0.0009	1058.8	34.0	1103.6	27.8	1052.0	25.5	105	1086	48	1.43	0.2
ja29A82				1.8436	0.1067	0.1768	0.0070	0.34	0.0753	0.0009	1061.2	38.8	1049.4	38.6	1077.6	24.6	97	1055	63	0.07	0.8
ja29A134				1.8510	0.1039	0.1811	0.0067	0.33	0.0758	0.0009	1063.8	37.0	1072.8	36.8	1090.7	24.7	98	1068	60	0.05	0.8
ja29A117				1.8632	0.0724	0.1903	0.0045	0.30	0.0737	0.0008	1068.1	25.7	1122.8	24.2	1032.1	22.7	109	1097	40	3.49	0.1
ja29A05				1.8664	0.0738	0.1835	0.0043	0.29	0.0755	0.0007	1069.2	26.1	1086.3	23.2	1080.7	18.5	101	1079	39	0.34	0.6
ja29A100				1.8858	0.1078	0.1780	0.0074	0.36	0.0770	0.0010	1076.1	37.9	1056.2	40.6	1121.7	25.3	94	1087	65	0.20	0.7
ja29A36				1.9042	0.0828	0.1788	0.0060	0.39	0.0753	0.0009	1082.6	26.9	1060.6	33.0	1077.4	24.1	98	1074	51	0.41	0.5
ja29A50				1.9098	0.1300	0.1876	0.0062	0.24	0.0748	0.0010	1084.5	45.4	1108.4	33.7	1064.3	25.8	104	1101	80	0.24	0.6
ja29A83				1.9170	0.1267	0.1807	0.0099	0.42	0.0740	0.0009	1087.0	44.1	1070.7	54.2	1041.9	25.4	103	1062	81	0.09	0.8
ja29A35				1.9179	0.0862	0.1763	0.0064	0.40	0.0761	0.0008	1087.4	30.0	1047.0	34.8	1097.0	22.1	95	1072	54	1.27	0.3
ja29A51				1.9180	0.1409	0.1842	0.0074	0.27	0.0762	0.0009	1087.4	49.0	1090.1	40.3	1100.6	22.7	99	1089	70	0.00	1.0
ja29A83				1.9311	0.0879	0.1801	0.0070	0.43	0.0750	0.0009	1091.9	30.5	1067.7	38.4	1067.2	23.8	100	1064	57	0.42	0.5
ja29A99				1.9403	0.1284	0.1852	0.0065	0.27	0.0761	0.0010	1095.1	43.7	1095.4	35.4	1097.8	25.9	100	1095	62	0.00	1.0
ja29A118				1.9856	0.1180	0.1842	0.0062	0.37	0.0778	0.0010	1103.8	40.4	1089.7	44.4	1142.2	24.4	95	1098	70	0.09	0.8
ja29A18				1.9705	0.0932	0.1879	0.0047	0.26	0.0808	0.0010	1105.5	31.9	1109.8	25.4	1216.2	25.4	91	1108	44	0.01	0.9
Plešovice zircon																					
au22A37				0.3974	0.0183	0.0537	0.0017	0.35	0.0530	0.0003	339.8	13.3	337.4	10.5	329.8	13.3	102	338	19	0.03	0.9
au22A10				0.3973	0.0181	0.0534	0.0016	0.32	0.0536	0.0004	339.7	13.2	335.1	9.5	354.5	16.2	95	336	18	0.12	0.7
au22A09				0.3912	0.0121	0.0532	0.0012	0.35	0.0527	0.0003	335.2	8.8	334.4	7.1	318.0	14.2	105	335	13	0.01	0.9
au22A25				0.3897	0.0133	0.0540	0.0010	0.28	0.0537	0.0004	334.1	9.7	338.8	6.2	356.9	17.3	95	338	12	0.22	0.6
au22A25				0.3888	0.0155	0.0544	0.0011	0.24	0.0544	0.0005	333.5	11.3	341.4	6.4	386.0	20.1	88	340	12	0.47	0.5
au24A03				0.4060	0.0147	0.0537	0.0014	0.38	0.0533	0.0003	347.4	10.6	337.1	8.5	340.9	14.3	99	340	15	0.88	0.3
au24A04				0.4021	0.0186	0.0525	0.0021	0.42	0.0527	0.0003	343.2	14.2	329.6	13.1	317.7	14.3	104	335	23	0.84	0.4
au24A20				0.3982	0.0113	0.0527	0.0012	0.40	0.0524	0.0003	338.9	8.2	331.0	7.4	302.5	15.0	109	334	13	0.84	0.4
au24A31				0.4050	0.0111	0.0533	0.0010	0.35	0.0532	0.0003	345.3	8.0	334.6	6.2	339.0	14.6	99	338	11	1.67	0.2
au24A32				0.4020	0.0118	0.0527	0.0012	0.40	0.0523	0.0003	343.1	8.6	331.2	7.6	300.1	13.2	110	336	13	1.78	0.2
au01a48				0.3174	0.0143	0.0448	0.0013	0.33	0.0517	0.0005	279.9	11.0	283.1	8.2	270.9	23.4	105	282	15	0.08	0.8
au01a20				0.3274	0.0091	0.0474	0.0007	0.25	0.0518	0.0005	287.6	7.0	298.4	4.1	276.4	19.9	108	296	8	2.30	0.1
au01a19				0.3316	0.0092	0.0471	0.0008	0.30	0.0525	0.0005	290.8	7.0	297.0	4.8	309.0	22.6	96	295	9	0.74	0.4
au01a86				0.3321	0.0105	0.0466	0.0011	0.39	0.0525	0.0005	291.1	8.1	293.6	7.1	307.3	20.3	96	293	12	0.08	0.8
au01a61				0.3402	0.0163	0.0460	0.0014	0.32	0.0528	0.0005	297.3	12.3	289.8	8.6	321.1	19.9	90	292	16	0.35	0.6
au01a72				0.3534	0.0099	0.0463	0.0011	0.44	0.0530	0.0005	307.3	7.4	291.5	7.0	330.0	20.4	88	298	12	4.25	0.0
au01a64				0.3745	0.0143	0.0527	0.0013	0.33	0.0525	0.0003	322.9	10.6	331.2	8.2	307.8	12.5	108	329	15	0.58	0.5
au01a80				0.3866	0.0098	0.0518	0.0012	0.45	0.0530	0.0002	331.9	7.2	325.3	7.2	328.9	9.0	99	329	12	0.75	0.4
au01a32				0.3904	0.0103	0.0523	0.0012	0.43	0.0533	0.0003	334.7	7.5	328.8	7.3	342.2	12.0	96	332	12	0.55	0.5
au01a74				0.3937	0.0134	0.0522	0.0015	0.41	0.0538	0.0003	337.1	9.7	328.1	9.0	361.2	13.6	91	332	16	0.79	0.4
au01a47				0.3940	0.0077	0.0535	0.0008	0.40	0.0530	0.0003	337.3	5.6	335.7	5.1	327.0	11.3	103	336	9	0.07	0.8
au01a17				0.3948	0.0082	0.0531	0.0009	0.41	0.0533	0.0003	337.9	6.0	333.4	5.5	342.1	11.1	97	335	10	0.51	0.5
au01a18				0.3956	0.0154	0.0556	0.0014	0.31	0.0528	0.0003	338.4	11.2	348.8	8.3	318.6	13.0	109	346	15	0.79	0.4
au01a65				0.4036	0.0099	0.0527	0.0008	0.32	0.0548	0.0004	344.3	7.2	330.9	5.1	402.3	16.8	82	334	9	3.31	0.1

Table D.7. continued

File name	U (ppm)	Th (ppm)	Th/U	207Pb/235U	1s error	206Pb/238U	1s error	Rho	207Pb/206Pb	1s error	207Pb/235U Ma	1s error Ma	206Pb/238U Ma	1s error Ma	207Pb/206Pb Ma	1s error Ma	U-Pb/Pb-Pb concordancy (%)	U-Pb Concordia age (Ma)	2s error Ma	MSWD	Probability (of concordance)
Plešovice zircon																					
je28A52				0.3821	0.0241	0.0522	0.0020	0.31	0.0532	0.0004	328.6	17.7	327.8	12.3	339.0	17.9	97	328	23	0.00	1.0
je28A16				0.3881	0.0184	0.0519	0.0015	0.31	0.0545	0.0004	333.0	13.5	326.3	9.3	392.8	17.4	83	328	17	0.23	0.6
je28A77				0.3908	0.0212	0.0540	0.0019	0.32	0.0527	0.0005	334.8	15.5	338.8	11.4	315.7	19.5	107	338	21	0.06	0.8
je28A85				0.3934	0.0177	0.0522	0.0018	0.39	0.0526	0.0004	336.8	12.9	328.0	11.1	313.0	18.1	105	331	20	0.44	0.5
je28A84				0.3949	0.0176	0.0533	0.0014	0.30	0.0532	0.0004	337.9	12.6	334.5	8.8	336.8	19.1	99	335	16	0.07	0.8
je28A78				0.3950	0.0287	0.0559	0.0021	0.28	0.0533	0.0005	338.0	20.9	350.7	12.7	340.1	19.8	103	348	24	0.35	0.6
je28A27				0.3955	0.0174	0.0523	0.0015	0.33	0.0531	0.0005	338.3	12.6	328.8	9.4	334.2	22.3	98	332	17	0.54	0.5
je28A52				0.3957	0.0153	0.0533	0.0013	0.32	0.0537	0.0004	338.5	11.2	335.0	8.0	356.7	17.0	94	336	15	0.10	0.8
je28A08				0.3980	0.0203	0.0524	0.0021	0.40	0.0531	0.0005	340.2	14.7	329.3	13.1	333.9	20.7	99	334	23	0.50	0.5
je28A36				0.3985	0.0098	0.0528	0.0010	0.38	0.0532	0.0004	340.5	6.9	331.9	5.9	338.8	17.6	98	335	11	1.45	0.2
je28A27				0.3997	0.0146	0.0526	0.0014	0.38	0.0532	0.0005	341.4	10.6	330.7	8.4	336.9	22.0	98	334	15	0.97	0.3
je28A04				0.4029	0.0192	0.0527	0.0017	0.34	0.0540	0.0005	343.7	13.9	331.1	10.3	370.0	19.4	89	335	19	0.78	0.4
je28A51				0.4040	0.0173	0.0530	0.0019	0.41	0.0527	0.0004	344.6	12.5	333.2	11.5	315.6	16.5	106	338	20	0.78	0.4
je28A51				0.4074	0.0104	0.0546	0.0011	0.39	0.0526	0.0004	347.0	7.5	343.0	6.7	321.5	15.8	107	345	12	0.25	0.6
je28A37				0.4084	0.0115	0.0540	0.0013	0.42	0.0539	0.0004	347.7	8.3	339.2	7.7	365.2	15.6	93	343	13	0.98	0.3
je28A05				0.4326	0.0194	0.0533	0.0018	0.38	0.0550	0.0005	365.2	13.8	334.6	11.1	413.3	20.4	81	344	20	4.68	0.0
je13A27	886	103	0.12	0.3854	0.0087	0.0531	0.0008	0.34	0.0538	0.0003	331.0	6.4	333.6	5.0	364.4	12.5	92	333	9	0.17	0.7
je13A18	949	119	0.12	0.3863	0.0077	0.0537	0.0008	0.37	0.0527	0.0003	331.7	5.6	337.3	4.8	314.5	10.9	107	335	9	0.91	0.3
je13A28	911	120	0.13	0.3903	0.0079	0.0531	0.0008	0.37	0.0533	0.0003	334.8	5.8	333.4	4.8	339.8	13.3	98	334	9	0.03	0.9
je13A72	961	135	0.14	0.3911	0.0085	0.0528	0.0007	0.39	0.0533	0.0003	335.2	4.7	331.5	4.2	340.0	10.8	98	333	7	0.56	0.5
je13A48	892	103	0.12	0.3937	0.0081	0.0533	0.0008	0.36	0.0531	0.0002	337.0	5.9	334.7	4.8	333.1	10.1	100	336	9	0.14	0.7
je13A05	841	82	0.10	0.3937	0.0084	0.0551	0.0008	0.36	0.0529	0.0002	337.1	4.6	345.5	3.9	323.9	10.8	107	342	7	2.98	0.1
je13A71	962	138	0.14	0.3938	0.0087	0.0528	0.0007	0.39	0.0533	0.0003	337.2	4.9	330.5	4.3	342.9	10.8	96	333	8	1.72	0.2
je13A07	985	126	0.13	0.3964	0.0084	0.0536	0.0008	0.38	0.0537	0.0002	339.0	4.0	336.7	3.4	357.3	9.8	94	336	6	0.32	0.6
je13A49	739	84	0.11	0.3997	0.0082	0.0528	0.0007	0.35	0.0540	0.0003	341.5	5.9	330.6	4.6	370.7	12.4	89	334	8	3.16	0.1
je13A71	962	138	0.14	0.3938	0.0087	0.0526	0.0007	0.39	0.0533	0.0003	337.2	4.9	330.5	4.3	342.9	10.8	96	333	8	1.72	0.2
je13A72	961	135	0.14	0.3911	0.0085	0.0528	0.0007	0.39	0.0533	0.0003	335.2	4.7	331.5	4.2	340.0	10.8	98	333	7	0.56	0.5
je13A91	806	85	0.11	0.3969	0.0059	0.0547	0.0007	0.45	0.0530	0.0002	339.4	4.3	343.1	4.5	326.9	10.6	104	341	7	0.65	0.4
je13A92	888	119	0.13	0.3990	0.0084	0.0536	0.0007	0.40	0.0528	0.0002	338.8	4.7	336.6	4.3	322.1	9.4	104	336	7	0.20	0.7
je28A88				0.3710	0.0134	0.0536	0.0012	0.30	0.0524	0.0008	320.4	9.9	336.5	7.1	304.7	25.1	110	332	13	2.48	0.1
je28A135				0.3777	0.0159	0.0508	0.0017	0.40	0.0531	0.0004	325.4	11.7	319.5	10.6	333.5	18.0	96	322	19	0.23	0.6
je28A09				0.3821	0.0114	0.0527	0.0010	0.33	0.0535	0.0004	328.6	8.4	331.0	6.3	349.5	18.1	95	330	11	0.06	0.8
je28A38				0.3857	0.0271	0.0540	0.0022	0.29	0.0535	0.0005	331.3	19.8	336.9	13.2	350.0	21.4	97	337	25	0.14	0.7
je28A37				0.3860	0.0207	0.0534	0.0019	0.34	0.0525	0.0005	331.5	15.2	335.5	11.6	306.6	19.7	109	334	21	0.06	0.8
je28A52				0.3870	0.0331	0.0530	0.0027	0.30	0.0536	0.0006	332.2	24.2	332.9	18.7	355.4	26.5	94	333	31	0.00	1.0
je28A85				0.3895	0.0155	0.0533	0.0014	0.33	0.0532	0.0004	334.0	11.4	334.6	8.7	335.6	19.0	100	334	16	0.00	1.0
je28A102				0.3900	0.0174	0.0542	0.0016	0.33	0.0527	0.0004	334.3	12.7	340.4	9.8	317.3	18.9	107	336	18	0.21	0.6
je28A136				0.3912	0.0129	0.0533	0.0012	0.35	0.0540	0.0005	335.2	9.4	334.5	7.8	371.8	19.2	90	335	14	0.01	0.9
je28A20				0.3976	0.0105	0.0533	0.0011	0.36	0.0535	0.0004	339.9	7.6	334.6	6.6	350.0	16.0	96	337	12	0.46	0.5
je28A08				0.4005	0.0284	0.0514	0.0030	0.41	0.0549	0.0005	342.0	20.6	323.3	18.4	409.8	18.5	79	331	33	0.77	0.4
je28A119				0.4010	0.0179	0.0544	0.0016	0.34	0.0542	0.0005	342.4	12.9	341.4	10.1	379.6	21.2	90	342	18	0.01	0.9
je28A89				0.4025	0.0165	0.0548	0.0014	0.31	0.0531	0.0005	343.4	11.9	343.7	8.5	334.4	23.1	103	344	16	0.00	1.0
je28A120				0.4047	0.0121	0.0553	0.0013	0.40	0.0527	0.0004	345.0	8.8	347.0	8.1	314.1	19.3	110	346	14	0.05	0.8
je28A53				0.4068	0.0183	0.0533	0.0020	0.42	0.0529	0.0004	346.4	13.2	334.7	12.3	323.5	19.2	103	340	22	0.72	0.4
je29A07				0.4109	0.0155	0.0536	0.0014	0.35	0.0550	0.0005	349.5	11.1	337.9	8.6	414.2	21.0	82	341	16	1.02	0.3
je29A101				0.4118	0.0106	0.0539	0.0013	0.46	0.0541	0.0004	350.1	7.6	338.4	7.8	375.9	18.2	90	344	13	2.18	0.1

Table D.8. LA-ICP-MS multi-element analysis of zircons from target rocks at Mistastin Lake Crater

Grain/spot Number	Isotope File name	SiO2 29 or 30 wt%	TiO2 49 wt%	Sr 88 ppm	Y 89 ppm	ZrO2 91 wt%	Nb 93 ppm	Ba 137 ppm	La 139 ppm	Ce 140 ppm	Pr 141 ppm	Nd 146 ppm	Sm 147 ppm	Eu 153 ppm	Gd 157 ppm	Tb 159 ppm	Dy 163 ppm	Ho 165 ppm	Er 166 ppm	Tm 169 ppm	Yb 172 ppm	Lu 175 ppm	Hf 178 ppm	Ta 181 ppm	Th 232 ppm	U 238 ppm
Granodiorite, North East shore (CM003)																										
2.1	au27a04	39.15		0.76	362	59.69	1.04	0.15	0.08	8.50	0.07	1.08	1.80	0.19	8.92	2.84	36.07	12.95	59.16	13.66	131.5	21.07	9341	0.62	39.4	46.0
2.2	au27a05	38.14		1.32	513	60.66	1.21	4.01	0.53	10.85	0.16	1.90	2.97	0.28	13.56	4.23	52.84	18.90	82.46	19.15	181.3	27.19	9372	0.92	72.3	71.0
5	au27a06	38.38		0.97	735	60.40	1.29	0.25	0.08	13.07	0.16	2.53	4.15	0.28	19.83	6.22	76.03	26.29	115.53	26.09	240.0	36.45	9257	0.84	99.4	78.9
6	au27a07	38.14		1.11	1006	60.68	6.98	0.31	0.46	10.48	0.48	6.80	8.72	1.12	35.55	9.83	113.00	36.84	152.42	32.47	295.4	44.59	8326	1.16	73.1	47.6
7	au27a08	38.23		1.14	703	62.43	1.85	0.02	0.07	17.37	0.10	1.69	3.04	0.14	16.83	5.63	72.47	25.61	116.21	28.02	271.0	39.05	10190	1.71	136.1	159.8
8	au27a09	38.15		1.04	568	60.76	1.11	0.34	0.44	10.55	0.25	2.74	3.42	0.48	16.15	5.01	61.29	20.79	90.07	20.33	196.2	28.83	8250	0.81	51.2	43.8
9	au27a10	36.15		1.83	430	62.69	1.02	5.13	11.94	38.44	3.62	16.67	4.60	0.34	11.59	3.45	42.00	15.14	68.16	15.85	153.3	23.97	9085	0.67	38.7	43.0
10	au27a11	37.85		1.04	445	61.01	1.38	1.35	2.32	14.15	0.76	4.53	3.17	0.53	11.78	3.80	45.08	15.73	72.38	16.84	182.2	24.35	8920	0.90	84.2	71.8
11	au27a12	37.17		0.72	416	61.79	0.94	0.21	0.02	7.34	0.07	1.17	2.11	0.28	10.03	3.28	41.45	14.75	66.03	15.37	146.4	22.99	8130	0.47	31.9	32.7
12	au27a13	38.70		0.75	292	60.19	1.33	0.63	0.44	8.37	0.16	1.34	1.56	0.17	6.15	2.12	28.61	10.36	48.14	11.83	115.4	18.21	9067	1.05	44.0	66.6
16	au27a14	36.51		0.87	605	62.37	1.56	0.13	0.03	11.20	0.09	1.58	2.73	0.18	14.50	4.68	60.80	21.42	98.38	22.39	215.2	31.97	8526	1.11	54.0	58.0
17.1	au27a15	36.72		0.87	535	62.19	1.37	0.10	0.09	10.17	0.12	1.84	2.92	0.16	13.91	4.38	55.32	19.14	84.61	19.51	182.7	27.94	8375	0.98	64.9	63.2
17.2	au27a16	41.01		3.45	505	57.99	1.36	24.78	1.98	11.70	0.28	2.07	2.63	0.19	12.09	3.95	50.27	17.63	78.91	18.21	177.6	26.66	7558	0.99	62.0	71.1
19	au27a17	36.04		0.88	469	62.84	1.54	0.08	0.22	11.40	0.20	1.69	2.47	0.22	11.89	3.77	48.85	17.76	80.14	19.18	186.7	26.46	8777	1.31	46.8	65.6
20	au27b04	37.68		0.84	363	61.29	1.28	0.44	3.01	18.77	1.56	11.52	5.20	1.21	11.88	3.21	39.10	12.87	58.95	13.70	131.9	19.69	8054	0.82	36.6	65.0
22	au27b05	36.87		0.69	361	62.32	1.04	0.01	0.10	7.48	0.07	0.99	1.60	0.15	8.59	2.66	35.05	12.82	57.84	13.44	131.1	19.48	7916	0.75	42.7	45.5
23	au27b06	35.10		0.88	518	63.89	0.92	0.07	0.07	8.92	0.12	1.54	3.13	0.26	14.48	4.39	55.79	18.88	81.82	19.18	182.9	24.35	7692	0.52	41.4	42.1
25	au27b07	35.93		0.87	604	62.99	1.07	0.14	0.05	8.50	0.10	1.50	3.20	0.26	15.97	4.93	61.28	21.41	93.71	21.30	199.3	29.48	8199	0.70	44.9	50.5
26	au27b08	36.84		1.09	832	61.98	1.60	0.18	0.08	12.68	0.10	1.59	3.09	0.17	18.21	6.08	78.82	28.39	129.80	29.80	283.5	40.78	8752	1.26	95.1	117.7
34	au27b09	37.11		0.78	526	61.84	1.45	0.31	0.03	10.54	0.08	1.36	2.49	0.13	12.36	4.01	52.21	18.70	84.29	19.31	185.5	27.95	8063	1.13	48.2	55.3
37	au27b10	35.80		0.81	590	63.12	1.42	0.22	0.03	12.01	0.10	1.80	3.13	0.17	14.83	4.86	60.46	21.02	93.61	21.57	203.3	29.36	8189	1.01	74.4	77.2
39.1	au27b11	36.82		0.96	659	61.97	2.25	0.13	0.09	18.44	0.09	1.54	2.89	0.13	15.36	4.97	65.85	23.43	108.43	24.59	233.6	34.52	9206	1.98	126.9	155.1
39.2	au27b12	36.50		0.80	572	62.46	1.34	0.13	0.22	9.81	0.10	1.47	2.78	0.17	13.82	4.43	56.25	19.90	89.48	20.50	194.7	29.20	7865	0.91	48.8	53.5
41.1	au27b13	37.00		0.68	604	62.00	0.93	0.63	0.14	8.83	0.19	2.58	3.95	0.38	16.80	5.18	83.36	21.43	93.44	21.15	198.0	28.52	7392	0.59	54.7	47.4
41.2	au27b14	36.16		0.77	404	62.85	1.13	0.22	0.01	7.20	0.08	1.15	2.05	0.15	9.73	3.16	40.56	14.23	64.82	15.28	150.9	21.76	7636	0.83	30.2	35.6
45	au27b15	36.31		0.89	722	62.56	1.30	0.02	0.02	9.94	0.09	1.52	3.13	0.17	16.47	5.60	70.76	25.31	113.54	26.13	246.2	36.11	8460	0.97	60.9	75.7
48	au27b16	36.63		0.87	549	62.32	1.05	1.70	0.56	9.94	0.16	2.00	3.10	0.29	14.45	4.47	55.49	19.52	85.53	18.62	172.6	27.60	8022	0.71	62.0	65.2
47	au27b17	35.97		0.82	592	63.08	0.81	0.19	0.18	8.09	0.25	3.34	4.54	0.55	18.08	5.43	64.94	21.00	89.99	19.79	184.5	26.67	7051	0.47	38.1	30.4
48	au27c04	36.15		0.78	514	62.68	0.93	0.31	0.13	8.59	0.12	1.55	2.63	0.29	13.85	4.16	51.21	18.04	79.42	18.01	169.4	25.10	7328	0.59	44.1	45.6
49	au27c05	35.61		1.09	1000	63.31	0.91	0.19	0.44	12.49	0.50	6.25	6.25	0.90	33.73	9.75	114.50	37.07	150.68	33.24	300.2	41.47	7452	0.56	81.1	65.5
52	au27c06	35.86		0.83	688	63.10	0.86	0.21	0.03	7.97	0.14	2.40	4.44	0.54	20.15	5.99	72.36	24.41	105.84	23.36	215.6	31.98	7664	0.54	51.2	49.0
53	au27c07	36.20		0.66	350	62.79	1.20	<0.02	0.05	7.23	0.07	0.91	1.66	0.11	7.72	2.85	34.49	12.23	55.98	12.95	125.2	19.62	7971	0.87	31.1	43.7
54	au27c08	36.44		0.76	452	62.49	1.05	0.08	0.08	9.44	0.13	1.52	2.28	0.23	10.59	3.51	45.29	15.90	71.82	16.72	158.5	24.33	8262	0.75	55.4	64.7
55	au27c09	36.43		0.89	616	62.47	1.29	0.73	0.07	10.20	0.09	1.39	2.78	0.18	15.42	4.70	60.70	21.68	95.65	21.72	202.7	31.60	8424	0.89	62.3	70.9
58	au27c10	36.35		0.72	530	62.60	0.90	0.17	0.01	7.85	0.07	1.29	2.60	0.27	13.35	4.19	52.90	18.63	81.93	18.82	176.6	26.62	7997	0.58	43.1	48.8
60	au27c11	36.48		0.88	698	62.46	0.94	0.21	0.02	8.34	0.14	2.44	4.29	0.42	19.20	5.78	72.37	24.80	107.08	23.85	217.7	33.08	8049	0.52	51.5	50.9
62.1	au27c12	36.09		1.08	915	62.80	1.00	0.47	0.28	11.46	0.40	4.89	7.00	0.62	29.22	8.56	100.21	33.09	136.40	29.98	280.4	39.88	7892	0.68	84.3	76.9
62.2	au27c13	37.55		0.71	383	61.43	1.05	0.25	0.01	6.79	0.06	0.99	1.79	0.16	8.16	2.74	35.53	12.77	57.62	13.56	132.6	20.30	8062	0.70	31.0	44.0
65	au27c14	35.80		0.87	502	63.11	1.21	0.05	0.15	12.22	0.14	1.62	2.71	0.19	12.33	3.94	51.99	17.68	77.91	18.58	183.3	25.36	8322	0.88	62.0	76.5

Table D.8. **Table D.8. continued**

Grain/spot Number	Isotope File name	Chondrite Normalized La	Ce	Pr	Nd	Sm	Eu	Gd	Tb	Dy	Ho	Er	Tm	Yb	Lu	ZrO2 - SiO2	Ratios Th/U	Lu/Hf	[La/Sm]r	[Gd/Yb]n	Nb/Ta	Eu/Eu*	Ce/Ce*
Granodiorite, North East																							
2.1	au27a04	0.32	13.9	0.80	2.31	12.2	3.32	45	79	147	237	370	553	817	856	20.54	0.855	0.0023	0.026	0.055	1.67	0.116	24.7
2.2	au27a05	2.22	17.7	1.96	4.15	20.1	4.59	68	117	215	346	515	776	1126	1105	22.52	1.019	0.0029	0.110	0.061	1.31	0.104	8.5
5	au27a06	0.38	21.3	1.70	5.54	28.0	4.99	100	172	309	481	722	1056	1491	1482	22.02	1.280	0.0039	0.013	0.067	1.53	0.078	20.8
6	au27a07	1.93	17.1	5.21	14.88	58.9	19.94	179	272	459	675	953	1314	1835	1813	22.54	1.536	0.0054	0.033	0.097	6.02	0.168	4.8
7	au27a08	0.28	28.3	1.06	3.71	20.5	2.47	85	156	295	469	739	1135	1683	1587	26.20	0.852	0.0038	0.013	0.050	1.06	0.047	41.8
8	au27a09	1.87	17.2	2.74	5.99	23.1	8.13	81	139	249	381	563	823	1218	1172	22.61	1.168	0.0035	0.081	0.087	1.81	0.156	7.5
9	au27a10	50.40	62.7	38.97	36.47	31.1	6.09	58	95	171	277	426	634	952	974	26.54	0.900	0.0026	1.621	0.061	1.53	0.136	1.4
10	au27a11	9.78	23.1	8.16	9.91	21.4	9.36	59	100	183	288	452	682	1007	990	23.16	0.895	0.0027	0.457	0.059	1.53	0.232	2.8
11	au27a12	0.08	12.0	0.79	2.55	14.2	4.54	50	91	168	270	413	622	910	935	24.62	0.976	0.0028	0.006	0.055	2.00	0.140	27.4
12	au27a13	1.86	13.7	1.70	2.92	10.5	3.07	31	59	116	190	301	479	717	740	21.49	0.661	0.0020	0.176	0.043	1.26	0.148	7.7
16	au27a14	0.14	18.3	0.99	3.45	18.5	3.16	73	130	247	392	602	907	1336	1300	25.85	0.930	0.0037	0.007	0.055	1.40	0.069	32.5
17.1	au27a15	0.40	16.6	1.27	4.03	19.7	2.87	70	121	225	350	529	790	1135	1136	25.47	1.027	0.0033	0.020	0.062	1.40	0.084	19.9
17.2	au27a16	8.29	19.1	3.05	4.52	17.8	3.29	61	110	204	323	493	737	1103	1084	16.98	0.871	0.0035	0.466	0.056	1.37	0.084	3.4
19	au27a17	0.92	18.6	2.12	3.70	16.7	3.83	60	105	199	325	501	777	1159	1076	26.80	0.713	0.0030	0.055	0.052	1.17	0.100	12.3
20	au27b04	12.70	30.6	16.82	25.21	35.1	21.52	60	89	159	236	368	555	819	800	23.61	0.563	0.0024	0.362	0.073	1.54	0.454	2.1
22	au27b05	0.43	12.2	0.70	2.17	10.8	2.62	43	74	142	235	360	544	814	792	25.66	0.938	0.0025	0.040	0.053	1.39	0.097	21.5
23	au27b06	0.28	14.6	1.27	3.38	21.2	4.99	73	122	227	346	511	776	1138	990	28.79	0.983	0.0032	0.013	0.084	1.78	0.106	18.8
25	au27b07	0.19	13.9	1.04	3.28	21.6	4.91	80	137	249	392	586	862	1238	1198	27.06	0.888	0.0036	0.009	0.085	1.52	0.096	22.5
26	au27b08	0.35	20.7	1.03	3.48	20.9	3.00	92	168	320	520	811	1208	1761	1658	25.15	0.807	0.0047	0.017	0.052	1.27	0.053	30.0
34	au27b09	0.12	17.2	0.91	2.98	16.8	2.26	62	111	212	342	527	782	1152	1136	24.73	0.835	0.0035	0.007	0.054	1.28	0.057	33.5
37	au27b10	0.11	19.6	1.06	3.93	21.2	2.99	75	135	246	385	585	873	1283	1194	27.32	0.963	0.0036	0.005	0.059	1.41	0.062	33.6
39.1	au27b11	0.39	30.1	1.01	3.37	19.5	2.27	77	138	268	429	665	995	1451	1403	25.14	0.818	0.0038	0.020	0.053	1.14	0.047	43.0
39.2	au27b12	0.94	15.7	1.06	3.22	18.8	3.01	68	123	229	365	559	830	1209	1187	25.98	0.912	0.0037	0.050	0.057	1.48	0.089	15.7
41.1	au27b13	0.59	14.4	2.07	5.65	26.7	6.80	84	143	258	392	584	856	1230	1159	25.00	1.155	0.0039	0.022	0.089	1.59	0.122	10.8
41.2	au27b14	0.06	11.8	0.68	2.52	13.8	2.84	49	88	165	261	404	619	938	885	26.89	0.847	0.0028	0.004	0.052	1.35	0.084	31.7
45	au27b15	0.10	16.2	0.93	3.33	21.2	3.09	83	155	288	464	710	1058	1529	1468	26.25	0.805	0.0043	0.005	0.054	1.33	0.059	31.3
46	au27b16	2.45	16.2	1.76	4.37	20.9	5.18	73	124	226	357	535	754	1072	1130	25.89	1.258	0.0035	0.117	0.068	1.48	0.111	7.7
47	au27b17	0.75	13.2	2.68	7.31	30.6	9.82	91	150	284	385	562	801	1148	1084	27.11	1.252	0.0038	0.025	0.079	1.73	0.162	7.7
48	au27c04	0.56	14.0	1.29	3.40	17.8	5.18	89	115	208	330	496	729	1052	1020	26.73	0.969	0.0034	0.032	0.085	1.57	0.119	15.2
49	au27c05	1.85	20.4	5.34	13.67	55.8	15.90	169	270	465	679	942	1346	1865	1686	27.89	1.238	0.0056	0.033	0.091	1.64	0.141	5.7
52	au27c06	0.11	13.0	1.53	5.25	30.0	9.56	101	166	294	447	662	946	1339	1299	27.25	1.046	0.0042	0.004	0.076	1.57	0.148	15.6
53	au27c07	0.23	11.8	0.72	1.99	11.2	1.96	39	73	140	224	350	524	778	798	26.59	0.712	0.0025	0.020	0.050	1.38	0.079	25.0
54	au27c08	0.34	15.4	1.42	3.32	15.4	4.05	53	97	184	291	449	677	985	989	26.05	0.856	0.0029	0.022	0.054	1.41	0.118	17.4
55	au27c09	0.31	16.6	0.97	3.04	16.8	3.16	77	130	247	397	598	879	1259	1285	26.04	0.878	0.0038	0.017	0.082	1.46	0.086	26.0
58	au27c10	0.08	12.8	0.78	2.83	17.6	4.86	67	116	215	341	512	762	1097	1082	26.25	0.883	0.0033	0.003	0.061	1.55	0.115	30.7
60	au27c11	0.10	13.6	1.46	5.34	29.0	7.39	96	160	294	454	669	966	1352	1345	25.99	1.012	0.0041	0.003	0.071	1.62	0.118	17.3
62.1	au27c12	1.17	18.7	4.28	10.71	47.3	10.92	147	237	407	606	852	1214	1742	1621	26.71	1.096	0.0051	0.025	0.084	1.47	0.113	6.9
62.2	au27c13	0.06	11.1	0.61	2.17	12.1	2.83	41	76	144	234	360	550	823	825	23.88	0.703	0.0025	0.005	0.050	1.50	0.106	33.2
65	au27c14	0.63	19.9	1.56	3.54	18.3	3.41	62	109	211	328	487	752	1138	1031	27.31	0.811	0.0030	0.034	0.054	1.38	0.085	18.3

Table D.8. Continued

Grain/spot Number	Isotope File name	SiO2 29 or 30 wt%	TiO2 49 wt%	Sr 88 ppm	Y 89 ppm	ZrO2 91 wt%	Nb 93 ppm	Ba 137 ppm	La 139 ppm	Ce 140 ppm	Pr 141 ppm	Nd 146 ppm	Sm 147 ppm	Eu 153 ppm	Gd 157 ppm	Tb 159 ppm	Dy 163 ppm	Ho 165 ppm	Er 166 ppm	Tm 169 ppm	Yb 172 ppm	Lu 175 ppm	Hf 178 ppm	Ta 181 ppm	Th 232 ppm	U 238 ppm
Mangerite, Horseshoe Island (W05-45)																										
1	au28a04	37.61		0.98	446	61.18	1.12	0.56	0.10	8.32	0.11	1.04	1.89	0.14	9.52	3.17	39.52	14.52	69.03	14.55	137.2	26.61	9920	0.71	46.7	63.3
2.1	au28a05	38.46		0.87	504	60.35	1.62	0.07	0.04	11.90	0.07	0.99	1.98	0.13	10.05	3.38	45.07	16.75	79.91	16.72	154.5	30.10	8628	0.99	65.3	84.3
2.2	au28a06	39.64		0.99	394	59.26	1.16	1.98	0.72	9.22	0.45	3.05	2.02	0.40	9.28	2.81	36.83	13.34	61.41	12.95	120.2	23.98	8980	0.87	35.5	42.5
3	au28a07	39.03		0.69	536	59.88	1.38	<0.20	0.09	9.30	0.11	1.44	2.27	0.25	11.63	3.83	47.59	17.92	83.38	17.41	154.3	30.89	8667	0.64	55.1	65.6
4	au28a08	38.81		0.77	457	60.09	1.38	0.34	0.02	9.38	0.06	1.03	1.91	0.12	9.66	3.26	40.87	15.23	70.44	14.34	136.2	26.71	8824	0.81	51.4	62.4
5	au28a09	39.11		0.80	472	59.83	1.37	0.72	0.16	8.43	0.11	1.23	2.10	0.21	10.31	3.31	42.43	15.89	73.83	15.29	142.6	28.03	8449	0.74	43.8	55.8
7	au28a10	38.78		0.71	398	60.14	1.28	0.14	0.04	7.74	0.06	0.82	1.68	0.11	8.14	2.79	35.07	13.04	62.77	13.39	123.7	24.25	8840	0.71	40.2	54.7
8.1	au28a11	36.60		0.79	602	62.26	1.62	0.01	0.11	10.69	0.17	1.81	2.58	0.24	14.61	4.69	55.92	20.09	91.52	19.23	173.0	33.11	8863	0.93	58.8	70.1
8.2	au28a12	36.15		1.12	638	62.77	1.00	3.95	0.85	9.42	0.83	5.94	5.82	0.91	19.88	5.69	64.23	21.89	93.95	18.66	167.3	31.87	8301	0.48	25.3	23.0
10	au28a13	35.68		0.91	644	63.20	1.06	0.36	0.17	8.01	0.24	2.73	3.56	0.26	18.04	5.13	61.25	21.61	96.42	19.30	170.7	32.56	8712	0.63	48.5	44.7
12	au28a14	35.70		0.79	422	63.19	1.25	0.28	0.35	8.62	0.21	1.46	1.56	0.21	8.87	3.06	37.15	14.28	66.39	14.16	132.5	25.70	9078	0.68	40.4	51.6
16	au28a15	38.46		0.69	518	60.50	1.09	0.48	0.27	7.91	0.21	2.28	2.90	0.18	13.07	4.07	48.27	17.52	78.83	16.14	145.5	27.98	8236	0.59	42.7	44.8
17	au28a16	37.27		0.80	568	61.83	1.53	0.07	0.53	13.97	0.41	3.19	2.75	0.29	13.46	4.11	50.74	18.88	89.75	18.79	172.8	32.28	8593	0.99	64.2	98.3
18	au28a17	37.87		0.93	912	60.95	1.44	0.21	0.61	15.08	0.51	4.23	5.27	0.36	22.31	7.02	85.31	30.98	141.21	29.17	264.2	49.15	8861	1.02	112.2	124.8
20	au28b04	33.86		0.92	374	65.17	1.16	3.80	0.12	7.82	0.09	0.98	1.55	0.10	7.90	2.61	33.22	12.43	57.83	12.39	113.5	22.09	7827	0.67	40.0	46.9
27	au28b05	33.57		0.85	630	65.29	1.99	0.72	1.17	19.19	0.96	5.64	3.58	0.47	14.27	4.48	57.31	21.30	101.01	22.02	202.3	38.22	8888	1.48	105.8	154.3
30	au28b06	32.28		0.88	606	66.69	1.09	0.14	0.09	8.05	0.16	1.91	3.26	0.20	14.80	4.75	57.37	20.26	92.23	19.22	170.2	31.43	8008	0.64	50.0	55.8
33	au28b07	34.43		0.86	441	64.56	1.06	0.14	0.03	7.85	0.06	0.94	1.75	0.14	8.81	3.16	38.67	14.75	69.75	14.87	138.4	25.96	8125	0.64	37.2	49.5
34	au28b08	34.43		4.15	1100	64.48	1.30	1.05	48.24	117.60	13.68	61.55	16.56	0.90	38.56	10.15	108.98	36.77	158.15	31.05	286.5	49.15	7486	0.85	113.4	95.6
36	au28b09	31.33		0.72	484	67.54	1.42	0.32	0.79	10.44	0.35	2.35	3.22	0.11	11.04	4.18	48.77	17.93	84.35	17.81	158.0	30.49	9063	0.74	50.1	66.4
39	au28b10	34.45		0.84	299	64.43	1.06	<0.01	0.07	7.17	0.10	0.94	1.31	0.11	5.80	2.03	26.39	9.91	47.58	10.35	95.4	18.68	9319	0.65	42.8	75.9
44	au28b11	33.37		0.93	523	65.54	1.19	0.84	0.23	9.30	0.23	2.26	3.03	0.08	12.50	3.79	48.76	17.46	80.84	17.34	154.6	29.34	8668	0.75	49.8	68.0
46.1	au28b12	35.28		0.83	345	63.69	1.20	0.01	0.05	7.88	0.07	0.86	1.45	0.13	7.80	2.43	30.54	11.94	55.33	11.87	107.8	21.33	8417	0.72	34.2	47.4
46.2	au28b13	34.19		0.75	626	64.74	1.19	0.14	0.31	9.41	0.30	2.73	2.87	0.27	14.91	4.89	58.34	21.08	96.50	19.72	177.2	33.93	8271	0.61	46.9	56.5
Anorthosite, Horseshoe Island (CMO32)																										
10-84_8	oc16a04	38.30	0.0014	0.14	230	60.85	0.91	0.11	0.02	6.84	0.11	2.13	4.18	0.52	14.94	3.61	32.65	8.82	35.73	7.85	74.1	16.87	6938	0.80	7.1	33.1
10-75_15	oc16a05	39.62	0.0028	0.79	298	59.39	0.61	0.78	0.84	7.62	0.69	3.80	1.71	1.95	5.89	1.92	25.22	9.83	47.74	10.88	109.3	22.84	8174	0.20	64.1	53.4
10-75_12	oc16a06	37.74	0.0070	0.20	694	61.27	0.97	0.08	0.13	8.96	0.79	10.34	11.41	1.21	39.62	10.22	109.92	34.59	144.70	28.17	244.0	45.94	7348	0.44	102.2	42.5
10-56_6	oc16a07	42.41	0.0084	0.25	850	56.83	0.92	0.08	0.09	8.90	0.87	9.02	10.44	1.01	35.55	9.40	105.15	32.94	139.28	27.11	228.6	41.13	6824	0.39	125.3	50.2
10-55_6	oc16a08	36.06	0.0070	1.30	536	62.69	0.81	8.69	1.56	14.09	1.17	7.28	3.95	2.14	12.91	3.31	40.44	16.34	76.57	17.73	175.9	37.52	9956	0.37	171.6	162.4
10-47_9	oc16a09	37.61	0.0064	1.02	894	61.40	0.82	1.56	0.28	7.27	0.29	3.07	5.77	0.60	25.77	7.32	84.18	26.87	119.41	23.16	202.7	39.10	7055	0.28	103.9	46.2
10-47_7	oc16a10	38.85	0.0014	0.15	418	60.06	0.88	0.15	0.01	8.89	0.04	0.62	1.12	0.20	8.21	2.07	30.10	11.94	63.69	15.28	160.9	38.86	8742	0.46	77.4	208.7
10-36_9	oc16a11	36.17	0.0014	0.43	273	62.62	0.74	2.73	0.12	5.25	0.10	0.62	0.96	0.20	5.44	1.89	25.07	9.24	44.62	10.09	93.3	17.48	10587	0.36	58.0	42.0
10-35-13	oc16a12	39.25	0.0000	1.00	216	59.34	0.67	0.52	0.12	4.57	0.09	0.63	0.61	0.21	3.37	1.28	17.55	6.72	33.51	7.57	72.8	14.45	12559	0.33	77.6	50.1
10-33-2	oc16a13	39.34	0.0014	0.26	236	59.64	0.61	1.25	0.05	3.99	0.06	0.58	0.85	0.28	4.33	1.46	20.26	7.89	39.50	9.22	93.7	19.36	8584	0.22	65.5	59.1
10-31-1	oc16a14	37.68	0.0014	0.18	654	61.37	0.90	0.25	0.02	7.35	0.10	1.88	3.87	0.48	18.87	5.83	70.63	24.34	110.07	23.58	223.5	42.84	7186	0.46	56.0	58.4
10-31-11	oc16a15	39.72	0.0128	0.18	490	59.35	0.69	0.76	0.12	6.23	0.06	1.31	2.77	0.37	13.26	4.07	48.26	16.93	75.29	16.42	158.5	29.68	7268	0.28	37.7	43.0
10-30-12	oc16a16	39.89	0.0014	0.15	889	59.08	0.69	0.33	0.04	7.67	0.13	2.51	5.54	0.77	28.73	8.46	98.60	31.45	131.50	26.53	236.3	45.02	7530	0.36	77.8	59.9
10-30-6	oc16a17	38.86	0.0070	7.01	485	60.21	1.01	4.72	0.18	5.76	0.18	2.69	3.99	0.50	15.87	4.28	48.72	16.38	71.50	14.73	138.1	26.85	7370	0.55	57.9	31.5
10-29-14	oc16b04	38.12	0.0014	0.24	522	60.96	0.89	0.85	0.05	8.31	0.07	1.41	2.86	0.39	14.15	4.30	52.06	17.75	80.06	17.77	177.9	35.18	6938	0.31	40.2	58.0
10-29-12	oc16b05	37.93	0.0014	0.09	256	61.21	0.66	0.07	0.04	7.58	0.31	5.20	8.20	1.07	23.78	5.42	44.34	10.81	39.14	7.58	67.7	12.69	7033	0.51	9.2	20.3
10-29-06	oc16b06	37.69	0.0151	1.21	242	61.47	0.71	6.45	1.15	8.48	0.49	2.17	1.92	0.35	4.85	1.61	21.03	7.22	33.47	6.90	59.7	14.06	6666	0.30	24.1	18.8
10-28-19	oc16b07	37.81	0.0014	0.18	564	61.52	0.79	0.10	0.07	6.70	0.09	1.53	2.73	0.40	14.13	4.57	56.00	19.51	87.93	19.59	195.0	38.59	6587	0.41	40.0	61.6
10-24-26	oc16b08	38.34	0.0014	0.40	60	60.59	2.16	0.12	0.06	22.48	0.83	11.10	24.18	3.03	110.72	31.30	345.99	108.77	451.21	91.76	830.0	150.09	8717	0.95	372.3	314.2
10-24-25	oc16b09	38.66	0.0014	0.18	17	60.56	72.46	1.71	3.58	82.12	8.55	28.63	2.74	16.05	1.60	0.28	2.30	0.65	3.04	0.66	6.9	1.43	6502	23.83	1.6	40.8
10-22-4	oc16b10	38.89	0.0014	0.12	208	60.12	0.73	0.07	0.01	4.45	0.02	0.33	0.74	0.09	4.10	1.42	18.60	6.78	31.78	6.68	62.2	11.93	8437	0.39	33.8	34.2
10-20-8	oc16b11	37.73	0.0014	0.15	509	61.41	0.80	0.04	0.02	6.03	0.06	1.06	2.32	0.30	12.01	3.85	47.15	16.57	75.73	16.53	160.9	31.90	6644	0.42	36.7	49.8
10-14-16	oc16b12	37.81	0.0014	0.19	413	61.12	0.81	0.20	0.04	5.33	0.04	0.56	1.46	0.24	8.37	2.76	35.68	13.10	61.00	12.87	120.7	22.28	8918	0.46	61.1	43.4
10-14-15	oc16b13	39.60	0.1583	2.38	1014	59.32	2.98	1.52	1.42	19.05	1.11	7.90	7.31	2.22	27.84	8.42	105.37	38.69	169.91	44.31	456.6	93.43	5956	0.94	128.0	370.4
10-11_21	oc16b14	38.06	0.0014	0.48	522	61.12	0.82	0.09	0.14	6.71	0.12	1.23	2.15	0.35	11.76	3.82	48.28	17.01	78.48	17.07	167.2	33.06	6183	0.47	43.1	55.9
10-11_11	oc16b15	36.31	0.0069	0.15	418	62.74	0.92	0.12	0.06	8.34	0.63	9.34	11.16	1.06	36.43	9.66	103.25	33.21	139.25	27.03	233.8	42.98	7132	0.42	134.2	52.1
10-10_25	oc16b16	36.48	0.0069	0.12	310	62.67	0.95	0.20	0.04	2.91	0.04	0.53	1.19	0.17	6.51	2.34	29.07	10.53	50.51	10.72	95.4	20.38	6924	0.57	116.3	70.0
10-8_24	oc16b17	37.63	0.0069	1.35	778	61.43	0.80	2.69	0.42	7.06	0.38	5.31	7.55	0.88	29.76	7.63	85.18	27.82	118.34	23.12	203.1	38.54	6735	0.38	223.5	66.4
10-8_22	oc16c04	37.90	0.0055	1.25	651	61.21	1.61	0.46	0.10	8.89	0.17	2.16	3.86	0.52	17.89	5.63	69.98	26.26	127.25	28.58	276.5	57.75	6389	0.95	61.0	130.5
10-5_8	oc16c05	37.55	0.0014	0.24	278	61.61	0.76	0.95	0.04	14.60	0.21	3.61	8.18	1.10	42.43	12.94	148.44	45.71	171.62	29.54	228.7	34.53	6067	0.47	77.3	148.1
10-5_7	oc16c06	37.91	0.0014	0.24	220	61.12	0.69	0.20	0.03	4.74	0.03	0.35	0.74	0.14	4.40	1.47	18.84	6.90	32.27	6.94	66.0	12.02	8363	0.37	34.9	36.4
1-62_5	oc16c07	37.02	0.0014	0.24	568	62.11	0.72	0.06	0.01	6.44	0.06	1.37	3.28	0.41	14.75	4.52	55.50	18.81	84.39	18.13	169.7	32.65	6612	0.31	40.1	46.1
1-54_1	oc16c08	39.03	0.0014	0.07	188	60.06	0.83	0.03	0.02	4.07	0.03	0.42	0.67	0.17	3.62	1.30	16.97	6.48	30.93	7.28	75.9	14.06	7665	0.23	55.6	54.7
1-33_3	oc16c09	37.87	0.0014	0.11	221	61.17	0.82	0.14	0.01	4.15	0.02	0.27	0.58	0.10	3.54	1.28	17.96	7.17	36.66	8.61	88.3	17.73	8003	0.24	78.2	70.9
1-1_9	oc16c11	39.02	0.0014	0.21	256	60.04	0.67	0.09	0.17	5.70	0.16	1.01	0.67	0.49	4.66	1.52	21.37	8.44	41.77	9.62	97.6	19.65	7882	0.26	96.8	82.2

Table D.8. continued

Grain/spot Number	Isotope File name	Chondrite Normalized La	Ce	Pr	Nd	Sm	Eu	Gd	Tb	Dy	Ho	Er	Tm	Yb	Lu	ZrO2 - SiO2	Ratios Th/U	Lu/Hf	[La/Sm]n	[Gd/Yb]n	Nb/Ta	Eu/Eu*	Ce/Ce*
Mangerite, Horseshoe Is																							
1	au28a04	0.40	13.6	1.17	2.27	12.7	2.54	48	88	161	266	431	589	852	1082	23.57	0.739	0.0027	0.032	0.056	1.57	0.084	17.2
2.1	au28a05	0.17	19.4	0.79	2.17	13.4	2.32	51	94	183	307	499	677	959	1224	21.89	0.774	0.0031	0.012	0.053	1.84	0.073	40.7
2.2	au28a06	3.05	15.0	4.90	6.66	13.6	7.05	47	78	150	244	384	524	747	975	19.82	0.835	0.0027	0.224	0.062	1.75	0.234	3.8
3	au28a07	0.37	15.2	1.23	3.14	15.4	4.38	58	106	193	328	521	705	958	1256	20.85	0.839	0.0036	0.024	0.061	1.65	0.119	19.0
4	au28a08	0.10	15.3	0.64	2.26	12.9	2.21	49	90	166	279	440	581	846	1066	21.28	0.824	0.0030	0.008	0.057	1.71	0.072	41.3
5	au28a09	0.69	13.8	1.23	2.89	14.2	3.64	52	92	172	287	460	619	886	1139	20.72	0.784	0.0033	0.049	0.059	1.85	0.110	14.3
7	au28a10	0.17	12.6	0.63	1.79	11.3	1.94	41	77	143	239	382	542	769	986	21.36	0.738	0.0027	0.015	0.053	1.77	0.074	31.8
8.1	au28a11	0.48	17.4	1.88	3.97	17.5	4.30	73	130	227	368	572	778	1074	1346	25.66	0.839	0.0037	0.027	0.068	1.73	0.095	14.8
8.2	au28a12	3.59	15.4	8.96	13.00	39.3	16.06	100	158	281	401	587	756	1039	1296	26.62	1.102	0.0038	0.091	0.096	2.08	0.231	2.4
10	au28a13	0.73	13.1	2.55	5.97	24.0	4.60	81	142	249	396	603	781	1060	1324	27.52	1.040	0.0037	0.031	0.076	1.67	0.068	8.0
12	au28a14	1.47	14.1	2.31	3.20	10.6	3.76	45	85	151	261	415	573	823	1045	27.49	0.783	0.0026	0.139	0.054	1.84	0.137	7.4
16	au28a15	1.15	12.9	2.28	4.99	19.6	3.16	66	113	196	321	491	653	904	1137	22.03	0.954	0.0034	0.059	0.073	1.84	0.074	7.5
17	au28a16	2.23	22.8	4.41	8.99	18.8	5.07	68	114	206	346	561	761	1073	1312	24.36	0.874	0.0038	0.120	0.063	1.55	0.118	6.9
18	au28a17	2.59	24.8	5.45	9.26	35.6	6.45	112	195	347	567	883	1181	1641	1998	23.06	0.899	0.0055	0.073	0.068	1.40	0.087	6.1
20	au28b04	0.53	12.4	0.96	2.15	10.5	1.84	40	72	135	228	361	502	705	898	31.31	0.817	0.0028	0.050	0.056	1.74	0.073	16.7
27	au28b05	4.92	31.3	10.38	12.33	24.2	8.27	72	124	233	390	631	891	1257	1554	31.72	0.685	0.0043	0.204	0.057	1.34	0.173	4.1
30	au28b06	0.37	13.1	1.77	4.17	22.0	3.63	74	131	233	371	576	778	1057	1278	34.41	0.896	0.0039	0.017	0.070	1.69	0.075	12.3
33	au28b07	0.13	12.5	0.60	2.06	11.8	2.50	44	87	157	270	436	602	847	1055	30.13	0.752	0.0032	0.011	0.052	1.69	0.089	34.0
34	au28b08	203.54	191.8	147.41	134.68	111.9	16.05	194	281	443	673	988	1257	1655	1998	30.05	1.167	0.0066	1.819	0.117	1.54	0.105	1.1
36	au28b09	3.34	17.0	3.74	5.15	21.7	1.98	55	116	196	326	527	721	981	1239	36.21	0.754	0.0034	0.154	0.057	1.92	0.051	4.8
39	au28b10	0.28	11.7	1.06	2.07	8.8	1.96	29	56	107	181	297	419	592	759	29.96	0.563	0.0020	0.031	0.049	1.64	0.103	17.2
44	au28b11	0.96	15.2	2.53	4.93	20.5	1.46	63	105	190	320	504	702	960	1193	32.17	0.732	0.0034	0.047	0.065	1.59	0.035	8.7
46.1	au28b12	0.19	12.5	0.80	1.69	9.8	2.25	38	67	124	219	346	473	669	867	28.41	0.722	0.0025	0.019	0.057	1.67	0.094	25.3
46.2	au28b13	1.31	15.4	3.28	5.96	19.4	4.83	75	130	237	386	603	798	1101	1379	30.55	0.868	0.0041	0.068	0.068	1.94	0.102	8.7
Anorthosite, Horseshoe																							
10-84_8	oc16a04	0.07	11.2	1.23	4.87	28.2	9.30	75	100	133	162	223	318	461	686	22.54	0.213	0.0024	0.002	0.183	1.14	0.180	17.3
10-75_15	oc16a05	3.52	12.4	7.45	7.87	11.8	34.82	30	53	103	176	298	440	679	920	19.77	1.200	0.0028	0.305	0.044	3.05	1.683	2.3
10-75_12	oc16a06	0.58	14.6	8.46	22.62	77.1	21.46	199	283	447	634	904	1141	1516	1867	23.53	2.408	0.0063	0.007	0.131	2.20	0.155	3.2
10-56_6	oc16a07	0.38	14.5	7.18	19.73	70.5	17.95	179	260	427	603	871	1098	1420	1672	14.22	2.494	0.0060	0.005	0.126	2.37	0.144	3.8
10-55_6	oc16a08	6.59	23.0	12.57	15.93	26.7	38.09	85	92	164	299	479	718	1093	1525	26.83	1.058	0.0038	0.247	0.059	2.21	0.832	2.4
10-47_9	oc16a09	1.19	11.9	3.11	6.71	39.0	10.68	130	203	342	489	746	938	1259	1589	23.78	2.247	0.0055	0.031	0.103	2.89	0.127	5.5
10-47_7	oc16a10	0.04	14.2	0.39	1.35	7.5	3.51	31	57	122	219	396	619	999	1498	21.21	0.371	0.0042	0.005	0.031	1.85	0.181	66.2
10-36_9	oc16a11	0.51	8.6	1.09	1.36	6.5	3.51	27	52	102	169	279	407	580	711	26.45	1.383	0.0017	0.078	0.047	2.05	0.207	10.7
10-35-13	oc16a12	0.49	7.5	0.97	1.38	4.1	3.80	17	35	71	123	209	307	452	588	20.09	1.549	0.0012	0.118	0.037	2.08	0.361	10.3
10-33-2	oc16a13	0.20	6.5	0.62	1.26	5.7	5.04	22	41	82	145	247	373	582	787	20.30	1.107	0.0023	0.034	0.037	2.83	0.366	16.0
10-31-1	oc16a14	0.10	12.0	1.08	4.12	26.1	8.45	95	162	287	446	688	955	1388	1741	23.69	0.959	0.0060	0.004	0.068	1.95	0.140	20.2
10-31-11	oc16a15	0.52	10.2	0.87	2.87	18.7	6.52	67	113	198	310	471	665	985	1207	19.63	0.878	0.0041	0.028	0.068	2.50	0.153	14.7
10-30-12	oc16a16	0.19	12.8	1.36	5.50	37.4	13.73	144	234	401	576	822	1074	1468	1830	19.19	1.298	0.0060	0.005	0.098	1.92	0.151	18.8
10-30-6	oc16a17	0.77	9.4	1.94	5.88	26.9	8.91	79	116	196	300	447	596	858	1063	21.35	1.835	0.0036	0.028	0.092	1.84	0.189	7.0
10-29-14	oc16b04	0.20	10.3	0.78	3.10	19.3	6.86	71	119	212	325	500	719	1105	1430	22.86	0.694	0.0051	0.010	0.064	2.25	0.152	21.0
10-29-12	oc16b05	0.17	12.4	3.39	11.37	55.4	19.02	119	150	180	198	245	307	421	524	23.29	0.455	0.0018	0.003	0.284	1.30	0.217	6.9
10-29-08	oc16b06	4.86	10.8	5.33	4.78	13.0	6.28	24	45	86	132	209	279	433	571	23.78	1.278	0.0021	0.375	0.056	2.34	0.336	2.1
10-28-19	oc16b07	0.29	10.9	1.00	3.34	18.4	7.12	71	126	226	357	550	793	1211	1569	23.90	0.848	0.0058	0.016	0.059	1.95	0.159	17.0
10-24-26	oc16b08	0.32	36.7	6.77	24.29	163.4	53.75	556	867	1408	1992	2820	3715	5155	6101	22.25	1.185	0.0223	0.002	0.106	2.29	0.149	10.3
10-24-25	oc16b09	15.09	134.0	92.14	62.65	18.5	285.07	6	7	9	12	19	27	43	58	21.90	0.039	0.0002	0.816	0.187	3.07	21.467	2.5
10-22-4	oc16b10	0.03	7.3	0.17	0.72	5.0	1.68	21	39	76	124	199	271	386	485	21.23	0.986	0.0014	0.007	0.053	1.88	0.131	71.5
10-20-6	oc16b11	0.08	9.6	0.68	2.36	15.7	5.36	80	107	192	303	473	669	999	1297	23.68	0.739	0.0048	0.005	0.080	1.88	0.141	28.3
10-14-16	oc16b12	0.15	8.7	0.40	1.26	10.0	4.33	42	78	145	240	381	521	750	906	23.32	1.410	0.0025	0.015	0.058	1.75	0.166	31.7
10-14-15	oc16b13	6.00	31.1	11.94	17.29	49.4	39.51	140	233	428	709	1187	1794	2836	3798	19.72	0.345	0.0157	0.121	0.049	3.17	0.417	3.5
10-11_21	oc16b14	0.60	11.0	1.29	2.70	14.5	6.24	59	106	196	312	491	691	1038	1345	23.06	0.772	0.0054	0.041	0.057	1.75	0.170	11.6
10-11_11	oc16b15	0.25	13.6	6.84	20.44	75.8	19.23	193	273	420	608	870	1094	1452	1747	26.43	2.577	0.0060	0.003	0.133	2.21	0.143	3.8
10-10_25	oc16b16	0.15	4.7	0.46	1.16	8.0	3.08	33	65	118	193	316	434	593	828	26.21	1.689	0.0029	0.018	0.055	1.68	0.150	15.5
10-8_24	oc16b17	1.77	11.5	4.10	11.61	51.0	15.72	150	217	346	509	740	936	1262	1567	23.81	3.366	0.0057	0.035	0.119	2.21	0.157	3.9
10-8_22	oc16c04	0.44	14.2	1.62	4.72	26.1	9.23	89	156	284	481	795	1157	1717	2348	23.31	0.620	0.0090	0.017	0.052	1.69	0.161	12.8
10-5_8	oc16c05	0.16	23.8	2.30	7.89	55.2	19.48	213	358	603	837	1074	1196	1420	1403	24.06	0.529	0.0057	0.003	0.150	1.60	0.145	19.3
10-5_7	oc16c06	0.11	7.7	0.34	0.78	5.0	2.40	22	41	77	126	202	281	410	489	23.21	0.958	0.0014	0.023	0.054	1.67	0.177	33.8
1-62_5	oc16c07	0.03	10.5	0.84	2.99	22.1	7.24	74	125	228	341	527	734	1054	1327	25.09	0.870	0.0049	0.001	0.070	2.28	0.150	31.3
1-54_1	oc16c08	0.10	6.6	0.37	0.91	4.5	3.04	18	36	69	119	193	295	471	572	21.03	1.017	0.0018	0.023	0.039	2.70	0.268	28.4
1-33_3	oc16c09	0.05	6.6	0.19	0.59	3.9	1.72	18	36	73	131	229	349	549	721	23.30	1.076	0.0022	0.013	0.032	2.65	0.158	56.5
1-1_9	oc16c11	0.73	9.3	1.69	2.20	5.9	8.68	23	42	67	155	261	397	606	799	21.02	1.175	0.0026	0.124	0.039	2.55	0.593	7.7

Table D.8. Continued

Grain/spot Number	Isotope File name	SiO2 29 or 30 wt%	TiO2 49 wt%	Sr 88 ppm	Y 89 ppm	ZrO2 91 wt%	Nb 93 ppm	Ba 137 ppm	La 139 ppm	Ce 140 ppm	Pr 141 ppm	Nd 146 ppm	Sm 147 ppm	Eu 153 ppm	Gd 157 ppm	Tb 159 ppm	Dy 163 ppm	Ho 165 ppm	Er 166 ppm	Tm 169 ppm	Yb 172 ppm	Lu 175 ppm	Hf 178 ppm	Ta 181 ppm	Th 232 ppm	U 238 ppm
Granodiorite gneiss, North East shore (CM001)																										
1	ia31a05	37.66	0.0041	1.41	1816	61.06	1.72	0.26	0.58	23.04	0.72	7.87	11.44	1.71	49.72	14.80	169.97	59.84	275.02	58.92	555.4	105.55	7681	0.87	176.0	312.0
2	ia31a06	36.13	0.0014	1.50	2485	62.21	2.20	0.01	0.34	22.87	0.39	5.08	9.61	0.18	50.31	16.85	223.83	81.95	383.85	74.84	629.0	101.42	10468	1.94	383.9	322.7
3	ia31a07	37.08	0.0027	0.89	966	61.74	1.42	0.05	0.03	24.69	0.12	2.11	4.60	0.56	24.33	7.35	91.90	32.54	149.97	32.02	289.1	52.52	8326	1.13	202.0	361.5
4	ia31a08	37.35	0.0027	1.33	2099	61.23	1.86	0.32	1.71	25.53	1.10	12.99	16.84	0.23	63.41	18.96	218.96	71.16	293.69	56.74	474.1	75.50	8967	1.58	264.2	201.5
5	ia31a09	37.63	0.0027	1.20	1993	60.99	1.40	0.03	0.06	18.23	0.69	10.89	15.18	0.29	62.84	18.58	212.06	69.38	278.41	53.76	437.2	69.40	8741	1.00	241.0	160.9
6	ia31a10	37.51	0.0027	1.08	1089	61.17	2.51	0.05	0.01	20.15	0.14	2.42	4.77	0.09	24.22	8.13	104.56	37.85	166.85	34.51	300.3	50.23	9872	1.85	138.0	141.9
7	ia31a11	38.09	0.0027	0.96	1088	60.60	2.40	0.04	0.02	19.76	0.14	2.49	4.83	0.06	22.73	7.69	101.33	35.70	160.69	33.33	291.5	47.40	9640	1.78	154.5	163.6
8	ia31a12	38.08	0.0027	1.38	2437	60.39	1.89	0.11	0.03	24.29	0.48	8.80	15.68	0.23	69.05	20.95	253.63	85.11	380.74	71.13	595.0	93.34	9453	1.45	290.1	196.2
9	ia31a13	37.01	0.0027	1.13	959	61.75	2.22	0.35	0.01	16.80	0.11	2.09	3.95	0.09	21.35	6.98	91.05	32.94	146.18	31.12	281.4	47.04	9115	1.51	100.5	112.1
10	ia31a14	39.11	0.0027	0.78	373	59.83	1.17	<0.11	0.16	7.02	0.10	1.11	1.94	0.15	7.82	2.69	35.04	12.24	58.63	12.97	121.4	22.19	8638	0.71	28.1	38.5
11	ia31a15	36.56	0.0027	1.31	1652	62.07	2.04	0.09	0.09	22.30	0.66	8.33	12.34	0.22	49.13	14.77	174.53	57.44	242.69	51.40	432.4	64.17	8845	1.86	238.5	223.7
12	ia31a16	39.33	0.0027	1.07	1313	59.37	2.13	0.08	0.05	18.80	0.27	4.51	7.45	0.11	35.44	10.88	130.86	45.57	197.89	41.22	364.2	60.53	9038	1.44	141.8	132.3
13	ia31a17	37.89	0.0027	1.40	2296	60.58	1.85	0.13	0.55	24.21	0.80	9.27	15.41	0.29	64.76	19.97	240.37	81.07	337.90	67.90	574.3	90.50	9594	1.35	244.8	179.8
14	ia31b05	33.30	0.0028	1.01	1095	65.44	2.87	<0.04	0.02	19.85	0.10	1.77	3.66	0.08	19.29	7.17	99.33	36.39	168.74	35.92	314.8	50.07	9138	2.25	161.2	177.2
15	ia31b06	35.17	0.0028	0.83	701	63.79	1.06	0.00	0.01	8.17	0.09	1.57	3.60	0.22	16.65	5.52	69.48	24.68	109.87	23.59	213.8	36.68	7778	0.59	58.1	69.5
16	ia31b07	35.15	0.0014	0.93	737	63.69	1.04	0.22	0.34	10.99	0.34	2.51	2.91	0.24	15.15	5.08	66.85	25.05	117.00	25.38	233.0	40.75	8694	0.84	94.7	223.5
18.1	ia31b08	35.55	0.0028	1.00	1203	63.27	2.05	0.13	0.02	19.31	0.22	4.05	7.20	0.11	33.20	10.23	125.33	42.38	179.83	36.31	318.1	50.42	8224	1.55	174.8	172.2
19	ia31b09	35.67	0.0028	0.99	1167	63.10	2.00	<0.04	0.02	19.15	0.22	4.04	6.80	0.11	30.73	9.85	120.21	40.82	174.85	35.50	306.2	49.51	8626	1.66	177.2	174.4
18.2	ia31b10	35.76	0.0041	0.88	1154	63.05	2.07	0.29	0.07	18.80	0.23	3.50	7.21	0.07	31.03	9.62	118.69	39.89	170.90	34.97	301.8	49.15	8304	1.81	164.4	167.7
20	ia31b11	35.42	0.0028	1.40	1847	63.37	5.74	0.46	3.52	70.01	1.35	8.14	11.19	1.12	49.83	16.00	198.96	68.87	296.53	60.55	539.8	82.77	6887	2.60	240.2	337.5
21	ia31b12	37.36	0.0028	0.94	963	61.50	2.12	<0.05	0.01	16.69	0.16	2.65	4.96	0.07	23.14	7.47	95.06	33.31	149.22	30.82	270.5	45.80	8281	1.49	110.4	118.4
22	ia31b13	35.90	0.0014	1.23	1160	62.91	1.72	0.17	7.52	67.73	4.98	24.13	15.15	2.22	37.44	10.06	118.06	39.94	182.53	41.18	417.3	79.28	8016	0.97	139.5	227.4
23	ia31b14	37.28	0.0028	1.05	1409	61.83	4.13	0.34	0.40	34.18	0.57	6.21	9.44	0.87	46.08	13.05	152.91	50.25	210.03	41.37	364.3	63.19	8515	1.98	266.9	382.9
24	ia31b15	36.31	0.0014	1.11	1149	62.27	3.49	0.00	0.12	21.25	0.12	1.94	3.16	0.04	18.23	6.86	99.03	38.29	181.32	40.80	356.8	58.36	10392	2.91	234.4	300.2
25	ia31b16	35.50	0.0028	1.09	987	63.25	1.18	0.16	1.24	14.01	0.70	5.23	6.01	1.00	24.15	7.53	92.83	32.07	149.36	34.41	348.7	63.21	8729	0.93	149.3	460.4
26	ia31b17	36.57	0.0028	0.94	976	62.19	2.52	0.13	0.01	18.74	0.11	2.19	4.23	0.07	19.76	7.06	91.24	33.31	151.47	32.00	278.2	45.69	9144	1.79	133.2	142.8
27	ia31c05	33.23	0.0027	1.02	1153	65.57	2.27	0.07	0.01	16.62	0.17	3.08	6.15	0.13	28.33	9.01	110.79	39.87	172.79	34.74	300.2	54.63	8501	1.57	146.6	136.9
28	ia31c06	33.75	0.0027	1.24	2136	64.78	2.15	0.03	0.01	19.34	0.22	3.53	7.61	0.10	41.84	14.12	188.47	69.39	315.86	63.48	536.3	94.83	9350	1.74	295.8	250.0
29	ia31c07	34.36	0.0027	0.99	1174	64.42	2.06	0.03	0.01	16.87	0.20	3.43	6.60	0.09	28.70	9.29	117.86	41.01	178.81	36.60	312.4	51.82	8422	1.50	164.0	147.0
30	ia31c08	34.23	0.0027	0.66	478	64.82	1.23	0.24	0.07	7.97	0.07	0.97	2.19	0.17	11.63	3.70	46.68	16.33	74.66	15.86	143.0	25.63	7391	0.69	39.3	43.0
31	ia31c09	34.50	0.0027	0.84	1019	64.35	2.15	<0.03	0.03	17.54	0.17	2.78	5.56	0.06	25.18	8.07	99.98	35.39	153.87	31.80	280.2	47.28	8283	1.53	122.6	128.0
32	ia31c10	33.77	0.0027	1.18	1886	64.92	1.37	0.01	0.45	16.20	0.66	6.43	8.12	0.25	36.40	12.97	169.07	60.95	262.99	50.25	412.7	71.92	8536	0.88	162.2	148.5
33	ia31c11	34.69	0.0027	1.45	2568	63.51	2.31	<0.07	0.02	22.90	0.38	6.75	12.64	0.17	57.33	18.87	237.91	84.79	367.94	71.34	583.6	102.15	9943	1.87	385.0	320.4
34	ia31c12	34.69	0.0027	1.10	1106	64.04	2.13	0.43	0.05	18.48	0.22	3.09	5.52	0.07	25.49	8.58	104.29	37.27	163.61	32.37	277.7	51.37	9230	1.59	143.7	140.8
35	ia31c13	34.95	0.0027	1.03	1341	63.70	2.79	<0.03	0.01	22.14	0.17	3.02	5.31	0.08	28.98	9.87	123.02	44.68	197.99	39.91	338.1	61.79	9611	2.01	192.4	173.7
37	ia31c14	35.52	0.0014	1.05	922	63.23	1.08	0.91	0.87	14.31	0.64	4.53	5.89	1.08	24.33	7.21	84.29	29.84	137.86	30.50	289.7	61.80	9089	0.90	105.1	439.8
39	ia31c15	35.36	0.0027	1.05	1057	63.31	2.22	0.03	0.01	19.53	0.14	2.23	4.72	0.06	23.19	7.59	95.94	35.11	155.60	30.83	285.6	48.27	9761	1.77	152.8	154.8
40	ia31c16	35.07	0.0014	0.75	371	63.81	1.29	0.04	0.01	7.71	0.04	0.71	1.44	0.08	8.13	2.54	32.33	12.34	57.20	12.54	116.4	22.92	9180	0.78	33.8	46.3
41	ia31c17	35.33	0.0027	1.37	2556	63.18	1.74	0.01	0.17	24.00	1.22	17.27	20.60	0.31	79.16	22.89	258.62	88.04	361.97	68.38	568.0	101.44	8873	1.59	277.2	208.3
42	ia31d06	37.09	0.0028	0.94	1260	61.51	3.61	0.03	0.04	20.60	0.10	1.68	3.27	0.05	19.40	7.39	108.17	41.32	197.92	42.32	383.4	64.42	10053	2.78	248.9	289.4
43	ia31d07	35.38	0.0028	1.25	2340	63.11	1.87	0.07	0.61	25.81	0.92	12.52	17.83	0.33	70.82	21.10	246.65	79.43	324.17	62.80	506.1	79.58	9430	1.45	340.7	249.1
44	ia31d08	34.92	0.0028	1.70	1053	63.75	1.78	2.16	0.75	44.41	0.54	3.87	4.45	1.31	19.94	8.52	83.94	32.63	164.67	40.93	419.6	83.88	8837	1.41	462.7	784.0
45	ia31d09	35.51	0.0042	1.09	897	63.32	1.87	1.94	0.61	15.54	0.17	1.63	3.25	0.08	17.53	6.62	84.29	30.36	136.14	27.93	240.2	38.46	8650	1.27	124.4	117.7
46	ia31d10	35.67	0.0028	1.25	2337	62.90	1.75	0.12	0.08	23.14	0.87	13.52	17.68	0.25	72.39	21.55	249.03	82.18	338.39	67.23	553.1	90.11	8692	1.34	253.8	181.8
47	ia31d11	35.48	0.0028	0.86	1078	63.33	2.30	<0.04	0.01	18.77	0.14	2.47	4.98	0.09	25.80	8.45	105.84	37.20	162.14	34.46	299.8	50.86	8577	1.52	128.1	129.2
48	ia31d12	36.40	0.0028	0.95	1144	62.34	2.22	<0.10	0.01	18.27	0.16	2.84	5.82	0.10	28.51	8.90	115.32	39.60	173.68	35.64	305.2	51.25	9073	1.67	140.3	142.4
49	ia31d13	36.70	0.0028	0.93	984	62.10	2.49	0.08	0.00	16.89	0.10	2.04	3.62	0.05	20.09	6.60	91.29	33.58	153.84	32.75	287.1	48.68	8853	1.67	118.0	123.8
50	ia31d14	35.69	0.0028	1.11	1630	62.88	2.62	<0.03	0.01	21.17	0.23	3.84	7.71	0.15	35.81	11.94	153.29	55.08	245.35	50.77	429.5	70.91	9704	2.13	274.8	274.8
51	ia31d15	35.90	0.0028	1.02	1099	62.85	2.28	0.05	0.01	20.18	0.15	2.54	4.94	0.07	25.98	8.36	108.77	37.81	162.72	33.71	293.2	47.83	9070	1.71	151.2	151.5
52	ia31d16	36.76	0.0028	0.93	1451	61.95	2.03	<0.03	0.03	19.16	0.32	5.68	9.07	0.16	39.94	12.12	149.88	51.00	214.29	43.80	377.4	61.95	8690	1.46	177.9	156.3
53	ia31d17	37.06	0.0014	1.16	2074	61.61	1.77	0.12	0.12	21.92	0.82	12.10	16.44	0.28	67.25	18.88	223.96	74.39	310.54	61.10	517.1	85.26	8097	1.41	241.4	187.6

Table D.8. continued

Grain/spot Number	Isotope File name	Chondrite Normalized La	Ce	Pr	Nd	Sm	Eu	Gd	Tb	Dy	Ho	Er	Tm	Yb	Lu	ZrO2 - SiO2	Ratios Th/U	Lu/Hf	[La/Sm]n	[Gd/Yb]n	Nb/Ta	Eu/Eu*	Ce/Ce*
Granodiorite gneiss, No																							
1	ia31a05	2.45	37.6	7.77	17.22	77.3	30.38	250	410	691	1096	1719	2386	3449	4291	23.42	0.564	0.0137	0.032	0.072	1.96	0.186	7.4
2	ia31a06	1.44	37.3	4.16	11.12	65.0	3.27	253	467	910	1501	2274	3030	3907	4123	26.08	1.190	0.0097	0.022	0.065	1.13	0.021	13.3
3	ia31a07	0.12	40.3	1.24	4.61	31.1	9.97	122	204	374	596	937	1296	1795	2135	24.68	0.559	0.0083	0.004	0.068	1.26	0.130	59.2
4	ia31a08	7.23	41.8	11.88	28.43	113.8	4.15	319	525	890	1303	1836	2297	2945	3069	23.88	1.311	0.0084	0.064	0.106	1.18	0.019	4.4
5	ia31a09	0.26	29.7	7.44	23.83	102.5	5.09	315	515	862	1271	1740	2177	2716	2821	23.35	1.332	0.0079	0.003	0.116	1.41	0.024	7.7
6	ia31a10	0.08	32.9	1.48	5.29	32.3	1.64	122	225	425	693	1042	1397	1865	2042	23.65	0.972	0.0052	0.002	0.085	1.36	0.021	42.6
7	ia31a11	0.08	32.2	1.50	5.48	31.3	1.48	114	213	412	654	1004	1349	1811	1927	22.51	0.944	0.0049	0.003	0.063	1.35	0.020	40.8
8	ia31a12	0.11	39.6	5.17	19.25	109.0	4.09	347	580	1031	1559	2255	2880	3695	3794	22.31	1.464	0.0099	0.001	0.094	1.31	0.018	15.0
9	ia31a13	0.04	27.4	1.21	4.56	26.7	1.55	107	193	370	603	914	1260	1748	1912	24.75	0.898	0.0052	0.002	0.081	1.47	0.023	43.6
10	ia31a14	0.68	11.5	1.08	2.43	13.1	2.67	39	75	142	224	368	525	754	902	20.72	0.731	0.0026	0.052	0.052	1.63	0.102	13.2
11	ia31a15	0.38	36.4	7.12	18.22	83.3	3.85	247	409	709	1052	1517	2081	2686	2808	25.49	1.086	0.0073	0.005	0.092	1.10	0.023	9.7
12	ia31a16	0.22	30.7	2.88	9.87	50.3	2.01	178	301	532	835	1237	1669	2262	2481	20.04	1.071	0.0067	0.004	0.079	1.48	0.016	19.8
13	ia31a17	2.33	39.5	8.58	20.28	104.1	5.20	325	553	977	1485	2112	2749	3587	3879	22.69	1.361	0.0094	0.022	0.091	1.37	0.024	7.2
14	ia31b05	0.08	32.4	1.09	3.88	24.7	1.37	97	199	404	666	1055	1454	1955	2036	32.14	0.910	0.0055	0.003	0.050	1.27	0.022	56.2
15	ia31b06	0.03	13.3	0.98	3.44	24.3	3.83	84	153	282	452	687	955	1328	1491	28.63	0.836	0.0047	0.001	0.063	1.79	0.071	27.0
16	ia31b07	1.43	17.9	3.65	5.48	19.6	4.28	76	141	272	459	731	1027	1447	1657	28.54	0.424	0.0047	0.073	0.053	1.25	0.069	7.1
18.1	ia31b08	0.07	31.5	2.42	8.87	48.7	1.94	167	283	509	776	1124	1470	1976	2050	27.72	1.014	0.0061	0.001	0.084	1.32	0.018	25.3
19	ia31b09	0.10	31.2	2.38	8.83	44.8	1.89	154	273	489	744	1093	1437	1915	2013	27.43	1.016	0.0057	0.002	0.081	1.20	0.019	25.2
18.2	ia31b10	0.31	30.7	2.43	7.66	48.7	1.30	156	272	482	731	1068	1418	1874	1998	27.29	0.980	0.0059	0.006	0.063	1.28	0.013	22.4
20	ia31b11	14.84	114.2	14.50	17.80	75.6	19.91	250	443	801	1261	1853	2451	3353	3365	27.95	0.712	0.0120	0.198	0.075	2.21	0.122	7.8
21	ia31b12	0.05	27.2	1.75	5.80	33.5	1.24	116	207	386	610	933	1248	1680	1862	24.15	0.932	0.0055	0.001	0.089	1.42	0.017	30.2
22	ia31b13	31.72	110.5	53.69	52.80	102.4	39.36	188	279	480	732	1141	1667	2592	3223	27.01	0.613	0.0099	0.310	0.073	1.78	0.271	2.6
23	ia31b14	1.70	55.8	6.11	13.59	63.8	15.39	232	361	622	920	1313	1675	2263	2589	24.35	0.897	0.0097	0.027	0.102	2.09	0.104	14.3
24	ia31b15	0.52	34.7	1.32	4.24	21.3	0.79	92	190	403	701	1133	1644	2218	2372	25.96	0.781	0.0056	0.024	0.041	1.20	0.014	37.7
25	ia31b16	5.23	22.9	7.50	11.45	40.6	17.77	121	209	377	587	934	1393	2186	2570	27.75	0.324	0.0072	0.129	0.056	1.27	0.219	3.6
26	ia31b17	0.08	30.6	1.20	4.79	28.6	1.19	99	198	371	610	947	1295	1728	1857	25.62	0.933	0.0050	0.002	0.057	1.41	0.019	48.8
27	ia31c05	0.05	30.4	1.85	8.73	41.6	2.23	142	250	450	730	1080	1408	1885	2221	32.34	1.070	0.0084	0.001	0.076	1.45	0.024	32.0
28	ia31c06	0.04	31.8	2.34	7.72	51.4	1.74	209	391	766	1271	1974	2570	3331	3855	31.03	1.183	0.0101	0.001	0.063	1.23	0.013	26.6
29	ia31c07	0.08	30.8	2.12	7.51	44.6	1.60	144	257	478	751	1105	1482	1940	2108	30.04	1.118	0.0062	0.001	0.074	1.37	0.017	28.2
30	ia31c08	0.30	13.0	0.72	2.13	14.8	3.07	58	102	190	299	468	643	888	1042	30.59	0.915	0.0035	0.021	0.066	1.77	0.084	25.5
31	ia31c09	0.12	28.8	1.79	6.09	37.8	1.10	127	224	408	648	980	1287	1740	1922	29.85	0.958	0.0057	0.003	0.073	1.41	0.013	29.9
32	ia31c10	1.88	26.4	7.11	14.06	54.9	4.51	183	359	687	1118	1644	2035	2563	2924	31.15	1.227	0.0084	0.034	0.071	1.56	0.038	5.9
33	ia31c11	0.09	37.4	4.13	14.77	85.4	3.01	288	523	987	1553	2300	2888	3625	4152	28.62	1.202	0.0103	0.001	0.079	1.24	0.016	17.7
34	ia31c12	0.23	30.1	2.38	6.76	37.3	1.29	128	238	424	683	1023	1311	1725	2088	29.35	1.020	0.0056	0.008	0.074	1.34	0.016	23.1
35	ia31c13	0.05	36.1	1.80	6.60	35.9	1.37	148	268	500	818	1237	1818	2100	2512	28.74	1.108	0.0084	0.001	0.069	1.38	0.015	39.1
37	ia31c14	3.67	23.3	6.90	9.91	39.8	19.25	122	200	343	547	862	1235	1799	2512	27.71	0.239	0.0068	0.092	0.068	1.21	0.237	4.4
39	ia31c15	0.03	31.9	1.50	4.88	31.9	1.40	117	210	390	643	973	1248	1650	1962	27.93	0.987	0.0049	0.001	0.071	1.25	0.019	41.7
40	ia31c16	0.03	12.6	0.48	1.55	9.7	1.47	41	70	131	226	358	508	723	932	28.75	0.725	0.0025	0.003	0.057	1.69	0.058	51.1
41	ia31c17	0.71	39.2	13.18	37.79	139.2	5.52	398	634	1051	1813	2262	2768	3528	4124	27.85	1.331	0.0114	0.005	0.113	1.10	0.021	5.8
42	ia31d06	0.17	33.6	1.08	3.69	22.1	0.90	97	205	432	757	1237	1713	2257	2619	24.41	0.860	0.0084	0.008	0.043	1.30	0.015	54.1
43	ia31d07	2.58	41.8	9.95	27.41	120.5	5.90	356	564	1003	1455	2026	2542	3143	3235	27.74	1.368	0.0084	0.021	0.113	1.15	0.025	8.7
44	ia31d08	3.18	72.4	5.85	8.48	30.0	23.31	100	181	341	598	1029	1657	2606	3410	28.84	0.590	0.0095	0.105	0.038	1.28	0.358	16.1
45	ia31d09	2.57	25.4	1.82	3.57	22.0	1.09	88	163	343	556	851	1131	1492	1564	27.81	1.058	0.0044	0.117	0.059	1.47	0.020	11.6
46	ia31d10	0.24	37.8	9.40	29.58	119.4	4.45	384	597	1012	1505	2115	2722	3435	3863	27.23	1.397	0.0104	0.002	0.108	1.31	0.018	7.8
47	ia31d11	0.03	30.8	1.51	5.41	33.7	1.54	129	234	429	681	1013	1395	1881	2088	27.85	0.991	0.0059	0.001	0.089	1.51	0.019	39.6
48	ia31d12	0.04	29.8	1.70	6.22	38.0	1.69	133	247	469	725	1066	1443	1895	2083	25.94	0.985	0.0056	0.001	0.070	1.33	0.020	34.1
49	ia31d13	0.00	30.8	1.11	4.45	25.8	0.94	101	188	371	615	980	1328	1783	1979	25.40	0.953	0.0055	0.000	0.057	1.49	0.015	55.6
50	ia31d14	0.06	34.5	2.47	8.41	52.1	2.81	180	331	623	1009	1533	2056	2868	2883	27.19	0.999	0.0073	0.001	0.087	1.23	0.023	27.3
51	ia31d15	0.04	32.9	1.85	5.56	33.4	1.24	131	232	434	689	1017	1365	1821	1938	26.94	0.997	0.0053	0.001	0.072	1.32	0.015	39.1
52	ia31d16	0.11	31.3	3.45	12.43	61.3	3.27	201	336	609	934	1339	1773	2344	2518	25.17	1.138	0.0071	0.002	0.066	1.39	0.025	17.5
53	ia31d17	0.51	35.8	8.82	28.47	111.1	5.01	338	523	910	1363	1941	2474	3212	3466	24.55	1.287	0.0105	0.005	0.105	1.25	0.022	7.7

Table D.9. LA-ICP-MS multi-element analysis of zircon clasts from impact melt rocks at Mistastin Lake Crater

Grain/spot Number	Isotope File name		SiO2 30 wt%	TiO2 49 wt%	Sr 88 ppm	Y 89 ppm	ZrO2 91 wt%	Nb 93 ppm	Ba 137 ppm	La 139 ppm	Ce 140 ppm	Pr 141 ppm	Nd 146 ppm	Sm 147 ppm	Eu 153 ppm	Gd 157 ppm	Tb 159 ppm	Dy 163 ppm	Ho 165 ppm	Er 166 ppm	Tm 169 ppm	Yb 172 ppm	Lu 175 ppm	Hf 178 ppm	Ta 181 ppm	Th 232 ppm	U 238 ppm
South Ridge (CM065)																											
1	ja30a06	c	39.44	0.0014	1.51	1248	59.19	1.74	0.07	0.05	20.66	0.20	3.55	7.12	0.18	29.52	10.27	130.03	46.35	205.58	45.49	419.91	81.14	9576	1.85	181.4	233.5
2	ja30a09	c	39.93	0.0028	1.18	811	58.90	1.19	2.15	0.36	12.62	0.26	3.47	5.18	0.28	22.20	7.01	85.28	29.35	127.25	28.15	252.84	38.88	8603	0.87	90.9	98.2
3	ja30a10	1	39.21	0.0028	0.87	336	59.73	1.16	<0.02	0.12	8.13	0.13	1.88	1.67	0.16	7.98	2.62	32.62	11.98	55.28	12.44	116.09	19.32	8471	0.63	31.8	42.2
4	ja30a11	1	37.94	0.0028	0.98	726	60.92	1.04	<0.05	0.02	9.34	0.16	2.54	4.30	0.35	20.70	6.12	75.35	25.99	113.71	24.99	227.36	35.94	8415	0.72	64.0	65.5
5	ja30a12	1	38.89	0.0028	1.04	828	59.94	1.29	0.12	0.13	11.42	0.19	2.53	4.68	0.26	22.83	6.96	84.09	29.18	129.07	27.84	246.17	40.44	8566	0.88	79.8	84.3
6	ja30a13	1	38.28	0.0089	7.89	582	60.62	1.06	29.24	0.71	8.28	0.22	1.91	2.83	0.34	12.49	4.42	57.00	19.88	90.30	19.41	175.86	34.17	8302	0.49	35.4	43.2
7	ja30a14	1	37.01	0.0041	0.90	403	61.92	0.90	<0.07	0.01	6.45	0.07	1.08	1.95	0.29	9.51	3.11	40.53	14.20	64.35	14.73	137.20	22.98	8395	0.58	20.4	24.7
8	ja30a15	1	37.25	0.0041	0.90	777	61.67	0.94	<0.03	0.01	9.91	0.23	3.45	5.93	0.50	27.04	7.18	86.86	28.53	120.52	24.53	219.89	35.21	7913	0.59	43.9	36.8
9	ja30a16	1	38.36	0.0055	1.41	1153	60.42	3.10	1.89	0.54	21.01	0.42	5.18	7.57	0.22	32.54	9.88	117.13	40.45	180.49	37.28	332.89	56.98	8324	2.35	222.6	175.7
11	ja30a17	1	38.20	0.0028	0.93	601	62.73	1.40	0.10	0.01	11.53	0.11	1.82	3.09	0.20	15.36	4.77	60.11	20.98	95.90	20.62	191.41	32.25	8109	1.02	72.4	81.4
12	ja30b05	c	32.71	0.0027	1.52	412	68.19	1.38	1.02	0.13	7.89	0.11	1.02	1.73	0.07	7.92	2.92	35.75	14.04	65.42	14.17	132.35	24.89	8662	0.57	32.2	39.7
14	ja30b06	c	33.48	0.0014	0.98	535	65.37	0.85	<0.09	0.03	14.37	0.05	0.84	1.75	0.15	10.80	3.73	49.80	18.55	86.86	19.80	186.85	31.37	9099	1.28	103.4	139.7
16	ja30b07	c	34.44	0.0027	0.71	421	64.54	1.05	<0.02	0.01	9.44	0.05	0.85	1.68	0.12	9.14	3.13	39.81	14.53	69.01	14.90	140.19	23.79	7994	0.88	46.4	59.8
18	ja30b08	c	34.14	0.0014	0.84	512	64.79	1.44	0.13	0.02	11.82	0.07	1.00	1.85	0.11	11.29	3.84	48.64	17.67	82.99	18.09	168.73	29.42	8327	0.94	76.8	67.2
19	ja30b09	c	34.27	0.0027	0.98	1051	64.63	1.09	<0.04	0.02	10.23	0.32	4.67	7.83	0.59	32.37	9.51	109.58	36.81	159.99	32.18	281.23	47.71	7750	0.63	83.6	65.4
20	ja30b10	*	33.35	0.0082	2.52	378	65.51	1.03	3.97	0.58	10.35	0.20	1.42	1.60	0.13	6.14	2.67	34.47	12.76	62.69	13.93	130.88	22.89	9144	0.90	63.6	69.5
22	ja30b11	*	32.46	0.0055	0.99	537	66.45	1.14	1.24	0.89	10.67	0.22	2.18	2.46	0.16	12.28	4.06	50.56	19.04	88.43	19.37	176.13	31.70	8244	0.78	61.4	67.1
23	ja30b12	*	33.63	0.0041	1.43	805	64.95	1.13	1.33	0.53	14.58	0.24	1.74	1.89	0.15	10.46	4.33	64.77	26.13	139.15	32.74	317.65	55.87	10802	4.01	242.0	554.1
25	ja30b13	*	32.54	0.0082	1.36	1044	66.35	0.54	1.79	0.79	12.78	0.52	5.68	8.44	0.32	29.34	8.79	103.58	35.54	159.60	33.08	289.80	48.31	7660	0.91	143.0	119.9
26	ja30b14	*	32.52	0.0027	0.77	284	66.48	0.88	0.09	0.04	5.40	0.04	0.85	1.28	0.11	6.16	2.03	25.85	9.58	45.96	10.22	97.18	18.59	8188	0.54	25.3	53.3
27	ja30b15	*	29.94	0.0014	1.13	1280	68.70	0.67	0.45	0.68	17.37	0.29	2.57	4.13	0.09	20.73	7.44	100.02	39.97	189.80	40.46	382.55	60.35	9758	1.85	185.0	198.3
28	ja30b16	*	30.90	0.0014	1.08	383	68.04	2.05	0.29	0.01	7.80	0.03	0.85	1.58	0.11	8.26	2.72	35.52	13.01	63.05	13.17	123.88	22.17	8473	0.89	37.1	52.7
29	ja30b17	*	32.57	0.0014	1.08	985	66.23	1.33	0.09	0.02	40.57	0.18	2.79	5.22	0.26	20.72	6.79	87.84	32.72	156.20	33.69	308.40	56.33	8661	1.44	180.7	119.4
30	ja30c05	c	39.57	0.0027	0.98	545	59.19	1.45	<0.02	0.31	10.85	0.18	1.83	2.47	0.20	12.78	4.02	50.99	18.52	85.78	18.13	167.72	30.51	9681	0.84	54.6	59.8
32	ja30c06	c	38.56	0.0014	1.82	477	60.18	1.66	0.11	0.05	10.47	0.09	1.14	1.89	0.11	9.59	3.26	41.74	15.65	75.23	16.47	153.09	28.18	10112	1.12	54.6	81.7
33	ja30c07	c	38.94	0.0014	0.90	372	59.67	1.18	<0.01	0.01	7.46	0.04	0.81	1.67	0.09	7.44	2.60	33.46	12.67	59.34	12.97	119.95	22.27	9637	0.73	36.9	49.8
34	ja30c08	c	37.04	0.0041	1.15	476	61.75	1.04	1.91	0.10	6.73	0.16	2.19	1.67	0.27	10.86	3.06	41.52	16.69	73.61	15.95	155.09	30.26	9130	0.84	78.4	44.0
36	ja30c09	c	38.30	0.0041	0.84	370	62.52	1.12	0.07	0.02	7.14	0.05	0.82	1.76	0.11	8.59	2.86	35.73	12.74	59.57	13.42	125.11	21.59	9584	0.62	29.1	37.5
37	ja30c10	1	38.94	0.0027	0.76	445	61.98	1.10	<0.08	0.01	7.01	0.06	1.10	2.22	0.21	10.64	3.42	42.45	15.44	69.81	14.65	139.61	25.16	8631	0.57	29.9	34.8
38	ja30c11	1	38.20	0.0027	0.82	378	62.72	1.10	0.20	0.01	5.58	0.05	0.94	1.82	0.19	7.89	2.72	34.73	12.99	60.91	13.21	127.23	22.53	8630	0.45	17.2	22.8
39	ja30c12	1	37.81	0.0014	0.89	527	61.03	1.22	<0.01	0.03	9.05	0.06	1.00	1.98	0.09	11.20	3.89	49.35	18.28	85.06	18.32	171.92	30.40	9071	0.62	52.8	68.8
40	ja30c13	1	38.20	0.0041	0.88	339	60.71	1.12	0.20	0.06	6.59	0.06	0.93	1.51	0.12	7.59	2.47	31.77	11.49	53.15	11.85	109.95	19.79	8751	0.61	26.8	32.2
41	ja30c14	1	35.04	0.0041	0.98	674	63.84	1.02	0.19	0.02	6.56	0.11	1.97	3.67	0.32	17.39	5.29	68.72	22.93	99.97	21.23	194.10	34.57	8439	0.48	31.9	32.7
42	ja30c15	1	37.06	0.0041	0.86	432	61.93	0.99	<0.02	<0.01	6.30	0.06	1.20	2.29	0.27	10.17	3.24	41.24	14.81	67.57	14.31	132.60	23.89	7878	0.53	25.4	26.8
44	ja30c16	1	38.18	0.0014	0.97	864	62.60	1.13	0.15	0.03	9.76	0.10	1.77	3.74	0.29	21.16	6.86	85.01	30.83	137.57	28.13	252.41	44.29	9125	0.72	97.7	102.2
45	ja30c17	1	36.86	0.0027	0.86	300	62.15	0.94	<0.10	0.01	5.22	0.05	0.86	1.81	0.22	7.51	2.39	29.74	10.52	47.36	10.31	95.48	16.80	7884	0.45	13.9	17.1
47	ja30d05	c	35.77	0.0027	0.76	373	63.23	1.02	0.46	0.05	6.90	0.05	0.84	1.70	0.11	8.04	2.71	34.08	12.57	57.89	12.87	120.20	20.79	7934	0.61	33.1	40.7
50	ja30d06	c	32.91	0.0041	1.21	733	65.98	0.98	0.98	0.05	7.54	0.13	1.74	4.85	0.36	18.33	5.88	69.54	24.28	108.89	21.93	202.82	37.32	8106	0.48	40.0	38.5
51	ja30d07	c	33.70	0.0027	0.76	372	65.28	1.14	0.12	0.02	8.24	0.07	0.86	1.94	0.15	8.92	2.86	35.76	13.19	60.55	13.95	131.21	21.46	8050	0.70	42.3	55.6
53	ja30d08	c	33.59	0.0041	1.97	1082	65.34	0.97	0.06	0.13	10.92	0.65	8.34	10.00	0.81	37.20	10.80	119.04	38.48	161.84	33.91	298.38	45.55	7341	0.81	67.2	54.0
54	ja30d09	c	32.99	0.0014	0.91	567	65.88	1.03	0.26	0.05	8.75	0.12	1.89	2.94	0.16	14.06	4.34	55.98	19.75	91.83	20.36	189.18	32.53	8767	0.74	86.9	133.9
55	ja30d10	*	33.45	0.0027	0.83	366	65.55	1.18	<0.08	0.04	8.11	0.05	0.97	1.56	0.11	8.05	2.89	34.13	13.00	58.12	13.17	123.75	20.74	7910	0.66	40.3	49.0
56	ja30d11	*	33.10	0.0027	1.18	539	65.76	1.83	1.54	0.26	13.70	0.11	1.31	1.87	0.12	10.42	3.68	49.56	18.75	89.53	20.74	194.36	33.31	8900	1.32	85.2	126.8
57	ja30d12	*	33.26	0.0027	0.79	788	65.72	1.01	<0.04	0.02	6.44	0.13	2.42	4.95	0.40	22.81	6.77	80.56	27.86	120.27	25.06	223.45	36.94	7260	0.58	53.8	53.4
58	ja30d13	*	33.10	0.0027	0.71	456	65.89	1.46	0.47	0.01	10.57	0.05	1.03	1.73	0.11	9.88	3.36	44.44	16.35	75.65	17.03	157.32	26.81	7619	0.94	66.2	61.9
59	ja30d14	*	32.09	0.0027	0.70	373	67.00	1.15	0.04	<0.01	6.90	0.04	0.97	1.81	0.13	8.53	2.76	35.39	12.78	58.46	13.20	122.53	20.77	7182	0.70	28.0	35.3
61	ja30d15	*	33.22	0.0027	0.73	509	65.84	1.00	<0.03	0.07	7.46	0.05	1.12	2.49	0.15	11.16	3.39	47.28	16.76	79.25	16.87	160.99	28.07	7192	0.70	45.7	55.8
62	ja30d16	*	31.80	0.0041	1.02	280	67.52	0.85	3.42	0.42	6.62	0.16	1.41	1.52	0.18	6.62	2.21	27.27	9.65	45.54	10.15	93.31	15.63	6911	0.42	26.0	28.3
63	ja30d17	*	27.90	0.1638	8.97	792	70.93	1.05	9.62	2.69	15.81	0.63	5.62	4.89	0.08	22.05	5.40	64.08	25.59	114.94	23.52	204.25	44.22	7031	0.24	46.5	37.0
64	ja30e05	c	31.97	0.0041	0.86	406	67.16	0.92	0.70	0.19	6.26	0.12	1.53	2.11	0.19	9.80	3.08	40.92	14.54	64.95	14.80	136.13	22.47	9653	0.53	30.6	39.0
65	ja30e06	c	30.90	0.0027	0.53	340	66.19	0.93	0.30	0.08	6.67	0.09	1.14	2.19	0.12	8.85	2.71	34.58	12.10	54.85	12.12	115.08	18.75	7184	0.66	31.4	39.5
67	ja30e07	c	32.62	0.0027	0.73	316	66.48	0.88	<0.02	0.01	5.62	0.08	0.81	1.73	0.17	7.40	2.55	31.85	11.07	50.64	11.61	107.81	17.67	8678	0.44	21.0	27.5
70	ja30e08	c	30.80	0.0027	0.75	491	68.40	1.16	0.23	0.02	7.59	0.07	0.90	1.95	0.17	10.49	3.57	46.50	16.63	74.97	17.97	167.33	28.09	7707	0.74	41.6	53.6
71	ja30e09	c	32.99	0.0014	0.91	484	68.01	1.33	0.16	0.05	10.63	0.09	1.10	1.88	0.08	10.30	3.65	46.46	17.27	78.98	17.81	164.86	27.18	7725	1.01	64.8	83.3
73	ja30e10	1	32.76	0.0041	1.38	846	68.14	1.43	2.19	0.63	13.90	0.39	3.66	4.76	0.24	22.12	7.05	87.46	30.47	138.71	29.71	269.48	42.67	7660	1.09	114.0	123.0
75	ja30e11	1	34.33	0.0014	0.72	430	64.81	1.34	<0.07	0.01	10.93	0.09	0.99	1.79	0.11	9.12	3.20	41.32	15.03	70.01	16.03	151.56	25.14	8434	0.90	68.0	67.1
76	ja30e12	1	34.83	0.0027	0.72	334	64.40	1.18	0.01	<0.01	7.09	0.04	0.80	1.72	0.12	7.52	2.45	31.76	11.82	52.20	11.74	112.57	16.97	7749	0.71	28.7	35.7
77	ja30e13	1	34.52	0.0014	0.81	492	64.44	1.42	0.18	0.01	11.58	0.09	1.03	2.24	0.13	10.62	3.61	46.23	16.76	79.81	17.91	165.29	27.29	8022	0.90	68.4	64.6
78	ja30e14	1	32.53	0.0014	1.25	353	66.26	1.08	0.49	0.55	10.23	0.19	1.18	1.31	0.09	6.81	2.50	32.51	11.82	57.20	13.20	129.00	22.39	9711	0.84	52.7	79.6
79	ja30e15	1	34.20	0.0027	0.70	335	64.81	1.12	0.17	0.02	5.97	0.05	0.74	1.56	0.13	7.09	2.51	32.73	11.56	52.64	12.07	115.12	19.36	7852	0.61	23.7	33.7
80	ja30e16	1	36.89	0.0027	0.89	385	63.11	1.05	<0.01	<0.01	6.95	0.05	0.86	1.74	0.12	8.63	2.74	35.82	12.74	58.41	13.08	120.77	20.66	7950	0.60	29.6	35.8
83	ja30e17	1	35.63	0.0027	0.78	437	63.12	1.21	0.14	0.01	7.84	0.06	0.93	1.81	0.13	9.83	3.17	41.06	15.12	69.38	15.39	148.02	24.87	8299	0.72	40.6	53.2
84	ja30l04	0	37.53	0.0027	0.87	824	61.34	1.08	<0.04	0.01	8.59	0.14	2.31	4.24	0.39	22.13	6.88	83.85	28.90	128.58	28.90	244.75	41.09	8288	0.58	59.2	60.9
85	ja30l05	0	36.09	0.0014	0.90	423	62.66	1.31	<0.01	<0.01	11.16	0.05	0.79	1.41	0.11	7.70	2.85	37.19	14.28	70.00	16.20	154.57	27.37	10086	0.67	90.5	129.9

Table D.9. **Table D.9 continued**

Isotope File name		La	Ce	Pr	Nd	Sm	Eu	Gd	Tb	Dy	Ho	Er	Tm	Yb	Lu	ZrO2 - BiO2	Ratios Th/U	La/Nd	(La/Sm)n	(Gd/Yb)n	Nb/Ta	Eu/Eu*	Ce/Ce*
(CM065)		South Ridge (CM065)																					
ja30s06	(	0.20	33.7	2.16	7.76	48.1	3.22	148	285	529	949	1265	1842	2808	2486	19.75	0.777	0.0064	0.004	0.057	0.94	0.033	28.5
ja30s09	(	1.52	20.6	3.02	7.59	35.0	5.01	112	194	347	536	765	1140	1589	1580	18.97	0.945	0.0045	0.044	0.071	1.36	0.088	9.1
ja30s10	1	0.49	13.3	1.36	3.63	11.3	2.93	40	72	133	218	346	504	733	785	20.52	0.747	0.0023	0.043	0.055	1.85	0.114	14.2
ja30s11	1	0.08	15.2	1.73	5.55	29.1	6.24	104	170	306	476	711	1012	1412	1451	22.98	0.977	0.0043	0.003	0.074	1.44	0.094	16.8
ja30s12	1	0.58	18.6	2.09	5.54	31.8	4.59	114	193	342	534	807	1119	1529	1644	21.05	0.945	0.0047	0.018	0.074	1.47	0.083	14.1
ja30s13	1	3.01	13.5	2.40	4.18	19.1	6.08	63	122	232	360	564	786	1091	1389	22.36	0.820	0.0041	0.157	0.058	2.21	0.146	5.0
ja30s14	1	0.04	10.5	0.76	2.32	13.2	5.14	46	86	165	260	402	597	852	934	24.92	0.826	0.0027	0.003	0.056	1.58	0.169	25.7
ja30s15	1	0.06	16.2	2.49	7.56	40.1	8.92	136	199	353	522	753	993	1365	1431	24.42	1.191	0.0044	0.001	0.100	1.60	0.101	12.7
ja30s16	1	2.27	34.3	4.55	11.33	51.2	3.82	164	274	476	741	1128	1506	2066	2316	22.08	1.267	0.0068	0.044	0.079	1.32	0.036	10.0
ja30s17	1	0.04	16.8	1.23	3.99	20.9	3.56	77	132	244	384	599	835	1169	1311	26.53	0.869	0.0040	0.002	0.065	1.36	0.073	29.6
ja30b05	(	0.56	12.5	1.19	2.23	11.7	1.27	40	61	145	257	409	574	822	1016	33.46	0.812	0.0029	0.046	0.046	2.40	0.049	14.3
ja30b06	(	0.11	23.4	0.59	1.83	11.8	2.72	53	103	202	340	555	794	1161	1275	31.91	0.740	0.0034	0.009	0.046	0.67	0.084	67.4
ja30b07	(	0.03	15.4	0.58	1.85	11.4	2.21	46	87	162	288	431	603	871	957	30.11	0.778	0.0030	0.002	0.053	1.23	0.077	50.6
ja30b08	(	0.07	19.0	0.74	2.18	12.5	1.59	57	108	198	324	519	732	1048	1196	30.65	0.861	0.0035	0.005	0.054	1.53	0.058	47.1
ja30b09	(	0.10	18.7	3.41	10.23	51.6	10.49	163	284	445	674	1000	1302	1747	1939	30.38	1.277	0.0062	0.002	0.093	1.73	0.098	9.5
ja30b10	"	2.44	16.9	2.20	3.11	10.8	2.34	41	74	140	234	392	584	813	930	32.16	0.711	0.0025	0.226	0.050	1.14	0.091	7.3
ja30b11	"	2.93	17.4	2.38	4.78	16.6	2.82	62	113	208	349	553	784	1094	1289	34.00	0.915	0.0038	0.177	0.056	1.61	0.072	6.6
ja30b12	"	2.23	23.6	2.55	3.81	12.7	2.64	53	120	263	479	870	1328	1973	2271	31.31	0.437	0.0053	0.175	0.027	0.28	0.081	9.9
ja30b13	"	2.94	20.9	5.80	12.43	43.5	5.67	147	244	421	651	998	1339	1800	1964	33.62	1.193	0.0063	0.088	0.082	0.59	0.059	4.9
ja30b14	"	0.19	8.8	0.45	1.45	8.5	1.88	31	58	105	175	287	414	604	756	33.94	0.474	0.0023	0.022	0.051	1.58	0.095	27.8
ja30b15	"	2.86	28.3	3.11	5.63	27.9	1.59	104	206	407	732	1185	1838	2252	2453	38.76	0.933	0.0062	0.102	0.046	0.53	0.024	9.5
ja30b16	"	0.03	12.4	0.36	1.85	10.5	1.94	42	75	144	238	394	533	789	901	37.14	0.704	0.0026	0.003	0.054	3.00	0.075	63.1
ja30b17	"	0.07	68.2	1.89	6.10	35.3	4.90	104	188	357	599	976	1384	1916	2290	33.66	1.514	0.0068	0.002	0.054	0.92	0.070	67.7
ja30c05	(	1.32	17.7	1.97	3.57	16.7	3.54	64	111	207	339	536	734	1042	1240	19.52	0.912	0.0032	0.079	0.062	1.74	0.068	10.8
ja30c06	(	0.23	17.1	1.00	2.49	12.8	1.98	46	90	170	287	470	667	955	1146	21.62	0.869	0.0026	0.018	0.050	1.40	0.065	27.7
ja30c07	(	0.03	12.2	0.43	1.78	11.3	1.80	37	72	135	232	371	525	745	905	20.93	0.741	0.0023	0.003	0.050	1.59	0.068	53.3
ja30c08	(	0.43	14.2	1.75	4.79	12.8	4.71	55	85	169	306	460	646	963	1231	24.71	1.781	0.0033	0.034	0.057	1.81	0.140	13.1
ja30c09	(	0.07	11.7	0.58	1.79	11.9	1.97	43	74	145	233	372	543	777	876	26.22	0.777	0.0023	0.008	0.058	1.79	0.072	38.0
ja30c10	1	0.08	11.4	0.84	2.41	15.0	3.79	53	95	173	283	436	593	866	1023	25.02	0.858	0.0029	0.004	0.062	1.83	0.111	25.5
ja30c11	1	0.03	9.1	0.57	2.08	10.9	3.44	40	75	141	236	381	535	790	916	28.52	0.760	0.0028	0.002	0.050	2.47	0.136	30.2
ja30c12	1	0.12	14.8	0.70	2.20	13.4	1.63	58	108	201	335	532	742	1068	1236	23.23	0.764	0.0034	0.009	0.053	1.49	0.047	38.1
ja30c13	1	0.27	10.7	0.81	2.03	10.2	2.21	36	68	129	210	332	480	683	805	22.50	0.831	0.0023	0.026	0.056	1.84	0.092	19.9
ja30c14	1	0.09	10.7	1.19	4.31	24.9	5.67	67	147	271	420	625	880	1208	1405	28.80	0.976	0.0041	0.004	0.073	2.12	0.101	16.7
ja30c15	1		10.3	0.85	2.63	15.5	4.74	51	90	168	271	422	579	824	983	24.67	0.945	0.0030	0.000	0.062	1.85	0.142	15.8
ja30c16	1	0.14	16.9	1.10	3.88	25.3	4.95	106	190	348	585	860	1139	1566	1800	28.43	0.956	0.0049	0.005	0.068	1.57	0.075	25.8
ja30c17	1	0.04	8.5	0.49	1.89	10.9	3.98	36	66	121	193	296	418	593	683	25.30	0.816	0.0021	0.003	0.054	2.08	0.163	32.1
ja30d05	(	0.19	11.2	0.59	1.84	11.5	1.95	40	75	139	230	362	521	747	845	27.48	0.811	0.0028	0.017	0.054	1.88	0.075	28.6
ja30d06	(	0.20	12.3	1.42	3.81	32.7	6.79	92	163	279	445	681	886	1260	1517	33.07	1.040	0.0048	0.008	0.073	2.16	0.109	15.2
ja30d07	(	0.06	13.4	0.78	1.89	13.1	2.06	45	74	145	241	376	585	815	872	31.58	0.761	0.0027	0.006	0.055	1.84	0.093	31.2
ja30d08	(	0.53	17.8	6.06	18.25	67.5	14.38	167	294	484	705	1010	1373	1853	1851	31.75	1.244	0.0062	0.008	0.101	1.88	0.113	4.8
ja30d09	(	0.24	14.3	1.28	4.13	19.9	2.92	71	120	226	362	574	824	1175	1322	32.89	0.649	0.0037	0.012	0.060	1.39	0.065	19.1
ja30d10	"	0.18	13.2	0.57	2.12	10.5	1.89	40	74	139	236	363	533	769	843	32.11	0.823	0.0026	0.017	0.053	1.76	0.074	35.3
ja30d11	"	1.20	22.3	1.19	2.86	12.6	2.10	52	102	201	343	560	840	1207	1354	32.67	0.672	0.0037	0.095	0.043	1.24	0.065	18.8
ja30d12	"	0.07	13.8	1.45	5.29	33.5	7.10	115	187	328	511	752	1015	1366	1502	32.44	1.009	0.0051	0.002	0.083	1.74	0.098	18.1
ja30d13	"	0.06	17.4	0.58	2.25	11.7	2.00	50	93	181	300	473	669	977	1090	32.79	0.809	0.0034	0.005	0.051	1.58	0.085	53.9
ja30d14	"		11.3	0.48	2.12	12.2	2.27	43	77	144	234	365	534	761	844	34.90	0.793	0.0029	0.000	0.056	1.83	0.082	23.5
ja30d15	"	0.30	12.2	0.54	2.44	16.9	2.63	56	94	192	307	495	683	1000	1141	32.62	0.820	0.0039	0.018	0.058	1.44	0.072	21.4
ja30d16	"	1.77	10.8	1.77	3.10	10.3	2.85	33	61	111	177	285	411	580	643	35.92	0.920	0.0023	0.172	0.057	2.03	0.131	6.1
ja30d17	"	11.38	25.6	6.85	12.30	33.1	1.40	111	150	342	499	718	952	1289	1708	43.03	1.258	0.0063	0.344	0.087	4.34	0.020	2.5
ja30e05	(	0.79	10.2	1.25	3.34	14.3	3.38	49	85	166	289	405	591	848	913	35.19	0.851	0.0034	0.058	0.058	1.72	0.108	10.0
ja30e06	(	0.28	10.9	0.94	2.49	14.8	2.13	45	75	141	222	343	491	715	762	37.29	0.795	0.0026	0.017	0.062	1.41	0.072	18.2
ja30e07	(	0.03	9.2	0.59	1.76	11.7	2.97	37	71	129	203	318	470	666	726	33.87	0.788	0.0026	0.002	0.058	2.02	0.122	29.6
ja30e08	(	0.08	12.4	0.75	1.98	13.2	2.95	53	98	189	305	469	728	1039	1080	37.80	0.774	0.0034	0.006	0.051	1.57	0.090	29.8
ja30e09	(	0.21	17.3	0.81	2.40	12.8	1.48	53	101	189	316	491	721	1024	1105	33.03	0.776	0.0035	0.016	0.052	1.33	0.045	34.1
ja30e10	1	2.65	22.7	4.20	8.00	32.2	4.31	111	195	356	558	854	1203	1674	1735	33.36	0.927	0.0054	0.082	0.086	1.32	0.060	6.8
ja30e11	1	0.03	17.8	0.85	2.17	12.1	1.98	46	89	166	275	435	649	941	1022	30.28	0.781	0.0030	0.002	0.049	1.48	0.068	52.9
ja30e12	1		11.6	0.47	1.74	11.6	2.08	36	68	129	213	328	475	689	759	29.77	0.781	0.0024	0.000	0.054	1.62	0.084	24.8
ja30e13	1	0.03	16.9	0.80	2.25	15.1	2.24	53	100	188	307	499	725	1027	1110	29.92	0.808	0.0034	0.002	0.052	1.59	0.065	60.4
ja30e14	1	2.34	16.7	2.06	2.58	6.8	1.52	33	59	132	216	357	534	801	910	33.76	0.883	0.0023	0.285	0.041	1.28	0.072	7.8
ja30e15	1	0.08	9.7	0.59	1.82	11.1	2.36	38	70	133	212	329	469	715	787	30.81	0.704	0.0025	0.007	0.050	1.88	0.102	29.2
ja30e16	1		11.3	0.58	1.89	11.8	2.17	43	75	146	233	365	529	750	841	27.22	0.825	0.0026	0.000	0.058	1.74	0.079	19.6
ja30e17	1	0.03	12.5	0.67	2.03	12.2	2.32	49	88	169	277	434	623	907	1011	27.29	0.767	0.0030	0.003	0.054	1.88	0.075	35.5
ja30f04	0	0.05	14.0	1.46	5.08	38.7	6.86	111	190	341	529	804	1089	1520	1671	23.81	0.973	0.0050	0.002	0.073	1.90	0.098	16.7
ja30f05	0		18.2	0.51	1.73	9.5	1.88	39	79	151	262	437	656	980	1113	26.57	0.696	0.0027	0.000	0.040	1.51	0.078	35.8

Table D.9 continued

Grain/spot Number	Isotope File name		SiO2 30 wt%	TiO2 49 wt%	Sr 88 ppm	Y 89 ppm	ZrO2 91 wt%	Nb 93 ppm	Ba 137 ppm	La 139 ppm	Ce 140 ppm	Pr 141 ppm	Nd 146 ppm	Sm 147 ppm	Eu 153 ppm	Gd 157 ppm	Tb 159 ppm	Dy 163 ppm	Ho 165 ppm	Er 166 ppm	Tm 169 ppm	Yb 172 ppm	Lu 175 ppm	Hf 178 ppm	Ta 181 ppm	Th 232 ppm	U 238 ppm
South Ridge (CM065)																											
88	ja30f06	0	36.32	0.0027	0.90	474	62.58	1.46	<0.01	0.02	10.94	0.07	0.86	1.74	0.11	9.91	3.57	44.20	16.05	75.60	18.90	159.36	27.66	6660	0.95	62.7	81.0
90	ja30f07	0	38.12	0.0027	0.75	457	62.77	1.27	0.08	<0.01	9.66	0.07	0.89	1.79	0.14	10.07	3.43	42.77	15.43	72.15	18.22	151.80	26.85	6807	0.84	57.8	67.8
94	ja30f08	0	34.75	0.0027	0.85	533	64.19	0.94	0.09	0.04	6.75	0.09	1.45	2.58	0.18	13.03	4.17	51.80	18.00	82.69	18.18	165.63	29.67	8221	0.54	34.0	43.5
95	ja30f09	0	34.50	0.0027	0.93	707	64.36	1.07	0.01	0.03	7.88	0.10	1.74	3.20	0.24	16.70	5.29	66.67	23.94	108.64	23.27	207.06	36.98	8500	0.59	51.5	54.8
98	ja30f10	1	35.50	0.0027	0.86	736	63.43	0.89	0.11	0.25	8.24	0.17	2.39	3.88	0.47	17.91	5.87	73.03	24.57	109.40	23.13	206.40	38.10	7881	0.45	42.7	41.4
99	ja30f11	1	34.27	0.0027	0.89	359	64.70	0.94	<0.01	<0.01	5.88	0.06	0.87	1.76	0.14	8.27	2.71	34.09	12.17	55.85	12.10	113.84	20.70	8219	0.51	23.4	28.7
100	ja30f12	1	34.46	0.0027	0.87	707	64.43	1.02	0.34	0.15	8.72	0.21	3.06	4.26	0.28	19.81	5.92	71.46	24.41	108.11	22.29	197.07	35.23	8255	0.58	55.5	50.6
102	ja30f13	1	31.55	0.0014	0.73	480	67.29	1.57	0.04	0.02	11.55	0.08	0.95	1.72	0.12	9.42	3.36	44.88	16.84	78.64	17.68	167.22	29.74	9213	1.08	69.9	98.4
103	ja30f14	1	33.26	0.0014	0.76	415	65.69	1.08	0.05	0.03	7.05	0.07	1.22	2.12	0.16	9.86	3.16	38.48	14.05	63.95	13.50	124.57	22.91	8305	0.84	38.5	45.6
105	ja30f15	1	33.73	0.0041	0.95	588	65.23	1.21	0.95	0.27	8.96	0.20	2.33	3.44	0.24	15.46	4.74	58.04	20.49	91.76	19.89	175.48	32.52	7930	0.75	55.4	59.7
108	ja30f16	1	33.48	0.0027	0.71	377	65.54	1.02	<0.01	0.01	6.83	0.05	0.85	1.51	0.12	8.29	2.80	35.09	12.82	58.93	12.70	117.81	22.25	7795	0.63	34.0	41.8
109	ja30f17	1	31.77	0.0027	0.72	344	67.24	1.14	0.01	0.01	7.42	0.05	0.71	1.53	0.09	7.39	2.45	30.91	11.45	53.48	11.93	112.31	20.84	7912	0.71	37.0	49.2
111	ja30a05	(	32.82	0.0041	0.86	756	66.12	0.89	0.13	0.02	13.23	0.10	1.91	3.66	0.41	18.89	5.82	72.26	25.41	112.45	22.92	208.51	38.22	7877	0.42	44.3	28.9
115	ja30a07	(	32.91	0.0041	0.84	407	66.04	0.98	0.05	0.01	6.45	0.08	1.09	1.80	0.17	8.63	2.93	36.20	13.72	64.23	14.12	130.88	23.80	8328	0.50	27.3	33.9
116	ja30a08	(	34.40	0.0027	0.80	443	64.55	1.27	0.11	0.04	8.85	0.08	0.95	2.00	0.13	10.02	3.19	40.58	15.25	71.17	15.31	139.87	25.79	8230	0.85	48.5	60.2
118	ja30a09	(	34.80	0.0027	0.74	424	64.40	0.93	<0.02	0.01	6.34	0.07	1.11	1.80	0.14	9.76	3.15	39.87	14.36	66.26	14.05	128.93	23.50	7890	0.57	28.3	33.4
119	ja30a10	'	34.32	0.0027	0.91	477	64.59	1.28	0.58	0.07	9.30	0.07	0.92	1.88	0.11	9.48	3.30	43.67	16.33	77.47	17.19	158.75	28.63	8635	1.04	53.4	76.0
120	ja30a11	'	34.30	0.0081	0.76	471	64.76	0.85	0.17	0.04	5.76	0.12	2.01	2.67	0.45	13.41	3.98	45.68	15.18	71.87	14.68	132.70	24.10	7055	0.43	17.7	17.9
121	ja30a12	'	35.58	0.0014	0.72	453	63.86	1.34	<0.04	0.03	10.19	0.05	0.85	1.88	0.13	9.20	3.11	41.52	15.38	72.09	15.12	144.29	25.98	8337	0.93	60.3	74.3
124	ja30a13	'	35.34	0.0014	0.78	333	63.50	1.14	<0.03	0.02	8.42	0.04	0.89	1.29	0.09	5.92	2.15	28.43	11.12	55.66	12.55	123.42	22.97	9429	0.63	73.3	130.5
125	ja30a14	'	36.17	0.0027	0.93	472	62.76	1.41	1.50	0.88	11.87	0.16	1.14	1.77	0.11	10.32	3.36	43.37	16.46	77.30	17.16	156.03	27.80	8405	1.05	61.6	62.4
128	ja30a15	'	36.13	0.0041	0.89	394	62.91	0.93	<0.05	0.01	4.78	0.08	1.07	1.95	0.20	10.07	3.07	37.82	13.63	62.16	13.42	123.03	22.18	7497	0.49	15.4	18.0
129	ja30a16	'	35.28	0.0027	0.85	692	63.62	1.51	<0.02	0.02	10.46	0.09	1.51	3.02	0.12	14.98	4.91	62.01	23.57	112.99	24.94	225.59	40.48	8299	0.88	82.6	92.3
129	ja30a17	'	37.83	0.0054	1.30	1037	61.08	1.04	0.62	0.30	11.18	0.54	8.31	7.89	0.56	33.46	9.44	108.51	36.20	158.65	31.71	272.95	46.98	7518	0.87	74.1	62.9
131	ja30h06	(	33.18	0.0028	0.87	594	65.73	1.24	<0.06	2.42	15.02	0.86	5.14	3.16	0.20	14.06	4.55	61.47	21.46	98.43	21.43	204.87	33.15	8334	0.87	80.0	74.0
134	ja30h07	(	32.31	0.0055	1.28	1151	66.59	0.86	0.12	0.13	7.53	0.88	11.82	12.74	2.21	49.51	12.18	127.76	40.03	169.95	31.54	271.55	47.71	7284	0.26	14.7	8.8
135	ja30h08	(	36.11	0.0136	3.28	776	60.81	1.80	26.25	2.86	16.19	0.58	4.30	4.94	0.23	20.06	6.26	76.70	27.51	122.33	25.81	231.81	40.70	7785	0.98	93.6	100.8
137	ja30h09	(	34.07	0.0055	0.87	274	65.01	0.78	0.09	0.02	3.84	0.07	0.80	1.58	0.28	7.95	2.22	27.41	9.95	44.31	9.18	88.91	15.47	7225	0.27	6.0	8.6
139	ja30h10	'	34.89	0.0028	0.76	409	64.03	1.07	0.07	<0.01	12.76	0.03	0.73	1.52	0.12	8.58	2.98	36.20	14.58	66.46	15.96	154.47	27.00	8601	0.70	32.9	29.4
142	ja30h11	'	36.20	0.0028	0.92	614	62.77	1.00	0.65	0.09	8.20	0.07	1.59	2.40	0.14	14.82	4.83	57.20	21.41	98.97	20.03	186.30	34.40	7705	0.56	50.0	56.8
143	ja30h12	'	34.20	0.0028	0.70	324	64.81	1.02	0.14	0.13	6.99	0.12	1.21	1.75	0.17	8.76	2.56	32.05	11.42	50.75	11.23	109.03	18.13	7908	0.84	33.3	40.8
144	ja30h13	'	33.85	0.0028	0.78	449	65.21	1.21	<0.13	0.01	8.03	0.05	0.97	2.01	0.14	10.73	3.46	43.10	15.70	70.83	15.59	148.21	24.06	7254	0.72	44.8	58.0
Cote Creek (CM023)																											
1.1	je20a05	(	37.63		2.37	464	61.13	1.43	5.93	2.02	21.02	0.84	5.18	2.95	0.51	9.70	3.10	40.85	16.24	80.83	20.02	203.88	37.43	9450	1.37	138.9	407.2
1.2	je20a06	(	37.64		1.92	450	60.83	1.33	4.01	1.57	20.07	0.58	3.38	2.31	0.32	9.49	3.07	40.72	15.38	73.39	17.70	173.26	30.43	9709	1.30	92.9	245.2
3	je20a07	(	37.93		1.16	701	60.91	1.20	0.61	0.16	8.16	0.15	2.21	3.87	0.15	17.99	5.80	69.74	24.87	107.45	23.44	211.89	35.68	8783	0.77	54.1	59.5
4	je20a08	(	38.46		10.48	420	60.42	1.24	57.63	1.42	12.02	0.39	2.38	2.56	0.20	10.18	3.23	38.83	13.97	53.46	13.59	134.80	23.83	5702	0.61	46.8	49.1
5	je20a09	(	37.43		0.93	375	61.50	0.88	0.14	0.16	7.23	0.10	1.05	1.52	0.18	8.89	2.85	34.82	12.76	57.83	12.72	119.67	21.25	8468	0.47	34.3	33.1
6.1	je20a10	1	38.03		1.04	652	62.64	1.27	0.18	0.03	9.16	0.11	2.38	3.61	0.26	18.48	5.13	66.12	23.37	103.40	22.65	208.77	33.81	8543	0.87	51.7	52.4
6.2	je20a11	1	37.28		0.93	517	61.59	1.88	<0.03	0.02	11.47	0.08	1.23	2.27	0.13	11.75	3.98	50.09	16.01	81.76	18.26	170.54	28.84	9005	1.08	62.5	76.1
7	je20a12	1	38.54		1.06	398	62.38	1.10	0.94	0.19	7.40	0.09	1.22	1.80	0.20	9.99	2.93	38.54	13.88	64.33	14.80	136.89	22.22	8668	0.61	28.1	35.9
8	je20a13	1	38.49		1.29	851	62.23	1.39	0.48	0.89	13.44	0.31	3.00	4.76	0.21	19.87	6.81	83.54	29.08	130.25	27.03	241.02	41.86	9807	0.94	71.5	72.0
9	je20a14	1	37.38		1.33	1393	61.47	0.92	0.22	0.11	9.36	0.55	8.89	13.44	1.05	51.42	13.22	147.44	46.53	193.16	38.51	318.47	54.31	7584	0.39	24.8	18.8
11	je20a15	1	35.66		1.58	743	62.99	2.33	0.47	0.44	19.23	0.37	2.63	3.66	0.06	20.05	5.81	74.80	28.41	119.23	28.27	245.08	38.05	10372	1.76	109.1	122.2
12	je20a16	1	36.89		1.20	998	61.94	1.24	1.41	0.18	10.55	0.31	4.41	7.03	0.55	30.25	8.84	102.06	34.19	149.72	31.58	282.35	46.19	8316	0.76	78.3	72.9
13	je20a17	1	37.27		1.22	1000	61.58	1.15	0.32	0.13	10.08	0.37	5.49	8.33	0.58	33.62	9.46	108.88	38.50	153.01	31.79	280.16	44.32	8220	0.60	68.4	51.9
14	je20b04	(	37.13		0.95	479	61.86	1.38	0.05	0.15	11.49	0.11	1.31	2.02	0.10	10.48	3.39	44.81	16.57	77.50	17.50	163.68	27.83	9652	0.98	72.6	99.3
15	je20b05	(	38.18		0.93	516	62.69	1.58	0.20	0.02	10.69	0.07	1.16	2.65	0.12	12.31	3.85	48.98	17.99	80.48	18.50	171.26	27.81	8743	0.98	57.7	71.3
16	je20b06	(	36.29		0.95	390	62.89	1.04	0.01	0.02	8.06	0.07	1.26	2.04	0.17	8.99	2.98	37.35	13.74	61.25	13.43	130.09	21.52	8039	0.46	19.9	28.1
18	je20b07	(	37.26		0.82	376	61.84	1.25	0.02	0.02	8.31	0.07	1.20	1.92	0.15	8.76	2.80	36.27	12.98	59.40	13.28	126.42	21.00	8890	0.81	39.0	48.9
19.1	je20b08	(	37.97		1.00	737	60.91	1.05	0.15	0.01	6.79	0.11	2.02	4.04	0.32	19.95	6.02	72.42	25.48	111.80	23.34	210.36	35.12	8397	0.63	57.8	54.9
19.2	je20b09	(	37.09		0.89	441	61.76	1.30	0.02	0.11	9.24	0.09	1.03	2.17	0.14	10.32	3.40	42.23	15.31	69.90	15.51	144.01	23.88	8909	0.85	42.7	53.0
20	je20b10	'	36.60		0.86	580	62.30	1.27	0.04	0.57	10.53	0.44	3.35	3.29	0.70	14.25	4.45	55.08	19.27	85.27	18.85	176.43	28.23	8449	0.76	46.8	64.0
21	je20b11	'	38.08		1.15	828	62.88	0.97	1.35	0.47	7.57	0.39	4.85	7.18	0.52	27.41	7.56	85.56	28.70	122.46	25.50	225.74	35.13	7476	0.48	15.9	14.2
22	je20b12	'	38.30		2.35	524	60.67	1.32	5.65	1.19	10.67	0.47	3.11	2.77	0.38	12.08	3.67	49.82	17.70	82.61	18.13	172.20	28.98	7764	0.89	57.8	81.1
23	je20b13	'	37.13		0.97	287	61.83	1.10	1.19	0.14	6.95	0.09	0.85	1.51	0.12	6.37	2.05	27.17	9.82	46.36	10.38	100.87	16.53	8344	0.89	27.8	41.0
25.1	je20b14	'	36.63		0.87	384	62.23	1.08	0.03	0.01	6.45	0.05	0.86	1.57	0.15	8.03	2.72	34.68	12.98	61.71	14.40	135.48	22.48	9245	0.88	42.2	63.9
25.2	je20b15	'	36.89		0.93	588	62.28	1.04	0.30	0.08	8.68	0.12	1.77	3.07	0.28	15.48	4.75	57.81	20.40	90.81	19.53	177.38	28.81	7947	0.83	47.1	45.2
26	je20b16	'	38.27		0.84	410	62.68	1.21	0.05	0.03	8.44	0.08	0.91	1.54	0.12	6.73	2.91	36.89	13.91	66.76	14.68	141.30	22.86	8171	0.80	40.9	58.4
27	je20b17	'	37.29		0.78	362	61.73	1.04	<0.05	0.01	5.65	0.05	1.03	1.91	0.13	7.98	2.69	34.16	12.36	56.86	13.09	123.52	20.49	7695	0.58	20.8	30.7
28.1	je20c04	(	35.95		1.34	474	62.99	1.53	0.51	7.83	28.75	2.37	10.44	3.41	0.14	11.36	3.39	45.24	16.14	73.82	16.38	158.83	24.70	8148	0.98	55.6	78.0
28.2	je20c05	(	35.47		0.85	417	63.50	1.40	0.05	0.18	9.72	0.10	1.20	1.90	0.12	8.83	3.11	38.80	14.38	68.82	15.13	143.65	22.75	6115	0.98	48.2	72.5
29.1	je20c06	(	35.62		0.80	313	63.42	0.89	0.27	0.21	5.50	0.11	1.14	1.72	0.20	8.01	2.55	30.69	11.30	49.79	11.31	109.71	17.41	7596	0.42	13.9	18.5
29.2	je20c07	(	35.76		1.15	980	63.13	1.34	0.21	0.10	11.90	0.39	5.39	7.66	0.33	29.69	8.69	104.40	35.57	153.68	32.10	283.90	44.33	7680	0.98	100.3	85.5
54	je20c08	(	35.90		0.79	395	63.16	0.94	0.50	0.17	5.25	0.11	1.51	2.51	0.19	10.48	3.23	39.23	13.89	61.75	13.15	123.04	20.87	7393	0.43	8.7	10.0
30	je20c09	(	37.20		3.05	600	61.77	1.23	35.52	3.16	14.71	0.89	4.13	3.74	0.27	16.32	4.93	58.50	20.50	90.84	19.54	174.43	28.71	7718	0.79	49.8	49.3
32	je20c10	1	35.44		0.87	813	63.52	1.11	0.17	0.05	6.24	0.16	2.28	3.75	0.38	17.17	4.94	62.07	21.01	93.73	20.27	180.13	28.87	7778	0.57	44.1	39.9
33	je20c11	1	36.48		0.90	373	62.54	1.09	0.12	0.03	7.58	0.08	1.15	1.90	0.14	8.49	2.77	35.43	12.80	58.19	12.70	120.85	20.55	7658	0.58	36.8	43.3
34	je20c12	1	35.70		0.90	307	63.31	0.98	0.85	0.53	7.34	0.23	1.82	1.91	0.18	7.41	2.51	30.27	10.73	46.05	10.71	101.89	16.30	7924	0.85	28.7	33.8

Table D.9 continued

Isotope / File name		Chondrite Normalized La	Ce	Pr	Nd	Sm	Eu	Gd	Tb	Dy	Ho	Er	Tm	Yb	Lu	ZrO2 - SiO2	Ratios Th/U	La/Hf	(La/Sm)n	(Gd/Yb)n	Nb/Ta	Eu/Eu*	Ce/Ce*
(CM065)		South Ridge (CM065)																					
ia30f05	0	0.10	17.9	0.72	1.88	11.8	2.02	50	93	180	294	473	664	990	1124	28.28	0.773	0.0032	0.009	0.050	1.54	0.088	43.6
ia30f07	0		15.8	0.76	2.17	12.1	2.49	51	95	174	283	451	657	943	1092	28.65	0.853	0.0030	0.000	0.054	1.51	0.079	20.2
ia30f08	0	0.17	11.0	0.83	3.17	17.4	3.23	65	115	211	330	517	735	1029	1208	29.44	0.782	0.0036	0.010	0.064	1.75	0.078	20.1
ia30f09	0	0.13	12.9	1.03	3.81	21.6	4.21	84	148	279	439	679	942	1286	1502	29.88	0.939	0.0043	0.008	0.065	1.83	0.080	22.1
ia30f10	1	1.05	13.4	1.83	5.22	28.9	8.31	90	163	297	450	664	937	1282	1549	27.93	1.030	0.0048	0.039	0.070	1.98	0.142	9.3
ia30f11	1		9.6	0.60	1.80	12.0	2.52	42	75	139	223	348	490	707	841	30.43	0.814	0.0025	0.000	0.059	1.82	0.094	16.1
ia30f12	1	0.63	14.2	2.30	6.89	28.8	5.00	100	184	290	447	676	902	1224	1432	29.95	1.098	0.0043	0.022	0.081	1.76	0.078	9.7
ia30f13	1	0.07	18.8	0.84	2.08	11.8	2.11	47	93	182	305	491	716	1039	1209	35.74	0.725	0.0032	0.006	0.046	1.49	0.072	41.4
ia30f14	1	0.11	11.5	0.77	2.67	14.3	2.90	50	88	156	257	400	547	776	931	32.43	0.800	0.0028	0.008	0.054	1.88	0.091	28.1
ia30f15	1	1.13	14.8	2.14	5.09	23.3	4.19	76	131	236	375	574	797	1090	1322	31.51	0.929	0.0041	0.049	0.071	1.80	0.083	8.9
ia30f16	1	0.02	11.1	0.49	1.85	10.2	2.18	42	77	143	235	368	514	730	905	32.06	0.813	0.0029	0.002	0.057	1.61	0.084	43.5
ia30f17	1	0.04	12.1	0.53	1.55	10.3	1.61	37	68	128	210	334	483	696	847	35.47	0.752	0.0028	0.004	0.053	1.80	0.098	42.9
ia30q06	(	0.08	21.8	1.08	4.17	24.7	7.28	95	161	294	465	703	928	1283	1554	33.30	1.645	0.0049	0.003	0.074	2.15	0.122	37.2
ia30q07	(	0.04	10.5	0.67	2.39	12.2	2.95	43	81	147	251	401	572	813	968	33.13	0.805	0.0029	0.003	0.053	1.85	0.107	29.6
ia30q08	(	0.18	14.1	0.81	2.08	13.5	2.27	50	88	165	279	445	620	869	1048	30.15	0.804	0.0031	0.013	0.058	1.46	0.071	35.7
ia30q09	(	0.04	10.3	0.76	2.44	12.2	2.52	49	87	162	263	414	569	801	955	29.79	0.849	0.0030	0.003	0.051	1.63	0.082	25.3
ia30q10	'	0.29	15.2	0.75	2.00	11.4	1.92	46	91	178	299	484	696	986	1172	30.27	0.703	0.0033	0.025	0.048	1.24	0.065	29.3
ia30q11	'	0.16	9.4	1.28	4.40	18.0	6.00	67	110	186	296	448	594	824	980	30.48	0.988	0.0034	0.009	0.082	2.00	0.167	13.1
ia30q12	'	0.13	16.6	0.54	1.85	12.7	2.25	45	86	169	282	451	653	898	1097	27.79	0.812	0.0032	0.010	0.052	1.44	0.078	49.6
ia30q13	'	0.07	13.7	0.48	1.30	8.7	1.54	30	60	116	204	348	508	767	934	28.16	0.582	0.0024	0.009	0.039	1.37	0.080	51.7
ia30q14	'	2.79	19.5	1.75	2.49	11.9	2.01	52	93	176	302	483	692	988	1134	28.59	0.748	0.0033	0.234	0.054	1.34	0.063	8.6
ia30q15	'	0.02	7.8	0.65	2.35	13.2	3.52	51	85	154	250	388	543	764	901	28.77	0.855	0.0030	0.002	0.086	1.89	0.110	17.9
ia30q16	'	0.10	17.1	0.97	3.30	20.4	2.10	75	136	252	432	706	1010	1401	1646	28.34	0.895	0.0049	0.005	0.054	1.71	0.044	31.9
ia30q17	'	1.25	18.2	5.78	13.82	53.3	9.93	168	281	441	683	982	1284	1695	1910	23.24	1.177	0.0062	0.024	0.089	1.58	0.080	5.2
ia30h06	(	10.22	24.5	9.30	11.24	21.3	3.60	71	126	250	393	615	869	1273	1348	32.55	0.810	0.0049	0.479	0.058	1.43	0.078	2.5
ia30h07	(	0.54	12.3	7.34	25.43	66.1	39.28	249	337	519	733	1062	1277	1687	1939	34.28	1.708	0.0065	0.008	0.148	3.37	0.235	3.1
ia30h08	(	11.21	28.4	6.05	9.40	33.4	4.09	101	173	312	504	765	1045	1440	1655	22.70	0.930	0.0052	0.336	0.070	1.64	0.061	3.1
ia30h09	(	0.10	5.9	0.71	1.75	10.6	4.97	40	61	111	182	277	371	552	629	30.94	0.928	0.0021	0.010	0.072	2.79	0.196	14.5
ia30h10	'		20.8	0.38	1.60	10.3	2.09	43	83	155	267	428	646	959	1096	29.15	1.116	0.0031	0.000	0.045	1.53	0.078	57.1
ia30h11	'	0.38	13.4	0.79	3.49	16.2	2.48	74	128	233	392	619	811	1170	1398	28.57	0.880	0.0045	0.023	0.064	1.74	0.054	22.8
ia30h12	'	0.57	11.4	1.28	2.64	11.8	3.05	44	71	130	209	317	455	677	737	30.80	0.816	0.0023	0.046	0.085	1.59	0.109	12.4
ia30h13	'	0.05	13.1	0.54	2.13	13.6	2.41	54	98	175	288	441	631	921	978	31.36	0.768	0.0033	0.004	0.059	1.87	0.071	44.2
CM023)		Cole Creek (CM023)																					
ia20a05	(	8.50	34.3	9.05	11.34	19.9	9.01	49	86	166	297	505	810	1265	1521	23.50	0.341	0.0040	0.426	0.039	1.05	0.262	3.9
ia20a06	(	6.83	32.7	8.00	7.40	15.6	5.81	46	85	166	282	459	717	1078	1237	23.09	0.379	0.0031	0.425	0.044	1.02	0.177	5.2
ia20a07	(	0.67	15.0	1.80	4.85	26.8	2.84	90	155	284	452	672	949	1315	1459	22.99	0.909	0.0041	0.025	0.089	1.56	0.045	13.2
ia20a08	(	5.99	19.6	4.74	5.17	17.3	3.62	51	90	156	258	397	586	837	958	21.88	0.980	0.0027	0.346	0.061	2.03	0.108	3.8
ia20a09	(	0.88	11.8	1.04	2.29	10.3	3.11	45	79	141	234	361	515	745	884	24.08	1.038	0.0025	0.054	0.080	1.88	0.113	13.9
ia20a10	1	0.12	14.9	1.19	5.22	24.4	4.54	83	142	269	428	646	917	1286	1374	28.81	0.986	0.0040	0.005	0.064	1.90	0.065	22.9
ia20a11	1	0.07	18.7	0.86	2.89	15.3	2.29	59	110	204	330	511	739	1059	1172	24.32	0.822	0.0032	0.005	0.058	1.55	0.062	40.2
ia20a12	1	0.79	12.1	0.96	2.88	12.1	3.57	50	81	157	254	402	599	851	903	25.84	0.726	0.0029	0.085	0.059	1.80	0.115	13.8
ia20a13	1	2.47	21.9	3.38	6.58	32.2	3.80	100	169	340	533	814	1094	1497	1701	25.75	0.993	0.0044	0.077	0.097	1.48	0.058	7.5
ia20a14	1	0.45	15.3	5.66	19.03	90.6	16.62	258	368	599	852	1207	1478	1966	2208	24.09	1.317	0.0072	0.005	0.131	2.34	0.107	4.8
ia20a15	1	1.88	31.4	3.97	6.19	24.9	1.41	101	161	303	484	745	1083	1522	1547	27.31	0.885	0.0037	0.075	0.066	1.31	0.022	10.8
ia20a16	1	0.76	17.2	3.34	9.84	47.7	9.83	152	239	415	626	936	1278	1754	1878	25.05	1.074	0.0056	0.016	0.087	1.63	0.088	8.4
ia20a17	1	0.56	16.4	4.03	12.01	56.3	10.25	169	282	443	668	986	1287	1740	1802	24.31	1.318	0.0054	0.010	0.097	1.92	0.091	7.2
ia20b04	(	0.83	18.7	1.19	2.87	13.8	1.79	53	94	182	303	484	708	1017	1131	24.52	0.731	0.0029	0.048	0.052	1.46	0.054	20.7
ia20b05	(	0.08	17.4	0.77	2.57	17.9	2.18	62	107	199	329	503	749	1064	1139	26.51	0.810	0.0032	0.004	0.058	1.98	0.058	40.8
ia20b06	(	0.11	9.9	0.73	2.75	13.8	2.97	45	82	152	252	383	544	808	875	26.40	0.765	0.0027	0.006	0.066	2.28	0.101	23.6
ia20b07	(	0.07	13.5	0.80	2.63	13.0	2.64	44	76	147	237	371	537	785	854	24.36	0.797	0.0024	0.006	0.056	1.64	0.093	31.0
ia20b08	(	0.04	14.3	1.19	4.43	27.3	5.61	100	167	294	467	699	945	1307	1428	22.94	1.048	0.0042	0.002	0.077	1.67	0.068	23.3
ia20b09	(	0.47	15.1	0.98	2.37	14.6	2.44	52	94	172	280	437	628	894	971	24.89	0.805	0.0027	0.032	0.058	1.53	0.074	21.1
ia20b10	'	2.40	17.2	4.76	7.32	22.2	12.36	72	123	224	353	533	763	1096	1148	25.71	0.782	0.0033	0.108	0.065	1.88	0.263	4.8
ia20b11	'	1.99	12.8	4.23	10.64	48.5	9.31	138	209	348	526	785	1033	1402	1428	26.80	1.128	0.0047	0.041	0.098	2.12	0.100	4.1
ia20b12	'	5.02	17.4	5.10	6.81	18.7	6.41	81	107	203	324	518	734	1070	1178	22.37	0.834	0.0037	0.288	0.057	1.90	0.161	3.4
ia20b13	'	0.89	11.3	0.92	1.89	10.2	2.12	32	57	110	180	290	420	627	672	24.70	0.679	0.0020	0.058	0.051	1.81	0.100	15.0
ia20b14	'	0.03	13.8	0.49	1.94	10.6	2.87	40	75	141	236	386	583	841	914	25.80	0.681	0.0024	0.003	0.048	1.57	0.105	52.8
ia20b15	'	0.35	14.1	1.31	3.87	20.8	5.04	78	132	235	374	566	791	1102	1171	25.56	1.041	0.0036	0.017	0.071	1.86	0.102	17.0
ia20b16	'	0.14	13.8	0.85	1.99	10.4	2.08	44	81	158	255	417	594	876	929	28.41	0.700	0.0028	0.013	0.050	1.51	0.076	34.4
ia20b17	'	0.05	9.2	0.57	2.26	12.9	2.24	40	74	139	226	355	530	767	833	24.43	0.679	0.0027	0.004	0.052	1.80	0.085	29.6
ia20c04	(	32.21	48.9	25.51	22.85	23.0	2.42	57	99	184	296	461	683	987	1004	27.04	0.713	0.0030	1.400	0.058	1.57	0.060	1.5
ia20c05	(	0.78	15.9	1.04	2.82	12.8	2.18	44	86	158	263	418	613	894	925	28.03	0.665	0.0026	0.059	0.050	1.43	0.076	17.6
ia20c06	(	0.88	9.0	1.20	2.49	11.8	3.53	40	71	125	207	311	458	681	706	27.79	0.749	0.0023	0.076	0.059	2.09	0.138	8.6
ia20c07	(	0.41	18.8	4.23	11.79	51.8	5.76	149	246	424	651	961	1300	1763	1802	27.35	1.174	0.0058	0.009	0.065	1.37	0.058	8.1
ia20c08	(	0.70	8.6	1.22	3.31	17.0	3.40	53	90	159	254	366	532	764	848	27.26	0.671	0.0028	0.041	0.069	2.20	0.098	8.9
ia20c09	(	13.32	24.0	7.49	9.05	25.3	4.76	82	137	236	375	566	791	1063	1167	24.57	1.011	0.0037	0.527	0.076	1.88	0.089	2.3
ia20c10	1	0.23	13.4	1.75	4.95	25.4	6.44	86	137	252	385	585	820	1119	1174	28.08	1.108	0.0037	0.009	0.077	1.94	0.115	13.6
ia20c11	1	0.13	12.8	0.88	2.53	12.8	2.40	43	77	144	231	364	514	751	835	28.08	0.846	0.0027	0.010	0.057	1.98	0.087	26.0
ia20c12	1	2.22	12.0	2.45	3.56	12.9	3.15	37	59	123	198	300	434	632	663	27.60	0.765	0.0021	0.172	0.059	1.78	0.128	5.1

Table D.9 continued

Grain/spot Number	Isotope File name		SiO2 29 wt%	TiO2 49 wt%	Sr 88 ppm	Y 89 ppm	ZrO2 91 wt%	Nb 93 ppm	Ba 137 ppm	La 139 ppm	Ce 140 ppm	Pr 141 ppm	Nd 146 ppm	Sm 147 ppm	Eu 153 ppm	Gd 157 ppm	Tb 159 ppm	Dy 163 ppm	Ho 165 ppm	Er 166 ppm	Tm 169 ppm	Yb 172 ppm	Lu 175 ppm	Hf 178 ppm	Ta 181 ppm	Th 232 ppm	U 238 ppm
Cole Creek (CM023)																											
35	ie20c13	1	35.53		1.01	295	63.30	1.07	1.48	0.24	8.22	0.11	0.83	1.22	0.13	6.13	2.12	27.08	9.98	47.43	10.84	105.63	17.82	9572	0.78	38.4	63.0
37	ie20c14	1	33.86		1.08	813	65.04	1.43	0.19	0.08	10.25	0.09	1.82	2.49	0.13	13.49	4.27	55.12	20.43	93.12	21.39	195.53	33.19	8343	1.03	59.2	63.5
38	ie20c15	1	36.52		1.08	429	62.50	1.02	1.03	0.08	7.58	0.31	2.05	2.45	0.33	9.88	3.53	43.11	15.24	67.74	14.39	135.50	21.70	7855	0.51	28.8	28.7
39	ie20c16	1	36.08		0.86	594	62.90	1.12	0.09	0.02	7.77	0.13	2.03	3.85	0.33	16.26	4.97	59.91	20.31	90.79	19.14	173.48	29.07	7726	0.80	38.8	38.6
42	ie20c17	1	35.90		0.81	310	63.11	1.07	0.26	0.21	6.95	0.10	0.87	1.51	0.11	7.18	2.28	28.42	10.57	48.98	10.86	104.26	17.80	7873	0.56	25.9	37.4
43	ie20d04	(	36.12		0.80	387	62.89	1.14	1.04	0.30	7.95	0.13	1.34	1.98	0.15	8.76	2.98	36.76	13.18	61.15	13.29	124.00	20.92	7846	0.61	30.0	35.4
44	ie20d05	(	35.66		0.74	323	63.34	1.05	<0.03	0.02	5.82	0.05	1.00	1.58	0.15	7.96	2.42	31.63	11.00	50.62	11.70	110.53	18.34	7941	0.61	19.9	29.8
45	ie20d06	(	35.11		0.92	427	63.75	1.15	0.23	0.03	9.39	0.08	0.84	1.71	0.10	9.98	2.99	39.83	15.05	69.68	15.57	145.60	23.78	9063	0.88	48.7	74.1
46	ie20d07	(	37.09		0.75	381	61.92	0.95	0.09	0.06	5.88	0.10	1.43	2.22	0.23	9.84	3.08	38.62	13.16	59.33	13.02	116.86	20.11	7776	0.48	24.0	25.3
47.1	ie20d08	(	37.94		1.27	1312	60.83	1.48	0.03	0.02	13.33	0.15	3.19	6.56	0.31	36.18	10.70	128.89	44.55	193.96	39.55	344.32	56.51	8577	0.87	103.8	90.5
47.2	ie20d09	(	37.46		1.21	1181	61.32	1.39	0.15	0.02	11.84	0.14	2.86	6.21	0.33	32.36	9.73	116.16	40.50	175.92	36.27	317.83	51.98	8525	0.77	87.1	77.7
48	ie20d10	"	37.81		0.73	331	61.20	0.92	0.13	0.01	5.55	0.08	0.57	1.89	0.18	8.01	2.65	31.32	11.50	51.99	11.27	105.29	17.85	7889	0.48	14.0	17.8
50	ie20d11	"	38.61		1.49	477	60.29	1.50	1.80	0.32	11.16	0.16	1.44	1.95	0.13	10.01	3.43	44.16	16.26	77.14	17.03	159.42	27.26	8657	0.95	62.7	62.6
51	ie20d12	"	39.30		0.77	413	59.68	1.35	0.08	0.07	8.98	0.08	1.00	1.54	0.11	9.10	3.00	38.20	13.94	65.94	14.64	137.01	23.44	7999	0.77	40.5	55.1
53	ie20d14	"	38.35		1.12	420	60.54	1.49	1.38	0.17	10.34	0.09	1.11	1.82	0.09	9.00	3.01	38.56	14.40	67.55	15.12	140.27	24.16	8886	1.03	51.4	77.3
Sleep Creek (CM005)																											
1	ie20f04	0	34.45		4.78	491	64.51	1.27	9.17	0.71	8.57	0.23	1.98	2.54	0.22	11.80	3.67	48.68	16.77	78.22	17.26	157.02	27.73	8117	0.56	33.1	39.9
2	ie20f05	0	36.45		0.79	423	63.52	1.38	0.28	0.08	8.47	0.09	1.50	1.80	0.11	9.27	3.14	38.41	14.19	68.55	14.45	134.98	24.30	6138	0.65	39.5	50.6
3	ie20f06	0	36.70		1.17	690	62.24	1.17	0.14	7.84	28.33	2.86	11.50	4.97	0.33	18.71	5.38	61.94	23.13	104.39	22.40	195.72	35.34	8093	0.55	44.8	47.2
6	ie20f07	0	33.71		3.45	395	65.26	1.98	8.83	2.07	10.48	0.73	4.18	2.88	0.32	9.64	3.04	35.70	12.86	61.52	13.19	120.61	22.08	8113	0.47	23.8	24.6
7	ie20f08	0	33.18		1.12	943	65.66	1.34	0.63	0.13	10.67	0.35	4.84	6.81	0.38	27.14	8.12	94.79	32.91	140.46	29.67	263.69	44.09	8355	0.77	79.0	74.3
8	ie20f09	0	33.08		0.61	531	65.71	1.22	0.08	0.02	8.16	0.07	1.21	2.48	0.10	12.09	3.82	49.56	17.96	83.31	18.86	177.09	31.00	9696	0.86	53.1	90.4
9	ie20f10	1	36.29		1.22	691	62.52	1.11	0.24	0.30	13.07	0.20	1.97	4.14	0.10	13.70	4.97	59.12	20.89	97.58	21.86	205.60	39.75	8938	0.59	183.3	147.1
10	ie20f11	1	34.00		0.71	343	65.04	0.90	0.06	0.01	5.28	0.07	1.15	1.68	0.28	9.04	2.74	33.60	11.92	53.55	11.22	103.57	18.67	7676	0.37	13.8	13.5
17	ie20f12	1	34.53		0.78	350	64.47	1.15	0.32	0.09	6.73	0.08	1.05	1.76	0.11	7.85	2.43	31.50	11.76	53.30	12.22	116.10	20.60	8022	0.67	25.3	36.0
16	ie20f13	1	33.76		0.95	448	65.22	1.27	0.74	0.09	7.80	0.10	1.44	2.42	0.21	10.89	3.46	41.43	15.11	68.35	14.71	133.33	24.05	8092	0.80	32.8	38.5
20	ie20f14	1	33.97		0.73	430	65.02	1.36	0.17	0.05	8.30	0.09	1.21	1.95	0.11	9.98	3.30	39.71	14.40	66.46	15.02	136.88	24.51	8021	0.62	39.0	47.9
23	ie20f15	1	34.06		1.22	467	64.92	1.36	0.85	0.09	9.54	0.11	1.03	2.11	0.15	10.24	3.47	43.03	15.93	72.83	14.30	139.03	25.57	7859	0.56	36.7	47.5
12	ie20f16	1	33.81		2.34	591	65.24	3.19	5.14	2.20	14.26	0.96	5.39	3.36	0.41	14.61	4.66	55.29	18.82	86.90	18.16	166.31	31.43	6630	0.66	36.0	42.1

Table D.9 continued

Isotope File name		La	Ce	Pr	Nd	Sm	Eu	Gd	Tb	Dy	Ho	Er	Tm	Yb	Lu	ZrO2 - SiO2	Ratios Th/U	La/Hf	(La/Sm)n	(Gd/Yb)n	Nb/Ta	Eu/Eu*	Ce/Ce*
CM023)		Cole Creek (CM023)																					
is20c13	1	1.01	13.4	1.15	2.03	6.3	2.35	31	59	110	183	298	439	682	725	27.76	0.609	0.0018	0.123	0.047	1.38	0.121	12.4
is20c14	1	0.24	16.7	0.99	3.54	16.2	2.33	68	118	224	374	582	866	1214	1349	31.19	0.916	0.0040	0.014	0.056	1.39	0.055	27.4
is20c15	1	2.89	12.3	3.31	4.48	16.6	5.95	50	99	175	279	423	583	842	882	25.98	1.005	0.0028	0.174	0.059	2.00	0.180	4.0
is20c16	1	0.89	12.7	1.45	4.44	28.0	5.92	82	138	244	372	567	775	1077	1182	26.83	1.004	0.0036	0.003	0.076	1.87	0.110	16.5
is20c17	1	0.89	11.3	1.10	1.91	10.2	1.90	38	63	116	194	308	440	648	715	27.20	0.893	0.0022	0.057	0.056	1.90	0.082	11.4
is20d04	(	1.25	13.0	1.38	2.94	13.4	2.62	44	82	150	241	382	536	770	850	26.77	0.848	0.0027	0.093	0.057	1.85	0.091	9.9
is20d05	(	0.10	9.5	0.51	2.18	10.5	2.59	40	67	129	201	316	474	687	745	27.68	0.886	0.0023	0.010	0.058	1.71	0.102	30.8
is20d06	(	0.14	15.3	0.91	1.84	11.5	1.73	50	83	182	276	436	630	904	987	28.64	0.857	0.0028	0.012	0.055	1.31	0.058	29.2
is20d07	(	0.24	9.8	1.07	3.13	15.0	4.01	49	84	150	241	371	527	736	817	24.83	0.951	0.0026	0.016	0.057	1.98	0.124	14.7
is20d08	(	0.08	21.7	1.80	6.97	44.5	5.48	182	298	524	818	1212	1602	2139	2297	22.89	1.148	0.0086	0.002	0.085	1.68	0.048	25.8
is20d09	(	0.10	19.3	1.55	6.26	42.0	5.89	163	269	472	742	1099	1459	1973	2112	23.85	1.120	0.0061	0.002	0.082	1.80	0.058	23.4
is20d10	'	0.03	9.1	0.68	1.91	12.8	3.16	40	73	127	211	325	456	654	725	23.39	0.794	0.0023	0.002	0.082	2.01	0.119	25.5
is20d11	'	1.33	18.2	1.71	3.15	13.2	2.27	50	95	180	298	482	690	990	1109	21.86	0.759	0.0031	0.101	0.051	1.58	0.071	12.0
is20d12	'	0.29	14.6	0.83	2.19	10.4	1.89	48	83	155	255	412	593	851	953	20.39	0.734	0.0029	0.028	0.054	1.74	0.057	28.1
is20d14	'	0.71	16.9	0.98	2.42	10.9	1.80	45	83	157	264	422	612	871	982	22.19	0.695	0.0027	0.065	0.052	1.45	0.057	20.1
CM005)		Steep Creek (CM005)																					
is20f04	0	2.98	14.0	2.47	4.33	17.2	3.92	59	102	191	307	489	700	975	1127	30.07	0.832	0.0034	0.173	0.051	2.27	0.102	5.1
is20f05	0	0.32	13.8	0.89	2.19	10.8	1.89	47	87	158	260	416	585	838	988	26.05	0.780	0.0030	0.030	0.058	2.14	0.088	27.3
is20f06	0	33.09	48.2	28.68	25.17	33.6	5.89	94	149	252	424	652	907	1216	1437	25.54	0.950	0.0044	0.985	0.077	2.12	0.092	1.5
is20f07	0	8.71	17.1	7.82	9.15	19.3	5.87	48	84	145	238	385	534	749	898	31.55	0.870	0.0027	0.451	0.085	4.19	0.187	2.1
is20f08	0	0.56	17.7	3.80	10.80	48.0	6.78	136	225	395	603	878	1201	1638	1792	32.50	1.063	0.0053	0.012	0.063	1.74	0.074	8.1
is20f09	0	0.10	13.3	0.80	2.65	16.8	1.83	61	108	202	329	521	755	1100	1260	32.63	0.586	0.0032	0.008	0.055	1.79	0.047	29.7
is20f10	1	1.28	21.3	2.12	4.30	28.0	1.89	89	138	240	384	610	877	1277	1616	28.23	1.110	0.0044	0.045	0.054	1.89	0.035	12.6
is20f11	1	0.04	6.8	0.76	2.52	12.5	4.60	45	76	137	218	335	454	643	759	31.04	1.024	0.0024	0.003	0.071	2.45	0.159	21.4
is20f12	1	0.38	11.0	0.85	2.31	11.9	1.91	39	67	128	215	333	495	721	845	29.94	0.702	0.0026	0.032	0.055	1.71	0.074	18.0
is20f13	1	0.36	12.4	1.10	3.14	16.4	3.71	55	96	168	277	427	596	828	978	31.45	0.851	0.0030	0.023	0.066	2.13	0.104	16.7
is20f14	1	0.20	13.5	0.95	2.64	13.2	1.93	50	91	161	264	415	608	850	997	31.05	0.813	0.0031	0.015	0.059	2.19	0.081	23.5
is20f15	1	0.38	15.6	1.18	2.25	14.3	2.70	51	86	175	292	455	579	864	1039	30.66	0.771	0.0033	0.027	0.060	2.41	0.082	19.9
is20f16	1	9.27	23.3	10.53	11.79	22.8	7.34	74	129	225	345	543	735	1033	1278	31.42	0.903	0.0046	0.406	0.072	4.84	0.151	2.4

Table D.10. LA-ICP-MS multi-element analysis of reference zircon Harvard 91500

Grain Number	Isotope File name	SiO2 30 wt%	TiO2 49 wt%	Sr 88 ppm	Y 89 ppm	ZrO2 91 wt%	Nb 93 ppm	Ba 137 ppm	La 139 ppm	Ce 140 ppm	Pr 141 ppm	Nd 146 ppm	Sm 147 ppm	Eu 153 ppm	Gd 157 ppm	Tb 159 ppm	Dy 163 ppm	Ho 189 ppm	Er 169 ppm	Tm 169 ppm	Yb 172 ppm	Lu 176 ppm	Hf 178 ppm	Ta 181 ppm	Th 232 ppm	U 238 ppm
91500chip5	la30a04	39.03	0.0014	0.74	135.4	60.19	0.94	0.05	<0.01	2.71	0.014	0.19	0.37	0.22	1.86	0.75	10.69	4.73	24.8	6.42	87.7	12.6	5785	0.58	28.7	61.1
91500chip5	la30a18	35.17	0.0014	0.65	120.9	64.13	0.80	0.05	<0.01	2.36	0.011	0.18	0.38	0.16	1.77	0.68	9.62	3.97	21.4	5.46	59.8	11.4	5211	0.49	23.4	70.2
91500chip5	la30b18	31.77	0.0014	0.53	108.2	67.80	0.70	<0.01	0.001	2.10	0.007	0.10	0.33	0.14	1.64	0.58	8.51	3.54	19.4	4.95	53.5	10.1	4681	0.48	20.6	62.4
91500chip5	la30c18	35.14	0.0014	0.51	118.9	64.17	0.80	<0.01	0.001	2.32	0.009	0.15	0.28	0.18	1.95	0.64	9.14	3.83	21.1	5.53	58.0	11.0	5159	0.49	22.9	68.0
91500chip5	la30e18	34.57	0.0014	0.59	121.3	64.73	0.81	<0.02	<0.01	2.46	0.009	0.17	0.38	0.18	1.76	0.71	10.06	4.00	21.8	5.66	62.9	11.8	5275	0.47	24.0	71.5
91500chip5	la30g04	33.66	0.0014	0.58	114.0	65.67	0.73	<0.01	0.001	2.24	0.005	0.16	0.27	0.16	1.74	0.62	8.79	3.72	20.0	5.25	54.5	10.5	4826	0.47	21.9	65.0
91500chip5	la30g18	34.20	0.0014	0.58	111.0	65.13	0.75	<0.06	<0.01	2.26	0.010	0.19	0.28	0.16	1.66	0.60	8.56	3.63	20.2	5.27	58.0	10.9	5048	0.50	21.4	66.6
91500chip5	la30h14	32.06	0.0014	0.51	112.1	67.28	0.72	<0.01	<0.01	2.22	0.007	0.15	0.33	0.15	1.74	0.63	8.83	3.68	20.3	5.19	55.3	10.7	4777	0.44	21.7	65.5
91500chip5	la30d18	29.06	0.0014	0.47	101.4	70.36	0.67	<0.06	0.004	2.07	0.011	0.17	0.26	0.13	1.51	0.59	8.04	3.32	17.8	4.81	50.9	9.5	4364	0.40	19.7	58.7
91500chip6	la30a03	39.75	0.0014	0.73	150.6	59.51	0.97	<0.05	<0.01	2.86	0.007	0.26	0.36	0.19	2.50	0.84	12.39	4.95	26.4	7.02	71.7	13.8	5351	0.52	31.9	92.0
91500chip6	la30b03	35.14	0.0014	0.61	128.0	64.21	0.84	0.11	0.008	2.43	0.012	0.19	0.44	0.19	1.83	0.70	10.17	4.16	23.2	5.93	61.7	12.3	4752	0.45	27.6	79.2
91500chip6	la30c03	40.31	0.0014	0.60	154.2	56.96	0.87	0.03	0.001	2.85	0.010	0.27	0.50	0.22	2.44	0.92	12.52	5.05	27.8	7.14	74.8	14.8	5295	0.59	32.7	94.9
91500 chip6	la30d03	34.40	0.0014	0.55	141.8	64.91	0.80	0.04	0.004	2.59	0.011	0.18	0.35	0.22	2.36	0.82	11.32	4.84	25.9	6.45	68.6	13.8	5030	0.48	30.4	83.1
91500chip6	la30e03	29.70	0.0014	0.48	112.7	69.74	0.68	<0.04	0.001	2.17	0.009	0.18	0.31	0.17	1.87	0.60	9.15	3.73	20.3	5.21	55.1	10.9	4165	0.39	23.6	67.8
91500chip6	la30f03	37.13	0.0041	0.59	137.1	62.21	0.81	<0.01	0.004	2.62	0.014	0.19	0.48	0.23	2.28	0.77	11.33	4.45	24.5	6.42	68.6	12.9	4820	0.44	29.8	86.6
91500chip6	la30g03	33.54	0.0014	0.50	128.6	65.64	0.74	<0.03	<0.01	2.35	0.008	0.19	0.33	0.20	1.70	0.70	10.24	4.28	22.9	5.88	61.0	12.2	4543	0.43	28.7	76.2
91500chip6	la30h03	35.05	0.0014	0.54	137.5	63.38	0.83	0.05	0.001	2.55	0.007	0.11	0.41	0.20	2.22	0.79	11.24	4.50	25.2	6.32	67.4	13.2	4959	0.48	28.9	83.0
91500chip6	la20a03	39.64		0.59	129.7	59.71	0.81	<0.06	0.002	2.42	0.013	0.21	0.35	0.19	1.87	0.74	10.49	4.32	23.5	6.06	62.5	12.3	4836	0.44	27.5	78.5
91500chip6	la20a18	37.25		0.55	130.5	62.08	0.82	0.10	0.015	2.46	0.011	0.21	0.51	0.20	2.24	0.77	10.94	4.32	23.6	6.13	64.6	12.3	5046	0.52	27.5	78.9
91500chip6	la20b18	35.54		0.51	126.9	63.81	0.75	<0.06	0.004	2.44	0.010	0.21	0.36	0.20	1.93	0.72	10.24	4.26	22.8	5.94	62.4	11.7	4728	0.49	27.1	77.1
91500chip6	la20c18	34.90		0.51	125.0	64.48	0.73	0.11	0.002	2.44	0.014	0.22	0.40	0.20	2.17	0.73	10.47	4.13	22.4	5.81	61.3	11.7	4675	0.43	28.4	77.8
91500chip6	la20d15	36.79		0.55	127.3	62.54	0.75	<0.06	0.005	2.49	0.013	0.14	0.35	0.22	2.07	0.75	10.43	4.16	23.1	5.90	62.2	11.7	4897	0.47	28.9	78.4
MUN91500	la20a04	38.60		0.62	139.3	62.74	0.84	0.04	0.003	2.53	0.013	0.21	0.32	0.22	2.28	0.79	11.48	4.63	25.1	6.52	67.1	13.3	5033	0.54	32.9	84.0
MUN91500	la20b03	38.02		0.59	148.4	63.34	0.84	0.01	0.003	2.83	0.016	0.22	0.55	0.24	2.48	0.85	11.57	4.75	25.7	6.43	68.7	13.5	4809	0.57	33.5	90.0
MUN91500	la20c03	34.07		0.60	140.5	65.31	0.80	<0.20	0.003	2.51	0.014	0.21	0.44	0.22	2.28	0.80	10.98	4.57	24.8	6.27	66.3	12.8	4568	0.53	31.7	85.7
MUN91500	la20d03	34.22		0.58	141.8	66.15	0.78	<0.04	0.004	2.55	0.014	0.19	0.46	0.25	2.27	0.79	11.30	4.55	24.9	6.22	65.2	13.0	4622	0.52	32.2	86.6
chip591500	la20b03	35.39		0.44	122.8	63.98	0.83	0.06	0.001	2.40	0.013	0.21	0.33	0.20	1.98	0.69	9.69	4.09	21.9	5.70	60.0	11.7	4651	0.44	25.4	75.1
chip591500	la20h17	32.76		0.44	118.7	66.70	0.76	0.09	0.004	2.27	0.009	0.23	0.43	0.20	1.92	0.70	9.59	4.05	21.4	5.62	59.8	11.4	4465	0.45	25.6	74.7
MUN 91500	au27a18	35.00		0.52	136.5	64.32	0.78	0.19	0.020	2.40	0.012	0.20	0.42	0.20	2.00	0.77	10.92	4.50	24.6	6.39	66.0	13.3	4917	0.49	28.7	71.3
MUN 91500	au27a18	33.89		0.53	141.7	65.67	0.80	0.20	0.011	2.49	0.012	0.19	0.42	0.21	2.07	0.81	11.12	4.63	25.5	6.58	68.0	13.2	4912	0.48	29.1	72.8
MUN 91500	au27c18	34.73		0.54	147.9	64.57	0.82	0.10	0.014	2.50	0.019	0.25	0.50	0.24	2.37	0.90	12.62	4.92	25.2	6.63	69.8	13.2	5138	0.51	30.3	75.2
MUN 91500	au27c18	35.31		0.55	150.2	63.98	0.83	0.11	0.013	2.53	0.019	0.25	0.52	0.25	2.42	0.91	12.83	4.99	25.4	6.72	70.5	13.3	5223	0.51	30.5	76.1
91500chip6	au27e03	37.30		0.57	148.8	62.02	0.89	0.08	0.005	2.65	0.014	0.23	0.41	0.25	2.32	0.84	11.62	4.95	28.5	6.92	71.9	14.0	5358	0.53	31.5	78.0
91500chip6	au27b18	33.53		0.49	131.2	65.80	0.76	0.04	0.006	2.35	0.013	0.20	0.34	0.21	1.97	0.77	10.74	4.39	23.8	6.12	64.4	12.2	4836	0.45	27.4	68.8
91500chip6	au27b18	32.88		0.46	128.8	65.47	0.75	0.05	0.007	2.32	0.013	0.21	0.34	0.21	1.94	0.75	10.61	4.32	23.4	6.01	63.5	12.0	4746	0.45	26.8	75.5
91500chip6	au27d09	33.95		0.49	131.8	65.39	0.75	0.07	0.008	2.43	0.014	0.23	0.41	0.20	2.10	0.73	10.88	4.32	23.7	6.09	64.9	12.5	4840	0.49	27.9	69.7
MUN 91500	au28a03	38.50		0.58	131.8	60.84	0.90	<0.19	0.006	2.51	0.010	0.25	0.38	0.22	1.99	0.73	10.67	4.23	23.9	5.89	60.0	12.6	5050	0.44	27.1	75.0
MUN 91500	au28b14	35.24		0.50	127.7	64.15	0.75	0.06	0.011	2.35	0.013	0.18	0.39	0.21	2.03	0.68	10.39	4.18	22.9	5.77	59.8	12.2	4813	0.41	28.4	69.9
91500chip6	au28a18	36.00		0.52	126.8	63.35	0.80	0.37	0.015	2.50	0.014	0.21	0.40	0.23	1.90	0.70	9.84	4.15	22.8	5.71	60.7	12.3	4917	0.47	28.7	73.5
91500chip6	au28a18	32.11		0.46	112.5	67.31	0.71	0.35	0.011	2.22	0.012	0.19	0.36	0.20	1.69	0.62	8.72	3.69	20.2	5.08	54.2	11.0	4363	0.41	23.5	64.5
91500chip3	oc16a03	38.20	0.0014	0.12	132.9	61.12	0.80	0.05	0.005	2.48	0.013	0.16	0.36	0.19	1.99	0.75	10.73	4.35	23.9	6.03	63.1	13.0	5567	0.50	25.6	75.9
91500chip3	oc16a18	37.24	0.0014	0.10	149.0	62.08	0.84	0.05	0.026	2.88	0.033	0.38	0.49	0.26	2.49	0.88	11.85	4.92	26.8	6.75	69.3	13.9	5360	0.53	26.8	84.3
91500chip3	oc16b03	37.77	0.0014	0.11	145.8	61.53	0.82	0.08	0.008	2.62	0.016	0.24	0.50	0.23	2.22	0.85	11.24	4.71	26.0	6.69	69.5	14.1	5669	0.55	26.8	82.0
91500chip3	oc16b18	37.20	0.0014	0.10	114.8	62.13	0.74	0.05	0.005	2.24	0.010	0.17	0.26	0.16	1.73	0.59	8.84	3.71	21.2	5.29	58.1	11.4	5404	0.48	21.3	65.8
91500chip3	oc16c03	38.44	0.0014	0.09	135.8	62.86	0.77	0.05	0.008	2.44	0.016	0.17	0.37	0.21	2.08	0.79	10.94	4.48	24.4	6.21	65.6	13.3	5431	0.52	28.4	75.7
91500chip3	oc16c12	38.97	0.0014	0.08	128.4	62.33	0.79	0.05	0.008	2.48	0.010	0.22	0.36	0.19	1.84	0.71	10.30	4.18	23.3	5.94	62.1	12.7	5665	0.49	24.5	73.0
91500chip6	la31a04	36.38	0.0014	1.82	145.1	61.00	0.81	0.73	0.010	2.49	0.022	0.20	0.30	0.28	2.33	0.87	12.13	4.54	24.6	6.24	63.8	12.0	4487	0.51	27.5	68.5
91500chip6	la31c18	38.13	0.0014	0.58	131.0	61.25	0.83	<0.21	<0.01	2.65	0.008	0.16	0.41	0.22	2.30	0.77	10.82	4.35	24.1	6.23	62.7	12.8	4503	0.47	29.1	69.8
91500chip6	la31b04	34.43	0.0014	0.45	122.1	64.98	0.76	<0.18	0.002	2.37	0.010	0.18	0.43	0.21	1.88	0.68	9.88	4.04	21.8	5.44	61.2	11.5	4336	0.43	28.0	77.2
91500chip5	la31a18	37.35	0.0014	0.57	121.6	61.95	0.80	0.04	0.002	2.45	0.011	0.20	0.33	0.17	1.78	0.71	9.58	4.03	21.5	5.71	62.4	11.4	5323	0.52	23.5	72.1
91500chip6	la31c04	32.49	0.0014	0.47	102.2	66.89	0.72	0.02	<0.01	2.03	0.005	0.12	0.29	0.16	1.41	0.58	8.15	3.31	18.5	4.76	51.5	10.4	4711	0.43	19.8	61.4
91500chip5	la31b18	38.08	0.0014	0.52	109.2	63.26	0.79	<0.04	<0.002	2.20	0.008	0.16	0.38	0.16	1.72	0.59	8.85	3.70	19.9	5.30	55.7	10.7	5008	0.49	21.2	67.4
Mean		35.44	0.0015	0.51	129.5	63.91	0.79	0.11	0.007	2.44	0.012	0.20	0.39	0.20	2.01	0.73	10.43	4.28	23.2	5.97	62.7	12.2	4936	0.48	28.7	75.8
SD		2.41	0.0005	0.22	13.3	2.43	0.06	0.14	0.008	0.19	0.005	0.05	0.07	0.03	0.26	0.09	1.19	0.43	2.3	0.57	5.5	1.1	374	0.05	3.8	8.2
rds (%)		7	34	43	10	4	8	129	86	8	38	23	19	15	14	13	11	10	10	10	9	9	8	9	13	11
count		52	29	52	52	52	52	32	42	52	52	52	52	52	52	52	52	52	52	52	52	52	52	52	52	52
Lab working reference values (1)																										
reference 91500Chip6		32.86		0.05	125.3	67.03	0.89	0.04	0.003	2.21	0.010	0.14	0.39	0.20	2.16	0.89	11.13	4.45	23.7	6.42	69.6	12.0	6340	0.60	27.3	70.5
reference 91500 Chip5				0.13	114.4		0.75	0.07	0.014	2.32	0.014	0.21	0.35	0.17	1.69	0.67	10.16	3.92	21.5	5.90	63.3	11.4	5911		24.7	71.1
reference 91500 Chip3				0.10	139.3		0.82	0.14	0.005	2.67	0.011	0.27	0.47	0.21	2.21	0.88	12.06	4.62	26.4	7.01	74.5	13.3	6949		30.8	68.8

1. 91500 chips are from study of Wiedenbeck et al. (2004)

Table D.11. LA-MC-ICP-MS Hf isotope data for zircons from target rocks of the Mistastin Lake Crater

File Name	Grain Number	Age (Ma) [1]	±2s	176Lu/177Hf	±2SE	176Yb/177Hf	±2SE	178Hf(V)	176Hf/177Hf	±2SE	176Hf/177Hf (t) [2]	ε Hf [3]	±2SE
Anorthosite, Horseshoe Island (CMO32)													
oc16a5	z84_4	1439	9	0.000354	0.000017	0.009050	0.000348	2.26	0.281554	0.000072	0.281545	-11.5	0.7
oc16a6	z75_12	1439	9	0.000843	0.000001	0.026698	0.000159	2.08	0.281549	0.000038	0.281526	-12.2	0.4
oc16a9	z35_13	1439	9	0.000195	0.000006	0.005830	0.000190	3.25	0.281492	0.000038	0.281487	-13.5	0.4
oc16a10	z33_2	1439	9	0.000341	0.000009	0.009888	0.000176	2.04	0.281483	0.000039	0.281473	-14.0	0.4
oc16a11	z32_1	1439	9	0.000911	0.000016	0.026437	0.000228	1.70	0.281549	0.000087	0.281524	-12.2	0.7
oc16a12	z31_11	1439	9	0.000706	0.000022	0.020069	0.000710	1.79	0.281537	0.000086	0.281518	-12.5	0.9
oc16a13	z30-12	1439	9	0.000701	0.000015	0.021311	0.000503	2.03	0.281515	0.000053	0.281496	-13.2	0.6
oc16a14	z30_6	1439	9	0.000441	0.000018	0.013247	0.000680	1.93	0.281522	0.000051	0.281510	-12.7	0.5
oc16a17	z29_12	1439	9	0.000331	0.000016	0.009701	0.000480	1.41	0.281517	0.000053	0.281508	-12.8	0.6
oc16a18	z29_19	1439	9	0.000757	0.000079	0.020940	0.002192	1.48	0.281451	0.000086	0.281430	-15.6	0.7
oc16a19	z24_26	1439	9	0.002297	0.000052	0.074522	0.002528	1.65	0.281554	0.000054	0.281492	-13.4	0.5
oc16a20	z14_15	1439	9	0.001875	0.000087	0.051847	0.002343	1.51	0.281566	0.000051	0.281541	-11.6	0.5
Mean and SD												-12.9±1.1	
Granodiorite, North East shore (CM003)													
oc16b4	z65	1429	10	0.000843	0.000027	0.018221	0.000688	1.49	0.281610	0.000096	0.281592	-10.0	1.0
oc16b5	z62	1429	10	0.000580	0.000037	0.017520	0.001181	2.76	0.281597	0.000026	0.281581	-10.4	0.3
oc16b6	z60	1429	10	0.000757	0.000032	0.021502	0.000825	2.35	0.281622	0.000058	0.281602	-9.7	0.6
oc16b7	z56	1429	10	0.000582	0.000026	0.017456	0.000821	2.55	0.281522	0.000029	0.281506	-13.1	0.3
oc16b8	z54	1429	10	0.000478	0.000009	0.014272	0.000274	2.95	0.281573	0.000031	0.281560	-11.2	0.3
oc16b9	z48	1429	10	0.000606	0.000025	0.018453	0.000801	2.47	0.281589	0.000027	0.281573	-10.7	0.3
oc16b10	z46	1429	10	0.000782	0.000054	0.022712	0.001531	1.84	0.281551	0.000038	0.281530	-12.3	0.4
oc16b11	z2	1429	10	0.000500	0.000014	0.013956	0.000531	1.81	0.281625	0.000051	0.281611	-9.4	0.5
oc16b14	z11	1429	10	0.000445	0.000009	0.014485	0.000425	2.23	0.281535	0.000041	0.281523	-12.5	0.4
oc16b15	z12	1429	10	0.000329	0.000011	0.010711	0.000293	2.49	0.281625	0.000039	0.281616	-9.2	0.4
oc16b16	z41	1429	10	0.000411	0.000004	0.013477	0.000219	2.34	0.281604	0.000045	0.281593	-10.0	0.4
oc16b17	z22	1429	10	0.000458	0.000015	0.014403	0.000418	2.18	0.281589	0.000054	0.281576	-10.6	0.5
Mean and SD												-10.8±1.3	
Mangerite, Horseshoe Island (W05-45)													
oc16c4	z33	1451	12	0.000530	0.000020	0.015796	0.000693	1.11	0.281515	0.000135	0.281500	-12.8	1.3
oc16c5	z36	1451	12	0.000725	0.000006	0.021730	0.000401	1.12	0.281699	0.000117	0.281679	-6.5	1.2
oc16c6	z17	1451	12	0.000504	0.000005	0.014886	0.000186	1.37	0.281580	0.000082	0.281567	-10.5	0.8
oc16c7	z18	1451	12	0.000924	0.000037	0.029553	0.001012	1.38	0.281630	0.000089	0.281604	-9.1	0.7
oc16c8	z40	1451	12	0.000563	0.000016	0.016915	0.000420	0.99	0.281657	0.000093	0.281641	-7.8	0.9
oc16c9	z2	1451	12	0.000813	0.000007	0.018124	0.000255	1.19	0.281613	0.000191	0.281596	-9.4	1.9
oc16c11	z5	1451	12	0.000832	0.000008	0.018859	0.000468	1.08	0.281674	0.000132	0.281657	-7.2	1.3
oc16c12	z8	1451	12	0.000818	0.000021	0.018964	0.000723	1.07	0.281671	0.000125	0.281654	-7.3	1.2
oc16c13	z39	1451	12	0.000558	0.000023	0.016950	0.001000	1.02	0.281683	0.000113	0.281668	-6.9	1.1
oc16c14	z46	1451	12	0.000825	0.000020	0.019012	0.000503	1.00	0.281600	0.000109	0.281583	-9.9	1.1
oc16c15	z12	1451	12	0.000884	0.000026	0.019733	0.001033	0.98	0.281589	0.000123	0.281571	-10.3	1.2
oc16c16	z27	1451	12	0.000682	0.000039	0.020548	0.001122	0.84	0.281755	0.000127	0.281736	-4.5	1.3
Mean and SC												-8.5±2.2	
Granodiorite gneiss, North East shore (CM001)													
Magmatic zircon													
oc17d3	z27	1440	13	0.000832	0.000007	0.036211	0.000429	3.18	0.281612	0.000035	0.281590	-9.9	0.4
oc17d4	z26	1440	13	0.001586	0.000079	0.081035	0.001458	3.29	0.281679	0.000052	0.281637	-8.2	0.5
oc17d5	z33	1440	13	0.001408	0.000004	0.063933	0.000338	3.35	0.281653	0.000030	0.281614	-9.0	0.3
oc17d6	z32	1440	13	0.001586	0.000084	0.059857	0.003551	2.59	0.281704	0.000070	0.281661	-7.3	0.7
oc17d7	z29	1440	13	0.001056	0.000018	0.045163	0.000367	3.26	0.281635	0.000037	0.281606	-9.3	0.4
Mean and SD												-8.7±1.0	
Inherited zircon [4]													
oc17d8	z25	2300	85	0.000426	0.000076	0.014193	0.002522	1.66	0.281504	0.000058	0.281485	6.0	0.6

1. U/Pb concordia age in millions of years (this study).
2. The 176Hf/177Hf(t) values are calculated using a Lu decay constant of 1.865×10^{-11} (Scherer et al. 2001).
3. Epsilon Hf values are calculated with 176Hf/177Hf and 176Lu/177Hf (CHUR) values of 0.282772 and 0.0332, respectively (Blichert-Toft and Albarède 1997).
4. Average concordia age of dated inherited grains used to calculate initial Hf isotopic ratio

Table D.12. LA-MC-ICP-MS Hf isotope data for xenocrystic zircons from impact melt rocks of the Mistastin Lake Crater

File Name	Sample/Spot	Age (Ma) [1]	±2s	176Lu/177Hf	±2SE	176Yb/177Hf	±2SE	178Hf(V)	176Hf/177Hf	±2SE	176Hf/177Hf (t) [2]	ε Hf [3]	±2SE
Steep Creek (CM005)													
oc17b11	z3	1425	28	0.000801	0.000014	0.026559	0.000583	1.46	0.281615	0.000086	0.281593	-10.1	0.9
oc17b12	z1	1404	60	0.000720	0.000057	0.022598	0.002199	1.01	0.281597	0.000192	0.281578	-11.1	1.9
oc17b13	z20	1430	35	0.000559	0.000010	0.017242	0.000490	0.77	0.281791	0.000099	0.281776	-3.5	1.0
oc17b4	z7	1422	35	0.001155	0.000113	0.037403	0.003216	1.11	0.281712	0.000109	0.281681	-7.0	1.1
oc17b5	z8	1433	31	0.000615	0.000014	0.018933	0.000679	1.55	0.281626	0.000065	0.281609	-9.4	0.6
oc17b6	z9	1420	33	0.000759	0.000021	0.022758	0.001272	1.61	0.281701	0.000111	0.281680	-7.1	1.1
oc17b7	z10	1449	53	0.000510	0.000012	0.016046	0.000172	1.26	0.281707	0.000120	0.281693	-6.0	1.2
oc17b8	z17	1400	43	0.000573	0.000011	0.016980	0.000336	0.91	0.281749	0.000101	0.281734	-5.7	1.0
oc17b9	z2	1430	26	0.000624	0.000022	0.020491	0.000966	0.71	0.281626	0.000132	0.281611	-9.3	1.3
Cote Creek (CM023)													
oc17a10	z12	1427	67	0.001092	0.000011	0.037741	0.000582	1.67	0.281626	0.000080	0.281597	-9.9	0.8
oc17a11	z13	1385	43	0.000643	0.000042	0.021909	0.001514	1.40	0.281666	0.000062	0.281649	-9.0	0.6
oc17a12	z14	1421	39	0.000461	0.000010	0.015057	0.000277	2.63	0.281621	0.000058	0.281608	-9.7	0.6
oc17a14	z16	1412	36	0.000596	0.000038	0.018680	0.001259	1.33	0.281545	0.000107	0.281529	-12.7	1.1
oc17a17	z18	1438	29	0.000604	0.000026	0.019073	0.000740	1.97	0.281582	0.000077	0.281566	-10.8	0.8
oc17a18	z19	1437	26	0.000849	0.000021	0.024763	0.000861	2.54	0.281569	0.000043	0.281551	-11.3	0.4
oc17a19	z20	1464	28	0.000584	0.000035	0.019709	0.001397	1.39	0.281623	0.000113	0.281607	-8.7	1.1
oc17a20	z21	1558	60	0.000918	0.000042	0.028885	0.001079	1.29	0.281651	0.000102	0.281624	-8.0	1.0
oc17a21	z25	1459	30	0.000613	0.000073	0.026847	0.002527	1.51	0.281599	0.000109	0.281577	-9.9	1.1
oc17a22	z26	1430	31	0.000599	0.000009	0.018894	0.000230	1.55	0.281656	0.000089	0.281640	-8.3	0.9
oc17a23	z28	1426	24	0.000654	0.000019	0.021028	0.000652	1.37	0.281708	0.000088	0.281690	-6.6	0.9
oc17a24	z27	1410	38	0.000573	0.000004	0.018518	0.000185	1.38	0.281464	0.000064	0.281449	-15.6	0.6
oc17a25	z53	1449	23	0.000607	0.000008	0.019738	0.000272	2.00	0.281659	0.000080	0.281642	-7.6	0.8
oc17a26	z48	1413	38	0.000745	0.000038	0.023915	0.000863	2.85	0.281648	0.000043	0.281628	-9.1	0.4
oc17a5	z3	1428	20	0.000942	0.000029	0.032030	0.000974	2.38	0.281593	0.000044	0.281567	-10.9	0.4
oc17a6	z5	1409	35	0.000571	0.000018	0.018519	0.000431	1.50	0.281600	0.000080	0.281585	-10.8	0.8
oc17a7	z6	1419	23	0.000727	0.000024	0.024555	0.000579	1.96	0.281598	0.000064	0.281578	-10.6	0.6
oc17a8	z7	1394	30	0.000453	0.000023	0.014702	0.000472	2.90	0.281707	0.000048	0.281695	-7.2	0.5
oc17a9	z8	1437	38	0.001133	0.000031	0.036647	0.001085	2.03	0.281659	0.000055	0.281628	-8.6	0.6
South Ridge (CM065)													
oc17c10	z86	1465	70	0.000629	0.000018	0.021360	0.000472	2.17	0.281677	0.000081	0.281659	-6.9	0.8
oc17c11	z46	1423	69	0.000324	0.000002	0.012891	0.000054	2.91	0.281549	0.000037	0.281540	-12.0	0.4
oc17c12	z42	1427	53	0.000490	0.000006	0.019628	0.000385	2.89	0.281571	0.000028	0.281558	-11.3	0.3
oc17c13	z40	1380	59	0.000382	0.000024	0.013746	0.000491	2.72	0.281638	0.000043	0.281628	-9.9	0.4
oc17c16	z37	1390	67	0.000814	0.000006	0.020467	0.000318	1.37	0.281666	0.000066	0.281650	-8.9	0.7
oc17c16	z30	1396	48	0.000531	0.000022	0.018048	0.000475	2.78	0.281702	0.000063	0.281688	-7.4	0.6
oc17c19	z19	1416	52	0.001187	0.000043	0.040114	0.001135	1.82	0.281683	0.000099	0.281652	-8.2	1.0
oc17c20	z20	1430	45	0.000576	0.000008	0.018339	0.000398	2.73	0.281611	0.000089	0.281596	-9.9	0.9
oc17c21	z11	1398	43	0.000566	0.000014	0.021799	0.000695	2.82	0.281574	0.000037	0.281559	-11.9	0.4
oc17c23	z9	1411	42	0.000551	0.000040	0.022080	0.001853	2.94	0.281562	0.000028	0.281547	-12.1	0.3
oc17c24	z8	1426	57	0.001033	0.000056	0.036021	0.001784	1.38	0.281529	0.000088	0.281501	-13.3	0.9
oc17c25	z55	1457	51	0.000549	0.000013	0.018201	0.000573	1.72	0.281626	0.000049	0.281611	-8.8	0.5
oc17c26	z54	1473	54	0.000797	0.000090	0.026116	0.003340	1.77	0.281650	0.000085	0.281628	-7.6	0.8
oc17c27	z53	1393	53	0.000984	0.000077	0.034293	0.002931	1.36	0.281612	0.000092	0.281586	-11.1	0.9
oc17c4	z75	1396	43	0.000486	0.000022	0.018754	0.000314	2.86	0.281537	0.000037	0.281524	-13.2	0.4
oc17c5	z73	1426	40	0.000872	0.000032	0.034224	0.000854	2.79	0.281649	0.000038	0.281625	-8.9	0.4
oc17c6	z76	1360	56	0.000388	0.000010	0.015671	0.000380	2.62	0.281589	0.000042	0.281579	-12.1	0.4
oc17c7	z77	1331	69	0.000668	0.000005	0.022746	0.000287	1.59	0.281570	0.000099	0.281554	-13.6	1.0
oc17c9	z84	1460	61	0.000955	0.000040	0.032712	0.001132	2.24	0.281680	0.000064	0.281654	-7.2	0.6

1. U/Pb concordia age in millions of years (this study).
2. The 176Hf/177Hf(t) values are calculated using a Lu decay constant of 1.865×10^{-11} (Scherer et al. 2001).
3. Epsilon Hf values are calculated with 176Hf/177Hf and 176Lu/177Hf (CHUR) values of 0.282772 and 0.0332, respectively (Blichert-Toft and Albarède 1997).

Table D.13. LA-MC-ICP-MS Hf isotope data for reference zircon Plešovice

File Name	Age (Ma) [1]	±2s	176Lu/177Hf	±2SE	176Yb/177Hf	±2SE	178Hf(V)	176Hf/177Hf	±2SE	176Hf/177Hf (t) [2]	e Hf [3]	±2SE
oc16a1	336.9	0.2	0.000086	0.000001	0.004003	0.000053	3.01	0.282486	0.000040	0.282485	-2.8	0.4
oc16a2	336.9	0.2	0.000092	0.000001	0.004260	0.000066	2.91	0.282477	0.000032	0.282476	-3.1	0.3
oc16a3	336.9	0.2	0.000065	0.000001	0.002990	0.000036	4.39	0.282491	0.000031	0.282491	-2.5	0.3
oc16a4	336.9	0.2	0.000073	0.000002	0.003334	0.000069	4.07	0.282481	0.000022	0.282480	-2.9	0.2
oc16a15	336.9	0.2	0.000084	0.000000	0.003814	0.000029	3.44	0.282454	0.000022	0.282453	-3.9	0.2
oc16a16	336.9	0.2	0.000076	0.000001	0.003506	0.000058	3.53	0.282489	0.000030	0.282488	-2.6	0.3
oc16a21	336.9	0.2	0.000096	0.000001	0.004361	0.000075	3.24	0.282438	0.000025	0.282437	-4.4	0.2
oc16b1	336.9	0.2	0.000087	0.000002	0.003684	0.000118	5.21	0.282460	0.000019	0.282459	-3.7	0.2
oc16b2	336.9	0.2	0.000100	0.000001	0.004204	0.000082	5.00	0.282492	0.000018	0.282491	-2.5	0.2
oc16b3	336.9	0.2	0.000070	0.000001	0.002954	0.000021	5.00	0.282483	0.000023	0.282482	-2.8	0.2
oc16b12	336.9	0.2	0.000075	0.000001	0.003111	0.000055	4.30	0.282487	0.000022	0.282486	-2.7	0.2
oc16b13	336.9	0.2	0.000086	0.000001	0.004005	0.000059	3.71	0.282488	0.000042	0.282488	-2.7	0.4
oc16c1	336.9	0.2	0.000086	0.000000	0.003994	0.000043	3.48	0.282495	0.000037	0.282495	-2.4	0.4
oc16c2	336.9	0.2	0.000059	0.000000	0.002759	0.000049	3.56	0.282440	0.000038	0.282440	-4.3	0.4
oc16c3	336.9	0.2	0.000064	0.000001	0.002971	0.000041	3.59	0.282495	0.000034	0.282494	-2.4	0.3
oc16c17	336.9	0.2	0.000083	0.000001	0.003846	0.000072	3.31	0.282492	0.000041	0.282492	-2.5	0.4
oc16c18	336.9	0.2	0.000060	0.000001	0.002790	0.000088	3.63	0.282448	0.000039	0.282448	-4.1	0.4
oc16c19	336.9	0.2	0.000059	0.000000	0.002677	0.000043	3.24	0.282509	0.000041	0.282509	-1.9	0.4
oc17b1	336.9	0.2	0.000065	0.000001	0.003438	0.000087	3.69	0.282498	0.000040	0.282497	-2.3	0.4
oc17b2	336.9	0.2	0.000083	0.000001	0.003367	0.000081	3.53	0.282478	0.000036	0.282478	-3.0	0.4
oc17b3	336.9	0.2	0.000067	0.000000	0.003471	0.000042	3.46	0.282501	0.000029	0.282501	-2.2	0.3
oc17b14	336.9	0.2	0.000068	0.000002	0.003680	0.000137	3.50	0.282494	0.000042	0.282493	-2.5	0.4
oc17b15	336.9	0.2	0.000084	0.000001	0.003480	0.000072	3.15	0.282465	0.000036	0.282465	-3.5	0.4
oc17c1	336.9	0.2	0.000066	0.000001	0.003932	0.000081	4.49	0.282476	0.000026	0.282476	-3.1	0.3
oc17c2	336.9	0.2	0.000068	0.000000	0.003980	0.000051	4.26	0.282508	0.000031	0.282508	-2.0	0.3
oc17c3	336.9	0.2	0.000065	0.000001	0.003845	0.000028	4.29	0.282451	0.000028	0.282451	-4.0	0.3
oc17c14	336.9	0.2	0.000104	0.000002	0.005868	0.000056	4.29	0.282464	0.000025	0.282464	-3.5	0.2
oc17c15	336.9	0.2	0.000090	0.000001	0.005118	0.000030	4.15	0.282453	0.000030	0.282452	-3.9	0.3
oc17d1	336.9	0.2	0.000064	0.000000	0.003717	0.000051	3.77	0.282483	0.000028	0.282483	-3.5	0.3
oc17d2	336.9	0.2	0.000067	0.000000	0.003839	0.000031	4.01	0.282476	0.000033	0.282476	-3.1	0.3
oc17d9	336.9	0.2	0.000072	0.000002	0.004047	0.000132	3.88	0.282497	0.000032	0.282497	-2.3	0.3
oc17d10	336.9	0.2	0.000073	0.000002	0.004113	0.000105	3.91	0.282466	0.000031	0.282466	-3.4	0.3
Mean								**0.282478**			**-3.0**	
SD								**0.000019**			**0.7**	
Accepted Mean[4]								**0.282481**				
SD								**0.000013**				

1. U/Pb age from Sláma et al. (2008) in millions of years.
2. The 176Hf/177Hf(t) values are calculated using a Lu decay constant of 1.865×10^{-11} (Scherer et al. 2001).
3. Epsilon Hf values are calculated with 176Hf/177Hf and 176Lu/177Hf (CHUR) values of 0.282772 and 0.0332, respectively (Blichert-Toft and Albarède 1997).
4. from Sláma et al. (2008).

Table D.14. Least-squares modelling of trace elements in Mistastin impact melt rocks

	Low HFSE bulk melt rocks													High HFSE bulk melt rocks						
	All Bulk Rocks	Coté Creek						South Shore						All Bulk Rocks	Discovery Hill				North Shore	
	Mean n=20	CM088 bulk rock	CM088 matrix	CM023 bulk rock	CM023 matrix	CM025 bulk rock	CM025 matrix	W05-65 bulk rock	W05-65 matrix	CM071 bulk rock	CM071 matrix	CM067 bulk rock	CM067 matrix	Mean n=11	CM042 bulk rock	CM042 matrix	CM035 bulk rock	CM035 matrix	CM055 bulk rock	CM055 matrix
Rb	24	21	26	32	35	26	26	27	30	17	26	29	31	38	45	46	51	39	25	20
Sr	609	637	584	577	542	580	519	587	606	616	606	606	517	525	500	447	486	503	558	552
Pb	8	7	7	8	10	13	10	<LD	9	6	9	9	9	12	11	12	17	13	11	9
Ba	879	642	611	984	1062	1099	985	879	967	691	685	824	760	1182	1172	985	1194	1113	1249	1103
Y	17	15	13	20	15	23	14	21	18	13	13	16	18	30	30	26	31	13	30	22
Nb	9	8	7	11	8	12	6	13	10	8	6	9	8	16	16	8	18	8	16	9
Ce	103	135	69	126	60	105	49	83	83	67	62	118	73	150	158	115	176	54	114	72
Proportions, %																				
Anorthosite	73.2	81.3	74.8	66.5	62.2	65.1	60.0	70.3	72.0	77.9	77.1	73.7	62.7	55.0	51.6	48.1	49.0	55.6	59.1	61.6
Mangerite	21.9	11.3	8.4	27.4	0.0	32.1	0.8	18.4	14.7	13.5	2.5	19.7	6.7	37.8	37.7	17.1	39.1	0.0	39.1	23.1
Granodiorite	0.0	0.0	5.5	0.0	37.7	0.0	33.4	4.8	13.2	0.0	13.2	0.0	15.1	0.0	0.0	16.5	0.0	41.5	0.0	11.7
Total	95.2	92.6	86.7	93.9	99.8	97.2	94.2	93.8	99.9	91.4	92.8	93.4	84.4	92.8	89.3	81.8	88.1	97.2	98.2	96.4
Modeled composition																				
Rb	18	10	13	21	48	25	41	21	28	12	19	16	24	28	28	36	29	49	29	32
Sr	608	634	583	576	582	580	521	587	606	616	606	605	517	524	498	476	484	505	558	553
Pb	10	8	8	11	14	12	12	10	12	8	9	10	10	12	12	12	12	14	13	12
Ba	882	652	614	989	1134	1100	982	881	968	693	687	830	762	1197	1178	1056	1202	1109	1249	1100
Y	13	8	8	16	17	18	15	13	14	9	9	12	11	20	20	17	21	17	21	18
Nb	7	4	4	8	9	9	6	7	7	4	4	6	8	10	10	9	11	9	11	9
Ce	74	49	45	86	90	98	78	73	80	54	50	69	60	110	109	91	112	90	115	96
Residuals	obs.-cal.	obs.-cal.	obs.-cal.	obs.-cal.	obs.-cal.	obs.-cal.	obs.-cal.	obs.-cal.	obs.-cal.	obs.-cal.	obs.-cal.	obs.-cal.	obs.-cal.	obs.-cal.	obs.-cal.	obs.-cal.	obs.-cal.	obs.-cal.	obs.-cal.	obs.-cal.
Rb	5.81	10.02	12.51	10.62	-10.36	1.63	-14.81	6.60	2.08	4.98	7.03	12.89	7.51	9.30	16.88	15.51	21.94	-9.78	-4.76	-11.95
Sr	1.12	2.62	1.11	0.91	-1.70	-0.23	-1.42	-0.23	-0.09	0.52	-0.13	0.94	0.52	0.78	1.68	0.92	1.83	-2.01	-0.02	-0.86
Pb	-1.98	-1.55	-0.70	-3.05	-4.08	0.86	-2.62	-10.19	-2.87	-2.53	-0.33	-0.18	-0.14	-0.34	-1.31	0.44	4.75	-1.41	-1.91	-3.46
Ba	-3.65	-9.87	-3.64	-5.12	2.98	-1.35	2.80	-1.52	-0.96	-2.03	-1.87	-5.58	-2.31	-4.81	-6.40	-3.76	-8.17	3.95	-0.52	2.18
Y	3.49	6.79	5.95	4.62	-2.01	5.87	-0.08	7.84	3.83	4.38	4.43	4.29	7.00	9.60	9.76	10.84	9.98	-4.36	8.68	4.40
Nb	2.57	3.95	2.86	3.32	-2.47	3.05	-1.96	6.35	2.24	3.19	1.90	2.91	2.27	5.90	5.32	-1.24	5.66	-1.48	4.85	0.02
Ce	28.77	86.13	23.86	39.37	-27.11	8.68	-29.34	9.40	3.76	13.15	12.62	47.20	12.80	39.76	49.08	29.07	64.22	-36.15	-0.65	-23.90